RIJKSUNIVERSITEIT GRONINGEN

A study of radio–selected gravitational lenses

PROEFSCHRIFT

ter verkrijging van het doctoraat in de
Wiskunde en Natuurwetenschappen
aan de Rijksuniversiteit Groningen
op gezag van de
Rector Magnificus, Dr. D. F. J. Bosscher,
in het openbaar te verdedigen op
maandag 7 februari 2000
om 16.00 uur

door

Luitje Vincent Ewoud Koopmans

geboren op 7 maart 1973
te Enschede

Promotor: Prof. Dr. A.G. de Bruyn

Beoordelingscommissie:
Prof. Dr. F. H. Briggs
Prof. Dr. K.H. Kuijken
Prof. Dr. R.H. Sanders

ISBN 90–901–3434–4

"I'm astounded by people who want to 'know' the universe when it's hard enough to find your way around Chinatown."

Woody Allen

Cover design: "L.V.E. KOOPMANS" lensed by a glass sphere. A spotlight illuminates the name *and* creates a shadow on the underlying plane. Created with Persistence of Vision(tm) Ray Tracer POV–Ray(tm) Version 3.0

Printed by Universal Press, Veenendaal

Contents

1

Introduction to Gravitational Lensing

Two of the most prominent problems in cosmology and astrophysics today are: (i) the uncertainty in the values of the cosmological parameters, which describe the geometry of the universe and (ii) the distribution and nature of the 'dark matter', that makes up most of the mass in the universe. In this thesis an attempt is made to address these questions, using arcsecond–scale strong gravitational–lens systems from the *Cosmic Lens All–Sky Survey* (CLASS).
To set the stage on which gravitational lensing plays a role, we shortly discuss general relativity and cosmology. Subsequently, we show what gravitational lenses are and how they can be used to solve some of the above–mentioned problems. We continue with a more detailed discussion of the key questions raised in this thesis: (1) What is the distribution of dark matter around (spiral) galaxies? (2) What is the nature of this dark matter? – Do they consist of massive compact objects? – and (3) What is the value of the Hubble parameter (H_0), i.e. the rate of expansion of the universe? Finally, we outline the framework of this thesis and how we have tried to (partially) answer these specific questions.

1.1 General Relativity

When Albert Einstein developed his theory of general relativity (GR) between 1905 and 1915, he could not have imagined its far reaching consequences, even though he already saw the special nature of his theory.

The difference between predictions, using either Newtons law of gravity or Einsteins field equations, are relatively small in almost all 'every–day' situations of gravitational dynamics. However, GR has several profound consequences, which not only sets it apart from Newtons law of gravity, but creates a much wider framework of physics. Whereas Newtons law of gravity acts in a framework of absolute space and time, GR does not. In fact GR was build around the central idea that both space and time are *not* absolute, but relative, depending on the space–time coordinates and velocities of both the observer and the occurring event, and on the distribution of matter and energy (e.g. Misner, Thorne & Wheeler 1973). Space had up to that moment always been regarded as 'flat' or Euclidean. This all changed when GR postulated that space–time should be curved in the presence of matter or energy. Space and time became dynamical entities.

Several of the profound consequences of GR are summarized below (e.g. Foster & Nightingale 1979):

- Perihelion advance: GR predicts an anomalous advance of perihelion of planetary orbits.
- Geodesic effect: GR predicts that the axis of a gyroscope freely orbiting a massive object will precess.
- Gravitational waves: GR predicts the existence of gravitational disturbances propagating with the speed of light.
- Spectral shift: GR predicts that radiation emanating from a potential is redshifted, whereas radiation going into a potential is blue shifted.
- Deflection of light: GR predicts that light is deflected from a straight line in the presence of a gravitational field.
- Time delay: GR predicts a time delay between light traveling in a straight line and light traveling through a gravitational field.

All these phenomena are a direct result of the curvature of space and time. They have all been confirmed by observations, except for the existence of gravitational waves, although indirect evidence for the latter has been gathered in the binary pulsar (Taylor, Fowler, & McCulloch 1979). If GR could only explain the dynamics of massive objects, it would not have had the same impact as it had with the unexpected consequences listed above. Especially in cosmology and gravitational lensing the last three phenomena play a defining role. The last two phenomena (underlined) form the basis of gravitational lensing (see Sect.1.3).

1.2 Cosmology

The success of GR in predicting the dynamics of the solar system raises the question whether it can *also* describe the dynamics of the universe as a whole.

Until the development of GR, no satisfactory theory existed that could describe the dynamics and evolution of the universe. It was widely believed to be static and in equilibrium, with masses moving under the influence of Newtonian gravity. The main objection against this description is that a static 'clumpy' universe cannot be stable and eventually collapses under the influence of gravity.

When GR was completed, it was clear that it would have profound implications for all aspects of cosmology. Many different space–time models were therefore studied. In 1922, Friedmann showed that for a homogeneous and isotropic universe there are three distinct classes of solutions for the space–time of the universe; open, flat and closed (see Appendix A). Although each solution implied that the universe was either expanding or contracting, the general misconception in those days was still that the 'real' universe was static. To obtain a static universe, Einstein introduced an extra term in his theory: the 'Cosmological Constant' (Λ). Although this was mathematically a correct solution, any small perturbation of the model parameters would result in either a collapsing or a forever expanding universe.

Through observations in the late 1920s by Slipher, Hubble and Humason, it became apparent that the universe was in fact expanding. This made Einstein drop this additional term, calling it the biggest mistake of his career. Recent observations, however, seem once more to support a non–zero value for Λ, but this time within the context of an expanding universe (e.g. Riess et al. 1998; Perlmutter et al. 1999).

Since the 1930s, GR has been the basis of our understanding of the dynamics and space–time curvature of the universe. Since then, a multitude of observational evidence has been gathered, building up to the standard cosmological model, which says that the universe started from a singular point some finite period of time in the past and expanded from thereon. This model will be discussed in somewhat more detail in the next section.

1.2.1 The Standard Cosmological Model

Because the universe is expanding, higher redshifts correspond to larger look–back times (see Appendix A). Hence, with increasing redshift the universe is smaller,

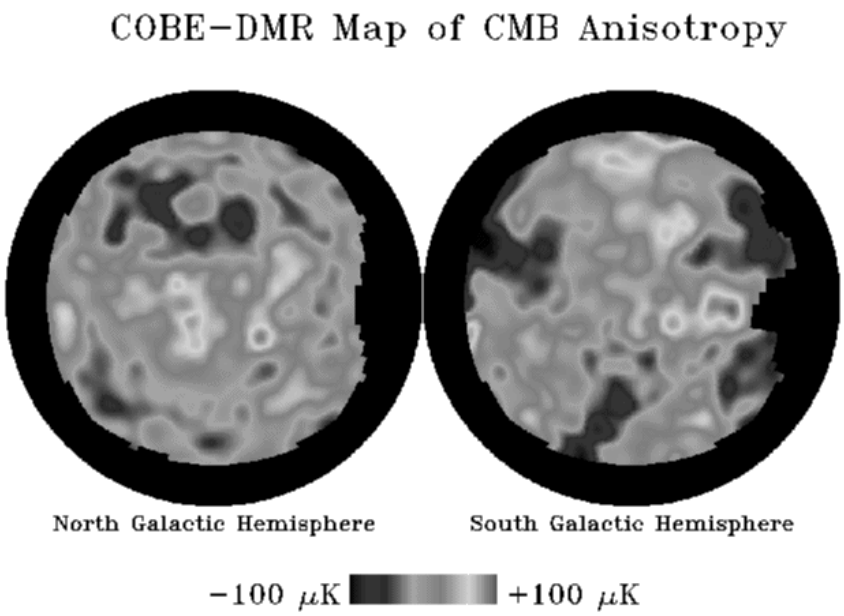

FIGURE 1.1— The COBE–DMR "Map of the Early Universe." This gray–scale image shows tiny variations in the intensity of the Cosmic Microwave Background (CMB) measured in four years of observations by the Differential Microwave Radiometers on NASA's Cosmic Background Explorer (COBE)[1].

large scale structures will smooth out and the temperature of the gas and the radiation increases. At some redshift the temperature was large enough to ionize the gas, which is predominantly hydrogen. Local thermodynamic equilibrium existed between the plasma and radiation. Looking back in time even further, the radiation temperature will keep increasing until the building–blocks of the elements, protons and neutrons, come into equilibrium, in a sea of photons, electrons, positrons and neutrinos. Still further back in time, eventually the size of the universe becomes zero (not counting possible quantum effects), i.e. the 'Big–Bang' singularity (see Kolb & Turner 1990 for a much more detailed description of the processes that are involved).

From this simple time–reversed picture of an expanding universe, a number of important elements emerge that form the pillars of the standard 'hot Big–Bang' cosmological model, which is based on a combination of GR and quantum mechanics, i.e. the cornerstones of modern physics and cosmology. The main observational evidence for this model is:

- In the context of some cosmological model, nucleosynthesis predicts the abundances of the light elements, i.e. hydrogen, deuterium, lithium and helium–3 and 4 (e.g. Kolb & Turner 1990). Observations of these abundances show remarkable agreement with the predictions from detailed numerical simulations. Although small deviations still exist, systematic effects, such as the creation (destruction) of helium (deuterium/lithium) in stars, uncertainties in the degrees of freedom of elementary particles, the half–life of the neutron and inhomogeneous nucleosynthesis, could explain these deviations (e.g. Peacock 1998).

- At some point during the expansion

[1] The COBE datasets were developed by the NASA Goddard Space Flight Center under the guidance of the COBE Science Working Group and were provided by the NSSDC.

of the universe, the radiation temperature decreases to ~3000 K at which point electrons and ions can recombine to form neutral gas, predominantly hydrogen and helium, leaving behind a sea of thermalized photons which we now detect as the *Cosmic Microwave Background* (CMB). Observations with the COBE satellite (e.g. Smoot et al. 1990) have revealed this black–body radiation in all directions on the sky, with an average temperature of 2.728±0.004 K (95% CL) (Fixsen et al. 1996). On a ~7° angular scale small temperature fluctuations have been found with $(\Delta T/T)_{rms}$=35±2 μK (Fig.1.1; Banday et al. 1997). Three fundamental processes could have generated these fluctuations:

1. Gravitational perturbations. Density perturbations introduce perturbations in the photon temperature through different gravitational redshifts.
2. Intrinsic (adiabatic) perturbations. Differences in the coupling between matter and radiation can suppress radiation in higher density regions thereby causing differences in temperature.
3. Doppler perturbations. Differences in velocity between regions causes different Doppler shifts in frequency and thus temperature.

Thus, perturbations in the CMB radiation are directly related to perturbations in the mass density and its velocity at the time of recombination ($z \approx 1100$). A detailed analysis of the CMB angular–power spectrum therefore provides an enormous amount of information about the cosmological parameters and the physics in the early universe (e.g. Efstathiou & Bond 1999).

- The expansion of the universe, as expected from the most general class of solutions to the field equations in GR (i.e. the Friedmann equations), also supports the standard cosmological model. It explains for example why the brightness of objects decreases with increasing redshift. The fact that the universe was smaller in the past also leads naturally to the occurrence of recombination and nucleosynthesis.
- The density perturbations, reflected in the temperature perturbations in the CMB, are the seeds for the formation of large–scale structure (LSS) as a result of gravitational instability (e.g. Kolb and Turner 1990; Peebles 1993; Padmanabhan 1993; Peacock 1998). Hence, they provide the seeds of most structures that we see in the universe today (i.e. galaxies, clusters, super-clusters, etc.). Comparison of numerical N–body simulations, using different cosmological scenarios, with observations can explain why the universe appears the way it is today (e.g. Bahcall et al. 1999; Peacock 1998).
- The age of the universe, as derived from the cosmological parameters (see Appendix A), agrees reasonably well with those determined from the oldest globular clusters. This agreement is not a priori expected, if the standard cosmological model were to be incorrect.

None of these observations by themselves definitively proves the standard hot Big–Bang cosmological model. However, combined they give a consistent picture of the evolution of the universe and seem to allow only a small range of values of the cosmological parameters (e.g. Bahcall et al. 1999). Hence, the expansion of the universe, the CMB anisotropy, the formation of LSS and the age of the universe all fit into a single consistent description of the universe, even though some important 'ingredients' are still unknown or very uncertain (e.g. Sect.1.2.2). This situation will, however, dramatically improve in the near future when (i) new observations of the CMB (e.g. the PLANCK and MAP satellite

missions), (ii) new large optical surveys up to redshifts of ∼0.2 (e.g. the Sloan–survey) and (iii) data of high–redshift sources from new 8–10 m class telescopes (VLT, Gemini, Keck, etc.), become available. The increase in computational power will furthermore provide a more detailed understanding of the evolution of structures, ranging from the LSS down to galaxies, using N–body simulations with ever increasing numbers of particles and the inclusion of gas hydrodynamics.

1.2.2 Remaining Problems

Several major questions about the standard cosmological model remain. These problems have to do with the facts that (i) the universe is homogeneous and isotropic on large scales, even though at high redshifts the present–day universe consisted of many causally disconnected regions, (ii) the curvature of the universe is small (i.e. $\Omega_m+\Omega_\Lambda$ is of order unity) and (iii) the LSS has formed from initial inhomogeneities, whose origin is not explained in the standard cosmological model.

To solve these problems, a short period of 'inflation' of the universe during an early phase transition was suggested by Guth (1981). It predicts the universe to be spatially flat ($\Omega_m+\Omega_\Lambda=1$), which indeed is supported by recent SNe–Ia observations (e.g. Riess et al. 1998; Perlmutter et al 1999) and observations of the CMB power–spectrum. It also predicts Gaussian density fluctuations in the primordial mass distribution, which form the seeds from which the LSS has evolved.

Perhaps the largest 'mystery' in cosmology is the apparent need for large amounts of *dark matter* in the universe. Both observations and theory suggest the presence of at most a few percent of the closure density of the universe (Ω_b∼few %) in the form of baryonic matter (Schramm & Turner 1998). However, more indirect evidence suggests that the density of matter in the universe (Ω_m) is as high as several tens of percent, based on (i) the mass-to-light ratio of clusters, (ii) the baryon fraction in clusters, (iii) the cluster abundance and evolution, (iv) the mass power spectrum of the LSS. Also less–constraining methods, based on measurements of the CMB power spectrum and gravitational lens statistics (e.g. Bahcall et al. 1999), seem to support this. It appears that this discrepancy of an order of magnitude between the total mass density and the baryon mass density in the universe will not be answered in the near future. Several dark–matter candidates in the form of MACHOs, WIMPs, AXIONs and massive neutrinos have been suggested (e.g. Kolb & Turner 1990). However, no strong support for either of these have been found so far.

1.3 Gravitational Lensing

We have seen in Sect.1.1 that general relativity (GR) postulates that space and time are curved in the presence of matter or energy. Based on the assumption that matter is distributed homogeneously on large scales – i.e. a consequence of the Cosmological Principle – one can derive the Friedmann equations that describe the dynamics of the universe on large scales (Sect.1.2 and Appendix A).

However, on small scales the universe is not smooth, but extremely clumpy. This is expressed in the hierarchical structure of the universe, which is built up from increasingly larger structures: stars, star–clusters, galaxies, galaxy groups, clusters, super–clusters and finally the LSS network.

Each of these deviations from a smooth mass distribution causes a deviation from the large–scale curvature of space–time, as described by the Robertson–Walker metric (see Appendix A). Depending on the density contrast of these structures with respect to their surrounding, these deviations can cause stronger or weaker observational effects. In particular they will distort the background emission from galaxies, quasars, the CMB, etc. This process of distorting our view of background emission is generally termed 'gravitational lensing'.

The effect of gravitational lensing was already studied by Einstein himself in 1912 and verified in the 1919 solar eclipse. Moreover, strong gravitational lensing by galaxies was predicted by Zwicky in

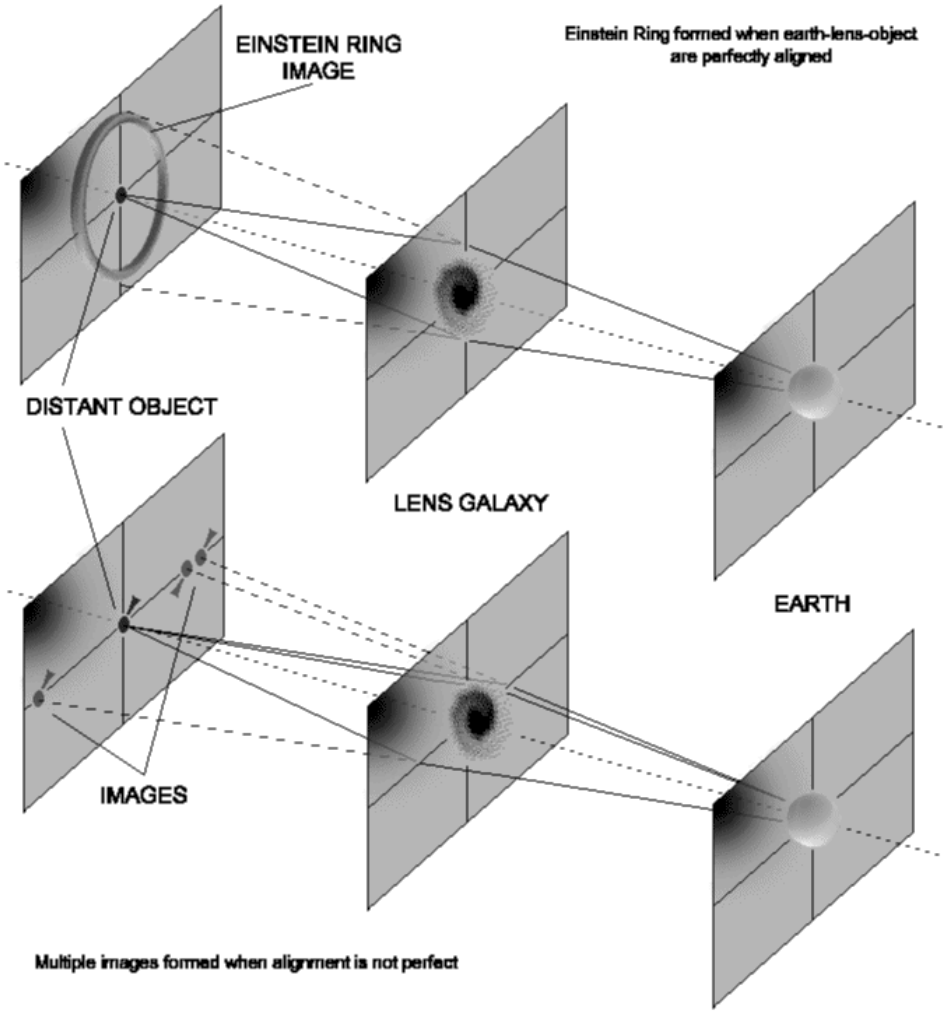

FIGURE 1.2— A diagram showing the formation of gravitational lens images. In the upper diagram the distant object, the lens galaxy and the Earth are perfectly aligned. The lens galaxy forms a perfect ring–like image, known as an 'Einstein Ring'. In the lower diagram the distant object, the lens galaxy and the Earth are not perfectly aligned. In this case the lens galaxy forms multiple images of the distant object. (Taken from the MERLIN PRESS RELEASE - PR9801).

1937. However, lensing only became a mature subject in 1979, when the first strong gravitational lens system, Q0957+561, was discovered by Walsh, Carswell & Weymann (1979). The system consists of two quasar images (z=1.39) that are separated by about 6 arcsec, lensed by a complex galaxy/cluster system at z=0.36. Since 1979, many new cases ($\sim$50) of multiple–image arcsecond–scale gravitational lens systems have been discovered, mainly the result of dedicated surveys.

One usually distinguishes three types of gravitational lensing: strong, weak and microlensing. Strong lenses are those systems where a foreground mass distribution creates multiple images of a single background source (Fig.1.2). In the case of weak lensing the background sources are distorted, but only singly imaged. The definition of microlensing is more ambiguous, because it is not based on the multiplicity

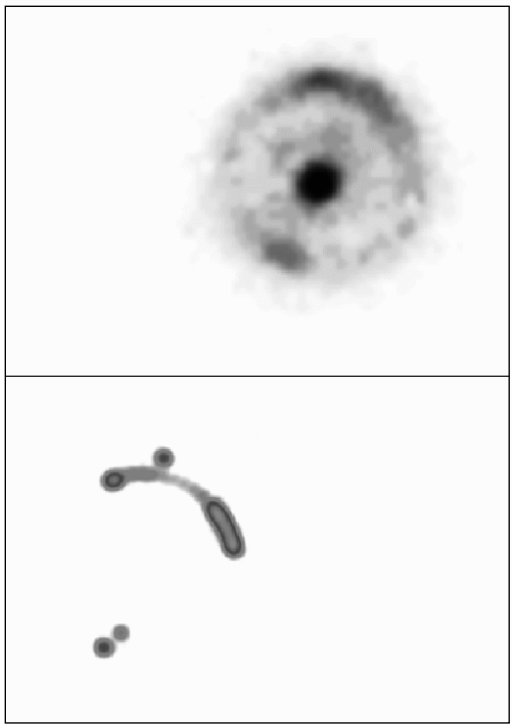

FIGURE 1.3— Upper: The Hubble Space Telescope picture of the distant galaxy 1938+666 which has been imaged into an Einstein ring by an intervening galaxy. The intervening galaxy shows up as the bright spot in the centre of the ring. The picture was taken in the infra-red region of the spectrum and the computer-generated color of the image has been chosen simply for ease of viewing. Lower: The MERLIN radio image of the radio source 1938+666 embedded in the distant galaxy. The double plus 'quad' structure shows that the radio source is not perfectly aligned with the lens galaxy and the Earth (Fig.1.2). The lens galaxy does not contain a radio source and hence does not show up in this image. The gray–scales are computer–generated and represent different levels of radio brightness. (MERLIN PRESS RELEASE - PR9801).

of images, but on the deflection angle (typically $\lesssim$1 mas) of the images. Hence, microlensing can be weak or strong in the sense described above. In the next three sections, we will discuss these three types of gravitational lens systems in somewhat more detail.

1.3.1 Strong Lensing

In this section, a brief overview of several of the major astrophysical and cosmological problems is given and in what way strong arcsecond–scale gravitational lens systems can help us to provide solutions. Some of these issues will also be discussed in more detail in Chapter 2.

Galaxy Structure and Evolution: In the case of multiple images of a single background source (Fig.1.2), the relative positions, brightnesses and distortions of the lens images, combined with the redshifts of the background source and foreground mass distribution, allows the observer to put constraints on the lens mass distribution, given a plausible cosmological model. Usually, this mass distribution is described by several parameters, such as a velocity dispersion, slope of the radial mass profile, ellipticity, position and position angle. Depending on the number of constraints, which usually depends on the number of lens images, one can solve for these parameters or constrain them from additional observations.

Strong gravitational lens systems can therefore be used to study the mass distribution of galaxies at intermediate redshifts, where most lens galaxies are situated (e.g. Turner, Ostriker & Gott 1984). A comparison of the mass–model of the lens galaxies with their surface–brightness distributions places them either on either the Tully–Fisher relation (Tully & Fisher 1977) or the Fundamental–Plane (Dressler et al. 1987; Djorgovski & Davies 1987), depending on the galaxy type. Changes in the slope or zero–point offset of these relations as a function of redshift can provide valuable information on the evolution of these galaxies.

The Determination of H_0: Another important application of strong arcsecond–scale gravitational–lens systems is the determination of the size of the universe or in particular the Hubble parameter H_0 (Refsdal 1964).

Light coming from different lens images travels along different paths before reaching the observer. It also travels through a different part of the gravitational potential of the intervening mass distribution. Both effects introduce a time delay between the

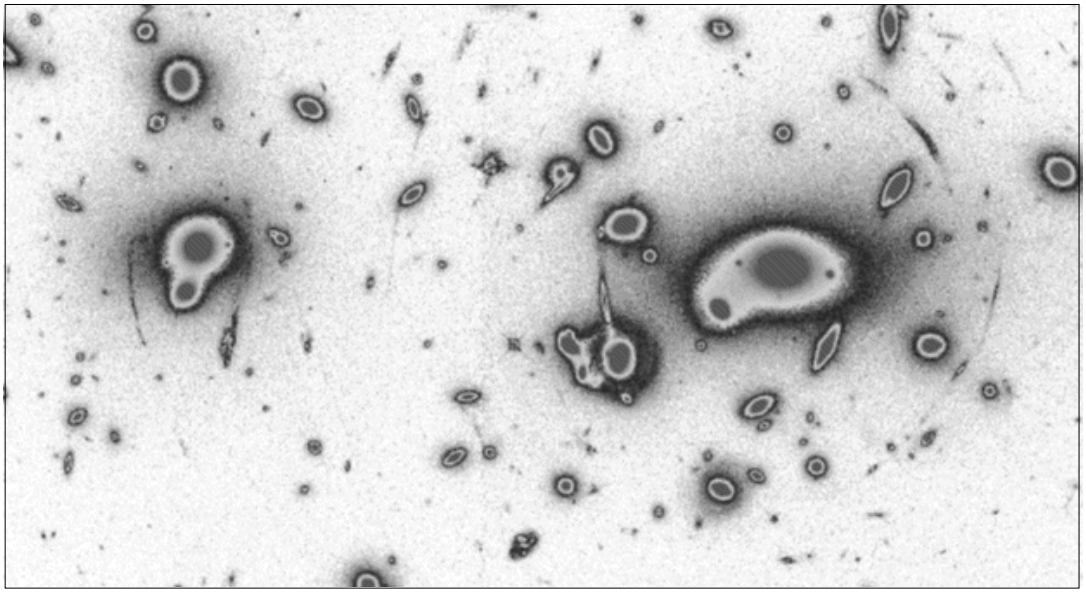

FIGURE 1.4— Gravitational lensing in the cluster Abell 2218, taken with the *Hubble Space Telescope* WFPC2 instrument (PF95–14 STScI OPO, April 5 1995 – W. Couch (UNSW), NASA)[2].

lens images, the first is called the 'geometrical time delay' and the second the 'potential time delay' (e.g. Schneider et al. 1992). Appendix B shows how these time delays are inversely proportional to H_0. Measuring the time delay between lens images can thus constrain H_0, given an appropriate mass distribution of the lens galaxy. A major advantage of measuring the value of H_0 this way, is the fact that it is a 'one–step' method. This avoids the difficulties that plague many of the 'distance–ladder' or 'standard–candle' methods. Moreover, gravitational–lens systems measure H_0 on cosmological scales, whereas distance–ladder methods are often locally confined and therefore suffer from larger fractional deviations from the Hubble flow. However also in the case of gravitational lensing, several systematic effects, in particular constraints on the slope of the radial mass profile of the lens galaxies need to be improved (e.g. Wucknitz et al. 1999).

The Determination of Ω_m and Ω_Λ: Given a representative mass model and distribution of the lens galaxies and the distribution of background sources, one can calculate the rate and properties of gravitational lens systems as a function of the cosmological parameters Ω_m and Ω_Λ. A comparison of the results from well–defined gravitational lens surveys with these calculations places constraints on these parameters. Although the measurement of Ω_m is very uncertain, a strong upper limit on Ω_Λ does result.

1.3.2 Weak Lensing

In the case of weak lensing, one cannot make use of the presence of multiple images of a single background source to reconstruct the foreground mass distribution. Instead, one has to determine the average distortion of many background sources (mostly galaxies) as function of position on the sky in order to reconstruct the mass distribution. The intrinsically randomly–oriented background galaxies are 'aligned' by the gravitational shear from the lensing mass distribution. One

[2]Based on observations with the NASA/ESA Hubble Space Telescope, obtained at the Space Telescope Science Institute, which is operated by the Association of Universities for Research in Astronomy, Inc. under NASA contract No. NAS5-26555.

can obtain information on this mass distribution by measuring a statistical average of the ellipticities and position angles of many background sources, resulting in a so called 'shear map'. By inverting this shear map, one obtains a map of the foreground mass distribution (e.g. Kaiser & Squires 1993).

The Mass Distribution of Galaxies, Groups and Clusters: One of the main applications of weak lensing is the reconstruction of the mass distribution of massive individual clusters. The mass distribution can be directly compared with independent methods, like dynamical or X–ray mass–distribution determinations. The study of substructure in the mass distribution, the cluster radial mass profile, the mass–to–light ratio, etc. are only a few of the many applications of weak lensing by clusters.

Similarly, although increasingly difficult, one can apply the technique of weak lensing to the study of the mass distribution of galaxies (e.g. Brainerd, Blandford & Smail 1996) and groups of galaxies (e.g. Hoekstra, Franx & Kuijken 1999) by averaging the shear of many of these systems and obtain a statistical average of their properties.

The Determination of Cosmological Parameters: A single cluster can contain many 'arclets', which are formed close to the critical curves. These arclets can span a range of different redshifts or angular diameter distances. Because the angular distance of these objects from the center of the cluster is a function of the mass distribution of the cluster and their redshifts, one obtains information on the relation between the angular–diameter distances and the redshift of these objects. This relation is a function of $\Omega_{\rm m}$ and Ω_Λ, independent of H_0. In the case of a relatively well understood mass distribution one can thus constrain both cosmological parameters (Link & Pierce 1998).

A less direct method to obtain constraints on $\Omega_{\rm m}$ is to assume that clusters and groups are systems, representative of the average mass distribution in the universe within their virial radius. By measuring the lensing mass–to–light ratios of these systems and multiplying them by the average luminosity density in a large volume of the universe, one can determine $\Omega_{\rm m}$.

Cosmic Shear and Large Scale Structure: The LSS, which has a small density contrast with respect to the average density of the universe, introduces very small distortions (i.e. the 'cosmic shear') on scales of $\sim 1^\circ$. By averaging the shapes of background objects over scales of tens of arcminutes to degrees, one obtains information on the mass distribution of the LSS. Comparing the observed cosmic shear with predictions from N–body simulations gives information about the structure formation in the universe, biasing (i.e. does light trace mass?) and the cosmological parameters (e.g. Schneider 1998).

1.3.3 Microlensing

Whereas strong and weak lensing play a role on galactic scales or larger, microlensing is caused by compact objects of stellar mass or less. The major goal of finding microlensing events is the possible detection of compact objects comprising the dark matter in the universe and the study of their mass function. Moreover, the extreme sharpness of the caustics in magnification pattern caused by stellar–mass objects sometimes allows a detailed study of the stellar atmosphere of the lensed star (Albrow et al. 1999), the study of the structure of AGNs and the detection of planets orbiting the lensing star (e.g. PLANET; see Sackett 1999 for a review).

Dark matter in the Galaxy: One of the biggest mysteries in cosmology is the nature of dark matter (Sect.1.2.2). Paczynski (1986) suggested that one could detect dark matter in the form of compact objects in the halo of our Galaxy through microlensing. A distribution of these compact objects can magnify background stars, resulting in a distinct shape of its lightcurve (Fig.1.5).

Several international teams have started surveys to search for these microlensing events [see Mao (1999) for a review of the current status on the results of several

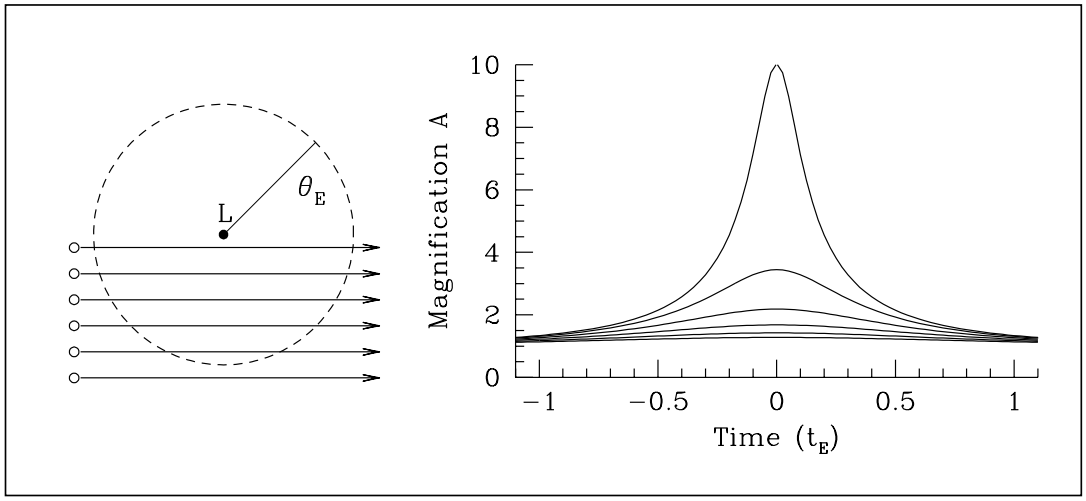

FIGURE 1.5— Microlensing light curve for a single–star lens. Sample source trajectories (left) and the resulting light curves (right). Taken from Sackett (1999).

microlensing surveys]. The results of the *MACHO* collaboration, for example, seem to suggest that ∼50% of the mass of the Galactic halo is composed of ∼0.5–$M_\odot$ objects (Alcock et al. 1997). If these compact objects consist of baryons, however, this result would be in disagreement with predictions from nucleosynthesis in the early universe. To alleviate these difficulties, a scenario of self–lensing of the LMC has been suggested, which can also account for the observed microlensing rate towards the LMC (Zhao 1998).

Quasar Microlensing: The optical regions of quasars are compact ($\lesssim 10^{16}$ cm) compared to the Einstein–ring radius of compact objects and could therefore be microlensed. Microlensing of an optical quasar has been shown in the strong–lens system 2237+0305 (Irwin et al. 1989). It has even been suggested that *all* high–redshift quasars are microlensed by compact objects (Hawkins 1996), based on their achromatic long–term variability.

1.4 Thesis motivation

The applications of strong, weak and microlensing listed in the previous sections raise several common questions:

1. What are the values of the cosmological parameters, in particular the value of H_0?
2. How do galaxies evolve from high redshifts to the present epoch (z=0)?
3. How is dark matter in (disk) galaxies distributed?
4. What is the nature of dark matter – i.e. Are they MACHOs?
5. If there exists so much dark matter, might there be galaxies with very large mass–to–light ratios – i.e. 'dark' galaxies?

The Cosmic Lens All–Sky Survey (CLASS) is a gravitational lens survey that was initiated in 1994 with the specific aim of finding strong arcsecond–scale GL systems suited to answer some of these questions, in particular 1 and 2. In Chapter 2, a description of the survey is given and the results that have been obtained thus far are summarized. The work in this thesis relies on several of the GL systems found in the CLASS

survey. Below, we will outline the chapters of this thesis and how they relate to, or are motivated by, the specific questions listed above.

1.4.1 Outline

One of the most prominent problems in cosmology and astrophysics today is the distribution and nature of dark matter. The flat rotation curves of spiral galaxies have long suggested the existence of 'dark–matter' halos (e.g. Van Albada & Sancisi 1986). However, even today the precise contribution of the luminous and dark matter components to the inner parts of spiral galaxies remains uncertain. Also the distribution of the dark matter is controversial. Whereas some believe that most of the dark matter can be found in the plane of the galaxy, others think that it is more spherically distributed (see Sackett 1999b for a review on the methods to determine the shapes of galaxy dark–matter halos). In Chapter 3, we present the first successful attempt to constrain the mass distribution of the dark–matter halo around an edge–on spiral lens galaxy (i.e. CLASS B1600+434), using gravitational lensing. This technique is unique in the sense that it is independent from the nature or the dynamical state of the lensing mass distribution.

The other 'classical' problem in cosmology is the precise value of the Hubble parameter (H_0). Until several years ago, its value was believed to lie somewhere in the range of 50 to 80 km s^{-1} Mpc^{-1}. Most determinations of H_0 rely on the combination of several different distance estimators, making these 'distance–ladder' methods inherently uncertain. Refsdal (1964) showed that GL systems can be used to determine H_0 in one single step by measuring the time delay between a pair of lens images. To determine H_0 from this time delay, however, one requires a representative model for the mass distribution of the lens galaxy. Although these mass models can be determined from the properties of the lens images in principle, the mass models for two–image GL systems, like B1600+434, are usually ill–constrained. Instead of using the measured time delay to constrain H_0, one can also use it to constrain the mass distribution of the dark–matter halo once H_0 is known to an accuracy of $\lesssim$10%. In Chapter 4, the light curves of the lensed images of B1600+434 are shown from an eight–month monitoring campaign in 1998 with the VLA at 8.5–GHz. From these we determine the time delay between the two lens images and place some preliminary constraints on H_0, assuming two different halo mass models.

Although there is much evidence in favor of the existence of dark matter, it is all circumstantial. Until now, no 'direct' detection of dark matter has been convincingly reported. One candidate for dark matter are massive compact objects (i.e. MACHOs), possibly stellar remnants or primordial black holes. Paczynski (1986) has suggested to detect these through microlensing (Sect.1.3.3). In Chapter 5, the serendipitous discovery of short–term 'non–intrinsic' variability in the VLA 8.5–GHz light curves of B1600+434 is presented, which is not caused by intrinsic source variability. Combined with multi–frequency WSRT monitoring data, we examine two plausible explanations: scintillation caused by the Galactic ionized ISM and microlensing of the background source caused by compact objects in the lens galaxy. The unique orientation of the lens galaxy – i.e. an edge–on spiral galaxy – offers two unique lines–of–sight through the lens galaxy; one going through the disk and bulge of the galaxy and one going through its dark–matter halo. Assuming the microlensing hypothesis is correct, which seems to be supported by the available observations, we place constraints on the mass of compact objects in the dark matter.

In the case of B1600+434 (Chapter 3) the determination of a detailed mass model of the lens galaxy is hindered by the small number of constraints coming from only two lens images. In the case of the CLASS GL system B1608+656, the number of images is four, which provide many more constraints on the lens mass distribution. Furthermore, three independent time delays between various image pairs have been

measured. This makes B1608+656 a much more suitable GL system than B1600+434 from which to determine H_0. The system provides even enough constraints to determine the radial mass profile of the mass distributions of the two lens galaxies. In Chapter 6, we present mass models for CLASS B1608+656 that were derived using VLA, VLBI and HST data. Additionally, we use the three time delays as independent constraints. Using these mass models, we derive constraints of the value of H_0, under a number of explicit assumptions.

In Chapter 7, a new CLASS GL system B1127+385 is presented. We derive its mass distribution, using substructure in the two lens images found from high–revolution VLBI observations.

The presence of dark matter around lens galaxies raises the question if maybe there exist galaxies that are completely composed of dark matter. This would imply that star–formation has either not started in these galaxies, or has somehow been prevented. The existence of this type of galaxy would clearly have profound consequences for the theory of galaxy formation. The CLASS survey is perfectly suited to find these systems if they make up a significant fraction of galaxies at intermediate redshifts. CLASS avoids any optical bias and selects galaxies only on the basis of their lensing properties. There should therefore be no a priori reasons not to find these systems in this survey, even if possible dust in the galaxy might obscure optical emission from the lens images. In Chapter 8, the best candidate for a 'dark lens' system or binary radio–loud quasar in the CLASS survey is presented.

In Chapter 9, we summarize the results obtained in this thesis and place them in a more general context. A short summary of related projects and future research is given as well. In Chapter 10, a Dutch summary is presented.

Appendix A: Cosmology

Here, we derive the equations that, for a given cosmological model, relate observables (e.g. redshifts, fluxes, etc) to particular distances (e.g. angular diameter, luminosty, etc.). We focus on those aspects that are important for gravitational lensing. For more details, the reader is referred to Peacock (1998) and references therein.

Field Equations

Einsteins theory of General Relativity states that the curvature of space-time is related to the distribution of matter and energy through the field equations

$$G_{\rm ab} - \Lambda g_{\rm ab} = \frac{8\pi G}{c^4} T_{\rm ab}, \qquad (1.1)$$

where $G_{\rm ab}$ is the tensor describing the geometry ('curvature') of space-time, $T_{\rm ab}$ is the energy-momentum tensor, describing the distribution of matter and energy, Λ is the cosmological constant and $g_{\rm ab}$ is the metric tensor (e.g. Misner et al. 1973).

If we know how matter and energy are distributed throughout space, we can solve these equations to obtain a relativistic description of the space-time curvature of the universe. However, to derive the solution to eqn.1.1, we first have to make two assumptions.

1. The cosmological principle: On large enough scales the properties of the universe are homogeneous and isotropic.
2. Weyls postulate: Matter and energy can be regarded as a perfect fluid (e.g. D'Inverno 1992).

Based on the field equation of GR, the cosmological principle and Weyls postulate, one can derive the complete space–time evolution of the universe.

Robertson-Walker Metric

From the cosmological principle it can be shown that the most general line element is given by

$$\begin{aligned} {\rm d}s^2 &= c^2{\rm d}t^2 - R(t)^2 \qquad (1.2)\\ &\times \left[\frac{{\rm d}r^2}{1-kr^2} + r^2({\rm d}\theta^2 + \sin^2\theta {\rm d}\,\phi^2)\right], \end{aligned}$$

the so called Robertson-Walker line element. $R(t)$ is a dimensionless scale factor

only depending on time, and k=+1, -1 or 0, which are related to spatial curvature. The dependence of $R(t)$ on time describes the spatial evolution of the universe and because the tensor $G_{\rm ab}$ can be fully described in terms of the metric tensor

$$\mathrm{d}s^2 = g_{\rm ab}x^{\rm a}x^{\rm b}, \tag{1.3}$$

it is clear that the R-W line element fully determines $g_{\rm ab}$ and $G_{\rm ab}$. Moreover, Weyls postulate tells us that

$$T_{\rm ab} = (\rho + p)u_{\rm a}u_{\rm b} - pg_{\rm ab}, \tag{1.4}$$

which is the energy-momentum tensor of a perfect fluid. The cosmological principle says that the density ρ and pressure p of matter and energy only depend on time through the scale factor $R(t)$. Combining eqn.1.4 with the full field equations – using the metric $g_{\rm ab}$ – gives us the desired relation between $R(t)$, the distribution of matter and energy in the universe and the cosmological constant.

Friedmann Equations

The Lagrangian determining the geodesic equation for a given metric $g_{\rm ab}$ is

$$\mathcal{L}(\dot{x}^{\rm c}, x^{\rm c}) = \frac{1}{2}g_{\rm ab}(x^{\rm c})\dot{x}^{\rm a}\dot{x}^{\rm b}, \tag{1.5}$$

where the dot denotes the derivative to some affine parameter u (see Foster & Nightingale 1979). For the R–W metric, one finds

$$\mathcal{L}(\dot{x}^{\rm c}, x^{\rm c}) = \tfrac{1}{2}\dot{t} - \tfrac{1}{2}R^2(t)\times \left[(1-kr)^{-1}\dot{r}^2 + r^2\dot{\theta}^2 + r^2\sin^2(\theta)\dot{\phi}^2\right]. \tag{1.6}$$

From the *Euler-Lagrange equations*

$$\frac{\mathrm{d}}{\mathrm{d}u}\left(\frac{\partial\mathcal{L}}{\partial\dot{x}^{\rm c}}\right) - \frac{\partial\mathcal{L}}{\partial x^{\rm c}} = 0, \tag{1.7}$$

one can subsequently determine four equations of the form

$$\ddot{x}^{\rm c} + \Gamma^{\rm c}_{\rm ab}\dot{x}^{\rm a}\dot{x}^{\rm b} = 0, \tag{1.8}$$

which are the required affinely parameterized geodesic equations. For the Lagrangian of the R–W metric, one finds the non–zero connection coefficients

$$\begin{aligned}
\Gamma^0_{11} &= RR'/(1-kr^2)\\
\Gamma^0_{22} &= RR'r^2\\
\Gamma^0_{33} &= RR'r^2\sin^2(\theta)\\
\\
\Gamma^1_{01} &= R/R'\\
\Gamma^1_{11} &= kr/(1-kr^2)\\
\Gamma^1_{22} &= -r(1-kr^2)\\
\Gamma^1_{33} &= -r(1-kr^2)\sin^2(\theta)\\
\\
\Gamma^2_{02} &= R'/R\\
\Gamma^2_{12} &= 1/r\\
\Gamma^2_{33} &= -\sin(\theta)\cos(\theta)\\
\\
\Gamma^3_{03} &= R'/R\\
\Gamma^3_{13} &= 1/r\\
\Gamma^3_{33} &= \cot(\theta),
\end{aligned} \tag{1.9}$$

with R'=$\mathrm{d}R/\mathrm{d}t$. Using the relation between the connection coefficients $\Gamma^{\rm c}_{\rm ab}$ and the Ricci tensor $R_{\rm ab}$

$$R_{\rm ab} \equiv \Gamma^{\rm c}_{\rm ac,b} - \Gamma^{\rm c}_{\rm ab,c} + \Gamma^{\rm d}_{\rm ac}\Gamma^{\rm c}_{\rm db} - \Gamma^{\rm d}_{\rm ab}\Gamma^{\rm c}_{\rm dc} \tag{1.10}$$

and the relation between the Ricci tensor and the Einstein tensor

$$G_{\rm ab} \equiv R_{\rm ab} - \frac{1}{2}Rg_{\rm ab}, \tag{1.11}$$

where $R \equiv g^{\rm ab}R_{\rm ab} = R^{\rm a}_{\rm a}$ is the curvature scalar, one ultimately finds two independent equations

$$\begin{aligned}
\left(\tfrac{\dot{R}}{R}\right)^2 &= \tfrac{8}{3}\pi G\rho - \tfrac{k}{R^2} + \tfrac{\Lambda}{3}\\
\ddot{R} &= \left[\tfrac{\Lambda}{3} - \tfrac{4\pi G}{3}\left(\rho + \tfrac{3p}{c^2}\right)\right]R,
\end{aligned} \tag{1.12}$$

which are called the Friedmann equations. These equations describe the dynamics of the scale factor $R(t)$, given the density ρ, pressure p and cosmological constant Λ. In the present universe $p/c^2 \ll \rho$, so normally one can put p=0.

Cosmological Parameters

We see from the Friedmann equations that $(\dot{R}/R)$ has units of s^{-1}. It represents the

rate of increase in the scale factor per unit length. In fact it precisely represents the observational relation between the speed by which galaxies move away from each other and their separation. This relation was first observationally discovered by Hubble and $(\dot{R}/R)$ is therefore called the Hubble parameter.

If we now define the dimensionless density parameters

$$\Omega_{\rm m} = \frac{8\pi G}{3H_0^2}\rho_0, \quad \Omega_k = -\frac{k}{R_0^2 H_0^2}, \quad \Omega_\Lambda = \frac{\Lambda}{3H_0^2}, \tag{1.13}$$

where the subscript zero denotes the present day values, we can write eqn.1.12 as

$$\Omega_{\rm m} + \Omega_k + \Omega_\Lambda = 1. \tag{1.14}$$

An often used definition is $\Omega_{\rm tot}$=$\Omega_{\rm m}$ + Ω_Λ, hence $\Omega_{\rm tot}$=1 − Ω_k. This implies that if $\Omega_{\rm tot}$=1, the curvature term Ω_k disappears (k=0) and the R–W line element reduces to that in Euclidean space. We call this a spatially flat universe.

In general $\dot{R}$ is not constant, but changes with time, determined by eqn.1.12. In this case $\ddot{R}\neq 0$. We can capture the change in $\dot{R}$ in the deceleration parameter q_0=$-(R\ddot{R}/\dot{R}^2)$, which reduces to

$$q_0 = \frac{1}{2}\Omega_{\rm m} - \Omega_\Lambda, \tag{1.15}$$

when combined with eqns 1.12 and 1.13. So, once we know $\Omega_{\rm m}$ and Ω_Λ, we can solve the Friedmann equations and get the dependence of R on time. Together with the R–W line element, we then know the description of the space–time evolution of the universe and are able to relate observables, such as redshifts, to distances.

Angular Diameter Distance

It can be shown that the ratio between the wavelength (λ_1) of light emitted at a redshift z, when the scale factor of the universe was R_1, and the wavelength (λ_0) that is observed at z=0, when the scale factor of the universe is R_0, is related by

$$(1+z) \equiv \frac{R_0}{R_1} = \frac{\lambda_0}{\lambda_1}. \tag{1.16}$$

All subscripts 0 denote the present epoch. If we write a=$(1+z)^{-1}$ and combine eqns 1.13 and 1.16 with the Friedmann equations (eqn.1.12), we get

$$\dot{a}^2 = H_0^2\left[1 + \Omega_{\rm m}\left(\frac{1}{a} - 1\right) + \Omega_\Lambda(a^2 - 1)\right], \tag{1.17}$$

or in terms of z,

$$\left[-\frac{{\rm d}z}{{\rm d}t}\right]^2 = H_0^2\,(1+z)^2 \times w(z). \tag{1.18}$$

Rewriting this equation and integrating over time, gives the look–back time of an object at redshift z_1 from the present epoch

$$t_0 - t_1 = \frac{1}{H_0}\int_0^{z_1} \frac{{\rm d}z}{(1+z)\times\sqrt{w(z)}}, \tag{1.19}$$

where

$$w(z) = (1+z)^2(1+\Omega_{\rm m}z) - z(2+z)\Omega_\Lambda. \tag{1.20}$$

For special cases of $\Omega_{\rm m}$ and Ω_Λ, this equation can be solved analytically. If $z_1\to\infty$ the look-back time will be the age of the universe. Typically the age of the universe lies in the range $(0.5\text{–}2.0)\cdot {\rm H}_0^{-1}$, were ${\rm H}_0^{-1}$ is called the Hubble time.

What we are really interested in, however, is the angular diameter distance to an object at some arbitrary redshift z_1. This distance relates observed angles with proper distances in the restframe of the observed object. From Lightmann et al. (1975) we find that the angular diameter distance is given by

$$d_{\rm A} = R_1 r_1. \tag{1.21}$$

So all we have to do is calculate r_1 to obtain $d_{\rm A}$. From the R-W metric we find for a light ray $({\rm d}s^2 = 0)$

$$\frac{{\rm d}r}{\sqrt{1-kr^2}} = \frac{c\,{\rm d}t}{R(t)}. \tag{1.22}$$

We can obtain ${\rm d}t$ as a function of z from eqn.1.19. Substituting ${\rm d}t$ and using the definitions in eqns 1.21 and 1.22, we find

$$\begin{aligned} d_{\rm A}(z_1) &= \frac{c(1+z_1)^{-1}}{H_0\sqrt{|\Omega_k|}} \\ &\times\; g\left(\sqrt{|\Omega_k|}\int_0^{z_1}\frac{{\rm d}z}{\sqrt{w(z)}}\right), \end{aligned} \tag{1.23}$$

where

$$\begin{array}{ll} g(x) = \sin(x) & \Omega_k < 0 \\ g(x) = \sinh(x) & \Omega_k > 0 \\ g(x) = x & \Omega_k = 0. \end{array} \quad (1.24)$$

From the angular diameter distance, one can also obtain the luminosity distance

$$d_{\rm L} = \sqrt{\frac{L}{4\pi F}}, \quad (1.25)$$

where L is the rest-frame luminosity and F the apparent flux, and the proper motion distance

$$d_{\rm M} = u/\dot{\theta}, \quad (1.26)$$

where u is the transverse velocity of an object and $\dot{\theta}$ its apparent angular motion. All three distances are related through

$$d_{\rm L} = (1+z)d_{\rm M} = (1+z)^2 d_{\rm A}, \quad (1.27)$$

using the definitions

$$d_{\rm M} = R_0 r_1 \quad \text{and} \quad d_{\rm L} = R_0^2 r_1 / R_1. \quad (1.28)$$

For applications in lensing both $d_{\rm A}$ and $d_{\rm L}$ are important. The first for calculating masses, delays, etc., the second for calculating the luminosity of the lens galaxy and from that its mass–to–light ratio.

Density and Volume

In lensing statistics one deals with distributions of lenses and sources. These distributions are typically characterized by the number density of objects as a function of redshift. To obtain the total number of objects, we first need to define a volume element. The best thing to do is to define a 'physical' volume in terms of the redshift z. If we define a volume with a width $\mathrm{d}r = -c\,\mathrm{d}t$, we obtain a volume element

$$\mathrm{d}V(z) = \left(\frac{c}{H_0}\right) \frac{d_{\rm A}^2(z)}{(1+z)\sqrt{w(z)}}\,\mathrm{d}z\,\mathrm{d}\Omega', \quad (1.29)$$

using eqn.1.19 and the fact the $d_{\rm A}^2\,\mathrm{d}\Omega'$ is the physical area inside the solid angle $\mathrm{d}\Omega'$ at $d_{\rm A}$. If the comoving density is constant, the physical density of objects is

$$n(z) = n_0(1+z)^3, \quad (1.30)$$

where n_0 is the density at $z = 0$. The number of object $\mathrm{d}N$ inside some volume becomes

$$\mathrm{d}N(z) = n(z) \cdot \mathrm{d}V(z) \quad (1.31)$$

We now have enough tools to continue with the theory of gravitational lensing.

Appendix B: Gravitational lensing

Here, we give a short introduction in the basic theory of gravitational lensing. For a more thorough treatment, one is referred to Schneider, Ehlers and Falco (SEF; 1992). Most of the following sections are based on SEF and the notation and mathematical derivations therein.

Light Deflection by a Point Mass

From General Relativity (GR) it can be shown that a light ray passing by a point mass, or more general, a spherical mass distribution, is deflected from a rectilinear motion by an angle

$$\hat{\alpha} = \frac{4GM(<\xi)}{c^2\xi}, \quad (1.32)$$

called the 'Einstein angle'. $M(\xi)$ is the mass enclosed inside the cylinder parallel to the light ray, with radius ξ (the impact parameter).

Light Deflection by a Surface Mass Density

One can extend the deflection angle by a point mass to that by a general surface mass distribution. If we write $M = \Sigma(\vec{\xi}')\mathrm{d}^2\xi'$, where $\Sigma(\vec{\xi}')$ is the surface density inside some small area $\mathrm{d}^2\xi'$, the total deflection angle vector at $\vec{\xi}$ becomes

$$\hat{\alpha}(\vec{\xi}) = \frac{4G}{c^2}\int_{R^2} \mathrm{d}^2\xi'\,\Sigma(\vec{\xi}')\frac{\vec{\xi}-\vec{\xi}'}{|\vec{\xi}-\vec{\xi}'|^2}, \quad (1.33)$$

where the sum over all masses M, contributing to the deflection angle, transforms into the integral over the surface density Σ, in the limiting when $\mathrm{d}^2\xi \to 0$. This deflection angle is valid for all surface mass distribution with velocities of matter much smaller than c and small deflection angles (i.e. the weak field limit).

The Lens Equation

Assuming that all angles are small, which is true for most astrophysical system, we can derive the following lens equation

$$\vec{\eta} = \frac{D_{\rm s}}{D_{\rm d}}\vec{\xi} - D_{\rm ds}\ \hat{\alpha}(\vec{\xi}), \qquad (1.34)$$

where $D_{\rm d}$, $D_{\rm s}$ and $D_{\rm ds}$ are the angular diameter distances between observer-lens, observer-source and lens-source, respectively (see Fig.1.2). The derivation of these angular diameter distances in the context of smooth Friedman-Robertson-Walker geometries of the universe with normalized densities $\Omega_{\rm m}$ and Ω_Λ was given in Appendix A.

Dimensionless Lens Equation

We can rewrite eqn.1.34 in a dimensionless form, using the following definitions

$$\vec{x} = \vec{\xi}/\xi_0 \quad ; \quad \vec{y} = \vec{\eta}/\eta_0, \qquad (1.35)$$

where ξ_0 is some arbitrary scale length and $\eta_0 = \xi_0 D_{\rm s}/D_{\rm d}$. If we write the surface density as

$$\kappa(\vec{x}) = \frac{\Sigma(\xi_0\vec{x})}{\Sigma_{\rm crit}}, \qquad (1.36)$$

with

$$\Sigma_{\rm crit} \equiv \frac{c^2 D_{\rm s}}{4\pi G D_{\rm d} D_{\rm ds}}, \qquad (1.37)$$

then the lens eqn.1.34 transforms into

$$\vec{y} = \vec{x} - \vec{\alpha}(\vec{x}), \qquad (1.38)$$

with the dimensionless deflection angle

$$\begin{aligned}\vec{\alpha}(\vec{x}) &= \frac{1}{\pi}\int_{\rm R^2} {\rm d}^2x'\kappa(\vec{x}')\frac{\vec{x}-\vec{x}'}{|\vec{x}-\vec{x}'|^2} \\ &= \frac{D_{\rm d}D_{\rm ds}}{\xi_0 D_{\rm s}}\hat{\alpha}(\xi_0\vec{x}). \qquad (1.39)\end{aligned}$$

The physical significance of $\Sigma_{\rm crit}$ is that a transparent lens needs to have only one point $\vec{x}$ with $\kappa(\vec{x})>1$ or $\Sigma(\xi_0\vec{x})>\Sigma_{\rm crit}$ to be able to produce multiple images. In all the next sections we will work with the dimensionless lens equation to simplify calculations. For applications to real physical lens systems it is trivial to reintroduce physical scales, using eqns 1.35 to 1.39.

The Deflection Potential

Equivalent to the relation between a gravitational force field and a gravitational potential, one can define the deflection angle $\vec{\alpha}(\vec{x})$ as the gradient of a deflection potential $\psi(\vec{x})$:

$$\vec{\alpha} = \nabla\psi, \qquad (1.40)$$

where we have dropped the explicit dependences on $\vec{x}$. Using this definition one finds that the deflection potential is given by

$$\psi(\vec{x}) = \frac{1}{\pi}\int_{\rm R^2} {\rm d}^2x'\kappa(\vec{x}')\ln|\vec{x}-\vec{x}'|. \qquad (1.41)$$

Combining eqn.1.40 with the lens eqn.1.38 we find

$$\vec{y} = \nabla\left(\frac{1}{2}\vec{x}^2 - \psi(\vec{x})\right), \qquad (1.42)$$

which can further be reduced to

$$\nabla\phi(\vec{x},\vec{y}) = 0, \qquad (1.43)$$

with the definition

$$\phi(\vec{x},\vec{y}) = \frac{1}{2}(\vec{x}-\vec{y})^2 - \psi(\vec{x}). \qquad (1.44)$$

We will see later on that the new potential ϕ is closely related to the light-travel time of ray going from source to observer. Eqn.1.43 is Fermats principle which states that in any optical lens system, images will always form at stationary points (extrema and saddle-points) on the light–travel time surface.

One can further show that

$$\nabla^2\psi = 2\kappa, \qquad (1.45)$$

if one inserts the identity $\nabla^2\ln|\vec{x}| = 2\pi\delta^2(\vec{x})$ into eqn.1.41. If we know the deflection potential ϕ, we can in principle derive all basic lens properties from this, such as the image positions, surface density of the lens, time-delays between images, etc. In the next section we show how an image of a background source is distorted by the presence of a foreground mass distribution.

The Magnification Matrix

To understand how an infinitesimally small vector in the source plane $\delta\vec{y}$ maps to a vector $\delta\vec{x}$ in the image plane, let us write the lens equation as

$$\vec{y} + \delta\vec{y} = \vec{x} + \delta\vec{x} - \vec{\alpha}(\vec{x} + \delta\vec{x}). \quad (1.46)$$

For sufficiently small $\delta\vec{y}$, we can do a first order Taylor expansion of eqn.1.46, such that

$$\delta\vec{y} = \delta\vec{x} - \begin{pmatrix} \frac{\partial\alpha_1}{\partial x_1} & \frac{\partial\alpha_1}{\partial x_2} \\ \frac{\partial\alpha_2}{\partial x_1} & \frac{\partial\alpha_2}{\partial x_2} \end{pmatrix} \delta\vec{x} = \left(\mathcal{I} - \frac{\partial\vec{\alpha}}{\partial\vec{x}}\right)\delta\vec{x}, \quad (1.47)$$

where $\mathcal{I}$ is the identity matrix. In the limit $|\delta\vec{x}| \to 0$, we get the Jacobian matrix

$$\mathcal{A} \equiv \frac{\partial\vec{y}}{\partial\vec{x}} = \left(\mathcal{I} - \frac{\partial\vec{\alpha}}{\partial\vec{x}}\right), \quad (1.48)$$

where $\mathcal{A}$ is called the magnification matrix. The determinant of $\mathcal{A}$ is the area ratio between an infinitesimally small region in the source plane and its mapping on to the image plane, as defined through the magnification matrix $\mathcal{A}$. So the magnification factor is

$$\mu(\vec{x}) = [\det \mathcal{A}(\vec{x})]^{-1}, \quad (1.49)$$

which can be positive or negative. Image with $\mu(\vec{x}) < 0$ are said to have negative parity, image with $\mu(\vec{x})>0$ positive parity. Those points $\vec{x}$ with $\det\ \mathcal{A}(\vec{x})=0$ are called 'critical points' and trace out a closed critical curve in the image plane. The mapping of a critical curve on the source plane, using eqn.1.38, is called a 'caustic'.

Convergence and Shear

Let us now examine the magnification matrix in more detail. If we combine eqn.1.40 :

$$\begin{pmatrix} \alpha_1 \\ \alpha_2 \end{pmatrix} = \begin{pmatrix} \frac{\partial\psi}{\partial x_1} \\ \frac{\partial\psi}{\partial x_2} \end{pmatrix}, \quad (1.50)$$

with eqn.1.48, one finds

$$\mathcal{A}_{ij} = \delta_{ij} - \psi_{ij}, \quad (1.51)$$

where δ_{ij} is the Kronecker delta function and ψ_{ij} are the second order derivatives to x_i and x_j, respectively. Using eqns 1.45 and 1.51, one can write the magnification matrix also as

$$\mathcal{A} = \begin{bmatrix} 1-\kappa-\gamma_1 & -\gamma_2 \\ -\gamma_2 & 1-\kappa+\gamma_1 \end{bmatrix}, \quad (1.52)$$

where

$$\gamma_1 = \frac{1}{2}(\psi_{11} - \psi_{22}) \text{ and } \gamma_2 = \psi_{12} = \psi_{21}. \quad (1.53)$$

The magnification becomes

$$\mu(\vec{x}) = \left[(1-\kappa)^2 - \gamma^2\right]^{-1}, \quad (1.54)$$

where $\gamma^2 = \gamma_1^2 + \gamma_2^2$. The eigenvalues of $\mathcal{A}$ are $a_{1,2} = 1 - \kappa \mp \gamma$ and the trace of $\mathcal{A}$ is $2(1-\kappa)$. Both the eigenvalues and magnification μ have a 'local' term κ (convergence), depending on the mass inside the beam, and a 'global' term $\gamma_{1,2}$ (shear) depending on the mass outside the beam.

Time Delay

Let us now derive an expression for the time delay between two gravitational lens images. This time delay is composed of two parts, the geometrical time delay and the potential time delay. The geometrical time delay reflects the difference in travel time due to the difference in light path between the images, the potential time delay reflects the time delay introduced by the difference in gravitational potential of the lens at the image positions.

The most elegant way to calculate the time delay is using the wavefront method. A spherical wavefront is emitted from a source at time t_0. This wavefront travels through space, but its spherical shape is deformed by the curvature of space-time around each mass distribution the wavefront encounters. In the weak-field limit the curvature of space and time can be decoupled and one can associate the geometrical time delay with the curvature of space and the potential time delay with the curvature of time.

If a mass distribution is massive enough, it can create a deformation in the wavefront, such that an observer sees the wavefront pass by him/her several times from different directions at different times t_i.

The number of times this wavefront passes the observer is the number of images created by the mass distribution (the gravitational lens). The time between two passes is the time delay between two lens images $t_i - t_j$.

The Wavefront:

Because a wavefront propagates independently from an observer, we can place the observer anywhere in space, without changing the wavefront itself. Let us therefore place the observer at a position $\vec{\zeta}_0$, where the wavefronts of two image pass simultaneously, but keep its redshift the same (z=0), such that there is no time delay between the two images. If we slowly move the observer away from this position towards its real position $\vec{\zeta}_\mathrm{f}$, the two wavefronts will not longer pass the observer simultaneously, but have some time delay between them. The time delay at $\vec{\zeta}_\mathrm{f}$ is what we want to know.

If the angle between the two images is $\vec{\vartheta}$ and we move the observer over some small distance $\mathrm{d}\vec{\zeta}$, the proper distance between the two wavefronts will be

$$\mathrm{d}l = c\,\mathrm{d}t = \vec{\vartheta}\cdot\mathrm{d}\vec{\zeta}. \tag{1.55}$$

So the time delay between the images becomes $\mathrm{d}t$. If we move the observer over $\mathrm{d}\vec{\zeta}$ obviously the image configuration (the image positions) will change as well. So the angular separation of the two images is a function of the observers position, $\vec{\vartheta} = \vec{\vartheta}(\vec{\zeta})$. Keep in mind that changing the observers position does not change the wavefront itself, but only the direction of the wavefront – hence the image position – as seen by the moving observer. By integrating over $\mathrm{d}l$, we can find an expression for the total time delay between two wavefront (two images) when the observer moves from $\vec{\zeta}_0$ to $\vec{\zeta}_\mathrm{f}$,

$$c\,\Delta t(\vec{\zeta}_f) = \int_{\vec{\zeta}_0}^{\vec{\zeta}_\mathrm{f}} \vec{\vartheta}(\vec{\zeta}')\mathrm{d}\vec{\zeta}' + c\,\Delta t(\vec{\zeta}_0). \tag{1.56}$$

All we have to do now is find the expression that links $\vec{\vartheta}(\vec{\zeta})$ to the source and image positions.

The Lens Equation Explicitly Including the Observer Position:

Suppose we define some point $\mathcal{O}'$ in the observer plane, such that the source lies at $\vec{\eta}'$ in the source plane, defined from the optical axis in the source plane going through $\mathcal{O}'$ and some fixed point $\mathcal{L}$ in the lens plane. If the observer is at point $\mathcal{O}$, displaced by some vector $\vec{\zeta}$ from $\mathcal{O}'$, the source will be displaced by some new vector $\vec{\eta}$ in the source plane, defined from the new optical axis going through $\mathcal{O}$ and $\mathcal{L}$. Both descriptions are equivalent and do not change the real physical lens system. However, the position of the observer has been explicitly taken into account.

The angles between the two optical axis for $\mathcal{O}$ and $\mathcal{O}'$ must be the same when going into or out of the lens plane at $\mathcal{L}$. From this we find

$$\frac{\vec{\eta} - \vec{\eta}'}{D_\mathrm{ds}} = \frac{\vec{\zeta}}{D(z_\mathrm{d}, 0)}, \tag{1.57}$$

where $D(z_\mathrm{d}, 0) = (1 + z_\mathrm{d})D_\mathrm{d}$ is the angular diameter distance between lens and observer (not observer and lens!). Combining this with the lens eqn.1.34, we find

$$\vec{\eta}' + \frac{D_\mathrm{ds}}{D_\mathrm{d}(1+z_\mathrm{d})}\vec{\zeta} = \frac{D_\mathrm{s}}{D_\mathrm{d}}\vec{\xi} - D_\mathrm{ds}\,\hat{\alpha}(\vec{\xi}), \tag{1.58}$$

thus the source position in dimensionless units becomes explicitly dependent on the observer position $\vec{\zeta}$, through

$$\vec{y} = \frac{1}{\eta_0}\left[\vec{\eta}' + \frac{D_\mathrm{ds}}{D_\mathrm{d}(1+z_\mathrm{d})}\vec{\zeta}\right]. \tag{1.59}$$

We can now start to simplify eqn.1.56.

Time Delay and Fermats Potential:

The angular separation between two lens images at $\vec{\xi}^{(1)}$ and $\vec{\xi}^{(2)}$ is given by

$$\vec{\zeta} = \frac{\xi_0(\vec{x}^{(2)} - \vec{x}^{(1)})}{D_\mathrm{d}}, \tag{1.60}$$

using eqn1.35. From eqn1.59 we furthermore find that

$$\mathrm{d}\vec{\zeta} = (1+z_\mathrm{d})\xi_0\frac{D_\mathrm{s}}{D_\mathrm{ds}}\mathrm{d}\vec{y}. \tag{1.61}$$

We then find that eqn.1.56 becomes

$$\begin{aligned} c\,\Delta t(\vec{y}_f) &= \xi_0^2 \frac{D_\mathrm{s}}{D_\mathrm{d} D_\mathrm{ds}}(1+z_\mathrm{d}) \\ &\times \int_{\vec{y}_0}^{\vec{y}_f} \mathrm{d}\vec{y}' \cdot \left[\vec{x}^{(2)}(\vec{y}') - \vec{x}^{(1)}(\vec{y}')\right] \\ &+ c\,\Delta t(\vec{y}_0). \end{aligned} \quad (1.62)$$

Using eqn.1.38, we furthermore find

$$\vec{x} \cdot \mathrm{d}\vec{y} = \mathrm{d}\left[\frac{\vec{y}^2}{2} - \phi(\vec{x},\vec{y})\right], \quad (1.63)$$

such that

$$\begin{aligned} c\,\Delta t(\vec{y}) = \xi_0^2 \frac{D_\mathrm{s}}{D_\mathrm{d} D_\mathrm{ds}}(1+z_\mathrm{d}) \times \\ \left[\phi(\vec{x}^{(1)},\vec{y}) - \phi(\vec{x}^{(2)},\vec{y})\right], \end{aligned} \quad (1.64)$$

with the suitable boundary condition that $\Delta t(\vec{y}_0) = 0$, when $\vec{x}^{(1)} = \vec{x}^{(2)}$. Eqn.1.64 shows us the relation between ϕ and the light travel time and confirms our initial suspicion that $\nabla\phi$=0 at the image positions is equivalent to Fermats principle.

The total 'extra' travel time of a deflected light ray compared to an undeflected ray (i.e. $\vec{x} = \vec{y}$) is

$$T(\vec{x},\vec{y}) = \xi_0^2 \frac{D_\mathrm{s}}{D_\mathrm{d} D_\mathrm{ds}}(1+z_\mathrm{d}) \cdot \phi(\vec{x},\vec{y}). \quad (1.65)$$

The first term in $\phi(\vec{x},\vec{y})$ (see Eqn.1.44) gives the geometrical time delay, due to the difference in path length between the deflected and undeflected light rays. The second term gives the potential time delay, due to the presence of a gravitational field in the case of a deflected light ray.

Classification of Images

Lens images can be classified into three different classes. Those that are formed at minima, at maxima or at saddle points of the time-delay surface ϕ. At minima (Type I) of ϕ, det$\mathcal{A} > 0$ and Trace$\mathcal{A} > 0$. At maxima (Type III), det$\mathcal{A} > 0$ and Trace$\mathcal{A} < 0$. At saddle points, det$\mathcal{A} < 0$. Following the definition of parity given previously, images formed at minima and maxima of ϕ have positive parity and those formed at saddle points have negative parity.

General Lens Theorems

We will state two theorems here (see SEF), which are of importance to gravitational lensing. We will not prove these, but those interested in the proof are referred to SEF.

Under the assumptions that $\kappa(\vec{x})$ is smooth and decreases faster than $|\vec{x}|^{-2}$ for $|\vec{x}| \to \infty$, the total lens mass is finite, the deflection angle $\vec{\alpha}(\vec{x})$ is continuous, tends to zero when $|\vec{x}| \to \infty$ and is bounded. Moreover,

1. Under the above assumptions, if $\vec{y}$ does not lie on a caustic, $n_I \geq 1$, $n < \infty$, $n_I + n_{III} \leq 1 + n_{II}$ and $n = n_I = 1$ for sufficiently large $|\vec{y}|$. The total number of images is $n = 1 + 2n_{II}$, hence odd. The number of even-parity images exceeds that of odd-parity images by one, $n_{II} \geq n_{III}$, and $n > 1$ if and only if $n_{II} \geq 1$.
2. Under the above assumptions, the image arriving at the observer first is of Type I and is brighter or equally bright as the image in absence of the lens.
3. If, and only if, an isolated lens has a point $\vec{x}$ with det$\mathcal{A} < 0$ can it produce multiple images. A sufficient, but not necessary condition is that there exist a point $\vec{x}$ with $\kappa(\vec{x}) > 1$.

References

Albrow, M. D., et al. 1999, ApJ 522, 1011

Alcock, C., et al. 1997, ApJ 486, 697

Bahcall, N. A., Ostriker, J. P., Perlmutter, S. & Steinhardt, P. J. 1999, Science, 284, 1481

Banday, A. J., Gorski, K. M., Bennett, C. L., Hinshaw, G., Kogut, A., Lineweaver, C., Smoot, G. F. & Tenorio, L. 1997, ApJ 475, 393

Brainerd, T. G., Blandford, R. D. & Smail, I. 1996, ApJ 466, 623

Caroll, S.M., 1997, "Lecture notes on General Relativity", gr-qc/9712019

D'Inverno, R., 1992, "Introducing Einsteins Relativity", Clarendon Press, Oxford

Djorgovski, S. & Davis, M. 1987, ApJ 313, 59

Dressler, A. , Lynden-Bell, D. , Burstein, D. , Davies, R. L., Faber, S. M., Terlevich, R. & Wegner, G. 1987, ApJ 313, 42

Efstathiou, G. & Bond, J. R. 1999, MNRAS 304, 75

Fixsen, D. J., Cheng, E. S., Gales, J. M., Mather, J. C., Shafer, R. A. & Wright, E. L. 1996, ApJ 473, 576
Foster, J., Nightingale, J.D., 1979, "A short course in General Relativity", Longman Inc, New York
Guth, A. H., 1981, Phys. Rev. D 23, 347
Hawkins, M. R. S. 1996, MNRAS 278, 787
Hoekstra, H., Franx, M., Kuijken, K. 1999, astro-ph/9911106
Irwin, M. J., Hewett, P. C., Corrigan, R. T., Jedrzejewski, R. I. & Webster, R. L. 1989, AJ 98, 1989
Mao, S. 1999, astro-ph/9909302
Kaiser, N. & Squires, G. 1993, ApJ 404, 441
Kolb, E. W. & Turner, M. S. 1990, "The early universe" Frontiers in Physics, Reading, MA: Addison-Wesley
Link, R. & Pierce, M. J. 1998, ApJ 502, 63
Misner, C. W., Thorne, K. S. & Wheeler, J. A. 1973, "Gravitation"
Paczynski, B. 1986, ApJ 304, 1
Padmanabhan, T. 1993, "Structure formation in the universe" Cambridge, UK: Cambridge University Press
Peacock, J. A. 1999, "Cosmological physics" Publisher: Cambridge, UK: Cambridge University Press
Peebles, P. J. E. 1993, "Principles of physical cosmology" Princeton Series in Physics, Princeton, NJ: Princeton University Press
Perlmutter, S., et al. 1999, ApJ 517, 565
Refsdal, S., 1964, MNRAS 128, 307
Riess, A. G., et al. 1998, AJ 116, 1009
Sackett, P.D. 1999, astro-ph/9907185
Sackett, P. D. 1999b, Galaxy Dynamics, proceedings of a conference held at Rutgers University, 8-12 Aug 1998. ASP Conference Series vol. 182 (San Francisco: ASP), edited by David R. Merritt, Monica Valluri, and J. A. Sellwood, 393
Schneider, P., Ehlers, J. & Falco, E. E. 1992, "Gravitational Lenses" Springer-Verlag Berlin Heidelberg New York
Schneider, P. 1998, ApJ 498, 43
Schramm, D. N. & Turner, M. S. 1998, Reviews of Modern Physics, 70, 303
Smoot, G., et al. 1990, ApJ 360, 685
Taylor, J. H., Fowler, L. A. & McCulloch, P. M. 1979, Nature 277, 437
Tully, R. B. & Fisher, J. R. 1977, A&A 54, 661
Turner, E. L., Ostriker, J. P. & Gott, J. R. , III 1984, ApJ 284, 1
van Albada, T. S. & Sancisi, R. 1986, Royal Society of London Philosophical Transactions Series, 320, 447
Walsh, D., Carswell, R. F. & Weymann, R. J. 1979, Nature 279, 381
Wucknitz, O. & Refsdal, S. 1999, astro-ph/9909291

2

The Cosmic Lens All–Sky Survey

THE *Cosmic Lens All–Sky Survey* (CLASS) is an international collaboration between institutes in the Netherlands, the UK and the US, that aims to find the largest statistically complete sample of gravitational lens systems to date. For this purpose ∼15 000 flat–spectrum radio sources in the northern hemisphere were observed with the VLA in A–array at 8.5 GHz. At least 17 new gravitational lens systems have been discovered thus far. The ultimate goal of the CLASS survey is to use these gravitational lens systems to constrain the cosmological parameters (i.e. H_0, Ω_m and Ω_Λ) and study the structure and evolution of intermediate redshift galaxies. The non–gravitational–lens systems furthermore provide a valuable database for the study of radio–loud quasars and AGNs and their use as nearby phase–calibrators for observations of weak radio sources.

2.1 Introduction

Since the discovery of the first gravitational lens Q0957+561 by Walsh et al. (1979), the interest in the phenomenon of gravitational lensing has only increased. The first gravitational lens (GL) systems, however, were discovered by coincidence. It is clear that this is not the way to compose a sample of GL systems which can be used for a variety of cosmological and astrophysical studies. Several optical and radio GL surveys were therefore initiated over the last two decades. [See the CASTLES[1] survey (e.g. Munõz et al. 1998) for an overview of all published GL systems and relevant references.]

In the optical waveband, one of the earliest systematic surveys was that by Webster et al. (1988), using the APM survey. More recently, the *Hubble Space Telescope Snapshot Survey* (Bahcall et al. 1992; Maoz et al. 1992, 1993a, 1993b), the Hubble Deep Field (e.g. Hogg et al. 1996; Blandford 1998) and the HST Medium Deep Survey (e.g. Ratnatunga, Griffiths & Ostrander 1999) were used to find new GL systems. A ground–based survey was done with the *Nordic Optical Telescope* (NOT; e.g. Jaunsen et al. 1995).

In the radio waveband, the first systematic GL survey was the *MIT–Green Bank survey* (MG; Bennett et al. 1986; Griffith et al. 1990, 1991; Langston et al. 1990). Because no spectral–index cutoff was enforced, many sources had a steep spectrum, which are usually extended. Such systems create Einstein–ring GL systems which are useful for detailed mass modeling, but not for the determination of the cosmological parameters (see Section 2.2). It is also hard to assess the completeness of the survey. The second radio GL survey, the *Jodrell Bank–VLA Astrometric Survey* (JVAS; Patnaik et al. 1992; Browne et al. 1998; Wilkinson et al. 1998; King et

[1] http://cfa-www.harvard.edu/glensdata/

al. 1998), restricted its selection criteria to include only flat–spectrum radio sources, thence limiting itself to sources dominated by simple compact components. This simplifies the selection procedure significantly, because GL systems will be dominated by multiple compact components and as such are easily recognizable. The third survey, the *Cosmic Lens All–Sky Survey* (CLASS; e.g. Browne 1998; Myers et al. 1999a) can be regarded as the fainter extension of the JVAS survey, having similar selection criteria and procedures.

In this chapter the scientific goals, the selection of the source sample, the data reduction, the GL–candidate selection and the results from the CLASS survey will be discussed.

2.2 Scientific goals

In this section several of the main scientific goals of the CLASS survey are discussed. For either a more general or a more detailed mathematical background the reader is referred back to Chapter 1.

2.2.1 The quest for H_0

Refsdal (1964) showed that the time delay between images in a GL systems can be used to constrain the expansion rate (i.e the Hubble parameter or H_0) of the universe. This can be understood as follows: Given a GL configuration, one can scale the size the universe – i.e change the value of H_0 – without changing any of the observables of the GL system. The reason for this is that the lens equation can be written in a dimensionless form such that the observables do not depend on H_0. However, the only observable that can not be written independent of H_0 is the light travel time between the source and the observer. The larger the size of the universe, the longer it takes a light ray to travel from the source to the observer. Thus if the light travel time can be measured, one can constrain H_0. In reality, however, it is not possible to measure this light travel time, because a photon does not carry any information about the time it was emitted.

In dealing with a GL system, however, one is looking at multiple images of the same background source. Light emitted from the source reaches the observer along different geometrical paths and through different parts of the lens–galaxy potential. This introduces a time delay between the lens images, which is inversely proportional to H_0. If the source is variable the light curves of the lens images can be cross correlated to obtain the time delays between image pairs and thus a measure of H_0 (see Appendix B in Chapter 1).

The time delay between arcsec–scale image pairs ranges from hours to weeks in most four–image GL systems. In most two–image GL systems it ranges from days to months. These time delays can be measured through long–term monitoring campaigns (e.g. Schechter et al. 1997; Kundic et al. 1997; Lovell et al. 1998; Haarsma et al. 1999; Biggs et al. 1999; Fassnacht et al. 1999b; Koopmans et al. 1999b). However, one essential criterion must be met in order to measure an accurate time delay: the source must be variable on time scales comparable or less than the time delay. This is one of the primary reasons that CLASS has observed only flat–spectrum radio sources, which are in many cases variable (e.g. Kellermann & Pauliny-Toth 1968, 1980). Because the emission of these sources comes primarily from a single region, which is much smaller than the Einstein radius of the lens galaxy, any confusion about the time delay (Yonehara 1999), which is a function of the position of the source in the source plane, can also be ruled out (see also Sect.2.3).

2.2.2 The determination of Ω_m and Ω_Λ

Whereas at relatively low redshifts H_0 is just a constant of proportionality between redshift and distance ($d \approx (cz/H_0)$), at higher redshifts also the overall density of the universe (Ω_m) and the cosmological constant (Ω_Λ) determine the geometry of space (see Appendix A in Chapter 1). However, these parameters are difficult to measure, because they are small second–order deviations from a simple linear function and only start playing a role at redshifts $\gtrsim 1$.

However, not only distances are a func-

tion of redshift and the cosmological parameters, but also the volume element within a given solid angle and redshift bin (Appendix A, Chapter 1). If we can measure the number of sources as function of their properties and redshift, we can in principle calculate the lensing rate for a well-defined GL survey, like CLASS. A comparison of the observed and expected lensing rates then puts constraints on both $\Omega_{\rm m}$ and Ω_Λ (e.g. Maoz & Rix 1993; Kochanek 1996; Falco et al. 1998; Cooray 1999; Quast & Helbig 1999; Helbig et al. 1999; Chiba & Yoshii 1999), whereas it is independent from H_0. Clearly, for this to work one needs a thorough understanding of all the selection effects of the GL survey (e.g. Kochanek & Lawrence 1990; Kochanek 1991), which might influence the observed lensing rate. A significant amount of effort has therefore been put into understanding and minimizing the selection effects of the CLASS survey, making it not only the largest but also the best understood GL survey.

2.2.3 The study of galaxy structure and evolution

Our knowledge of intermediate and high–redshift galaxies has improved dramatically over the last decade, mainly due to the arrival of new and powerful optical telescopes, such as the *Hubble Space Telescope* (HST), the Keck telescopes and recently the ESO *Very–Large–Telescope* (VLT). However, research has mostly focussed on the luminosity and colors, not on the mass distribution of these galaxies. Without accurate knowledge of the mass distribution, however, it is difficult to interpret their color and luminosity evolution. Only in the case of massive and luminous elliptical galaxies can a measure of their mass be obtained through spectroscopic determinations of their (central) velocity dispersions (e.g. Faber & Jackson 1976; Dressler et al. 1987; Djorgovski & Davies 1987). For low–luminosity ellipticals and spiral galaxies this is generally not possible. Especially in the case of spirals, which are supported against gravity by rotation and not by a high velocity dispersion (e.g. van Albada & Sancisi 1986).

Because the image separation in a GL system only weakly depends on the distribution of the mass enclosed by the Einstein radius, the mass of the inner part of the lens–galaxy can usually be determined with an accuracy of $\lesssim$10%. A comparison of this mass with the luminosity and color of the lens–galaxy places them directly on the local mass–luminosity relation and places constraints on their evolution (e.g. Mao & Kochanek 1994; Keeton, Kochanek & Falco 1998; Munõz et al. 1998).

This technique does not rely on the measurement of a velocity dispersion, which is biased towards those galaxies at intermediate and high redshifts that are bright enough to measure a velocity dispersion in the first place. Gravitational lensing therefore offers an opportunity to study the evolution of the luminosity, colors *and* mass–distribution of field galaxies, independent of any optical bias.

2.2.4 The study of the high–redshift universe

GL surveys, such as CLASS and JVAS, provide not only new GL systems, but also a very large statistically complete sample of radio–loud quasars and AGNs. To study these systems and related problems, a collaboration between six European institutes was set up: the *Consortium for European Research on Extragalactic Surveys*[2] (CERES), which is a research network funded by the European Union through its Training and Mobility of Researchers (TMR) program.

2.2.5 The search for phase calibrators

Most flat–spectrum CLASS sources are compact when observed with the VLA at 8.5–GHz. Hence, they provide a valuable database of phase–calibrators over the northern hemisphere. With an average source density of $\sim$0.75 per sq. degree, the average angular distance between sources is $\sim1^\circ$, which is a significant improvement over previous phase–calibrator catalogs, such as JVAS (Patnaik et al. 1992; Browne et al. 1998; Wilkinson et al. 1998). Nearby

[2] http://www.jb.man.ac.uk/~ceres1/

phase–calibrators provide more accurate phase and gain solutions, because the difference in atmospheric properties above the individual interferometer telescopes is smaller between more closely separated calibrators and sources. Moreover, the positional accuracy of the optically identified CLASS sources (∼20 mas; Myers et al. 1999a) provides a dense network of sources which can be used for accurate positional determinations of optical sources in large fields of view.

2.3 Source selection

To find a sample of GL lens systems, CLASS has only observed flat–spectrum radio sources. Although the limit on the radio spectral index ($\alpha \leq 0.5$; Sect.2.3.1) strictly speaking is not flat (i.e. $\alpha \sim 0$), in most radio sources this selection criterion almost guarantees the presence of a bright flat–spectrum compact component, next to a more extended region of steep–spectrum of emission ($\alpha \sim 0.8$).

There are a number of reasons to use flat–spectrum radio sources as the 'parent–sample' from which to select GL systems:

1. Flat–spectrum radio sources are often compact when observed with the VLA in A–array at 8.5 GHz. This makes them easily recognizable, when multiply imaged by a foreground mass distribution.
2. It is significantly easier to quantify the magnification bias and completeness level of the survey, in the case of lensed point sources. If the sources are extended, as is often the case for steep–spectrum radio sources, detailed knowledge on the structure of the observed radio sources is necessary to calculate these biases. This is both observationally and computationally an impossible task.
3. Radio sources are not affected by dust extinction, which can severely bias against "dusty" lens galaxies, such as spiral galaxies (e.g. Malhotra et al. 1997; Perna et al. 1997; Falco et al. 1999)
4. Because of their compact nature, flat–spectrum radio sources are often variable (e.g. Kellermann & Pauliny-Toth 1968, 1980). This allows the determination of a time delay between lens images through a correlation of their light curves. Steep spectrum radio sources usually do not vary on human time scales.

The major disadvantage of lensed compact radio sources remains that they give only a limited number of constraints on the mass distribution of the lens galaxy, compared to more extended sources. However, optical images often show more structure that can help the lens mass modeling.

2.3.1 Selection criteria

The following selection criteria were used, to select a sample of flat–spectrum radio source from a number of large radio surveys (i.e. GB6, Texas, NVSS and WENSS):

- A total flux–density between 30 and 200 mJy at 5 GHz.
- A two–point spectral index $\alpha \leq 0.5$ with $S_\nu \propto \nu^{-\alpha}$.
- A declination $0° < \delta < 75°$ and a Galactic latitude $|b| \geq 10°$. This corresponds to ∼42% of the sky.

The lower flux–density limit at 5 GHz was chosen to allow short snapshots of all selected sources to be made (∼1 min. per source, including slewing and calibration). The upper limit is chosen to avoid overlap with the JVAS survey, which is a survey with similar selection criteria, but with $S_{5\mathrm{GHz}} \geq 200$ mJy.

The expected noise–level of the 8.5–GHz VLA images (∼0.2 arcsec resolution) in 30 seconds on–source integration time is ∼0.2 mJy beam^{-1} (Sect.2.5). This allows the detection of ≥0.3–arcsec separation doubles with a flux–density ratio of ≤10 to 1 (i.e. the secondary component would still be detectable at the 5–σ level). Because of the point–source nature of the lensed source, selection biases and completeness levels can be calculated in a straightforward manner for these selection criteria,

using Monte–Carlo simulations (e.g. Myers et al. 1999a). Both the noise level and resolution of the VLA 8.5–GHz snapshots are furthermore little affected by atmospheric conditions, which might play a role in ground–based optical GL surveys (e.g. Kochanek & Lawrence 1990).

2.3.2 Source catalog

In the first phase of the survey (CLASS 1a), part of the source sample was selected between the 6–cm GB87 and GB6 catalogs (e.g Gregory et al. 1996) and the 80–cm Texas catalog (Douglas et al. 1996). The GB6 catalog consists of $\sim$75 200 ($\gtrsim$18 mJy at 4.9 GHz) radio sources, observed with the former 91–m Greenbank radio telescope. All these radio sources were observed twice (November 1986 and October 1987). Whereas the GB87 catalog is based on the October 1987 dataset only, the GB6 catalog is based on the combined datasets from both epochs and has a signal–to–noise ratio which is a factor $\sim\sqrt{2}$ better than the GB87 catalogue.

In subsequent phases (CLASS 1b and 2a), sources were selected between GB87/GB6 and the 92–cm WENSS catalogue (e.g. Rengelink et al. 1997) or GB87/GB6 and a combination of the Texas and WENSS catalogs (CLASS 2b). In CLASS 3a–c all sources were selected between GB6 and the 20–cm NVSS catalogs (Condon et al. 1998). The combinations of different catalogs were necessary, because in the early phases of the survey neither a complete GB6, nor a complete NVSS survey was available.

To obtain a uniform sample for statistical purposes, CLASS recently reselected the entire source sample from the completed GB6 and NVSS surveys, using the criteria listed in Section 2.3.1. This time no upper limit on $S_{5\mathrm{GHz}}$ was used, in order to include the brighter JVAS sample. As a result some sources dropped out of the sample which were initially selected, whereas other sources were included. All new sources were observed in the third phase of the CLASS survey to obtain a complete uniformly–selected sample of radio sources, including JVAS. The current statistical sample contains $\sim$11 700 sources, whereas the total observed number of sources is $\sim$15 200 sources (Myers et al. 1999a). The remaining sources that make up the statistical sample have been observed in August 1999 and are currently being reduced and analyzed.

2.4 VLA observations and data reduction

The selected sources were observed with the VLA in three phases, corresponding to the 1994, 1995 and 1998 A–array configurations. In 1994 and 1995 the (central) observing frequency was 8.4 GHz, whereas this was 8.5 GHz in 1998. A total bandwidth of 50 MHz was used and a total integration time on–source of typically 30 sec, with 3.3–sec integrations. In the case the sources were selected using the positionally less accurate Texas 80–cm catalog, a bandwidth of 25 MHz was used to limit bandwidth smearing and allow for a larger field–of–view to search for the source. The nominal resolution in this configuration is $\sim$0.2 arcsec.

Every 8–14 targets a bright compact JVAS phase–calibrator was observed, to allow initial phase and gain calibration of the fainter CLASS sources. Including slewing and calibration, each source took about 1 min. of observing time (Myers et al. 1999a).

The data was flagged and calibrated in the data–reduction package AIPS, using standard routines. The calibrated uv–data sets were stored for automatic imaging in DIFMAP. This AUTOMAP algorithm has three cycles. During the first cycle, one searches for peaks in a large image above some signal–to–noise ratio (SNR). Typical SNRs of 8–10 were used to avoid too many spurious features in the initial $128'' \times 128''$ fields. During the second cycle the images are centered on the peaks found in the first cycle and small CLEAN boxes are placed around these peaks. During the third cycle the image is CLEANed and self–calibrated. The products of this procedure are the calibrated uv–data, the CLEAN model, the set of CLEAN windows, the list of MODELFIT Gaussian components fitted to the calibrated uv–data and a radio map with a typ-

Criterion	# Points
Number of compact components >2	10
$S_{8.5GHz}$>5 mJy for all components	7
Spectral index <0.4	6
Spectral index 0.4–0.6	3
Flux–density ratio brightest components <2.5:1	3
Flux–density in compact components >30 mJy	2

TABLE 2.1— Criteria to rank the GL lens candidates on the basis of the results from the AUTOMAP MODELFIT procedure (taken from Fassnacht 1999).

ical rms noise of ∼0.2 mJy beam^{-1}. This automatic procedure has proven successful in creating good maps and selecting lens candidates.

2.5 Lens selection procedure

The selection procedure of lens candidates is done through two parallel, but complementary, procedures (see Fassnacht 1999). The first is a fully objective algorithm which ranks candidates on the basis of the MODELFIT components obtained from the AUTOMAP procedure, whereas the second is the 'select–by–eye' method, where a few CLASS members independently go through all VLA images and select possible lens candidates on the basis of their knowledge what these systems typically look like. Whereas the first method is best in finding systems made up of closely separated compact components, the second is better in finding those systems that contain more extended components as well. To be on the conservative side, however, all extended sources (≥170 mas, determined from a Gaussian model fit) in the VLA maps are selected for further radio imaging, except for those that show unambiguous jet–like structure and no multiple or extended compact components. Because >95% of all sources are compact (<170 mas), this reduces the number of sources from several thousand to several hundred, of which a significant fraction will be listed for follow–up high–resolution (∼50 mas) observations with MERLIN at 5 GHz.

The automatic selection program works in the following way (Fassnacht 1999). First, all sources meeting the following criteria are rejected as possible GL candidates:

- There is only one compact component and no other emission features.
- There are multiple components of which all but one are clearly resolved.
- The flux–density ratio between the brightest two components is >15:1.
- The spectral index between GB6 and NVSS is α>0.8. These sources initially appeared to be flat–spectrum (α<0.5), when selected using lower–frequency surveys other than the NVSS (i.e. Texas and WENSS).
- The total flux–density of the source at 8.5 GHz is <20 mJy.

Some of these criteria directly relate to the nature of multiply–imaged GL systems, whereas others are based on the completeness level that we aim for. If the sources pass these criteria, they are subsequently ranked according to the total number of points scored on the basis the criteria listed in Table 2.1.

Candidates that score ≥15 points are marked "A", with 10–14 point "B", with 6–9 points "C" and with 1–5 points "D". Around ∼5% of the initial candidates observed with the VLA survive all criteria and are marked for follow–up observations. The method has extensively been tested through both Monte–Carlo simulations (Myers et al. 1999a), as well as by putting in confirmed GL systems. Only the lens systems B1938+666 (King et al. 1997) and B0712+472 (Jackson et al. 1998) were not selected as GL candidates by the automatic procedure. In the case of B1938+666, because of the extended nature of its radio emission and in the case of B0712+472,

#	Survey	Name	# images	$\Delta\theta''$	z_l	z_s
1	JVAS	B0218+357	2+radio ring	0.33	0.68	0.96
2	JVAS	MG0414+054	4	2.09	0.96	2.64
3	CLASS–1	B0712+472	4	1.27	0.41	1.34
4	CLASS–2	B0739+366	2	0.54	–	–
5	JVAS	B1030+074	2	1.56	0.60	1.54
6	CLASS–2	B1127+385	2	0.70	–	–
7	CLASS–3	B1152+199	2	1.56	0.44	1.02
8	CLASS–3	B1359+154	4	1.65	–	3.24
9	JVAS	B1422+231	4	1.28	0.34	3.62
10	CLASS–2	B1555+375	4	0.43	–	–
11	CLASS–1	B1600+434	2	1.39	0.42	1.59
12	CLASS–1	B1608+656	4	2.08	0.64	1.39
13	CLASS–1	B1933+507	4+4+2	1.17	0.76	–
14	JVAS	B1938+666	4+radio arc	0.93	0.88	–
15	CLASS–2	B2045+265	4	1.86	0.87	1.28
16	JVAS	B2114+022*	2+2 or 4	2.57	0.32/0.59	–
17	CLASS–2	B2319+051*	2	1.36	0.62/0.59	–
18	CLASS–2	B0827+525**	2	2.82	–	2.06

TABLE 2.2— Table containing the properties of the CLASS/JVAS GL systems and a possible binary radio–loud quasar. Column 2: The name and phase of the survey in which the GL systems was discovered. Column 3: Name of the GL system. Column 4: The number of GL images. Column 5: The maximum separation between GL images. Columns 6–7: The redshift of the lens galaxy and source, respectively. (*) GL system with two lens galaxies at different redshifts; (**) Possible binary radio–loud quasar. References: (1) Patnaik et al. 1993, (2) Hewitt et al. 1992, (3) Jackson et al. 1998, (4) Marlow et al. 1999a, (5) Xanthopoulos et al. 1998, (6) Koopmans et al. 1999c, (7,8) Myers et al. 1999b (9) Patnaik et al. 1992 (10) Marlow et al. 1999b, (11) Jackson et al. 1995, (12) Myers et al. 1995, (13) Sykes et al. 1998, (14) King et al. 1997, (15) Fassnacht et al. 1999a, (16) Augusto et al. in prep., (17) Marlow et al. 1999c, (18) Koopmans et al. 1999b.

because of the faintness of the fourth lens image. However, both lens systems were immediately recognized as such by the 'select–by–eye' method, because of their distinctive morphology (Fassnacht 1999).

2.6 Follow–up observations

The next step in the follow–up of the GL candidates that survived the first selection process from the VLA images, are observations with higher resolution using the *Multi Element Radio–Linked Interferometer Network* (MERLIN) at 5 GHz and 1.6 GHz. The resolution of these images are ∼50 mas and ∼120 mas, respectively, which is a factor 2–5 improvement over the VLA images. The higher resolution is necessary to resolve possible closely separated compact doubles or quads (e.g. B0712+472; Jackson et al. 1998) and to see if the surface brightness, which is conserved in the projection of the source on the image plane, is similar between the radio components. The observations at 1.6 and 5 GHz also provide two–point spectral indices between the radio components. This acts as a further filter. However, this criterion is handled with care, because the source can be variable and therefore introduce differences between the image spectral indices.

On the basis of similar criteria and the procedures delineated in the previous sections, we reject another ∼80% of the GL candidates, after the MERLIN observations. Only those which exhibit multiple compact components (i.e. are not resolved in the 5–GHz MERLIN observations) did we consider as prime GL candidates and were listed for even higher resolution (∼1 mas) imaging with the *Very Long Baseline Array* (VLBA) at 5 GHz. All candidates remaining after the VLBA observations and associated criteria (e.g. compact components, roughly similar spectral indices, possibly similar substructure in the lens images, etc.) have thus far turned out to be

genuine GL systems (e.g. Fassnacht 1999). Only one system, B0827+525 (Koopmans et al. 1999b; Chapter 8) has survived all criteria, but has of yet not been confirmed as lens system. It might be the first binary radio–loud quasar.

In addition to this standard follow–up procedure, we are also engaged in multi–frequency observations with the VLA, WSRT and sometimes single–dish telescopes to study spectral properties and test for variability. Systems that are immediately recognized as bona-fide GL systems (i.e. four–image GL systems) were put on the 'fast–track' to speed up the selection process. Most systems (i.e. two–image GL systems), however, follow the standard procedures and are only observed with other telescopes, once they survive also the final radio imaging using VLBI.

Once a source has been recognized as a GL system, which we should emphasize is purely based on radio observations and thus avoids any optical bias, the standard optical follow–up imaging is done with the *Hubble Space Telescope* (HST) and additionally, depending on availability, with the Palomar, Keck, WHT, INT telescopes, etc. The systems are observed with HST in V & I (WFPC2) and H (NICMOS) to obtain detailed imaging and colors of the lens galaxy (e.g. Jackson et al. 1998). The latter is essential in providing information necessary to properly model the mass distribution of the lens galaxy. These optical observations strengthen the GL interpretation, but are *not* part of the selection procedure. Moreover, nearly three quarters of all confirmed GL systems have measured redshifts, mostly obtained with the Keck 10–m telescopes, a fraction that increases gradually (Table 2.2).

Next to the follow–up observations indicated above, the CLASS members pursue their own specific projects, using these GL systems, which might require specific observations with other telescopes and at other frequencies.

2.7 Results

CLASS and JVAS have together observed ∼15 200 sources with the VLA, from which at least 17 new lens systems have been found (Myers et al. 1999a) and one possible binary radio–loud quasar (Koopmans et al. 1999b). The standard radio follow–up of CLASS 1 & 2 has been completed and we are currently doing the optical and spectroscopic observations of the GL systems in these phases. The third phase of the survey is still ongoing and we expect to find several additional new doubles, bringing the total number of GL systems at ∼20. Two new GL systems have already been identified in the third phase (see Table 2.2). The current list of CLASS/JVAS GL systems is shown in Table 2.2. To complete the survey and create a statistically complete and uniform sample, we recently observed another ∼700 sources.

References

Bahcall, J. N., Maoz, D., Doxsey, R., Schneider, D. P., Bahcall, N. A., Lahav, O. & Yanny, B. 1992, ApJ, 387, 56

Biggs, A.D., Browne, I.W.A., Helbig, P., Koopmans, L.V.E., Wilkinson, P.N., & Perley, R.A., 1998, MNRAS 304, 349

Blandford, R. D. 1998, Ap&SS 261, 233

Bennett, C. L., Lawrence, C. R., Burke, B. F., Hewitt, J. N. & Mahoney, J. 1986, ApJS, 61, 1

Browne, I. W. A., Wilkinson, P. N., Patnaik, A. R. & Wrobel, J. M. 1998, MNRAS 293, 257

Browne, I. 1998, Observational Cosmology with the New Radio Surveys, Proceedings of a Workshop held in Puerto de la Cruz, Tenerife, Canary Islands, Spain, 13-15 January 1997, Dordrecht: Kluwer Academic Publishers, 1998, Astrophysics and space science library (ASSL) Series vol no: 226, ISBN: 0792348850., p.323, 323

Chiba, M. & Yoshii, Y. 1999, ApJ 510, 42

Condon, J. J., Cotton, W. D., Greisen, E. W., Yin, Q. F., Perley, R. A., Taylor, G. B. & Broderick, J. J. 1998, AJ 115, 1693

Cooray, A. R. 1999, A&A 342, 353

Douglas, J. N., Bash, F. N., Bozyan, F. A. , Torrence, G. W. & Wolfe, C. 1996, AJ 111, 1945

Djorgovski, S. & Davis, M. 1987, ApJ 313, 59

Dressler, A. , Lynden-Bell, D. , Burstein, D. , Davies, R. L., Faber, S. M., Terlevich, R. & Wegner, G. 1987, ApJ 313, 42

Faber, S. M. & Jackson, R. E. 1976, ApJ 204, 668

Falco, E. E., Kochanek, C. S. & Munoz, J. A. 1998, ApJ 494, 47
Falco, E. E., et al. 1999, ApJ 523, 617
Fassnacht, C. D., 1999, PhD thesis, Caltech
Fassnacht, C. D., et al. 1999a, AJ 117, 658
Fassnacht, C. D., Pearson, T.J., Readhead, A. C. S., Browne, I. W. A., Koopmans, L. V. E., Myers, S. T., Wilkinson, P. N., 1999b, ApJ in press
Gregory, P. C., Scott, W. K., Douglas, K. & Condon, J. J. 1996, ApJS 103, 427
Griffith, M. , Langston, G. , Heflin, M. , Conner, S. , Lehar, J. & Burke, B. 1990, ApJS 74, 129
Griffith, M. , Heflin, M. , Conner, S. , Burke, B. & Langston, G. 1991, ApJS 75, 801
Haarsma, D. B., Hewitt, J. N., Lehar, J. & Burke, B. F. 1999, ApJ 510, 64
Helbig, P., Marlow, D., Quast, R., Wilkinson, P. N., Browne, I. W. A. & Koopmans, L. V. E. 1999, A&ASS 136, 297
Hewitt, J. N., Turner, E. L., Lawrence, C. R., Schneider, D. P. & Brody, J. P. 1992, AJ 104, 968
Hogg, D. W., Blandford, R. , Kundic, T. , Fassnacht, C. D. & Malhotra, S. 1996, ApJL 467, L73
Jackson, N., et al. 1995, MNRAS 274, L25
Jackson, N., et al. 1998, MNRAS 296, 483
Jackson, N., Helbig, P., Browne, I., Fassnacht, C. D., Koopmans, L., Marlow, D. & Wilkinson, P. N. 1998, A&A 334, L33
Jaunsen, A. O., Jablonski, M., Pettersen, B. R. & Stabell, R. 1995, A&A, 300, 323
Keeton, C. R., Kochanek, C. S. & Falco, E. E. 1998, ApJ 509, 561
Kellermann, K. I. & Pauliny-Toth, I. I. K. 1968, ARA&A 6, 417
Kellermann, K. I. & Pauliny-Toth, I. I. K. 1969, ApJL 155, L71
Kellermann, K. I. & Pauliny-Toth, I. I. K. 1981, ARA&A 19, 373
King, L. J., Browne, I. W. A., Muxlow, T. W. B., Narasimha, D., Patnaik, A. R., Porcas, R. W. & Wilkinson, P. N. 1997, MNRAS 289, 450
King, L. J., Browne, I. W. A., Marlow, D. R., Patnaik, A. R. & Wilkinson, P. N. 1999, MNRAS, 307, 225
Kochanek, C. S. & Lawrence, C. R. 1990, AJ 99, 1700
Kochanek, C. S. 1991, ApJ 379, 517
Kochanek, C. S. 1996, ApJ 466, 638
Kochanek, C. S., et al. 1999, astro-ph/9910165
Koopmans, L. V. E., De Bruyn, A. G. & Jackson, N. 1998, MNRAS 295, 534 (Chapter 3)
Koopmans, L. V. E. & Fassnacht C. D. 1999, ApJ in press (Chapter 6)
Koopmans, L. V. E., de Bruyn A. G., Xanthopoulos, E., Fassnacht C. D. 1999a, A&A submitted (Chapter 4)
Koopmans, L. V. E. & de Bruyn A. G. 1999a, A&A, submitted (Chapter 5)
Koopmans, L. V. E. & de Bruyn A. G. 1999b, astro-ph/9910189
Koopmans, L. V. E., et al. 1999b, A&A, submitted (Chapter 8)
Koopmans, L. V. E., et al. 1999c, MNRAS 303, 727 (Chapter 7)
Kundic, T. , et al. 1997, ApJ 482, 75
Langston, G. I., Heflin, M. B., Conner, S. R., Lehar, J. , Carrilli, C. L. & Burke, B. F. 1990, ApJS 72, 621
Lovell, J. E. J., Jauncey, D. L., Reynolds, J. E., Wieringa, M. H., King, E. A., Tzioumis, A. K., McCulloch, P. M. & Edwards, P. G. 1998, ApJL 508, L51
Malhotra, S., Rhoads, J. E. & Turner, E. L. 1997, MNRAS 288, 138
Mao, S. D. & Kochanek, C. S. 1994, MNRAS 268, 569
Maoz, D., Bahcall, J. N., Doxsey, R., Schneider, D. P., Bahcall, N. A., Lahav, O. & Yanny, B. 1992, ApJ 394, 51
Maoz, D., Bahcall, J. N., Doxsey, R., Schneider, D. P., Bahcall, N. A., Lahav, O. & Yanny, B. 1993a, ApJ 402, 69
Maoz, D., et al. 1993b, ApJ 409, 28
Maoz, D. & Rix, H. -W. 1993, ApJ 416, 425
Marlow, D. R., et al. 1999a, submitted
Marlow, D. R., et al. 1999b, AJ 118, 654
Marlow, D. R., et al. 1999c, submitted
Munõz, J. A., Falco, E. E., Kochanek, C. S., Lehar, J., McLeod, B. A., Impey, C. D., Rix, H. -W. & Peng, C. Y. 1998, Ap&SS, 263, 51
Myers, S. T., et al. 1995, ApJL 447, L5
Myers, S.T., et al., 1999a, http://multivac.jb.man.ac.uk:8000/ceres/papers/boston99/MYERS_A4.PS-GZ
Myers, S. T., et al. 1999b, AJ 117, 2565
Ostensen, R., et al. 1997, A&ASS 126, 393
Patnaik, A. R., Browne, I. W. A., Wilkinson, P. N. & Wrobel, J. M. 1992, MNRAS 254, 655
Patnaik, A. R., Browne, I. W. A., Walsh, D., Chaffee, F. H. & Foltz, C. B. 1992, MNRAS 259, 1P
Patnaik, A. R., Browne, I. W. A., King, L. J., Muxlow, T. W. B., Walsh, D. & Wilkinson, P. N. 1993, MNRAS 261, 435
Perna, R. , Loeb, A. & Bartelmann, M. 1997, ApJ 488, 550
Quast, R. & Helbig, P. 1999, A&A 344, 721
Ratnatunga, K. U., Griffiths, R. E. & Ostrander, E. J. 1999, AJ 118, 86

Refsdal, S., 1964, MNRAS 128, 307
Rengelink, R. B., Tang, Y., De Bruyn, A. G., Miley, G. K., Bremer, M. N., Roettgering, H. J. A. & Bremer, M. A. R. 1997, A&ASS 124, 259
Schechter, P. L., et al. 1997, ApJL 475, L85
Sykes, C. M., et al. 1998, MNRAS 301, 310
Van Albada, T. S. & Sancisi, R. 1986, Royal Society (London), Philosophical Transactions, Series A, vol. 320, no. 1556, 1986, p. 447-464;
Walsh, D., Carswell, R. F. & Weymann, R. J. 1979, Nature, 279, 381
Webster, R. L., Hewett, P. C. & Irwin, M. J. 1988, AJ 95, 19
Wilkinson, P. N., Browne, I. W. A., Patnaik, A. R., Wrobel, J. M. & Sorathia, B. 1998, MNRAS 300, 790
Xanthopoulos, E., et al. 1998, MNRAS 300, 649
Yonehara, A. 1999, ApJL 519, L31

3

The edge–on spiral gravitational lens B1600+434

Originally published as L.V.E. Koopmans, A.G. de Bruyn & N. Jackson, 1998, Monthly Notices of the Royal Astronomical Society, 295, 534

We present new observations of the gravitational lens (GL) system B1600+434, strongly suggesting that the lens is an edge–on spiral galaxy. These observations are used to constrain the mass model of the system, in particular the oblateness and velocity dispersion of the dark matter halo around the lensing galaxy. From an analytical model we find a lower limit on the halo oblateness $q_{\rm halo}$=$(c/a)_\rho \gtrsim$0.4; more detailed numerical models give a lower limit $q_{\rm halo}\gtrsim$0.5. We determine an average halo velocity dispersion of $\sigma_{\rm halo}$=190$\pm$15 km/s over all non–singular isothermal elliptical (NIE) halo models. Constraining the models to larger and more massive disks, decreases this average by only 10 km/s. A lower limit of $\sigma_{\rm halo}\gtrsim$150 km/s is found, even for disk masses larger then the mass inside the Einstein radius. This lower limit indicates the need for a massive dark matter halo, contributing at least half of the mass inside the Einstein radius. Time delay calculations give $(54 \pm 3)\, h_{50}^{-1}$ days for the NIE halo model and $(70 \pm 4)\, h_{50}^{-1}$ days for the modified Hubble profile (MHP) halo model. Although the time delay for both NIE and MHP halo models is well constrained on our parameter grid, it strongly depends on the halo surface density profile. We furthermore find that the presence of a flat luminous mass distribution can severely alter the statistical properties of the lens.

3.1 Introduction

Over the last two decades, gravitational lensing has proved a very effective tool in constraining the shape of the mass distribution responsible for weak and strong lensing. Moreover, a time delay between two images can be used to determine the Hubble parameter, given an appropriate mass model (Refsdal 1964; 1966). In this paper we focus on the oblateness and velocity dispersion of the dark matter halo around the edge–on spiral galaxy lens in the GL system B1600+434 and calculate the expected time delays for this system for two different halo mass models.

Different techniques have been used to determine the oblateness $q_{\rm halo}$=$(c/a)_\rho$ of the dark matter halo around spiral galaxies. Most of these indicate an oblateness $\gtrsim$0.4 [dissipationless N–body calculations, stellar dynamics in the solar neighborhood and polar ring galaxies (e.g. Rix 1995; Sackett 1995)]. On the other hand, flaring of the gas layer and the HI velocity dispersion in NGC 4244 seem to indicate a more

oblate dark matter halo with $q_{\rm halo}$=0.1–0.5 for that galaxy (Olling 1996). This could support the idea that dark matter is mostly baryonic and perhaps consists of molecular hydrogen (Pfenniger, Combes & Martinet 1994; Pfenniger & Combes 1994). Obviously one would like to put stronger constraints on the oblateness of dark matter halos around spiral galaxies, less dependent of the chosen mass model, assumptions about the type of dark matter or its dynamical state. This opportunity is offered by the GL system B1600+434.

The lensing galaxy of B1600+434 is an edge–on spiral galaxy between two lensed QSO images and therefore presents the opportunity to determine the oblateness of the halo $(c/a)_\rho$ by means of lensing. This method is different from and independent of methods used previously, in the sense that it is not dependent on the type of lensing matter (e.g. baryonic or non–baryonic) or its dynamical state.

In Section 3.2 we describe new observations of B1600+434; in Section 3.3 the basic lensing theory is summarized; in Section 3.4 the mass models used to describe the lensing galaxy, its dark matter halo and the companion galaxy are presented; in Section 3.5 we describe the parameter space of the fixed parameters in the mass models; and in Section 3.6 we present our results and analyses. The main results are summarized in Section 3.7.

3.2 Observations

The double QSO lens system B1600+434 was discovered by Jackson et al. (1995) in the Cosmic Lens All Sky Survey (CLASS; Myers et al. 1997). First we briefly summarize the observational status of this system and then present new radio and optical observations.

Observational status B1600+434 was discovered as a compact flat spectrum radio double with a separation of 1.39±0.01 arcsec. Very Large Array (VLA) 8.4–GHz observations show no structure due to extended emission (e.g. lobes) around the compact flat spectrum radio core and no sign of a central third image above the noise level is found (Jackson et al. 1995). On February 24 1996, B1600+434 was observed with the VLBA at 6 and 18 cm to search for possible substructure in the radio maps, which can further constrain a mass model for the lensing galaxy. The VLBA 18–cm maps of QSO images A and B do not show signs of substructure, but the 6–cm maps show possible substructure 1–2 mas from the brightest component (Jackson, private communications). The redshift of the lensed source was measured to be 1.61 with the William Herschel Telescope (WHT), La Palma (Jackson et al. 1995). Subsequently, more accurate redshifts of the source and the lens galaxy were determined with the Keck telescope (Fassnacht et al. 1998). The redshift of G1 was determined at 0.415 and the redshift of the source 1.59, consistent with the source redshift found previously. We will use the Keck redshifts, because of their superior signal–to–noise ratio.

Hubble Space Telescope observations On November 18 1995, a 700–s WFPC2 *Hubble Space Telescope (HST) I*–band and an 800–s *V*–band exposure were obtained of B1600+434. The *I*–band image clearly shows the two QSO images A and B, the lensing galaxy (G1) between the QSO images and the companion galaxy (G2) south–east of G1 (Fig. 3.1). The luminous component of G1 appears to be a flat edge–on system that exhibits a prominent dust lane. Both the dust lane and flat luminous mass distribution indicate that G1 is most likely a nearly edge–on spiral galaxy. The *V*–band exposure shows both images A and B and galaxy G2, but not the lens galaxy G1.

We performed *I* and *V*–band photometry on galaxies G1 and G2, on the small (∼3 arcsec) moderately inclined disk galaxy ∼10 arcsec west of G1 (G3; see Jaunsen and Hjorth (1997) (JH97)) and on the QSO images A and B. We applied corrections for the gain of the different chips, the transfer efficiency and the long exposure time, amounting to a total correction in both *V* and *I* of approximately -0.08 magnitude. We also determined the magnitudes of two field stars S1 and S2 (stars 1 and 2 in

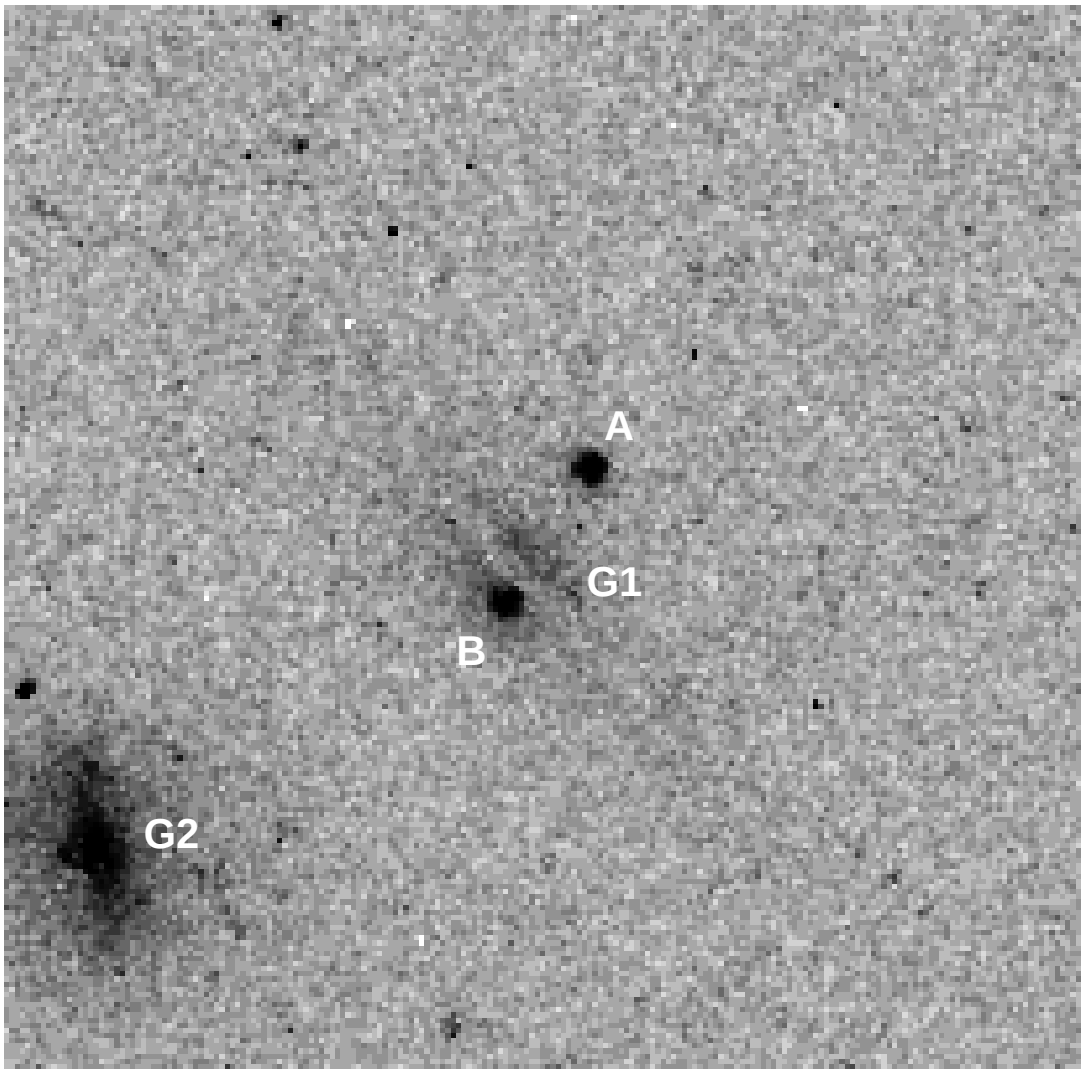

FIGURE 3.1— *HST I*–band image. North is up, east is left.

JH97). The photometric results are listed in Table 3.1. Comparing our *HST* photometry with the ground based photometry of JH97, we find that the magnitudes of all three galaxies and both stars do not differ by more than ∼0.1 magnitude in both V and I. However, over the same period (July to November 1995) the QSO images A and B have dimmed significantly. Image A by some 0.5–0.6 magnitudes in V and 0.5 in I and image B by some 0.2 magnitudes in both V and I bands. The decrease in brightness of image A is very significant and indicates strong optical variability over the order of months. The smaller decrease in brightness of image B can be explained by a time delay between the two images, which is also in the order of months (see Sect.3.6), but subtracting the emission of G1 could also have caused a systematic error in the brightness determination of image B. This effect will be stronger for less resolved ground based observations.

The companion galaxy G2 south–east of G1 appears to be a nearly face–on luminous barred spiral galaxy (Fig. 3.1). The bar–like structure can also be seen in the deconvolved NOT R–band image (Fig. 3.2). From

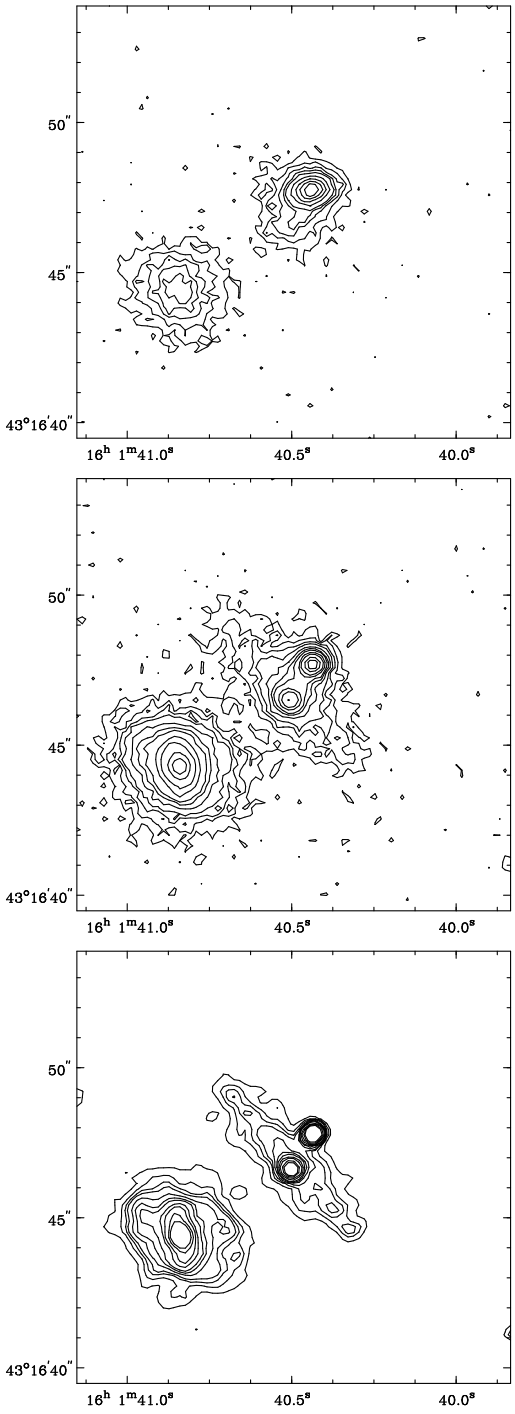

FIGURE 3.2— *Upper* : Nordic Optical Telescope (NOT) *B*–band image, *middle* : NOT *R*–band image, *lower* : deconvolved NOT *R*–band image. 1 arcsec corresponds to a physical size of 6.5 kpc at redshift z_l=0.415 and h_{50}=1.

Fukugita, Shimasaku & Ichikawa (1995) we find that the *HST* F555W–F814W color of 1.40±0.15 could either indicate an early type spiral galaxy at relative low redshift (∼0.2) or a somewhat later type spiral galaxy at higher redshift (∼0.5). Judging from the bar–like structure G2 does not appear to an E/S0 galaxy, as suggested by JH97. As the photometric redshift of G2 is rather uncertain, we assume it to be the same as for G1 (0.415) as most reasonable first estimate. In Sect.3.6 we will describe the dependence of our results on this assumption. The small galaxy G3 is a moderately inclined (spiral) galaxy some 10 arcsec west of B1600+434. Because this galaxy is much smaller and ∼2 magnitudes fainter than G2 (∼6 times less massive for the same M/L ratio and redshift), we do not incorporate this galaxy in the mass models (both the convergence and shear of G3 will be ∼10 times smaller than that of G2 at images A and B).

Nordic Optical Telescope observations Exposures in *B* and *R* band (both 600–s) were taken July 30 1995 with the BroCam 1 camera (TEK1024 CCD) on the Nordic Optical Telescope (NOT). They show the lensing galaxy G1, the two QSO images and galaxy G2 (Fig. 3.2). Comparing the two QSO images in *B* and *R*, we clearly see the effect of extinction on image B, which almost passes through the dust lane of G1 (Fig. 3.1). To enhance the resolution, we deconvolved the *R*–band image with the maximum entropy method MEM in the IRAF package STSDAS. The result clearly shows the extent of G1 (∼7 arcsec) and G2 (∼5 arcsec). There seems to be no clear evidence in the NOT and *HST* images to support the presence of a prominent massive bulge component in galaxy G1.

MERLIN observations On March 14 1995, a MERLIN 5–GHz observation was made of B1600+434 (Fig. 3.3). The map shows two compact (∼50 mas) radio components, with no visible sign of extended emission above the noise level. The flux densities of both components are given in Table 3.1. The flux ratio between components A and

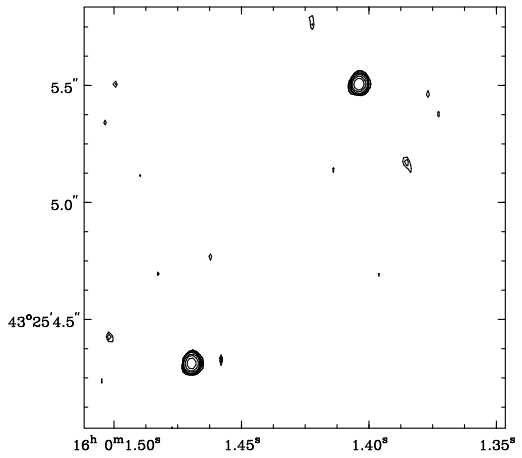

FIGURE 3.3— MERLIN 5–GHZ observation of B1600+434 (March 14, 1995).

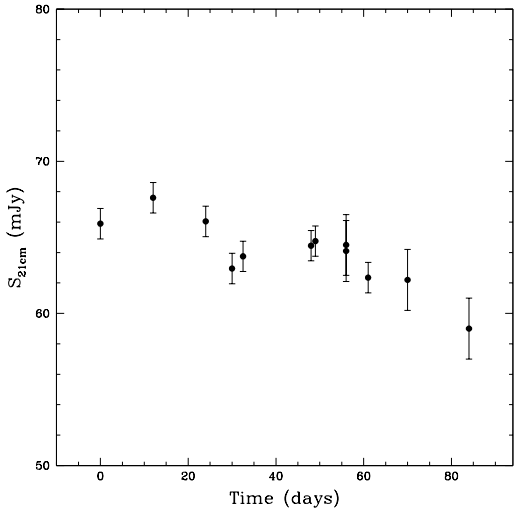

FIGURE 3.4— Total flux density of the two QSO images at 21 cm radio continuum measured with the WSRT as a function of time from April 8, 1996. The error bars indicate the flux error in fitting the model to the visibilities.

B is ∼1.2, comparable to the flux ratio from the VLA observations of Jackson et al. (1995). This consistency in flux ratio is either a coincidence (although VLA observation in August 1995 also indicate a flux ratio of ∼1.2 at 8.4 GHz, see Table 3.1) or the typical time scale of variability in the radio is much larger than the time delay, resulting only in slight variations in the radio flux ratio.

Variability of the source VLA 8.4–GHz observations of B1600+434 at two epochs indicate that the lensed source is variable by at least a factor of two over a period of one year (Table 3.1). Moreover, observations over a period of three months (April to July 1996) at 21–cm continuum with the WSRT (Fig. 3.4) indicate variability on time scales of the order of the expected time delay (Sect.3.6.3). It appears there is a steady decrease of flux density over this period, totaling ∼10% over three months.

This variability does not appear to strongly affect the flux ratio in the radio, which stayed between 1.2–1.3 at three epochs over a period of some two years. A ratio between the QSO images was found to be 1.38±0.05 in *R* (Jackson et al. 1995). Our new *HST* *I*–band magnitudes give a ratio of 1.2±0.2. The observations of JH97 give a ratio of 1.6 in *I* (epoch 1). Although they could have underestimated the *I* magnitude of image B as a result of subtracting the lensing galaxy, it can also indicate a much stronger and perhaps more rapid variability in the optical. Furthermore, optical ratios will be effected by dust extinction and therefore give more or less upper limits, even if corrected for time delay. Overall our radio flux ratios appears to stay consistently around 1.2, whereas the optical ratios are slighly higher. We adopt a ratio $r_{\rm AB}$=1.25±0.10.

3.3 Lensing theory

In describing basic lensing theory we will follow the definitions and notations as in Schneider, Ehlers & Falco (1992).

Given a length scale ξ_0 in the lens plane and the corresponding length scale η_0=$\xi_0 D_s/D_d$ in the source plane we can define the dimensionless vectors

$$\mathbf{x} = \xi/\xi_0 \text{ and } \mathbf{y} = \eta/\eta_0. \qquad (3.1)$$

We can then define the dimensionless surface mass density

$$\kappa(\mathbf{x}) = \Sigma(\xi_0\mathbf{x})/\Sigma_{cr}, \qquad (3.2)$$

	V (magn.)	I (magn.)	S_5	$S^1_{8.4}$	$S^2_{8.4}$
A	22.5 ± 0.1	21.4 ± 0.1	45.2	58.1	28.5
B	23.1 ± 0.1	21.6 ± 0.1	37.3	48.1	23.8
G1	—	20.2 ± 0.1			
G2	20.6 ± 0.1	19.2 ± 0.1			
G3	22.5 ± 0.1	21.0 ± 0.1			
S1	17.73	—			
S2	17.86	—			

TABLE 3.1— Column 1–2: *HST V* and *I*–band magnitudes of the GL system B1600+434 (November 18, 1995). The stars were saturated in *I*. G1 was not seen in *V*. Column 3: MERLIN 5–GHz flux density (mJy) (March 14, 1995). Column 4–5: VLA 8.4–GHz flux densities (mJy) in March 1994 (1) and August 1995 (2).

where the critical surface mass density is given by

$$\Sigma_{cr} = \frac{c^2 D_s}{4\pi G D_d D_{ds}}. \tag{3.3}$$

The lens equation

$$\eta = \frac{D_s}{D_d}\xi - D_{ds}\hat{\alpha}(\xi) \tag{3.4}$$

then becomes

$$\mathbf{y} = \mathbf{x} - \alpha(\mathbf{x}), \tag{3.5}$$

with

$$\begin{aligned} \alpha(\mathbf{x}) &= \frac{1}{\pi}\int_{R^2} d^2x' \kappa(\mathbf{x}') \frac{\mathbf{x}-\mathbf{x}'}{|\mathbf{x}-\mathbf{x}'|^2} \\ &= \frac{D_s D_{ds}}{\xi_0 D_s}\hat{\alpha}(\xi_0 \mathbf{x}). \end{aligned} \tag{3.6}$$

We can then define the deflection potential

$$\psi(\mathbf{x}) = \frac{1}{\pi}\int_{R^2} d^2x' \kappa(\mathbf{x}') \ln|\mathbf{x}-\mathbf{x}'|, \tag{3.7}$$

in order to get

$$\alpha = \nabla\psi. \tag{3.8}$$

The dimensionless lens equation then becomes

$$\mathbf{y} = \nabla\left(\frac{1}{2}\mathbf{x}^2 - \psi(\mathbf{x})\right), \tag{3.9}$$

which can also be written, using

$$\phi(\mathbf{x},\mathbf{y}) = \frac{1}{2}(\mathbf{x}-\mathbf{y})^2 - \psi(\mathbf{x}) \tag{3.10}$$

as

$$\nabla\phi(\mathbf{x},\mathbf{y}) = 0. \tag{3.11}$$

The image distortion from the source to the image plane can be described by the Jacobian matrix

$$\begin{aligned} A(\mathbf{x}) &= \frac{\partial \mathbf{y}}{\partial \mathbf{x}} \\ &= \begin{bmatrix} 1-\kappa-\gamma_1 & -\gamma_2 \\ -\gamma_2 & 1-\kappa+\gamma_1 \end{bmatrix} \end{aligned} \tag{3.12}$$

with $\kappa(\mathbf{x})$ being the local surface mass density (convergence) and the shear components

$$\gamma_1 = \frac{1}{2}(\psi_{11}-\psi_{22}), \;\; \gamma_2 = \psi_{12} = \psi_{21}. \tag{3.13}$$

The magnification factor is then given by

$$\mu(\mathbf{x}) = \frac{1}{\det A(\mathbf{x})} = \frac{1}{(1-\kappa)^2 - \gamma^2} \tag{3.14}$$

with

$$\gamma^2 = \gamma_1^2 + \gamma_2^2. \tag{3.15}$$

The time delay between to images at $\mathbf{x}^{(1)}$ and $\mathbf{x}^{(2)}$ is given by

$$\begin{aligned} \Delta t &= \frac{\xi_0^2}{c}\frac{D_s}{D_d D_{ds}}(1+z_d) \\ &\times \left[\phi\left(\mathbf{x}^{(1)},\mathbf{y}\right) - \phi\left(\mathbf{x}^{(2)},\mathbf{y}\right)\right]. \end{aligned} \tag{3.16}$$

Because $\Delta t \propto \mathrm{H}_0^{-1}$ we can use the above equation to determine the Hubble parameter H_0, given the observed time delay between two lensed images and an appropriate mass model for the lens (Refsdal 1964; 1966).

3.4 Mass model

To model B1600+434, we construct a mass distribution consisting of four components: the luminous disk and bulge of G1,

the dark matter halo around G1 and the combined luminous+dark matter distribution of galaxy G2. We will describe these components separately below. We use a Cartesian coordinate system and define our x_1–axis to lie along the dust lane. The origin is defined on the point where x_1 and the line joining A and B intersect. The line joining images A and B makes an angle of $17°\pm2°$ with the x_2 axis, consistent with what we find from our NOT images and the angle of $15°\pm3°$ derived from JH97. We determine the image and galaxy positions with respect to this fixed coordinate system (Table 3.2). Fitting ellipses to the bright inner part of G1 (masking images A and B) in *I* band we find that the center of the brightness distribution of G1 is consistent with our defined origin (Fig. 3.1). This indicates that there is no significant angle between image A, the origin and image B. Lower surface brightness contours indicate a slight shift in the center of the ellipse center towards $x_1<0$, but smaller than the difference in lens center between us and Maller, Flores & Primack (1997), who used the results of JH97 to model B1600+434. The center of G1 that we use in this paper is also consistent with the position of the surface brightness of G1 in recent NICMOS *H*–band observations by Jackson et al. (private communications). But much deeper optical or near infrared observations are still necessary to accurately pin down the center of G1.

In all calculations we will assume a smooth Friedmann–Robertson–Walker (FRW) universe with Ω=1, Λ=0 and h_{50}=1 (H_0=50·h_{50} km/s/Mpc), if not explicitly specified otherwise.

3.4.1 Disk and bulge and halo of G1

The surface brightness distribution of most disk galaxies can be described by an exponential profile (e.g. Mihalas & Binney 1981). Assuming a constant mass–to–light (M/L) ratio, the surface mass distribution of the disk of G1 becomes

$$\Sigma_{\rm G1,disk}(x_1,x_2)=\frac{\Sigma^0_{\rm G1,disk}}{e^{\sqrt{(x_1^2+f_{\rm disk}^{-2}\cdot x_2^2)/h^2_{\rm disk}}}}, \tag{3.17}$$

where $h_{\rm disk}$ is the radial exponential scale length and $f_{\rm disk}$ is the axis ratio of the disk surface brightness (mass) distribution projected on the sky. Although, when seen edge–on, this exponential surface mass distribution is not completely valid anymore, we assume that this relation stays valid in first order at large inclinations.

Many bulges can be well described by a de Vaucouleurs surface brightness profile, i.e. $R^{1/4}$ law (e.g. Mihalas & Binney 1981). By also assuming that the M/L ratio is constant for the bulge, we find

$$\Sigma_{\rm G1,bulge}(x_1,x_2)=\frac{\Sigma^0_{\rm G1,bulge}}{e^{7.67[(x_1^2+f_{\rm bulge}^{-2}\cdot x_2^2)/r_e^2]^{1/8}}}. \tag{3.18}$$

From de Jong (1996) we find $r_e\approx\frac{1}{7}\cdot h_{\rm disk}$ and assume this relation to hold for the effective radius of the bulge of G1. We assume $f_{\rm bulge}$=0.6, as found for NGC891 (Bottema, van der Kruit & Valentijn 1991), which looks morphologically quite similar to G1. The optical extent of NGC891 (∼30–35 kpc) is somewhat but not significantly smaller to that of G1 (∼45 kpc, h_{50}=1). The disk mass of G1 is assumed 30 times more massive than the bulge mass (e.g. NGC891) in all our mass models. Although we have tried several models with free disk and bulge masses, they all give results in contradiction to our observations (Sect.3.6.1).

Because little is known about the actual surface mass distribution of the halo around disk galaxies, we model the halo around G1 with two different surface mass distributions: the non–singular isothermal ellipsoid model (NIE) and the modified Hubble profile (MHP). Following Kormann, Schneider & Bartelmann (1994) we find for the NIE models

$$\Sigma_{\rm G1,halo}(x_1,x_2)=\frac{\Sigma^0_{\rm G1,halo}}{\sqrt{1+(f^2_{\rm halo}x_1^2+x_2^2)/r_{\rm c}^2}} \tag{3.19}$$

where $r_{\rm c}$ is the halo core radius and $f_{\rm halo}$ the flattening. The velocity dispersion is defined as

$$\sigma^2_{\rm halo}=2G\Sigma^0_{\rm halo}r_{\rm c}\sqrt{f_{\rm halo}}. \tag{3.20}$$

	x_1 ($''$)	x_2 ($''$)	Flux
A	-0.33 ± 0.01	1.09 ± 0.01	1.25 ± 0.10
B	0.07 ± 0.01	-0.24 ± 0.01	$\equiv1.00$
G1	0.00 ± 0.05	0.00 ± 0.05	
G2	-0.80 ± 0.10	-4.40 ± 0.10	

TABLE 3.2— Positions and flux ratio of images and positions of galaxies G1 and G2, w.r.t. the defined origin of the coordinate system.

For the MHP models we use

$$\Sigma_{\rm G1,halo}(x_1,x_2)=\frac{\Sigma^0_{\rm G1,halo}}{1+(f^2_{\rm halo}x_1^2+x_2^2)/r_{\rm c}^2}. \tag{3.21}$$

We align the major axes of the disk, bulge and halo of G1 along the x_1–axis and center them on the origin. Because G1 is close to edge–on, we assume that the axis ratio of the surface mass distribution of the halo is very close the its oblateness, hence $f_{\rm halo}$=$q_{\rm halo}$=$(c/a)_{\rho,{\rm halo}}$. For inclinations $\gtrsim$75° and $q_{\rm halo}\gtrsim$0.5 the difference between $f_{\rm halo}$ and $q_{\rm halo}$ is $\lesssim$10%.

3.4.2 The galaxy G2

Because galaxy G2 appears to be a nearly face–on luminous disk galaxy, we use a non–singular isothermal sphere (NIS) as surface mass model, consistent with the assumption that disk galaxies have a flat rotation curve, as observed in many luminous nearby disk galaxies (e.g. Begeman 1987; Broeils 1992). The projected distance between G1 and G2 is ∼30 kpc, a distance at which most of these galaxies still have flat rotation curves and the dark matter halo dominates the surface mass density (e.g. Begeman 1987; Broeils 1992). The oblateness $q^{\rm G2}$=$(c/a)^{\rm G2}_\rho$ of the mass distribution of G2 doesn't influence the radial profile of the surface mass distribution. We therefore assume that a NIS is a reasonable model to describe the surface mass distribution of G2 in first order

$$\Sigma_{\rm G2}(x_1,x_2)=\frac{\Sigma^0_{\rm G2}}{\sqrt{1+(x_1^2+x_2^2)/r^2_{\rm G2,c}}}, \tag{3.22}$$

where $r_{\rm G2,c}$ is the core radius of the mass distribution of G2. The velocity dispersion is given by

$$\sigma^2_{\rm G2}=2G\Sigma^0_{\rm G2}r_{\rm G2,c}. \tag{3.23}$$

We assume a small core radius of 0.1 kpc. We center G2 on the position given in Table 3.2 and assume the redshifts of G1 and G2 to be the same, as explained in Sect.3.2.

3.5 Parameter space

Our knowledge of the galaxies G1 and G2 is rather limited by the low signal–to–noise and/or low resolution of the optical images. To asses the reliability of the results that we obtain on the halo flattening, halo velocity dispersion and time delay between the two lensed images, we examine a large grid of parameters that describe the mass distributions of G1 and G2. We calculate a grid of ∼5000 models using the NIE halo model, each with different core radius of the halo ($r_{\rm c}$), velocity dispersion of galaxy G2 ($\sigma_{\rm G2}$), radial exponential scale length of the disk of G1 ($h_{\rm disk}$), disk mass of G1 ($M_{\rm disk}$) and stellar disk flattening of G1 ($f_{\rm disk}$) (see Table 3.3). We do the same for the MHP halo model. Keeping these parameters fixed, we vary the velocity dispersion $\sigma_{\rm halo}$ and flattening $f_{\rm halo}$ of the halo of G1 to achieve the minimum value of χ^2 ($\chi^2_{\rm min}$), where we define (Kayser 1990)

$$\begin{aligned}\chi^2\cdot{\rm N_{dof}} &= \frac{|\mathbf{y}(\mathbf{x}_{\rm A})-\mathbf{y}(\mathbf{x}_{\rm B})|^2}{\delta y^2}\\ &+ \frac{|r_{\rm AB}-\frac{|\mathbf{J}_{\rm B}|}{|\mathbf{J}_{\rm A}|}|^2}{\delta r^2_{\rm AB}}.\end{aligned} \tag{3.24}$$

Here $\mathbf{y}(\mathbf{x})$ is the lens equation, $\mathbf{x}_{\rm A/B}$ are the positions of lensed images A and B, $r_{\rm AB}$ is the flux ratio, $\mathbf{J}_{\rm A/B}$ are the Jacobians at

Fixed model parameters:	
G1: M_{disk} ($\times 10^{10}$ $M_\odot$)	1.0, 2.0, 3.0, 4.0, 5.0, 10.0, 20.0
G1: f_{disk}	0.1, 0.2, 0.3
G1: h_{disk} (kpc)	1.0, 2.0, 4.0, 8.0, 16.0
G1: r_c (kpc)	(0.05), (0.10), 0.20, 0.40, 0.80, 1.60, [2.40], [3.20]
G2: σ_{G2} (km/s)	0, 50, 100, ..., 350
G1: M_{bulge}	$\frac{1}{30} \cdot M_{disk}$
G1: r_e (kpc)	$\frac{1}{7} \cdot h_{disk}$
G1: f_{bulge}	0.6
G2: $r_{G2,c}$ (kpc)	0.1

TABLE 3.3— Parameters used for the NIE and MHP halo models. The parameters within parenthesis are only used for the NIE models. The parameters within brackets are only used for the MHP models.

$\mathbf{x}_{A/B}$ and $N_{dof}=N_{data}-N_{pars}$[1] is the number of degrees of freedom. For the flux ratio we adopt an error $\delta r_{AB}=0.1$, as explained in Sect.3.2. Furthermore δy is the position error of the source in the source plane. We examined different descriptions for δy, because the circular error regions around the lensed images A and B do in fact not project back to circles on the lens plane, but project back onto ellipses. First we adopted a circular error region with δy=0.02 arcsec, which roughly corresponds to an error of 0.05 arcsec in the image plane for typical magnifications of a few. This error is comparable to the error of the image positions with respect to the lens center. A choice of the δy=0.005 arcsec does not change our results significantly. When projecting the error regions around the lens images back on the source plane, we find that they become two orthogonal ellipses. This increases the allowed region somewhat inside which the two lens images can be projected back on the source plane. However, redoing a sizeable subsample of our models indicates only a slight change in results, being on average only a shift of 10–20% of the rms value. This shift is therefore not significant.

Our choice of error region (0.05 arcsec around both images) allows for a spread in image separation, which is more than the observed 0.01 arcsec (Jackson et al. 1995). So we also looked at those solutions with an image separation of 1.39±0.01 arcsec and again find no significant change in our results compared with the other methods. We are therefore quite confident that our results are not strongly dependent on the choice of the allowed region (δy) in the source plane (e.g. the topology of the χ^2–space is quite robust as function of the error region). The results presented in this paper were obtained using the circular error region with δy=0.05 arcsec.

We minimize χ^2 in the source plane to avoid having to search for the image positions, thereby significantly reducing the computational costs. Minimizing χ^2 for the ∼10 000 models takes ∼5 days CPU time on a SPARC 10 workstation. We minimize χ^2 using a multi–dimensional Downhill Simplex method (Press et al 1992). Using σ_{halo} and f_{halo} at χ^2_{min}, we calculate the time delay Δt_{AB} between lensed images A and B (Eqn. 3.16) and the magnifications μ_A and μ_B (Eqn. 3.14). In total we have 5 fixed parameters (Table 3.3) and 5 constraints (flux ratio, x_1 and x_2 positions of lensed images A and B, so N_{data}=5). We solve for the position of the source (x_s and y_s), the velocity dispersion of the halo σ_h and the flattening of the halo f_{halo} (N_{pars}=4). To avoid under constraining the system we only solve for a total of 4 parameters (N_{dof}=1).

[1] N_{data} is the number of constraints from the observations and N_{pars} is the number of free parameters in the mass model.

3.5.1 Mass model parameters

Below we will describe our choice for the fixed parameter space. For each of the fixed parameters we take a broad range of values, in order not to exclude possible models beforehand. All parameters are listed in Table 3.3.

For the disk mass M_{disk} we take values of $(1.0–20.0)\times10^{10}$ $M_\odot$, spanning the range where most 'maximum disk' masses[2] of luminous disk galaxies lie (e.g. Broeils 1992). A 'maximum disk' mass maximizes the influence of the disk both on the dynamics and the lensing properties. From the deconvolved NOT *R*–band image (Fig. 3.2) we determine an axis ratio of the luminous disk of $\sim$0.3. The *HST I*–band image however shows that most emission (partly bulge) lies clearly between the two QSO images, which are separated by 1.4 arcsec. This would imply an axis ratio $\lesssim$0.2. We therefore choose to model the disk with axis ratios between 0.1 and 0.3, where an axis ratio of 0.1 is typical for an edge–on disk (spiral) galaxy. The scale length of the disk is hard to determine from either the NOT or the *HST* images. Also the dust lane makes such a determination hard. We therefore choose the large range of 1–16 kpc, knowing that the smaller values are probably too small (as is also true for the small disk masses). But these large parameter ranges make sure that we don't underestimate the spread in the results that we obtain. We choose the halo core radius between 0.05 and 3.2 kpc, depending on the choice of mass model (NIE or MHP). The absence of the central third image seems to imply a high central surface density (small core radii; e.g. Narayan & Bartelman 1996), whereas rotation curve analyses seem to imply close–to 'maximum disk' galaxies and therefore large halo core radii (Rhee 1996; Broeils 1992). As a central massive black hole in lensing galaxies can significantly demagnify the central image, we won't use the absence of this image as constraint on the core radius. For the velocity dispersion of G2 we take the very large range from 0 to 350 km/s. No velocity dispersion means that G2 has no influence on the lensing properties. A redshift of G2 different from G1 is approximately equivalent to decreasing its velocity dispersion. In Sect.3.6.1 we will estimate a velocity dispersion for G2 from its luminosity and use that to further constrain our results.

[2]The maximum disk mass is the maximum mass one can attribute to the luminous mass (stellar+gas) of a galaxy and still be in agreement with the observed HI rotation curve.

3.6 Results and analysis

Here we describe the results of the minimization of χ^2 for the parameter space described in the previous section. We assume that the errors in the data have a Gaussian distribution. In which case 95% of the χ^2 distribution of each individual model has $\chi^2<4$ for $N_{dof}=1$. In the analysis we therefore only consider models with $\chi^2_{min}<4$ and $f_{halo}\leq1$ (oblate halo models), although in a sense the χ^2 defined in the source plane is not exactly equivalent to that in the source plane. A smaller cut–off value (e.g. $\chi^2_{min}<1$) does not significantly affect the results. Each model is weighted equally in the determination of the average halo parameter values. Of the $\sim$5000 NIE halo models, 736 have $\chi^2_{min}<4$. Of the $\sim$5000 MHP halo models 182 reach $\chi^2_{min}<4$. This indicates that most combinations of the fixed parameters cannot lead to a satisfactory fit to the observational constraints. We will use all of the above models in the determination of the halo flattening, halo velocity dispersion and time delays between the two lensed images. We will also examine if there are correlations between the fixed parameters (Table 3.3) and the non–fixed parameters (σ_{halo} and f_{halo}).

3.6.1 Flattening of the halo

Analytical models First the flattening of the total lensing mass distribution (luminous+dark) is calculated, modeling G1 and its dark matter halo by a single Singular Isothermal Ellipsoidal (SIE) mass distribution. We assume that θ_A=1.14 arcsec, θ_B=−0.25 arcsec and θ_{G2}=−4.5 arcsec, with the lensed images and galaxy G2 lying on the x_2–axis of the coordinate system. Using the exact positions of the lensed images

and galaxy G2 gives essentially the same results. We find the relation (Kormann et al. 1994):

$$\frac{|\theta_{\rm A}-\theta_{\rm B}|{\rm D_d}}{\xi_0}=\frac{2\sqrt{f}\sinh^{-1}\left[\frac{\sqrt{1-f^2}}{f}\right]}{\sqrt{1-f^2}} \tag{3.25}$$

with

$$\xi_0=4\pi\left(\frac{\sigma}{c}\right)^2\frac{{\rm D_d}{\rm D_{ds}}}{\rm D_s}, \tag{3.26}$$

independent of the presence of G2. In Eqns. 3.25 and 3.26, f is the axis ratio $(b/a)_\Sigma$=$(c/a)_\rho$ of the SIE mass distribution (f equals the oblateness for an edge–on mass distribution), σ is the velocity dispersion of the combined luminous+dark mass distribution, ξ_0 is the Einstein radius, $\rm D_s$, $\rm D_d$ and $\rm D_{ds}$ are the angular diameter distances between respectively observer–source, observer–lens and lens–source. The magnification ratio is given by

$$\frac{\mu_{\rm A}}{\mu_{\rm B}}=\frac{\left(1-\frac{\xi_0}{\rm D_d}[\frac{\sqrt{f}}{|\theta_{\rm B}|}-\left(\frac{\sigma_{\rm G2}}{\sigma}\right)^2\cdot\frac{1}{|\theta_{\rm B}-\theta_{\rm G2}|}]\right)}{\left(1-\frac{\xi_0}{\rm D_d}[\frac{\sqrt{f}}{|\theta_{\rm A}|}-\left(\frac{\sigma_{\rm G2}}{\sigma}\right)^2\cdot\frac{1}{|\theta_{\rm A}-\theta_{\rm G2}|}]\right)}, \tag{3.27}$$

which can be reduced to

$$\frac{\mu_{\rm A}}{\mu_{\rm B}}=\left[\frac{1-2(\kappa^{\rm B}+\kappa^{\rm B}_{\rm G2})}{1-2(\kappa^{\rm A}+\kappa^{\rm A}_{\rm G2})}\right], \tag{3.28}$$

where $\kappa^{\rm A/B}$ and $\kappa^{\rm A/B}_{\rm G2}$ are the dimensionless surface densities (Eqn. 3.2) at the positions of the lensed images A and B. In Fig. 3.5 we plot the magnification ratio (flux ratio) given by Eqn. 3.28 as function of f and σ. Using $\mu_{\rm A}/\mu_{\rm B}$=−1.25, where the minus sign comes from the parity difference between the lensed images, we can solve f and σ from Eqns. 3.25–28. If a non–zero core radius is introduced in the mass distribution we find that for a constant flux ratio ($|\mu_{\rm A}/\mu_{\rm B}|$) the corresponding flattening f of the mass distribution increases. This implies that Eqn. 3.28 gives a lower limit on the flattening. Also the exclusion in Eqn. 3.28 of the flat luminous mass distribution implies that f is smaller than the flattening $f_{\rm halo}$ of the dark matter halo, because the combined luminous+dark matter is flatter then the dark matter (if $f_{\rm disk}$<$f_{\rm halo}$).

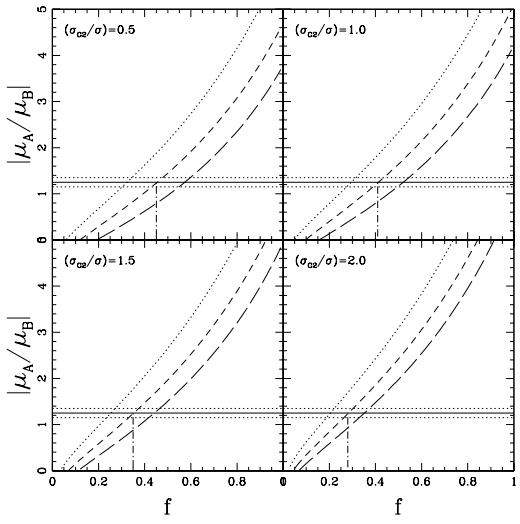

FIGURE 3.5— The flux ratio $|\mu_{\rm A}/\mu_{\rm B}|$ plotted as function of f for $\theta_{\rm B}$=−0.20″(dot), −0.25″(dash), −0.30″(long dash) and for $(\sigma_{\rm G2}/\sigma)$=0.5, 1.0, 1.5, 2.0, using a simple SIE surface mass model to describe G1 and SIS mass model for galaxy G2. The horizontal solid line gives the flux ratio of 1.25, the dotted lines border the region 1.15–1.35.

Numerical models One can compare the analytical results for the mass flattening with what is found from the more detailed numerical models where the disk, bulge and core radius of the halo are taken in to account. We examined the correlations between $f_{\rm halo}$ and the fixed parameters in Table 3.3 and only found a clear anti–correlation with $\sigma_{\rm G2}$. In Fig. 3.6 we plot the flattening $f_{\rm halo}$ of the NIE halo models against $\sigma_{\rm G2}$ for all models with $\chi^2_{\rm min}$<4. If $\sigma_{\rm G2}$ increases $f_{\rm halo}$ decreases, which is qualitatively in agreement with the analysis given above (Fig. 3.5). The solutions of $f_{\rm halo}$ from these more detailed models are systematically slightly higher than the values found for f from Eqn. 3.28, especially for the smaller values of $\sigma_{\rm G2}$.

It is evident from Fig. 3.6 that $\sigma_{\rm G2}$ is a very important parameter in the determination of limits on $f_{\rm halo}$. In the next section con-

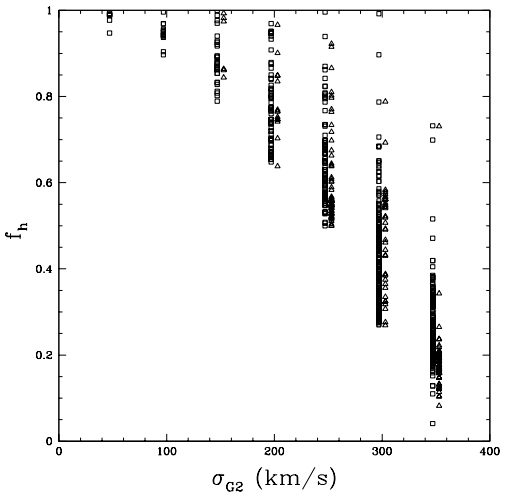

FIGURE 3.6— The flattening parameter $f_{\rm halo}$ plotted against $\sigma_{\rm G2}$ for the NIE (square) and MHP halo models (triangle) with $\chi^2_{\rm min}$¡4. The velocity dispersion $\sigma_{\rm G2}$ has been shifted by −3 km/s and +3 km/s for respectively the NIE and MHP halo models.

straints on $\sigma_{\rm G2}$ will be derived, which are subsequently used to constrain $f_{\rm halo}$, using both analytical and more detailed numerical models.

The velocity dispersion of galaxy G2 and limits on $f_{\rm halo}$

To estimate the velocity dispersion $\sigma_{\rm G2}$ we use the Tully–Fisher relation and the V–magnitude of galaxy G2. From our *HST* V–band observation we find a V–magnitude of 20.6 for G2, consistent with the results of JH97. From Coleman, Wu & Weedman (1980) we find a K correction of 0.6 and 1.2 for $(B-V)$ (if G2 is a Sbc galaxy at $z_{\rm d}$=0.415; From JH97 $(B-V)\sim1.4$). The luminosity is given by

$$\mathrm{L}_B = 10^{0.4\,(\mathrm{M}_{B\odot}-V-(B-V)+\mathrm{DM}+\mathrm{K})}\ \mathrm{L}_\odot, \tag{3.29}$$

where $\mathrm{M}_{B\odot}$=5.48 is the total solar B magnitude and DM is the distance modulus. Using $z_{\rm d}$=0.415 we find DM=42.2$-5\cdot\log(h_{50})$. The luminosity of G2 in B is then $L_B^{\rm G2}\sim4\cdot10^{10}\,h_{50}^{-2}\ \ \mathrm{L}_\odot$. Using this luminosity we find from Rhee (1996) that $\log v_f\approx2.3$ (h_{50}=1), where v_f is the rotation velocity of the HI gas in the flat part of the rotation curve. Using the relation $v_f\approx\sqrt{2}\sigma$ we find that the velocity dispersion of G2 must be $\sigma_{\rm G2}\sim140$ km/s, under the assumption that G2 can be described by a Singular Isothermal Sphere and that the local (z=0) Tully–Fisher relation holds at a redshift of z=0.4. To find a strong upper limit on the velocity dispersion of G2 we go through the sample of luminous spiral galaxies of Broeils (1992) and Rhee (1996). No galaxies with $\log v_{\rm max}>2.54$ are found. This implies an upper limit on $v_{\rm max}$ of 350 km/s, or an upper limit of about 250 km/s on the velocity disperion of G2 ($\sigma\sim v_{\rm f}/\sqrt{2}$). We find from Fig. 3.6 that $\sigma_{\rm G2}\sim140$ km/s would imply an almost spherical halo with $f_{\rm halo}\gtrsim0.8$. The more stringent upper limit of $\sigma_{\rm G2}\lesssim250$ km/s gives a lower limit of $f_{\rm halo}\gtrsim0.5$. This compares well with the lower limit $f_{\rm halo}\gtrsim0.4$ for the same range of velocity dispersions of G2, which we find from equation 28 and Fig. 3.5.

Moreover, Fig. 3.6 shows $f_{\rm halo}$ plotted against $\sigma_{\rm G2}$ for all MHP halo models with $\chi^2_{\rm min}<4$. For the range $\sigma_{\rm G2}$=140–250 km/s we find $f_{\rm halo}\gtrsim0.50$, identical to the limit on $f_{\rm halo}$ from the NIE halo models.

Except for the strong anti–correlation between $\sigma_{\rm G2}$ and $f_{\rm halo}$, no other significant correlations are found. The spread in $f_{\rm halo}$ for fixed values of $\sigma_{\rm G2}$ appears therefore to result mainly from the spread in image positions and flux ratio.

So for both halo models (NIE and MHP) we find a lower limit $f_{\rm halo}\gtrsim0.5$ on the halo flattening, using the range of velocity dispersion of G2, $\sigma_{\rm G2}$=140–250 km/s. We also see that the lower limit on $f_{\rm halo}$ is not strongly dependent on the chosen halo model. We recalculated a subsample of the models, using different starting values of $f_{\rm halo}$ and $\sigma_{\rm halo}$, finding the same solutions for both parameters for $\chi^2_{\rm min}$. The agreement between the lower limits on $f_{\rm halo}$ between the NIE and MHP halos are therefore not an artifact of the initial values of both parameters. Moreover one would expect to find lower values for $f_{\rm halo}$ for the more centrally concentrated MHP models, compared with the NIE halo models. We find that the low $f_{\rm halo}$ solutions for the MHP halo are mostly models with $r_{\rm c}\geq1.6$ kpc.

These models are not very centrally concentrated and therefore allow for larger values of $f_{\rm halo}$. The lower limits therefore appear genuine and not artificial.

From the analytical models (Fig. 3.5) we find that the flux ratio $r_{\rm AB}$ strongly constraints the flattening of the SIE mass distribution. An error of $\pm$0.05 arcsec in the distance of images A and B to the lens center of G1 gives an error of 0.1 in the flattening. Using the same range of $\sigma_{\rm G2}$=140–250 km/s, we find a lower limit on the combined mass distribution (halo+disk+bulge) of 0.40$\pm$0.1. Because the disk is much flatter than the halo and on first sight much more massive than the bulge, the same lower limit applies to the halo. Moreover a non–zero core radius will increase the value of $f_{\rm halo}$.

Moreover, we have tried modeling B1600+434, using only the disk and bulge components. If we constrain the bulge mass, we find that the axis ratio of the disk typically will increase to $f_{\rm disk}\gtrsim$0.5, larger than the observed limit of 0.3. On the other hand, if the disk flattening is constraint to $\leq$0.3, we find solutions that required extremely large bulge masses ($\rm M_{bulge}>M_{disk}$). This again supports the need for a mass component rounder than the disk, but much more massive than the bulge.

Critical curves and caustics

In Fig. 3.7 the critical and caustic curves for two distinct NIE halo mass models are shown. Both models give good fits to the observed image positions and flux ratio, but the critical and caustic structure is quite different.

Figs 3.7a–b both show a mass model with an almost spherical halo and velocity dispersion near 200 km/s. The difference between both models is the mass and flattening (axis ratio) of the disk. Also the velocity dispersion of G2 is different between both models. It is already evident from these two models that the presence of a flat stellar mass distribution can significantly alter the critical and caustic structure of the lens and still be in agreement with the observed image postions and flux ratio. The model shown in Fig. 3.7a has a larger 5–image cross section and one expects therefore a different ratio of 5 to 3–image systems between these models. A precise model of the stellar mass distribution is therefore needed to understand exactly the statistical properties of gravitational lenses with highly flattened luminous mass distributions. This is particulary evident in the case of B1600+434. A more detailed analysis of the statistics of spiral galaxy lenses can be found in Koopmans & Nair (1997).

All our models place the source position close to the radial caustic, whereas Maller et al. (1997) find a source position close to the tangential caustic. This is the result of a difference in adopted lens center. The difference between our and their lens center is $\sim$0.2 arcsec, whereas our *HST* observations allow only a $\sim$0.05 arcsec difference. If we move our lens center to the position found by Maller et al. (1997), we find that the source position moves from the radial to the tangential caustic. Our observations allow a very small shift in the lens center, but much smaller than 0.2 arcsec. This shift would move the source postion slighty away from the radial caustic.

The importance of the redshift of G2

From Kochanek & Apostolakis (1988) we find that two lenses interact significantly if the transverse separation between the two lenses is $\lesssim 4$ times the radius of the outer critical curve. From Fig. 3.7 we find that the radius of the outer critical curve in the direction of G2 is $\sim$0.7 arcsec (approximately the Einstein radius or half the image separation). We see that $4\times0.7''=2.8''<4.5''$, where the separation between G1 and G2 is $\sim$4.5 arcsec. Although the critical curves of G1 will be somewhat distorted (Fig. 3.7), galaxy G2 can in first order be approximated by a perturbing external shear. The strength of this shear is a function of both the redshift and velocity dispersion of G2. According to Kochanek & Apostolakis (1988) both lenses will work together most efficiently, if they are at the same intermediate redshift. Changing the redshift of G2, will therefore decrease the strength of this perturbing shear, which in first or-

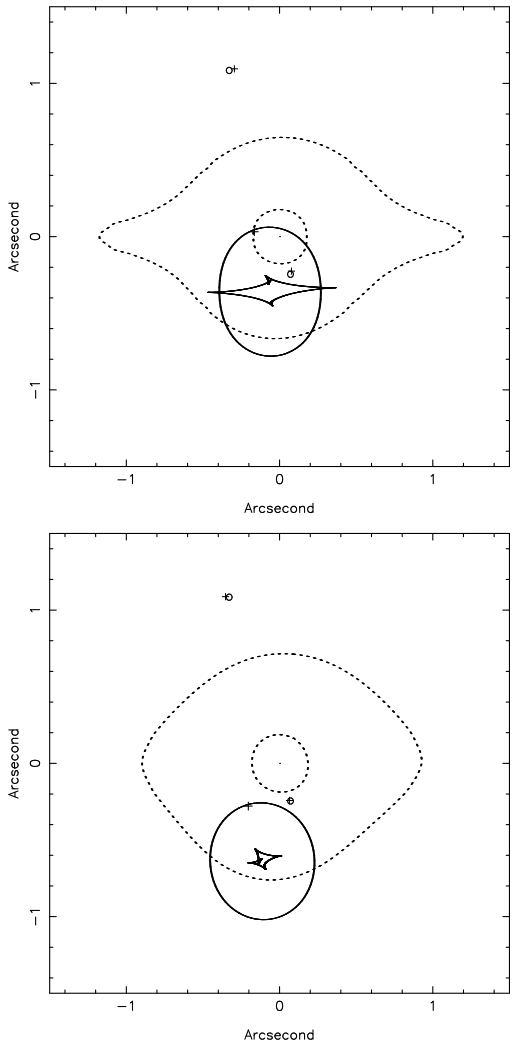

FIGURE 3.7— The critical lines (dashed) and caustics (solid) for two distinct NIE halo mass models of B1600+434 with an NIE halo. The small plusses give the model positions of the lensed images. The circles give the positions of the lensed images listed in Table 3.1. The larger cross indicates the calculated position of the source in the source plane. The large shift in the position of the caustics is the result of the presence of G2. In the upper figure (a) we see a model with r_c=0.40 kpc, $f_{\rm halo}$=0.89, $\sigma_{\rm halo}$=199 km/s, $h_{\rm disk}$=8 kpc, $f_{\rm disk}$=0.1, $\rm M_{disk}$=5.0 $\times$ $10^{10}\rm M_\odot$ and $\sigma_{\rm G2}$=150 km/s. In the lower figure (b) we see a model with r_c=0.40 kpc, $f_{\rm halo}$=0.95, $\sigma_{\rm halo}$=193 km/s, $h_{\rm disk}$=8 kpc, $f_{\rm disk}$=0.3, $\rm M_{disk}$=1.0 $\times$ $10^{11}\rm M_\odot$ and $\sigma_{\rm G2}$=200 km/s.

der is equivalent to decreasing the velocity dispersion of G2. This effect only becomes significant when $z_{\rm G2}$ is outside the range of $z_{\rm G1}\pm$0.3=0.1–0.7. Furthermore a much higher redshift for G2 can change the geometrical part of the timedelay surface, changing the expected time delay. However, the colors of G2 seem to indicate that a redshift smaller than 0.4 is more likely than a redshift larger than 0.4. The $B-V$ and $V-I$ colors from JH97 and our F555W−F814W colors indicate that a redshift of 0.8 for G2 cannot be accomodated by either E/S0 or spiral galaxies. A mucher larger redshift than 0.4 is therefore unlikely for G2. The effect of G2 on the timedelay will therefore in first order be included in our range of velocity dispersion for G2 and as we will see the effect of G2 will be marginal.

3.6.2 Velocity dispersion of the halo

In this section we will describe our results for the velocity dispersion of the NIE halo. We only give the results of $\sigma_{\rm halo}$ for the NIE halo models, because it can directly be related to rotation curve observations of spiral galaxies.

Velocity dispersions and mass From Eqns. 3.25 and 3.26 we find that $\sigma_{\rm halo}\approx$200 km/s, nearly independent of the flattening of the halo ($\theta_{\rm A}$-$\theta_{\rm B}$)$\rm D_d/\xi_0\approx$2 for $f\gtrsim$0.1). This velocity dispersion implies a total mass inside the Einstein radius $\rm M(\xi<\xi_0)\approx 1.3\cdot 10^{11}M_\odot$ (h_{50}=1). In Fig. 3.8 we plot the histogram of $\sigma_{\rm halo}$ for the NIE halo models with $\chi^2_{\rm min}<4$. It appears that $\sigma_{\rm halo}$ is restricted to a small range of values. Simply taking the average for all models with $\chi^2_{\rm min}<4$ we find $\sigma_{\rm halo}$=190$\pm$15 km/s, consistent with what we found analytically. This velocity dispersion gives a rotation velocity outside the optical disk of $v_{\rm f}\approx$270 km/s, comparable to rotation velocities found for large luminous spiral galaxies (e.g. Broeils 1992). Restricting to the larger and more massive models with $h_{\rm disk}\geq$8 kpc and $\rm M_{disk}\geq 5\cdot 10^{10}\ M_\odot$, we find only a slight decrease in the halo velocity dispersion, $\sigma_{\rm halo}$=180$\pm$15 km/s. Both distributions have a wing towards to lower velocity dispersions (Fig. 3.8).

Using the WFPC2 F814W magnitude of 20.2 and the $V-$F814W$\approx$2.0 magnitude for a Sab galaxy at $z\sim$0.5 (Fukugita et al. 1995),

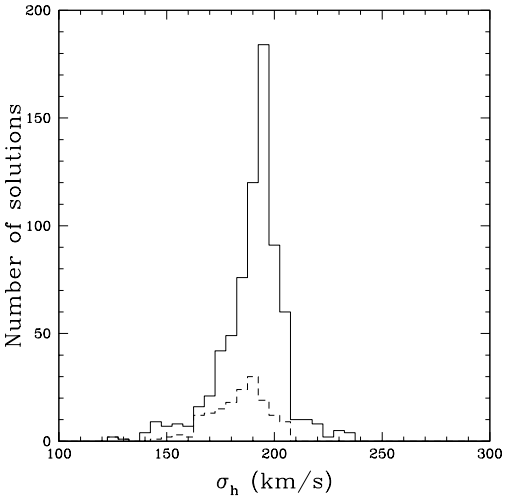

FIGURE 3.8— Histogram (solid) of the velocity dispersion of the NIE halo for $\chi^2_{\rm min} < 4$. The dashed histogram are those models with $M_{\rm disk} \geq 5 \cdot 10^{10}$ $M_\odot$ and $h_{\rm disk} \geq 8$ kpc.

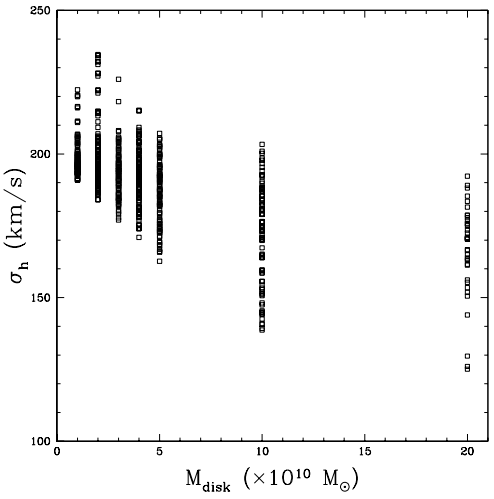

FIGURE 3.9— Correlation between $\sigma_{\rm halo}$ and $M_{\rm disk}$ for the NIE halo model.

we expect a lower limit (due to dust obscuration) on the *V*–magnitude of 22.2, close to the 22.0 found by JH97. This results in a luminosity of $L_B^{G1} \sim 10^{10}$ $L_\odot$. From Rhee (1996) we expect that an Sab galaxy at this redshift should be ∼2.5 magnitudes brighter in B. This difference again indicates the presence of a large amount of obscuring dust. Calculating a sensible mass–to–light ratio is therefore difficult in the inner parts of G1. Moreover the presence of image B in the bulge of G1 makes this even harder. Because of the expected few magnitudes of extinction, the M/L ratio of 51 in *B* (JH97) could be ∼5–10 times smaller. The ratio would then be in the range of spiral galaxies.

Correlations of $\sigma_{\rm halo}$ with disk mass We find an anti–correlations between the $\sigma_{\rm halo}$ and $M_{\rm disk}$ (Fig. 3.9). The separation between the two lensed images is a strong function of the mass inside the Einstein radius. This means that an increase in $M_{\rm disk}$ increases the mass inside the Einstein radius (between the lensed images). This increase in mass must be compensated by the other mass component, the dark halo, hence $\sigma_{\rm halo}$ decreases. For the massive disk models ($M_{\rm disk} \gtrsim 10^{11} M_\odot$) we find that only models with large exponential scale lengths[3] (≥4 kpc), give solutions with $\chi^2_{\rm min} < 4$ and that $\sigma_{\rm halo}$ does not drop below ∼150 km/s (for $\sigma_{G2} \lesssim 250$ km/s). We conclude that even very high disk masses (masses larger than that needed for the image splitting) do not significantly reduce the velocity dispersion of the halo. Indeed a massive halo is in needed to fit the observations. Also a small anti–correlation is found between $\sigma_{\rm halo}$ and σ_{G2}, which could be explained by the model trying the match the flux ratio when changing σ_{G2}.

3.6.3 Time delay

For the SIE mass distribution and under the same assumptions as in Sect.3.6.1 we find for the time delay between the lensed images (Kormann et al. 1994):

$$\Delta t_{AB} = \frac{\xi_0}{c}\frac{D_s}{D_{ds}}(1+z_d) \times \frac{\sqrt{f}}{\sqrt{1-f^2}}\cosh^{-1}(\frac{1}{f})(|\theta_A| - |\theta_B|). \quad (3.30)$$

Eqn. 3.30 is equivalent to the time delay without the presence of G2 in the mass model. This indicates that one does not

[3] e.g Most of the disk mass is outside the Einstein radius.

expect a very large influence of G2 on the time delay between the lensed images. Using Eqn. 3.25 we can reduce Eqn. 3.30 to

$$\Delta t_{\rm AB} = \frac{1}{2c}\left(\frac{\rm D_d D_s}{\rm D_{ds}}\right)(1+z_{\rm d}) \quad (3.31)$$
$$\times \ |\theta_{\rm A}-\theta_{\rm B}|(|\theta_{\rm A}|-|\theta_{\rm B}|).$$

For $z_{\rm d}$=0.415, $z_{\rm s}$=1.59, $\theta_{\rm A}$=1.14 arcsec, $\theta_{\rm B}$=−0.25 arcsec and an error in $\theta_{\rm AB}\sim$0.05 arcsec we find a time delay $\Delta t_{\rm AB}$=(57±7) h_{50}^{-1} days. We will now compare this predicted time delay with the time delays found from our numerical models.

In Fig. 3.10 we plot the histogram of the time delay for all numerical models with $\chi^2_{\rm min}$<4. We see in this figure that the time delay depends only weakly on variations in the input model parameters. Taking the average of all time delays with $\chi^2_{\rm min}$<4 we find $\Delta t_{\rm AB}^{\rm NIE}$=(54 ± 3) h_{50}^{-1} days. Using only the larger and more massive models with $h_{\rm disk}\geq$8 kpc and $\rm M_{disk}\geq 5\cdot 10^{10}M_\odot$, we find $\Delta t_{\rm AB}^{\rm NIE}$=(53±3) h_{50}^{-1} days. This is in excellent agreement with the time delay we found from our simple analysis, indicating the stability of the time delay against changes in the fixed NIE model parameters.

In Fig. 3.10 we also plotted the histogram of the time delay for all MHP models with $\chi^2_{\rm min}$<4. Taking the average of these time delays, we find $\Delta t_{\rm AB}^{\rm MHP}$=(70 ± 4) h_{50}^{-1} days. For the larger more massive models we find $\Delta t_{\rm AB}^{\rm MHP}$=(68 ± 2) h_{50}^{-1} days. Also for the MHP halo models a small spread in the time delay is found. It is therefore clear, as in the case of the NIE halo model, that changes in the fixed model parameters do not severely influence the time delay between the lensed images. We have not calculated the time delay for the MHP mass models analytically .

The difference in time delays between the MHP and NIE halo models are ∼30%, because the more centrally concentrated MHP mass distribution gives rise to a much larger potential timedelay between images A and B. Although the flat rotation curves of spiral galaxies seem to favor a NIE mass distribution, we do not know the distribution of mass in the z–direction very well.

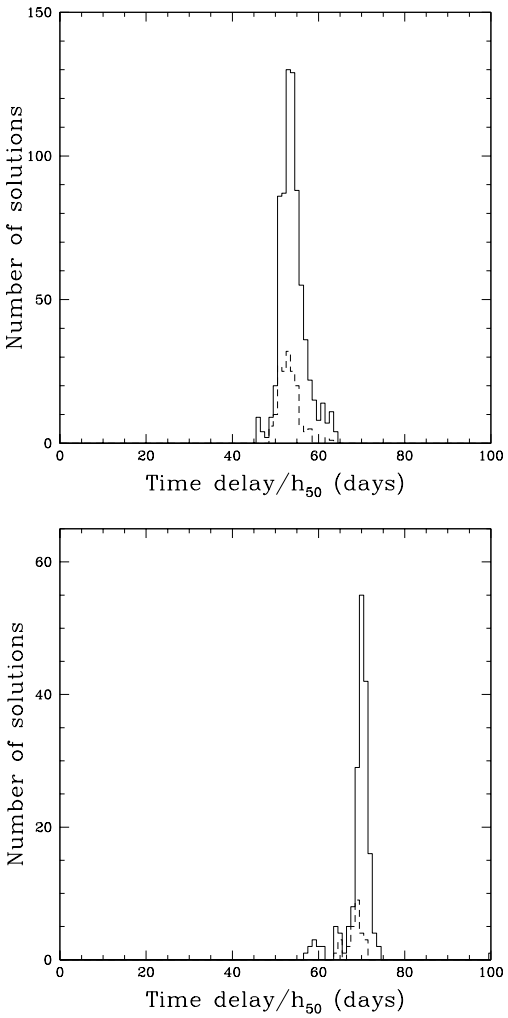

FIGURE 3.10— Histogram of the NIE (upper) and MHP (lower) model time delays for $\chi^2_{\rm min}$<4. The dashed histograms are those models with $M_{\rm disk}\geq 5\cdot 10^{10}\rm M_\odot$ and $h_{\rm disk}\geq$8 kpc.

More contraints on the mass distribution are therefore needed (e.g VLBI structure in the images A and B).

3.6.4 Magnification of images A and B

We have calculated the magnification of the lensed images for every model with $\chi^2_{\rm min}$<4. The averages of the magnifications and flux ratios for the NIE and MHP halo models are listed in Table 3.3. We see that the average magnifications for both halo models are not very large, but typical for a two image system. One also notes that the

	NIE	MHP
μ_A	2.69±0.26	2.03±0.15
μ_B	−2.14±0.22	−1.64±0.11
μ_A/μ_B	−1.25±0.03	-1.24±0.03

TABLE 3.4— Average magnifications and flux ratios of the source for images A and B.

magnification from the MHP halo models is smaller than the magnification from the NIE halo models. The difference between the magnifications is about 33%, which results in a different calculated absolute magnitude for the lensed source for the two (NIE and MHP) halo models.

3.7 Conclusions

New *HST* and NOT observations of the GL system B1600+434 strongly suggest that the lensing galaxy in this system is an edge–on spiral galaxy. Because the system is nearly edge–on, we can use the lensing properties of this system to constrain the velocity dispersion and oblateness (flattening) of the dark matter halo around the lensing spiral galaxy. This system is unique in the sense that for the first time gravitational lensing has been used to constrain the dark matter distribution around an individual spiral galaxy. Moreover, the lensed QSO is highly variable both in the radio and the optical and can therefore be used to determine the time delay between the two lensed images. This time delay gives us either H_0, once the mass model has been well constrained, or an extra constraint on the mass model, once H_0 has been constrained from other GL systems (e.g. B0218+357, B1608+656, etc).

3.7.1 Flattening of the halo

From detailed numerical modeling we find a lower limit of $f_{\rm halo} \gtrsim 0.50$ on the axis ratio of both the NIE and MHP halo mass distribution around the edge–on spiral galaxy lens in B1600+434.

When we use a simplified analytical SIE mass model we do not find a surface mass distribution significantly flatter than ∼0.4. Using a core radius $r_c > 0$ increases this limit. This lower limit is significantly larger than the typical flattening (∼0.1) of the luminous stellar component of spiral galaxies and also larger than the upper limit on the flattening of G1 ($\lesssim$0.3) from the *HST* and NOT observations. We conclude that the halo dark matter around G1 is not as flat as the luminous stellar component (or gas). This implies that the suggestion by Pfenniger at al. (1994), that dark matter could be cold molecular hydrogen associated with HI gas, is inconsistent with our results for G1. In that case one would expect to find a halo flattening in the same order or smaller than the luminous stellar component ($f_{\rm halo} \leq f_{\rm disk}$), which we clearly do not find.

3.7.2 Velocity dispersion and mass of the halo

The average velocity dispersion over all models of the NIE halo is found to be 190±15 km/s, which gives a rotation velocity outside the optical disk of ∼270 km/s ($f_{\rm halo} \sim 1$), consistent with luminous spiral galaxies (e.g. Broeils 1992). For large disk masses ($10-20 \cdot 10^{10}$ $M_\odot$) the velocity dispersion of the halo decreases, but never drops below ∼150 km/s, even for disk masses larger than the mass needed for the image splitting. This indicates that a massive halo is needed around the much flatter luminous stellar component to fit the observed image positions and flux ratio.

The mass inside the Einstein radius is $\sim 1.3 \cdot 10^{11} M_\odot$ of which at least half (if $\sigma_{\rm halo} \gtrsim$ 150 km/s) can be attributed to the halo. Using the Tully–Fisher relation and the observed 10^{10} $L_\odot$ in the *B* band, we suspect some 2.5 magnitudes of extinction in the *B* band. If this is the case, the mass–to–light ratio of 51 in *B* (JH97) would be reduced to ∼5, consistent with spiral galaxy mass–to–light ratios.

3.7.3 Time delay

The time delays found for the different halo models are quite different and do not significantly depend on the presence of G2. The NIE halo model gives in a time delay of $\Delta t^{\rm NIE}_{\rm A/B} = (54 \pm 3)\ h_{50}^{-1}$ days, whereas the MHP halo model gives $\Delta t^{\rm MPH}_{\rm A/B} = (70 \pm 4)\ h_{50}^{-1}$ days.

These delays decrease by only a few percent if only models with $h_{\rm disk} \geq 8$ kpc and $M_{\rm disk} \geq 5 \cdot 10^{10}$ $M_\odot$ are used. It is clear that more observations are necessary to constrain the mass model and discriminate between different halo mass models. Because flat rotation curves of spiral galaxies seem to point at a NIE halo, the time delay from the NIE halo model is probably closest to the actual time delay. The time delay from the MHP can still be used to put an upper limit on H_0.

Acknowledgments

LVEK and AGdeB acknowledge the support from an NWO program subsidy (grant number 781–76–101). We would like to thank Sunita Nair for the many valuable discussions about the modeling of lens systems and many more aspects of lensing. We furthermore thank Chris Fassnacht for kindly supplying us with the redshifts of the lensing galaxy and the lensed source and Penny Sackett for giving a number of constructive comments and suggestions. This research used observations with the *Hubble Space Telescope*, obtained at the Space Telescope Science Institute, which is operated by Associated Universities for Research in Astronomy Inc. under NASA contract NAS5–26555. MERLIN is a national facility operated by the University of Manchester on behalf of SERC. The Westerbork Synthesis Radio Telescope (WSRT) is operated by the Netherlands Foundation for Research in Astronomy (ASTRON) with the financial support from the Netherlands Organization for Scientific Research (NWO).

References

Begeman K.G., 1987, PhD thesis, University of Groningen
Bottema R., van der Kruit P.C., Valentijn E.A., 1991, A&A, 247, 357
Broeils A., 1992, PhD thesis, University of Groningen
Coleman G.D., Wu C-C., Weedman D.W., 1980, ApJS, 43, 393
Fassnacht C.D., Cohen, J.G., 1998, AJ 115, 377
Fukugita M., Shimasaku K., Ichiwaka T., 1995, PASP, 107, 945
Jackson N., de Bruyn A.G., Myers S., Bremer M.N., Miley G.K., Schilizzi R.T., Browne I.W.A., Nair S., Wilkinson P.N., Blandford R.D., Pearson T.J., Readhead A.C.S., 1995, MNRAS, 274, L25
Jaunsen A.O., Hjorth J., 1997, A&A, 317, 39
de Jong R.S., 1996, A&A, 313, 45
Kayser R., 1990, ApJ, 357, 309
Kochanek C.S., Apostolakis J., 1988, MNRAS, 235, 1073
Koopmans, L.V.E., Nair, S., 1997, in preparation
Kormann R., Schneider P., Bartelmann M., 1994, A&A, 284, 285
Maller A.H., Flores R.A., Primack J.R., 1997, astro-ph/9701110
Mihalas D., Binney J., 1981, Galactic Astronomy. W.H. Freeman, San Francisco
Myers et al., 1997, in preparation
Narayan, R., Bartelmann, M., 1996, Lectures on Gravitational Lensing, Jerusalem Winter School 1995, astro-ph/9606001
Olling, R.P., 1996, AJ, 112, 481
Pfenniger D., Combes F., Martinet L., 1994, A&A, 285, 79
Pfenniger D., Combes F., 1994, A&A, 285, 94
Press W.H., Teukolsky S.A., Vetterling W.T., Flannery B.P., 1992, Numerical Recipes in C. Second Edition, Cambridge University Press, Cambridge
Refsdal S., 1964, MNRAS, 128, 295
Refsdal S., 1966, MNRAS, 134, 315
Rhee M-H., 1996, PhD thesis, University of Groningen
Rix H., 1995, in Blitz, L., Teuben, P., eds, Proc. IAU Symp. 169, Kluwer, Dordrecht, p.23
Sackett P.D., 1995, in Kochanek, C.S., Hewitt, J.N., eds, Proc. IAU Symp. 173, Kluwer, Dordrecht, p.165
Schneider P., Ehlers J., Falco E.E., 1992, Gravitational Lenses, Springer Verlag, Berlin

4

A time–delay determination from CLASS B1600+434

Based on L.V.E. Koopmans, A.G. de Bruyn, E. Xanthopoulos & C.D. Fassnacht, 1999, Astronomy & Astrophysics, submitted

We present *Very Large Array* (VLA) 8.5–GHz light curves of the two lens images of the *Cosmic Lens All Sky Survey* (CLASS) gravitational lens B1600+434. We find a long–term gradual decrease of 15–20% in the flux densities of both lens images over a period of eight months (February–October) in 1998. The brightest image A shows furthermore modulations up to 10% peak–to–peak on scales of days to weeks over a large part of the observing period. Image B varies significantly less on this time scale. We conclude that most of the short–term variability in image A is therefore not intrinsic source variability, but either scintillation or microlensing.
Using the minimum–dispersion method from Pelt et al. (1996), we determine a median time delay between the lens images of 47^{+5}_{-6} d (68% statistical confidence) or 47^{+12}_{-9} d (95% statistical confidence). We estimate a maximum systematic error of $-8/+7$ d. With the isothermal lens mass models from Koopmans, de Bruyn & Jackson (1998), this time delay gives a value for the Hubble parameter, H_0=57^{+14}_{-11} (95%) $^{+26}_{-15}$ (maximum systematic error) km s^{-1} Mpc^{-1} ($\Omega_{\rm m}$=1 and Ω_Λ=0). Using the Modified–Hubble–Profile (MHP) mass model gives H_0=74^{+18}_{-15} (95%) $^{+22}_{-22}$ (maximum systematic error) km s^{-1} Mpc^{-1} for the same cosmological model. For $\Omega_{\rm m}$=0.3 and Ω_Λ=0.7, these values increase by 5.4%. These values of H_0 are very uncertain. However, they agree remarkably well with other GL systems for which the mass models have been used.
In the case of relatively ill–constrained gravitational lens systems, like B1600+434, we believe that it might be much more interesting to constrain the radial mass profile of the dark–matter halo around the lens galaxy, once the time delay and H_0 (from independent methods) have been determined with much greater accuracy.

4.1 Introduction

Gravitational lens systems can be used to determine the Hubble parameter, H_0 (Refsdal 1964). However, both a good mass model of the lens galaxy as well as a time delay between an image pair are necessary ingredients to accomplish this. The mass model can be constrained from the lens–image properties, whereas a time delay can be obtained through correlations between two image light curves. Intrinsic source variability should occur in all light curves, lagging by time delays which depend on

(i) the source and lens redshifts, (ii) the lens–mass distribution and (iii) the cosmological parameters, most prominently H_0 (e.g. Schneider et al. 1992).

Recently, values of H_0 were determined from several different gravitational lens (GL) systems: Q0957+561 (e.g. Kundić et al. 1997), PG1115+080 (e.g. Schechter et al. 1997), B0218+357 (Biggs et al. 1999), B1608+656 (Fassnacht et al. 1999; Koopmans & Fassnacht 1999) and PKS 1830-211 (Lovell et al. 1998). Not only do these GLs – except for PG1115+080 – give values of H_0 that are consistent within their errors, using isothermal mass models to describe the lens mass distribution, but they also agree with the local, SNe Ia and S–Z determinations of H_0 (e.g. Koopmans & Fassnacht 1999). This indicates a possible convergence towards a consistent value of H_0 from different local and cosmological determinations, even though several systematic effects in all methods still remain to be resolved.

In this paper, we present a determination of the time delay between the two lens images of the CLASS gravitational lens B1600+434, using the light curves obtained during an 8-month VLA monitoring campaign. In section 4.2, we describe the 8.5–GHz VLA observations of B1600+ 434 and the data reduction. In section 4.3, we apply the minimum dispersion method from Pelt et al. (1996) to find a time delay between the lens images and apply that to estimate a tentative value for H_0. In section 4.4, our conclusions are summarized.

4.2 Data & Reduction

4.2.1 Observations

We observed the CLASS gravitational lens B1600+434 (Jackson et al. 1995; Jaunsen & Hjorth 1997; Koopmans, de Bruyn & Jackson 1998) with the VLA in A– and B–arrays at 8.5 GHz (X–band), during the period February 13 to October 18 1998. The typical angular resolution of the radio images ranges from about 0.2 arcsec in A–array to 0.7 arcsec in B–array, sufficient to resolve the 1.4–arcsec double. In total we obtained 75 epochs of about 30 min each, including phase– and flux–calibrator observations and slewing time. The average time interval between epochs was 3.3 days. A typical observing run consisted of the sequence listed in Table 4.1. This sequence was repeated, typically twice, until about 30 min observing time was filled. Several epochs consisted of only 10 or 20 min, making it necessary to reduce the number of sequences, or the time spent on each of the sources. At the end of a sequence, we again observed 2 min on the phase calibrator J1549+506 (Fig.4.1; Patnaik et al. 1992).

The flux calibrator, B1634+627 (3C343), is a slightly extended steep-spectrum source (Fig.4.1; e.g. van Breugel et al. 1992), which should not be variable. Its flux density at 8.5 GHz is 0.84 ± 0.01 Jy, which we obtained with the *Westerbork–Synthesis–Radio–Telescope* (WSRT) in December 1998. This value agrees with the average flux density of 0.83 Jy, obtained with the 26–m University of Michigan Radio Astronomy Observatory (UMRAO) telescope, which has been monitoring this source for the past 15 years. We use the WSRT flux–density determination to bring all flux densities to the correct absolute scale (Sect.4.2.4).

4.2.2 Calibration

The initial flux and phase calibration is done in the NRAO data–reduction package AIPS (version 15OCT98). We fixed the flux density of the phase calibrator at 1.17 Jy[1] at all epochs and subsequently solve for the telescope phase and gain solutions. The phase calibrator (J1549+506; Patnaik et al. 1992) is an unresolved flat–spectrum point source ($<$10 mas)[2] at 8.5 GHz when observed with the VLA in A–array (Fig.4.1). A single delta function is therefore sufficient to describe the source structure. Because the phase calibrator is a flat spectrum and compact source, it could vary significantly over a monitoring period of eight months. Thus, the flux density of 1.17 Jy could be wrong by a large fraction. We therefore

[1] Taken from the VLA Calibrator Manual.
[2] See the VLBA Calibrators List.

1	J1549+506	2 min	phase calibrator
2	B1634+627	2 min	flux calibrator
3	B1600+434	6 min	CLASS gravitational lens
4	B1634+627	2 min	flux calibrator

TABLE 4.1— Basic observing sequence on B1600+434 and the phase and flux calibrators. This sequence was repeated typically twice per session.

use the flux calibrator to determine the proper flux–density scale and correct for 'variability' introduced in both images of B1600+434, due to intrinsic flux–density variability of the phase-calibrator. This is the price one has to pay to avoid solving for phase and gain solutions on an extended non–variable flux calibrator source – by an iterative procedure of phase/gain solving and imaging – which will undoubtedly introduce additional errors. As we will see in Sect.4.2.4, however, the strategy that we have chosen works well.

We smooth (1–min intervals) and interpolate the phase and gain solutions between the phase calibrator scans for the entire observation period of about 30 min. These are then used to determine initial phase and gain solutions for the flux calibrator B1634+627 and the gravitational lens system B1600+434. No flagging was done in *AIPS*, because it is hard to assess if phase and/or gain errors can be corrected through self–calibration. Flagging is only done in the *DIFMAP* package (Shepherd 1997), where the visibility amplitudes and phases can be compared with a model of the source structure and possibly corrected through self–calibration. Only if the latter fails, do we manually flag those visibilities which most strongly deviate from the model.

4.2.3 Imaging and model fitting

First we make maps of B1600+434 for all epochs, in DIFMAP (version 2.2c), using a process of iterative model fitting and self–calibration. Because the two lens images are compact ($\leq$1 mas) at 8.5–GHz, determined from *VLBA* observations (Fig.4.3), and also show no extended emission from either the lens or quasar on mas or arcsec scales in MERLIN 5–GHZ observations (Koopmans et al. 1998), we can safely model the lens image structure by two delta functions, for which we determine the positions and flux densities. We fit these delta functions to the visibilities, until the model–χ^2 converges. We perform a phase–only self–calibration, using this model. Typically, this decreases the χ^2 of the model and the rms noise in the map significantly. We repeat this process several times, until no further decrease in either χ^2 or rms noise level is obtained. Finally, a global gain–self–calibration is performed, solving for small gain errors of each telescope. This gain–self–calibration does not significantly change the flux densities of the images and individual telescope gain corrections are typically less than a few percent. We repeat the process of model fitting and self–calibration, until it converges again. The visibilities are then compared with the best model and obviously errant points are manually flagged. Once more, we iterate between model fitting and self–calibration until convergence is reached. Finally, we average the visibilities over 300 sec and repeat the convergence process, after having flagged those points which still deviate significantly ($\gtrsim$3–sigma) from the model.

The flux–density ratio between images A and B changes by at most a few tenths of a per cent before and after these calibration cycles, as long as there are no visibilities which deviate by orders of magnitude from the model. The reduced–χ^2–value of the final model fit typically lies between 1.0 and 1.1. The residual maps show no spurious features due to bad visibilities. Fig.4.3 shows a radio map of B1600+434, created from A–array data-sets of seven epochs.

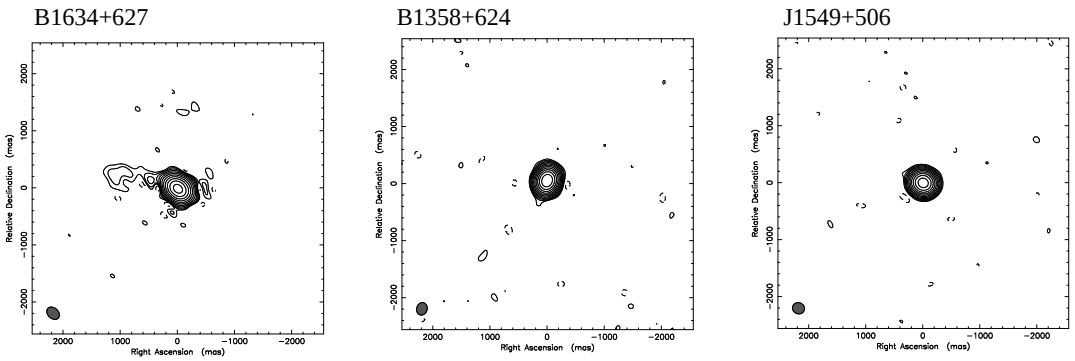

FIGURE 4.1— VLA 8.5–GHz A–array images of the flux density calibrators B1634+627 and B1358+624, and the phase calibrator J1549+506 (epoch 1998 May 25). Contours starts at 3–σ and increase by factors of two. The lowest contours are 0.53, 0.56 and 0.56 mJy/beam for B1634+627, B1358+624 and J1549+506, respectively.

4.2.4 Flux calibration

We subsequently make maps of the flux calibrator, B1634+ 627, using the same procedure as for B1600+434. B1634+627 can be well represented by a single Gaussian component with a 1–σ major axis of 90 mas, an axial ratio of 0.8 and a position angle of -70 deg, in good agreement with the source structure as seen in 50–cm VLBI images (Nan et al. 1991) . We use this component to model fit the image structure and self–calibrate the visibilities. We subsequently remove this Gaussian component and clean the map to find a better description of the extended structure of the source. The ratio between the flux density in the Gaussian component and the total flux density in all extended emission (seen with the VLA in A and B–arrays on a scale $\lesssim$10 arcsec) is 0.98. The ratio appears independent of epoch (within the errors). The determination of the flux density using a single Gaussian component is better defined than the flux density derived from an iterative cleaning procedure. The latter procedure seems to introduce $\lesssim$1% errors, depending on how the maps were cleaned, what array was used and inside which box the total flux density was determined. Using only a single Gaussian to represent the source, does not involve cleaning or choosing a box size.

We determine the normalized light curve of the flux calibrator B1634+627 by dividing its flux–density light curve by the flux density of 0.84 ± 0.01 Jy (Sect.4.2.1). The resulting curve shows a linear increase of approximately 5% over the eight–month observing period, which we attribute to a similar change in the flux density of the flat–spectrum phase calibrator, J1549+506. We also see that we have overestimated the flux density of B1634+627 by some 20–30%. In other words, our initial estimate of the flux density of the phase calibrator, based on the value given in the VLA calibrator manual, was 20-30% too high, which comes as no surprise for a variable flat–spectrum radio source.

From May 12 1998 onwards, we added a second flux calibrator, B1358+624[3] (Fig.4.1) to the observations, to estimate the reliability of the flux density determination of B1634+627. We followed the same calibration and mapping procedure as for B1634+627. Also B1358+624 shows the same 5% linear increase in flux density, supporting the idea that this is the result of variability of the phase calibrator. We scale the flux density curve of B1358+624 to fit the calibrated light curve of B1634+627 and find its flux density to be 1.14 ± 0.02 Jy. The final normalized flux density curve of

[3]Taken from the VLA Calibrator Manual.

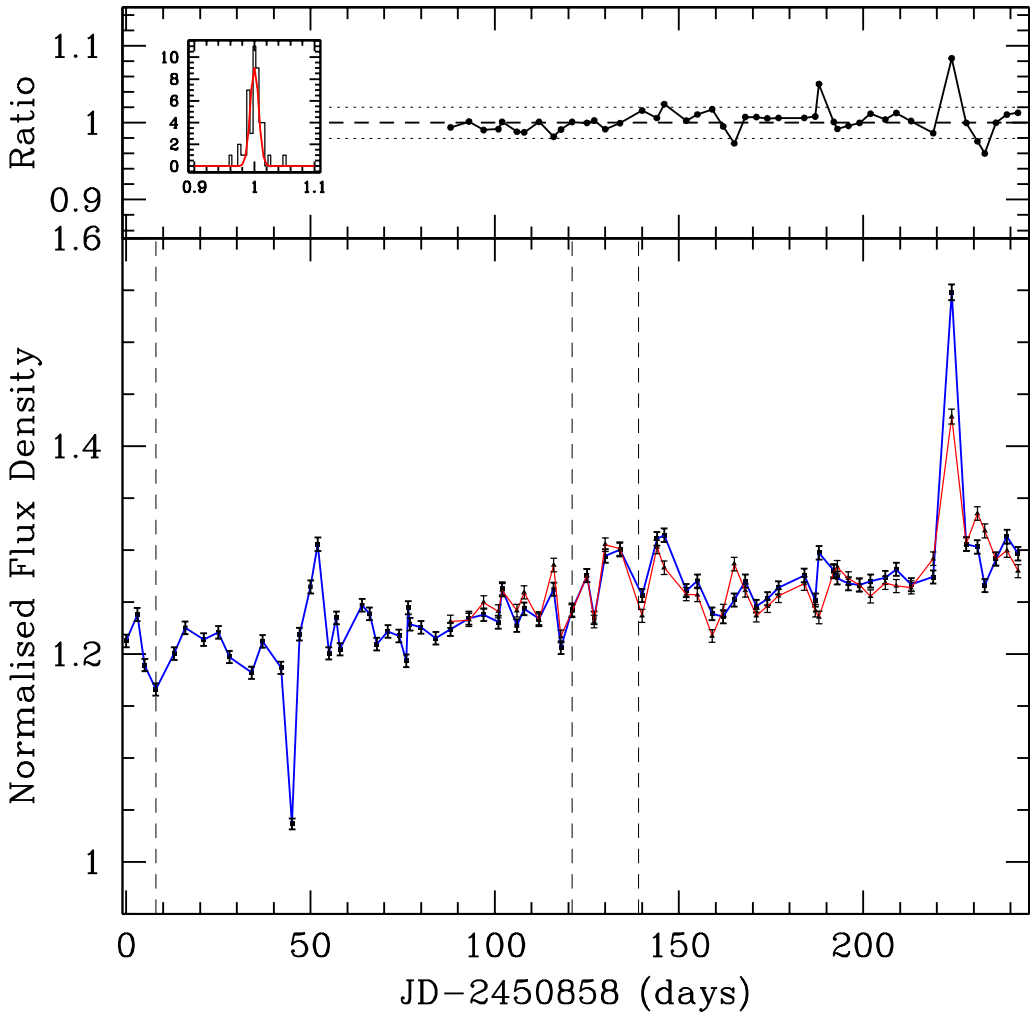

FIGURE 4.2— The lower panel shows the normalized light curves of B1634+627 (squares) and B1358+624 (triangles). The upper panel shows the ratio of the two curves, where they overlap. The small sub panel shows a histogram of this ratio, fitted by a Gaussian with a 1–σ value of $\approx$0.7%. The dotted lines in the upper panel indicate the $\pm$3–σ region from the Gaussian fit. The error bars on the light curves are $0.7\%/\sqrt{2} \approx 0.5\%$ (Sect.4.2.6), assuming the errors on both light curves are similar. The vertical dashed lines indicate the array changes D$\rightarrow$A, A$\rightarrow$BnA and BnA$\rightarrow$B, respectively, from left to right.

B1358+624 is also shown in Fig.4.2.

4.2.5 Light curves of B1600+434

To correct the light curves of B1600+434 for flux–density calibration errors, we divide them by the average of the normalized light curves of B1634+627 and B1358+624.

We assume both flux calibrators do not vary intrinsically over the eight–month observing period. We also assume that the phase and gain solutions found from J1549+ 506 do not change significantly over a time span of several minutes, such that interpolation can be used to make a first–order correction for phase and gain errors in data of B1600+434, B1634+627 and B1358+624. This flux density correction removes the largest errors in the light curves of B1600+434, after which only statistical

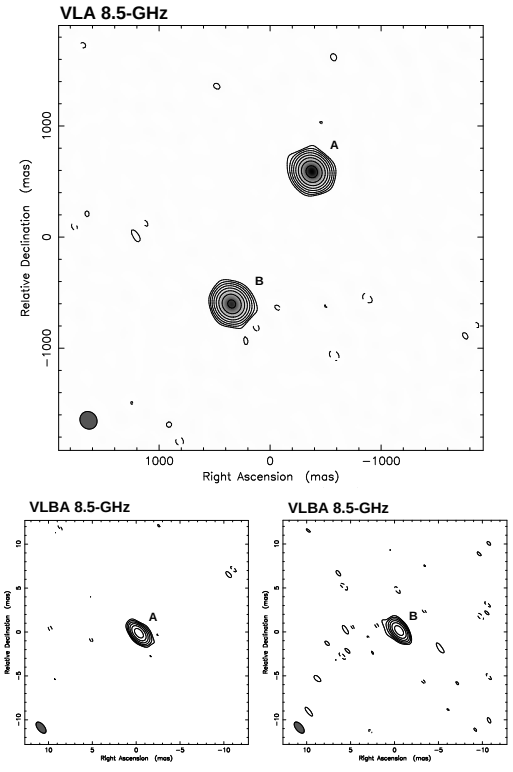

FIGURE 4.3— Top: VLA 8.5–GHz A–array image of B1600+434, showing the two compact lens images A and B. The image was created from a combined data set from 7 different epochs. The contours indicate (-3,3,6,12,24,48,96,192,384)×rms noise, where the rms noise is 0.059 mJy. Bottom: VLBA 8.5–GHz images of the lens components B1600+434 A and B (5–h integration) taken 1996 November 4. For a full discussion on the VLBA data reduction see Koopmans et al. (1999), where this has been explained in detail for B1127+385, which was observed during the same run as B1600+434. The contours indicate (-2,2,4,8,16,32,64) per cent of the map peak, where the map peak is 30.1 (23.4) mJy for image A (B). Both lens images show no sign of any extended structure larger than about 1 mas.

errors, second–order systematic errors and intrinsic variations are left. Any deviations between the two normalized light curves are most likely due to short–term calibration errors, either instrumental or atmospheric. Remaining systematic errors can partially be removed by self–calibration. The final flux–calibrated light curves of the lens images A and B are shown in Fig.4.4.

Both light curves show a gradual decrease of about 0.02 mJy/day over a period of 242 days (Sect.4.3.1). Superposed on this gradual long–term variability, image A also exhibits strong (up to 10% peak–to–peak) modulations on a time scale of a few days to several weeks. Image B only shows a few (up to 5% peak–to–peak) features, but separated in time by about one month. The modulation index (i.e. rms variability) around the gradual long–term decrease in flux density (indicated by the dashed lines in Fig.4.4) is 2.8% and 1.9% for images A and B, respectively.

External variability In a forthcoming paper (Koopmans & de Bruyn 1999) it is shown with 15–σ confidence that most of the observed short–term variability is of external origin. A number of possible origins of this short–term variability are examined: (i) scintillation caused by the ionized component of the Galactic ISM and (ii) radio microlensing of a core-jet structure by massive compact objects in the lens galaxy.

The short–term variability in the VLA 8.5–GHz light curves of B1600+434 (Fig.4.4) are re–analyzed in combination with long–term monitoring data obtained with the *Westerbork–Synthesis–Radio–Telescope* (WSRT) at 1.4 and 5 GHz. A comparison between this data and theoretical models support the hypothesis that the short–term variability in the image light curves is caused by microlensing in the disk/bulge *and* dark–matter halo of the lens galaxy. However, if image B is significant scatter–broadened in the lens galaxy, this conclusion might have to be reevaluated.

Throughout the rest of this paper, we assume that the statistical properties of the external variability are symmetric around the long–term, presumably intrinsic, source variability. In other words, if we subtract the two images light curves (when they are corrected for the intrinsic time delay and flux–density ratio), the difference light curve shows *only* external variability, which has a symmetric distribution function around zero.

4.2.6 Error analysis

The errors on light curves are a combination of noise errors and systematic errors (e.g. modeling, self–calibration, instrumental, atmospheric, etc.). The noise errors on the $\gtrsim 1$ Jy flux density calibrators are of the order of 0.01% after a few minutes of integration. The noise error on each of the lens images is about 0.3%, determined from the residual maps (i.e. the radio image after subtracting the model of the source structure). This noise level agrees well with the theoretically expected value for the typical integration time of $\approx$10 min.

To estimate the systematic errors, we compare the two normalized light curves of B1634+627 and B1358+624. In Fig.4.2, we see that both curves follow each other extremely well. Their ratio has a rms scatter of 0.7%, determined from fitting a Gaussian to its distribution function. Assuming the errors on both normalized light curves are similar, the errors on the individual points are therefore $0.7/\sqrt{2}\approx 0.5\%$. This error is probably a mixture of modeling, self–calibration and short–term atmospheric and instrumental effects, which are hard to remove. We assume that the data of B1600+434 contains a similar 0.5% error.

During the B–array observations, six points lie outside the 3–σ region (Fig.4.2, upper panel), whereas during the A– and BnA–array observations, the ratio seems much more more stable. This stability during A– and BnA–array observations is reflected in the extremely small scatter in the measured distance between the two lens images (Fig.4.4, upper panel), which is similar to the theoretical expectation value of $\Delta r_{\rm AB}$=0.5 mas, where we used $\Delta r_{\rm AB} = \sqrt{2} \times \Delta\theta/(2 \cdot {\rm SNR})$, with $\Delta\theta$ being the beam size of 0.2 (0.7) arcsec in A–array (B–array) and SNR the signal-to-noise ratio of about $1/0.003\approx 330$.

The six "outliers" are given an error equal to their difference in normalised flux density divided by $\sqrt{2}$, which is the expectation value if their errors are equal and drawn from a Gaussian distribution. The errors are around 2–5%. Although this approach is rather ad–hoc, we will later on in the determination of a time–delay use the light–curves both with and without these points, to investigate the effect they have on our analysis. As it will turn out, the effect is negligible (Sect.4.3.1).

To explain why we find these outliers, we investigated the system temperature ($T_{\rm sys}$) as function of time, during these epochs. Fast or systematic changes in $T_{\rm sys}$ could indicate instrumental, atmospheric (e.g. precipitation) problems or electromagnetic interference. During day 224 (i.e. JD-2450858), $T_{\rm sys}$ shows rapid changes of up to 20% on time scales of a few minutes, which could explain (i) the large difference in the normalised flux density from the running mean and (ii) the large difference in the ratio between the normalised flux densities of B1634+627 and B1358+624 from unity. During the observations, Cumuloform type clouds were forming (50% sky coverage) over the array, possibly indicating strong interference caused by nearby thunderstorms (i.e. lightning). Also the other five outliers, during B–array, show some erratic behavior of $T_{\rm sys}$, although less serious than on day 224 and typically for only several of the telescopes ($\approx$3). Only day 165 shows a $\approx$50% decrease in $T_{\rm sys}$ over a 1h time interval for all telescopes. Because this decrease is relatively smooth, gain-self–calibration can solve for most of the errors.

No such behavior is found between days 45 to 52 (in A–array) for example, which shows a much more gradual change in $T_{\rm sys}$ and maximum differences less than 10%. On day 45, $T_{\rm sys}$ behaves similar to epochs with no severe data problems. Its system temperature, however, is on average higher, which explains why the normalised flux density is lower. The higher system temperature for each of the telescopes is explained by the fact that it was snowing during the observations over the entire array (100% sky coverage). However, because $T_{\rm sys}$ changes only gradually, the error on the corrected flux densities of images A and B will be similar to those of the other well behaved epochs.

Finally, we average the overlapping parts of the two normalised light curves, such that the errors decrease by a factor $\sqrt{2}$.

Adding all errors quadratically, we find a total error of 0.8% on the light curves of B1600+434 A and B in the region where the normalised flux calibrator light curves do not overlap, and 0.7% where they do overlap. The six outliers have assumed errors between 2–5%.

Moreover, at a given epoch the systematic errors in the flux densities of images A and B are the same (i.e. because of their small angular seperation of 1.4 arcsec, instrumental and atmospheric errors should be the same, as well as initial phase calibrator errors, which have been transferred to both images). Their flux density ratio is therefore much better determined and has an error of only $\sqrt{2}\times 0.3\% \approx 0.4\%$. The errors at different epochs, however, are independent, which is important if the light curves are shifted to determine a time delay (Sect.4.3.1).

4.3 Analysis

In this section we use the light curves to put constraints on the time delay between the two lens images. In Koopmans & de Bruyn (1999) , a more detailed analysis will be done to explain the strong short term differences between the light curves as a result of external causes.

4.3.1 The time delay

The light curves of lens images A and B differ significantly over a period larger than any reasonable time delay, either observationally determined (Sect.4.3.1) or expected from mass models (Koopmans et al. 1998). The strong variations seen in image A are therefore unlikely to be intrinsic to the source (Koopmans & de Bruyn 1999). The rms variability in image A (B) is 2.8% (1.9%), after removing the long-term linear decrease of 15–20% in their light curves. The remaining difference in light curves complicates a straightforward determination of the time delay between the images.

The rapid strong modulations seen in the light curve of image A makes interpolation questionable. This excludes the use of either the χ^2–minimization or cross–correlation methods in determining the time delay, because the light curves have to be resampled on to a similar grid through some form of interpolation.

Another way of obtaining a simple estimate of the time delay, is the use of the long–term gradients in both light–curves combined with the flux–density ratio of 1.212. Fitting a straight line to both curves (Fig.4.4) gives a flux–density decrease of $-1.98\cdot 10^{-2}$ mJy day^{-1} for curve A and $-1.87\cdot 10^{-2}$ mJy day^{-1} for curve B. Correcting the latter value by multiplying it by the flux–density ratio of 1.212 gives $-2.27\cdot 10^{-2}$ mJy day^{-1}. This value is, however, different from that of curve A by some 15%. This clearly indicates that the rate of decrease in the flux–density changes over the time–scale of the observations. One can therefore not simply divide the difference in flux–density between curve A and curve B (multiplied by the intrinsic flux–density ratio) by the rate of decrease in flux–density to obtain a time delay. This would leave a strong gradient in the flux–density or difference curve over the observing period of 242 days.

We have therefore chosen to use the non–parametric minimum–dispersion method developed by Pelt et al. (1996). As an additional constraint we use a flux density ratio of 1.212 ± 0.005, determined from 28 epochs of VLA 8.5–GHz observations during a period of $\approx$4 months in 1996-1997 in which there was relatively little variability (C.B. Moore 1999, private communication). Because this period is significantly longer than the time delay between images A and B (Sect.4.3.1), the low rms variability implies that the above value probably represents the intrinsic flux density ratio quite closely. We would like to emphasise the preliminary nature of this value, which might still change slightly in a final analysis.

Because (i) the fainter image (B) lags the brighter image (A) (Koopmans et al. 1998) and (ii) the flux densities of both images decrease almost linearly over a period of eight months, the flux–density ratio will on average be smaller than the flux-density ratio of 1.212. Shifting the light curve of image B back in time will increase the flux-density

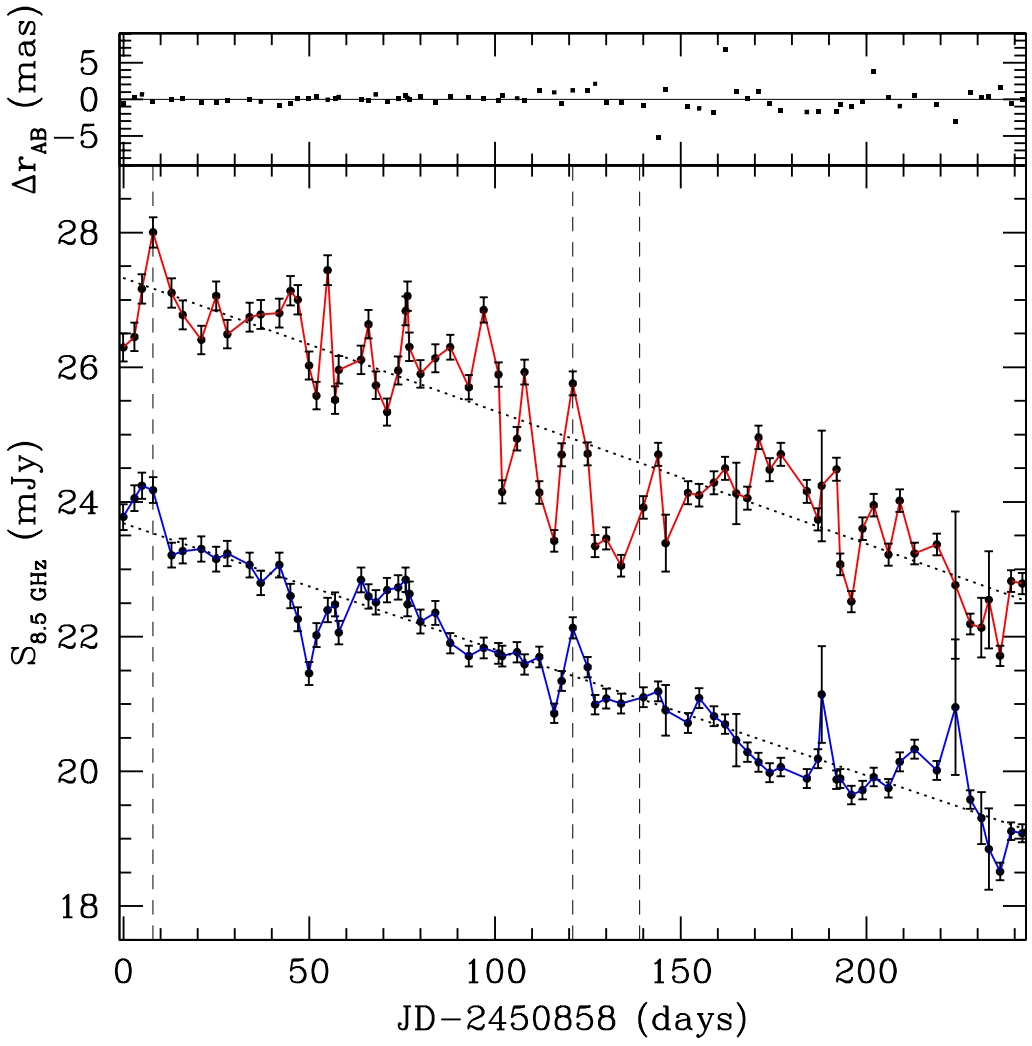

FIGURE 4.4— Lower panel: VLA 8.5–GHz light curves of B1600+434 A and B, starting Febr. 13 1998. The error bars indicate the 1–σ error, including systematic errors. The dotted lines are linear fits to the light curves. The vertical dashed lines indicate the array changes D→A, A→BnA and BnA→B, respectively, from left to right. Upper panel: The distance between images A and B, minus its median distance of 1392 mas (mean distance is also 1392 mas).

ratio between the overlapping parts of the light curves. When the shift in time equals the time delay between the lens images, the average flux-density ratio between the light curves should be 1.212. Hence, if we multiply the light curve of image B with the flux-density ratio of 1.212, we expect the minimum dispersion between the two light curves to occur near the intrinsic time delay.

Minimum dispersion method

From the simple consideration that the observed flux-density ratio (≈1.16) is smaller than the ratio of 1.212, we immediately see that image B lags image A in time, in agreement with lens models (Koopmans et al. 1998). Thus, the time delay $\Delta t_{\mathrm{B-A}}$ is positive. A composite light curve is created by multiplying light curve B with the flux-density ratio of 1.212 and shifting it back-

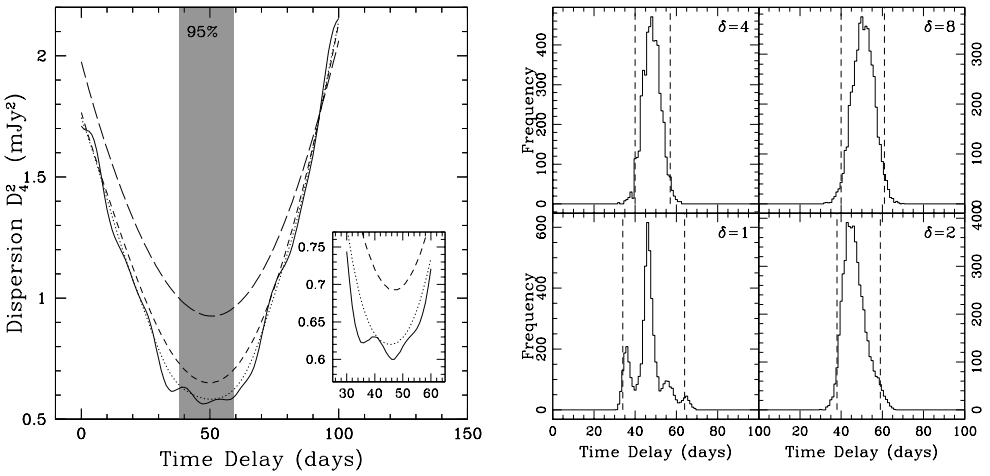

FIGURE 4.5— Left: Dispersion measure D_4^2 (Pelt et al. 1996) between the light curves of images A and B, using $r_{AB} = 1.212$. The decorrelation time scale δ is 1,2,4 and 8 (lower to upper curve), in units of the average time span between observations (i.e. 3.3 days). The dispersion minimizes between 46-51 days. The shaded region indicates the 95% statistical confidence region for the minimum–dispersion time delay. Right: Time–delay PDFs from Monte–Carlo simulations (Sect.4.3.1). Shown are the four distributions for $\delta = 1, 2, 4, 8$. The bin size is 1 day and the dashed lines indicate the region containing 95% of the time–delay PDF.

ward in time by $\Delta t_{\rm B-A}$. The dispersion of the composite light curve is calculated as in Pelt et al. (1996), using the dispersion measure

$$D_4^2(\Delta t) = \frac{\sum_{n=1,m=n+1}^{N-1,N} H_{m,n}(C_{\rm n} - C_{\rm m})^2}{\sum_{m=n+1}^{N} H_{m,n}}$$
$$H_{m,n} = S_{\rm m,n} W_{m,n} G_{m,n} \qquad (4.1)$$

where $C_{\rm n}$ is the n–th point on the composite light curve and $G_{m,n}$=1 (0), if $C_{\rm n}$ and $C_{\rm m}$ are from different (the same) light curves. We calculate the dispersion for all time delays $\Delta t_{\rm B-A}$=0–100 days, in steps of 1 day. This process is performed for four different decorrelation time scales, δ=1,2,4,8, in units of the average time span between epochs, i.e. 3.3 days. We use a decorrelation weight function $S_{\rm m,n} = \exp[-(t_{\rm m} - t_{\rm n})^2/(2\Delta^2)]$, where $\Delta = 3.3 \times \delta$ is the decorrelation time scale in days. The statistical weights are $W_{m,n} = (W_n W_m)/(W_n + W_m)$, where $W_i = 1/\sigma_i^2$ and σ_i the 1–σ error on the flux density at the i-th epoch. Clearly, the six strong outliers with large errors (Sect.4.2.6) contribute relatively little to the dispersion measure.

In Fig.4.5 the dispersion D_4^2 is plotted versus the time delay, for δ=1,2,4 and 8. The dispersion minimizes near a time delay of 46 to 51 days.

Median values for the time delay and statistical error ranges

To determine a statistical confidence region for the time delay, we performed Monte–Carlo simulations for δ=1,2,4 and 8. First, we re–sampled the light curves, using the sampling–interval distribution determined from the VLA observations. Because the light curves exhibit variability due to external causes (Sect.4.2.5), we do not create a composite light curve, by combining the image light curves, as has been done for B0218+357 (Biggs et al. 1999) and B1608+656 (Fassnacht et al. 1999). Such a light curve only resembles the true underlying light curve, if all variability were intrinsic to the source, which is not the case for B1600+434. We therefore linearly interpolate the observed light curves and errors to obtain the flux densities and errors at the re–sampled intervals. Subsequently, Gaussian distributed errors are added to (i) each point on the re–sampled light curves (1–σ equal to the interpolated flux-density error) and (ii) the assumed intrinsic flux-

δ	$\Delta t_{\rm B-A}$ (d)	68% (d)	95% (d)
1	46	38–53	34–64
2	46	41–52	38–59
4	48	44–52	40–57
8	51	45–56	40–64

TABLE 4.2— The median time delays ($\Delta t_{\rm B-A}$) between B1600+434 A and B, determined from the PDFs for different decorrelation time scales (δ). The 68% and 95% statistical confidence regions are listed in the last two columns, respectively.

density ratio (σ_r=0.005). The process described above was repeated 5000 times for each decorrelation time scales. The delays were stored, where D_4^2 minimizes. The resulting time–delay probability distribution functions (PDF) for the four decorrelation time scales are shown in Fig.4.5.

From the PDFs of $\Delta t_{\rm B-A}$, we determine the median values for the time delay and the statistical confidence regions. The final result of this procedure, for the different decorrelation scales, are listed in Table 4.2.

For δ=1, multiple strong peaks are found (Fig.4.5). For δ>1, only one peak is found. The small decorrelation time scale for δ = 1 makes the dispersion measure especially sensitive to the modulations in both light curves. These peaks, however, are much stronger in the light curve of image A and probably the result of external causes (Koopmans & de Bruyn, 1999). Hence, a somewhat larger decorrelation time scale will give a better estimate of the time delay, because it is less sensitive to these modulations (i.e. it averages over these modulations). For very large decorrelation time scales, however, one becomes sensitive to the fact that both light curves show a long–term gradient. The gradient introduces a systematic difference in the flux–density level between points on the two different light curves, if they are separated by a large time interval. This artificially increases the dispersion with increasing δ, as can clearly be seen in Fig.4.5. This effect also seems to increase the width of the 95% statistical confidence interval.

The intermediate decorrelation time scales (δ=2 and 4) therefore seem to give a better estimate of the time delay, as it avoids most of the problems indicated above. For the median value of the time delay we take the average of δ=2 and δ=4, which seems to give a stable solution (see also Sect.4.3.1 and Fig.4.6). For the 68% and 95% statistical confidence regions, we conservatively take their combined maximum ranges. Hence,

$$\begin{aligned} \Delta t_{\rm B-A} &= 47^{+5}_{-6} \ \ {\rm d} \ \ (68\%) \\ &= 47^{+12}_{-9} \ \ {\rm d} \ \ (95\%), \end{aligned} \qquad (4.2)$$

which we take as our best estimate of the time delay between the images in the gravitational lens system B1600+434 and the statistical confidence intervals.

Systematic uncertainties in the time delay determination

Several systematic uncertainties remain, which we will investigate below:

1. The first has to do with the six "outliers" on the light-curves (Sect.4.2.6). Although we gave them significantly larger errorbars, they can still affect the determination of the time delay.

2. The choice of the decorrelation time scale seems to influence the median time delay (Sect.4.3.1). Larger decorrelation time scales give larger median time delays.

3. The flux density ratio that we used in our analysis (Sect.4.3.1) is preliminary and the error was *assumed* to be Gaussian, which might not be the case. A systematic error on this flux density ratio will influence the determination of a delay.

To address the first two points, we ran Monte–Carlo simulations (500 redistributions), for decorrelation time scales of Δ=3,5,...,25 d, using *all* epochs shown in Fig.4.4. We repeated this without the six "outliers" (Sect.4.2.6). The results are shown in Fig.4.6. The values for the median time delays range between 43 to 51 d, for the assumed range of decorrelation time–scales. The width of the 95% statistical confidence interval seems to minimize in the

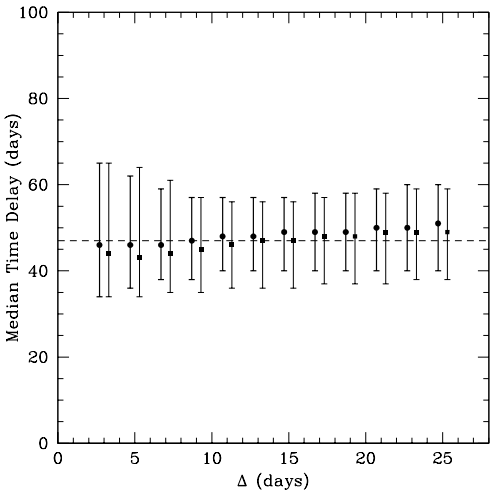

FIGURE 4.6— The median time delay determined from the time delay PDFs, as function of the decorrelation time scale Δ. The errorbars indicate the region containing 95% of the PDF. The circles indicate the time delays, using *all* epochs of the light curves shown in Fig.4.4. The squares indicate the time delays, omitting the six strongest "outliers" (Sect.4.3.1). The dashed line indicates a time delay of 47 days (Sect.4.3.1).

range $\Delta \approx$10–15 d, as was already noted in the previous section.

To estimate the effect of a wrongly chosen intrinsic flux–density ratio, we also ran models for r_{AB}=1.202 and 1.222, which are the assumed intrinsic flux–density ratio plus–minus twice its estimated error. The first value decreases the median time delay systematically by about 8 days, whereas the latter value increases it by about 7 days. This range includes the previous range of -4 to +4 days around the time delay of 47 d, using the intermediate decorrelation time scales. We thus take the range of about -8 to +7 days as a good indication of the maximum systematic error range.

4.3.2 The Hubble parameter

To estimate a tetative value for the Hubble parameter (H_0), we use the mass models for B1600+434 from Koopmans et al. (1998). Spectroscopic observations of the lens system on 1998 April 20 with the W.M. Keck–II telescope, have recently confirmed the assumption that the nearby companion galaxy (G2) has the same redshift (z=0.41) as the lensing galaxy (G1). For a lens galaxy with oblate isothermal dark matter halos, the relation between the time delay and Hubble parameter was found to be

$$H_0 = 50 \times \left[\frac{54^{+11}_{-9}\ \mathrm{d}}{\Delta t_{\mathrm{B-A}}} \right]\ \mathrm{km\ s^{-1} Mpc^{-1}}, \quad (4.3)$$

for Ω_{m}=1 and Ω_Λ=0. The errors indicate the maximum range of the isothermal–model time delays from Koopmans et al. (1998). Recently, the time–delay dependence of H_0 found for this isothermal mass model was corroborated by Maller et al. (1999), who did a similar analysis of B1600+434, using a deep NICMOS–F160W HST exposure.

Combining this relation with the median time delay (eqn.4.2), we estimate the Hubble parameter to be

$$H_0 = 57^{+14}_{-11}\ \mathrm{km\ s^{-1} Mpc^{-1}},$$

for (Ω_{m}=1, Ω_Λ=0) and with 95% statistical statistical confidence. A maximum systematic error of -15 to +26 km s^{-1} Mpc^{-1} is estimated from the combination of model and systematic time–delay errors. This estimate of H_0 is in agreement with most other gravitational lens systems from which at present H_0 has been estimated, using isothermal lens mass models (Koopmans & Fassnacht 1999), although the errors are substantial. In fact, for a Modified Hubble Profile (MHP) halo mass model we find a significantly different value for the Hubble parameter, $H_0=74^{+18}_{-15}$ km s^{-1} Mpc^{-1} (95% statistical confidence), with a maximum systematic error of -22 to +22 km s^{-1} Mpc^{-1}, for the same cosmological model (Koopmans et al. 1998). For a flat universe with Ω_0=0.3 and Ω_Λ=0.7, these values of H_0 increase by 5.4%.

Clearly at this points B1600+434 is not a GL system from which H_0 can be constrained reliably at present.

4.3.3 The radial mass profile of the lens-galaxy dark matter halo

What is perhaps more interesting in the future is the use of a well–determined time delay to constrain the profile of the dark–matter halo around the edge–on spiral lens

galaxy in B1600+434 (e.g. Jaunsen & Hjorth 1997; Koopmans et al. 1998).

In Wucknitz & Refsdal (1999) it was shown that the time delay is a strong function of the steepness of the radial mass profile of the dark mater halo around the lens galaxy. If in the near future H_0 can be determined with much greater accuracy, the time delay can subsequently be used to constrain the radial mass profile of the halo. For example, if H_0=65 km s^{-1}Mpc^{-1} – a value consistent with many measurement of H_0 – a time delay of 47 days would imply a mass profile slightly steeper than isothermal. Larger time delays would need even steeper profiles.

4.4 Conclusions

We have monitored the CLASS gravitational lens B1600+ 434 at 8.5 GHz with the VLA in A and B–arrays, during the period from February to October 1998. The light curves show a linear decrease of about 15–20% in flux density in both lens images over this period. However, image A also shows rapid variability on scales of days to weeks, which is not seen in image B, although the observing period is much longer than any conceivable time delay.

We suggest two plausible explanations of this external variability: scintillation caused by the ionized component of the Galactic ISM or radio microlensing of a core-jet structure by massive compact objects in the lens galaxy. Both possibilities are worked out in more detail in Koopmans & de Bruyn (1999). At present the hypothesis of microlensing is preferred, although several uncertainties remain.

Using a flux-density ratio of 1.212 between images A and B (C.B. Moore 1999, private communication) as an additional constraint, we have determined a median time delay, $\Delta t_{A-B}=47^{+12}_{-9}$ days (95% statistical confidence) between the lens images. A maximum systematic error between −8 and +7 d is estimated.

Combining this with the isothermal lens mass models from Koopmans et al. (1998), we find a value for the Hubble parameter of $H_0=57^{+14}_{-11}$ km s^{-1}Mpc^{-1} (95% statistical confidence) for Ω_m=1 and Ω_Λ=0. A maximum systematic error of −15 to +26 km s^{-1} Mpc^{-1} is estimated. Using the MHP mass models, one finds $H_0=74^{+18}_{-15}$ km s^{-1} Mpc^{-1} (95% statistical confidence), with a maximum systematic error of −22 to +22 km s^{-1} Mpc^{-1}, for the same cosmological model. We hope to improve on the determination of this time delay with an ongoing three–frequency VLA monitoring campaign (June 1999 to Feb. 2000).

If H_0 can be determined very accurately from independent methods and no extra constraints on the lens model can be found, it is more interesting to use that time delay to constrain the radial mass profile of the dark matter halo around the edge-on spiral galaxy in B1600+434.

Acknowledgments

We like to thank Chris Moore for useful discussions and several very good suggestions to improve the manuscript. We also thank Phillip Helbig, Peter Wilkinson and Ian Browne for carefully reading the manuscript and giving suggestions for improvement. LVEK and AGdeB acknowledge the support from an NWO program subsidy (grant number 781-76-101). This research was supported in part by the European Commission, TMR Program, Research Network Contract ERBFMRXCT96-0034 'CERES'. The National Radio Astronomy Observatory is a facility of the National Science Foundation operated under cooperative agreement by Associated Universities, Inc. The Westerbork Synthesis Radio Telescope (WSRT) is operated by the Netherlands Foundation for Research in Astronomy (ASTRON) with the financial support from the Netherlands Organization for Scientific Research (NWO). This research has made use of data from the University of Michigan Radio Astronomy Observatory which is supported by funds from the University of Michigan.

References

Biggs, A.D., Browne, I.W.A., Helbig, P., Koopmans, L.V.E., Wilkinson, P.N., Perley, R.A., 1999, MNRAS 304, 349

van Breugel, W.J.M, Fanti, C., Fanti, R., Stanghellini, C., Schilizzi, R.T., Spencer, R.E., 1992, A&A 256, 56
Fassnacht, C.D., Pearson, T.J., Readhead, A.C.S., Browne, I.W.A., Koopmans, L.V.E., Myers, S.T., Wilkinson, P.N., 1999, ApJ in press
Jackson, N., et al., 1995, MNRAS 274, L25
Jaunsen, A.O., Hjorth, J., 1997, A&A 317, L39
Koopmans L.V.E., de Bruyn, A.G., Jackson N., 1998, MNRAS 295, 534
Koopmans, L.V.E., et al., 1999, MNRAS 303, 727
Koopmans, L.V.E. & Fassnacht, C.D., 1999, ApJ in press
Koopmans, L.V.E. & de Bruyn, A.G., 1999, å, submitted
Kundić, T., et al., 1997, ApJ 482, 75
Lovell, J. E. J., Jauncey, D. L., Reynolds, J. E., Wieringa, M. H., King, E. A., Tzioumis, A. K., McCulloch, P. M., Edwards P. G., 1998, ApJ 508, L51
Maller, A.H., Simard, L., Guhathakurta, P., Hjorth, J., Jaunsen, A.O, Flores, R.A., Primack, J.R., 1999, ApJ, in press (astro-ph/9910207)
Nan, R., Schilizzi, R.T., Fanti, C., Fanti, R., 1991, A&A 252, 513
Patnaik, A.R., Browne, I.W. A., Wilkinson, P.N., Wrobel, J.M., 1992, MNRAS 254, 655
Pelt, J., Kayser, R., Refsdal, S., Schramm, T., 1996, A&A 305, 97
Refsdal S., 1964, MNRAS 128, 295
Schechter, P.L., et al., 1997, ApJL 475, L85
Schneider P., Ehlers J., Falco E.E., 1992, Gravitational Lenses, Springer Verlag, Berlin
Shepherd, M.C., 1997, in Hunt, G., Payne, H.E., eds, ASP Conf. Ser. vol. 125, ADASS VI. Astron. Soc. Pac., San Francisco, p. 77
Wucknitz, O. & Refsdal, S., 1999, astro-ph/9909291

5

Microlensing of multiply–imaged compact radio sources

Evidence for MACHOs in disk galaxies at $\mathbf{z}$=0.4

**Based on L.V.E. Koopmans & A.G. de Bruyn, 1999,
Astronomy & Astrophysics, submitted**

We present the first *unambiguous* case of external variability of a gravitational lens, CLASS B1600+434. The system consists of two flat–spectrum radio images of a quasar at z=1.6, separated by 1.4 arcsec. The brightest image A passes through the halo, whereas image B passes predominantly through the disk and bulge of the edge–on lens galaxy at z=0.41. The VLA 8.5–GHz difference light curve of the lens images shows the presence of external variability with 14.6–σ confidence.

We investigate two plausible sources of this external variability: scattering by the ionized component of the Galactic interstellar medium (ISM) and microlensing by massive compact objects in the bulge/disk and halo of the lens galaxy. The VLA 8.5–GHz observations do not conclusively exclude either possibility. However, based on the relation between the modulation index and variability time scale *and* the quantitative difference between the light curves of both lens images, we conclude that the observed short–term variability characteristics of the lens images are incompatible with scintillation in our Galaxy, although this conclusion needs to be reevaluated if evidence is found for significant scatter broadening of lens image B in the lens galaxy. This conclusion is supported by multi–frequency WSRT observations at 1.4 and 5–GHz, which are in strong disagreement with predictions based on the scintillation hypothesis, if the short–term variability at these frequencies is also predominantly external.

A superluminal jet–component microlensed by compact objects in the lens galaxy, on the other hand, can reproduce the observed modulation index and variability time scale at 8.5–GHz. It also reproduces the modulation–index ratio determined from the independent WSRT 1.4 and 5–GHz observations. The difference between the modulation indices of the lens images (i.e. 2.8% and 1.6% for images A and B, respectively), if not affected by scatter broadening of component B in the ionized ISM of the lens galaxy, can be explained through a different mass–function of compact objects in the bulge/disk and halo of the lens galaxy. From detailed microlensing simulations we can then set a conservative lower limit of $\gtrsim$0.5 $M_\odot$ on the average mass of compact objects in the halo.

Under the assumptions that the short–term variability in both lens images is dominated by microlensing and that a core plus a single superluminal jet component can describe the source, we find a consistent, although not unique, set of source parameters; the superluminal ($9 \lesssim \beta_{\rm app} \lesssim 26$) jet component has a radius of 2–5 μas and contains 5–11% of the observed 8.5–GHz source flux–density, during the observing period (i.e. these values might change as function of time). However, independent knowledge of the bulk velocity and surface brightness distribution of the lensed radio source would be required to set more stringent limits on the mass function of compact objects in the halo.
The only conclusion fully consistent with the data gathered thus far is that we see radio microlensing. The far reaching consequence of this statement is that a significant fraction of the mass in the dark–matter halo at $\sim$6 kpc (h=0.65) above the lens–galaxy disk in B1600+434 consists of MACHOs.

5.1 Introduction

Gravitationally lensed compact radio sources have many astrophysical and cosmological applications. The foremost being the determination of a time–delay between the individual lens images in order to constrain the Hubble parameter (e.g. Refsdal 1964). Considerable progress has been made during the last few years in accomplishing this (e.g Kundić et al. 1997; Schechter et al. 1997; Lovell et al. 1998; Biggs et al. 1999; Fassnacht et al. 1999; Koopmans & Fassnacht 1999). They also allow a detailed study of the mass distribution of the lens galaxy and sometimes the background source, through a large magnification by the lens galaxy (e.g. Schneider, Ehlers and Falco 1992). Absorption lines in the spectrum of the background source allow the study of the ISM in the lens galaxy and the HI distribution along the lines of sight to the source.

Temporal changes in the brightness or spectrum of the lens images also allow the study of uncorrelated external variability. The most important sources of external variability are scintillation at radio wavelengths and microlensing in all wavelength bands. Differencing the image light curves removes intrinsic source variability, leaving only uncorrelated external variability. These difference light curves thus provide valuable information on either compact objects in the lens galaxy and/or on the intervening ionized medium.

The study of the ionized component of the Galactic interstellar medium (ISM) through scattering of radio emission from pulsars has had a long tradition (e.g. Rickett 1977, 1990). Scattering by the ionized ISM can explain long–term variability at meter wavelengths (e.g. Condon et al. 1979), as well as large amplitude variability in very compact extra–galactic radio sources (e.g. Rickett, Coles & Bourgois 1984). Lower–amplitude variability at shorter wavelengths (about 10 cm), called 'flickering', has been observed by Heeschen (1982, 1984) and is probably associated with refractive interstellar scattering of an extended source (e.g. Rickett et al. 1984). Strong intra–day variability of very compact radio sources might result from refractive interstellar scattering as well (e.g. Wagner & Witzel 1995). A power–law model of the plasma–density power spectrum (e.g. Rickett 1977, 1990), combined with some distribution of this plasma in our galaxy (e.g. Taylor & Cordes 1993 [TC93]) is able to explain most of the observed dispersion measures and variability in pulsars at low frequencies, as well as the variability of extra–galactic radio sources at both low and high frequencies. However, especially for compact flat–spectrum radio sources it remains exceedingly difficult to separate intrinsic variability from scintillation by the Galactic ionized ISM.

Gravitationally lensed (i.e. multiply–imaged) flat–spectrum compact radio sources could offer a solution to this problem. As mentioned previously, these systems provide two or more lines–of–sight through the Galactic ionized ISM. For

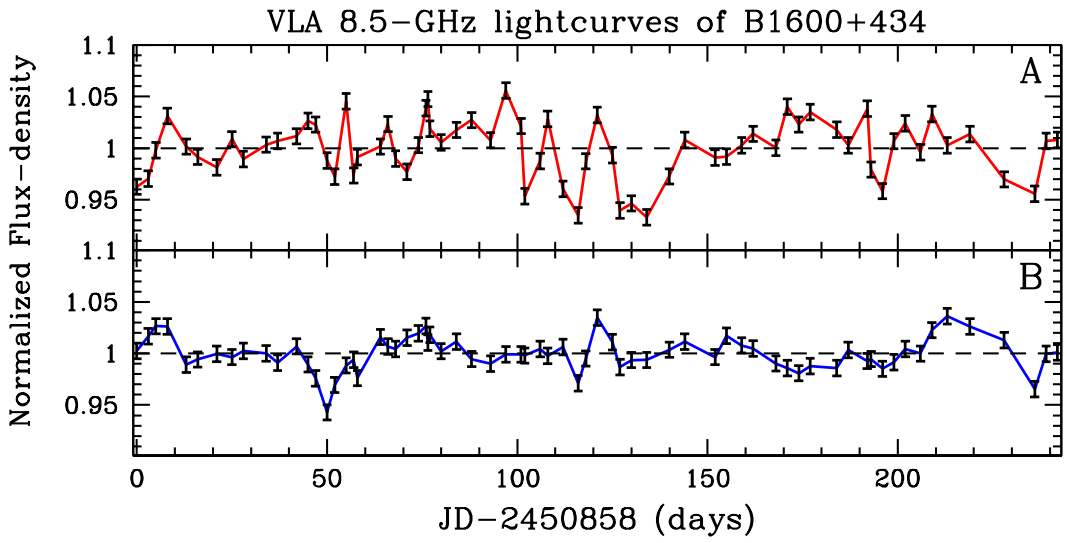

FIGURE 5.1— The normalized light curves of B1600+434 A (upper) and B (lower), corrected for a long–term gradient (Sect.5.2). The error on each light–curve epoch is 0.7 to 0.8%. Day 0 corresponds to 1998 Febr. 13.

typical image separations of a few arcsec, one is looking through parts of the Galactic ionized ISM separated by a few hundred AU. One can expect the scattering of radio waves to be independent for the different lines–of–sight. Differencing the image light curves, after a correction for the appropriate time delay and flux–density ratio, produces a difference light curve that only shows uncorrelated external variability. This difference light curve can be studied to obtain information on the Galactic ionized ISM independent of intrinsic source variability.

However, uncorrelated external variability in the lens images might also originate from microlensing in the lens galaxy (e.g. Chang & Refsdal 1979). This offers the additional opportunity to study the properties of compact objects in the lens galaxy (e.g. Wambsganss 1990), if microlensing variability dominates or can be separated from scintillation. Optical microlensing in the lens galaxy of 2237+0305 has unambiguously been shown (e.g. Irwin et al. 1989). In the radio, several suggestions of microlensing variability have been made (e.g. Stickel et al. 1988; Quirrenbach et al. 1989; Schramm et al. 1993; Romero et al. 1995; Chu et al. 1996; Wagner et al. 1996; Lewis & Williams 1997; Takalo et al. 1998; Quirrenbach et al. 1998; Kraus et al. 1999; Watson et al. 1999). In none of these cases, however, has one really been able to convincingly distinguish between intrinsic and external variability. Claims of external variability in singly–imaged radio sources through microlensing should therefore be regarded with some caution in these cases.

In this paper, we report the first unambiguous case of external variability of an extra–galactic radio source, the CLASS gravitational lens B1600+434 (Jackson et al. 1995; Jaunsen & Hjorth 1997; Koopmans, de Bruyn & Jackson 1998 [KBJ98]; Koopmans et al. 1999 [KBXF99]). The system consists of two compact flat–spectrum radio images, separated by 1.4 arcsec. The background source, at a redshift of 1.59, is lensed by an edge–on disk galaxy at a redshift of 0.41 (Fassnacht & Cohen 1998; KBJ98). A time delay of 47^{+12}_{-9} days (95% statistical confidence) was recently found (KBXF99).

What is furthermore of interest is that this system offers two *unique* lines–of–sight through the lens galaxy. Image A only passes through the dark–matter halo around the edge–on lens galaxy, whereas image B passes predominantly through its disk and bulge. This makes image A especially sensitive to microlensing by com-

pact objects in the halo (i.e. MACHOs) and image B to microlensing in the disk and bulge (i.e. stars). This might therefore offer a unique opportunity to study MACHOs in the dark–matter halo around the lens galaxy of B1600+434.

The outline of the paper is as follows. In Section 5.2, we present the VLA 8.5–GHz data from KBXF99 in a different way, unambiguously showing the presence of external variability. We also present additional WSRT 1.4 and 5–GHz monitoring data of B1600+434. In Section 5.3, we investigate whether Galactic interstellar scattering (ISS) can explain the fractional rms variabilities (modulation indices) and time scales of the short–term variability seen in both VLA 8.5–GHZ light curves. Similarly, in Sections 5.4 and 5.5 the possibility of microlensing by compact objects in the lens galaxy is studied. In Section 5.6, we present microlensing simulations of a more complex jet structure and compare the results to B1600+434. In Section 5.7, we discuss a critical test (i.e. the frequency–dependence of the modulation index) to discriminate between scintillation and microlensing and compare predictions from the VLA 8.5–GHz light curves with independent multi–frequency WSRT data. In Section 5.8 our results and conclusions are summarized.

5.2 Short–term variability in B1600+434–A & B

B1600+434 is a compact ($\lesssim$1 mas at 8.5–GHz; KBXF99) radio source, which has varied strongly at 8.5–GHz since its discovery in 1994 (Jackson et al. 1995). Its flux–density decreased from 58 (48) mJy in March 1994 to only 29 (24) mJy in August 1995 for image A (B) (KBJ98). From February to October 1998, another decrease from 27 (24) to 23 (19) mJy was found (KBXF99). In June 1999, the flux–densities appear to have stabilized to 23 (17) mJy. Strong variability was also seen at 5–GHz, where a total flux density was measured of 34–37 mJy in 1987 (GB87; Becker, White and Edwards 1991). Observations in March 1995 gave 45 (37) mJy for image A (B) (KBJ98), whereas in June 1999 this had reduced to only 23 (18) mJy. At 1.4–GHz, the total WSRT flux–density of B1600+434 has decreased from 60–65 mJy in April–July 1996 (KBJ98) to about 50 mJy in June 1999.

Because of this strong variability, B1600+434 was observed from February to October 1998 with the VLA at 8.5–GHz, in order to determine a time delay between the two lens images. In KBXF99, the VLA 8.5–GHz light curves of the two lens images were presented, showing short–term variability, as well as a long–term decrease in the flux density of both lens images, which we assume to be intrinsic source variability, similar to that seen in 0957+561 (e.g. Haarsma et al. 1997).

In Fig.5.1, the normalized VLA 8.5–GHz light curves of both lens images are shown. The curves were created by dividing the light curves by linear fits (KBXF99). The resulting curves show the fractional variability on short time scales (i.e. shorter than the observing period of about 8 months) with respect to the running mean. The 1–σ error for each point on the light–curve is 0.7 to 0.8% (KBXF99). We omitted the six strongest outliers from both plots, which show clear systematic problems with the data or calibration (KBXF99). The resulting normalized light curves have modulation indices of 2.8% and 1.6% for images A and B, respectively. We use these values throughout this paper. Lens images A and B have modulation indices significantly larger than expected on the basis of the measurement errors only, indicating the clear presence of short–term variability, either intrinsic or external. The structure functions (e.g. Simonetti, Cordes, & Heeschen 1985) of the normalized light curves are shown in Fig.5.6 (Sect.5.3.2).

5.2.1 Intrinsic or external variability?

To show that the most short–term variability is of external origin, the linearly–interpolated light curve of image B was subtracted from the light curve of image A, after having corrected it for a flux density ratio of 1.212 and a time delay of 47 days (KBXF99). The time delay was de-

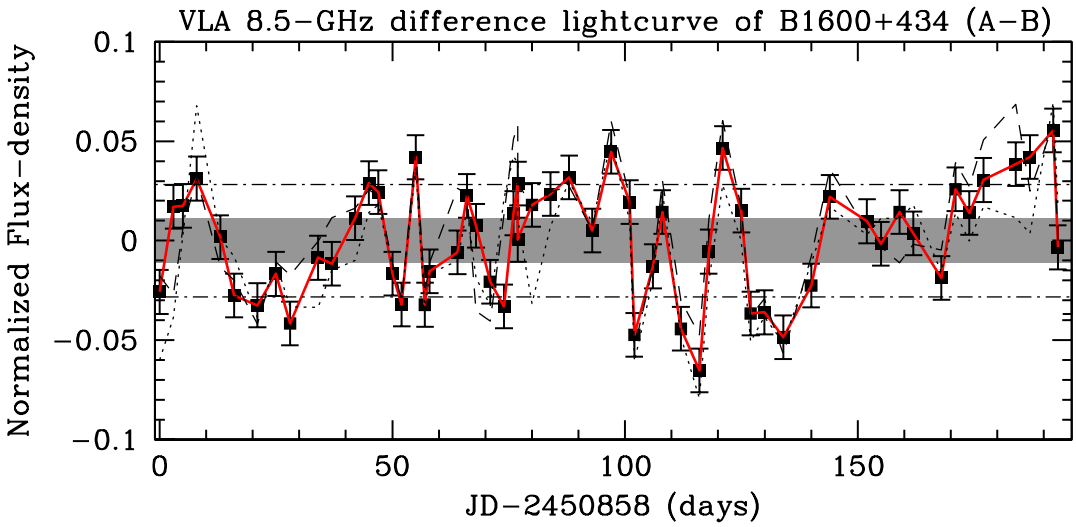

FIGURE 5.2— The normalized difference light curve between the two lens images, corrected for both the time-delay and flux density ratio (Sect.5.2.1). The shaded region indicates the expected 1–σ (1.1%) region if all variability were due to measurement errors. The dash–doted lines indicate the observed modulation index of 2.8%. The dotted and dashed curves indicate the normalized difference curves for a time delay of 41 and 52 days, respectively. Obviously most variations can not be explained by any reasonable error in the time delay. There seems to be no evidence of any change in the typical time scale of variability over 6 months. Day 0 corresponds to 1998 Febr. 13.

termined, using the minimum dispersion method from Pelt et al. (1996). Hence, the modulation index of the normalized difference curve, shown in Fig.5.2, is by definition a lower limit. This is illustrated by the dotted and dashed lines, which show the normalized difference light curves for a time delay of 41 and 52 days (i.e. the 68% confidence region), respectively. Both curves show a larger modulation index, as expected.

The normalized difference light curve, obtained this way, has a modulation index of 2.8%, which is significantly larger than the expected modulation index of 1.0–1.1% from the measurement errors, as indicated by the shaded region in Fig.5.2. Thus, most of the short–term variability present in the light–curves must be of external origin. A χ^2–value of 377 was determined from the 58 points composing the difference light curve. This is inconsistent with a flat difference light curve at the 14.6–σ confidence level. This is further illustrated by the fact that only $\sim$10 epochs lie within the 1–σ region (Fig.5.2), whereas we would expect $\sim$40 epochs (i.e 68% of the 58 epochs) if the scatter were due to measurement errors only.

If the short–term variability of the two lens images is uncorrelated, the expected modulation index in the normalized difference curve should be $\sqrt{(2.8^2+1.6^2)}\approx$3.2%, which is slightly larger than the observed value of 2.8%. It remains hard to assess whether individual features in the light curves might be of intrinsic origin. In this paper we will therefore assume that *all* short–term variability in both lens images is of external origin, although one might take $\sqrt{(2.8^2-1.6^2)}\approx$2.3% as a very conservative lower limit on the external variability of image A.

This is the first *unambiguous* case of external variability of an extra–galactic radio source. In all singly–imaged radio sources the major difficulty thus far has been the separation of intrinsic from external variability.

5.2.2 WSRT 1.4 & 5–GHz monitoring

Before proceeding with the analysis of the VLA 8.5–GHz light curves, we first present multi–frequency WSRT total–flux–density data of B1600+434 obtained in 1998/9 at 1.4 and 5–GHz. This data will play an essential

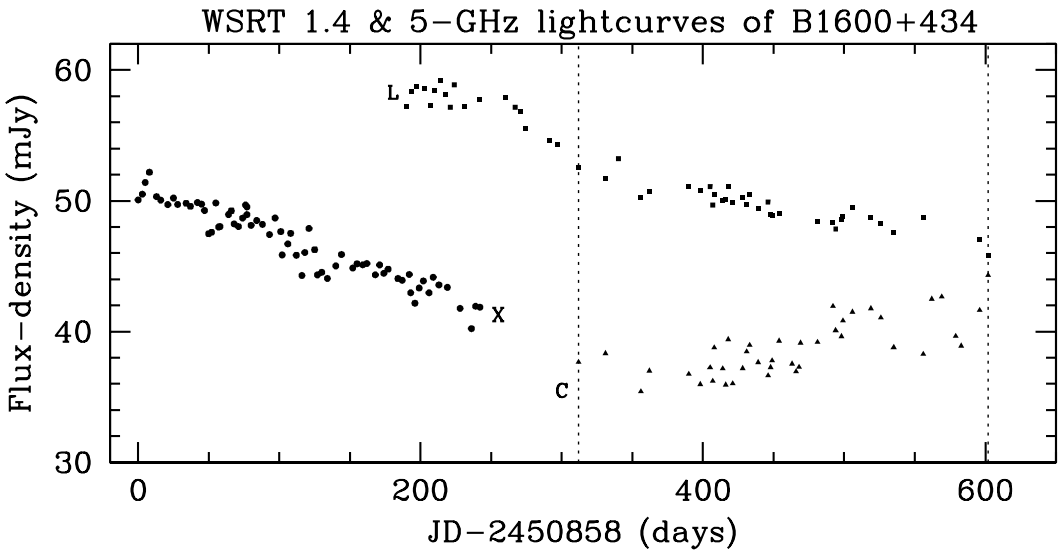

FIGURE 5.3— The total flux–density light curves of B1600+434 in X–band (VLA 8.5–GHZ), C–band (WSRT 5-GHz) and L–band (WSRT 1.4–GHz). The two vertical dashed lines indicate the time–span, where the WSRT 1.4 and 5–GHz observations overlap. Day 0 corresponds to 1998 Febr. 13.

role in distinguishing between the different physical mechanisms causing the external variability observed in the VLA 8.5–GHz lens–image light curves, as we will see in Sect.5.7.

Starting in August 1998 the WSRT was outfitted with a series of new multi-frequency front–ends (MFFE's) that can operate at frequencies from 0.3 to 8.5 GHz. When the WSRT observations of B1600+434 were begun in August 1998 only 6 front-ends were available at 1.4 GHz. The available number of telescopes with MFFE's increased at a rate of about 1 per month until the full array was outfitted in February 1999. Towards the end of 1998 the monitoring was extended to include 5 GHz. In the spring of 1999 we also included 8.5 GHz observations. However, the analysis of the 8.5 GHz data is still encountering some problems and we therefore do not report on the results of the 8.5 GHz observations here.

Each run consisted of two sets of observations (at up to 3 frequencies) on B1600+434 and the nearby reference source B1558+439. The latter is a strong steep spectrum double radio source (0.8–arcsec size) about 40 arcmin north-east of B1600+434. In each run we also observed two primary calibration sources (3C286, 3C343 and CTD93). Although we changed the details of the observing sequence during the year the basic structure did not change.

The resolution of the WSRT is about 12×18 arcsec (1.4–GHz) and 3.5x5 arcsec (5–GHz). B1600+434 is therefore always unresolved at 1.4–GHz. At 5–GHz the source, however, shows slight hour–angle dependent resolution effects [the WSRT is an east-west synthesis array, hence the instantaneous synthesized response is a fan beam rotating clockwise on the sky]. Because the observations were scheduled at random hour angles the resolution effect is therefore variable from session to session. We minimized the magnitude of this effect by determining the flux density using only baselines up to 1300 meter wavelength; the residual effect on the flux density is below the thermal noise error.

The amplitude and flux calibration was performed in NEWSTAR using standard procedures starting with a selfcalibration on the primary reference source. The complex telescope gains were then transferred to the target and reference source. The

flux densities of B1600+434 and B1558+439 were then determined using a uv–plane fitting algorithm in the program NMODEL. Selfcal phase solutions on the reference source B1558+439 usually showed only very slight decorrelation effects due to slow instrumental/atmospheric phase–drifts. Because these would be very similar for B1600+434 and the reference source we decided not to apply a phase selfcal solution.

The flux density of the reference source B1558+439 was found to show a scatter of about 1–2% around 700 mJy at 1.4 GHz and about 1.0% around 204 mJy at 5 GHz. This scatter is still larger than the noise error on the flux density. We believe these can be attributed to small changes in atmospheric opacity and small instrumental gain drifts (e.g. due to pointing) . Normalizing the amplitudes of B1600+434 by those of the reference source should eliminate them. We therefore expect that the final errors on the flux density of B1600+434 are determined by the thermal noise only. Still, to be on the safe side we adopted as a final error on the flux density of B1600+434 the quadrature sum of the thermal noise level and a 1% scale error. This amounts to a typical error of 1.0% and 1.3% at 1.4 and 5–GHz, respectively.

In Fig.5.3, we have shown the calibrated WSRT 1.4–GHz (L–band) and 5–GHz (C–band) light curves, together with the total–flux–density VLA 8.5–GHz (X–band) light curve (KBXF99). We note the following properties: (i) All light curves are dominated by systematic trends with decreasing intensity at 8.5 and 1.4 GHz, but increasing at 5 GHz. We believe these changes to be due to intrinsic variations. (ii) If the VLA 8.5–GHz and WSRT 5-GHz long–term intrinsic flux–density variations are correlated, there has been a clear trend–break in the gradient of the light–curves around day 300 (Fig.5.3). The WSRT 1.4–GHz light curve still shows a similar gradient as the VLA 8.5–GHz in 1998, hence there appears to be a time–lag of at least 200 days between long–term intrinsic source variability at 8.5 and 1.4–GHz. This trend–break is supported by the first results from the 1999 VLA campaign. (iii) At those epochs where the light–curves overlap, the higher–frequency light curves show a larger short–term modulation index around the long–term linear gradient.

An important statistical property of the light curves is their modulation index on short time scales (i.e. time scales shorter than the length of the light curves), as function of frequency. To calculate the modulation indices, we divide the light curves through a linear fit (see Sect.5.2) in order to remove most of the presumably intrinsic source variability. The results are normalized light curves, similar to the normalized VLA 8.5–GHz light curves shown in Fig.5.1. We only calculate the 1.4 and 5–GHz modulation indices ($m_{\rm part}$) for those epochs, where we have both a 1.4 and 5–GHz WSRT flux–density measurement. The normalized light curves of these epochs are shown in Fig.5.4. The resulting modulation indices are listed in Table 5.1. Because the modulation index at 1.4–GHz is very close to the estimated flux–density error, we regard it as an upper limit.

The total flux–density modulation indices in Table 5.1 are a combination of the individual modulation indices of images A and B. If we assume that the ratio of modulation indices are equal to those at 8.5 GHz (i.e. $(m_{\rm A}/m_{\rm B})_\lambda \approx 2.8/1.6=1.75$) for each wavelength, we only make a slight error ($\lesssim$15%) compared to the assumption that image B does not vary at all on short time scales. Because we will *only* use modulation–index ratios (see Sect.5.7), which are independent from these assumptions in first order, this is of no importance.

5.2.3 Possible origins of the external variability

What can be the origin of the external variability seen in the VLA 8.5–GHZ light curves, why does the modulation index differ between the two image light curves and what causes the short–term variability in the WSRT 1.4 and 5–GHz light curves? Below we have listed different physical mechanisms which can introduce external variability in the flux–density of compact radio

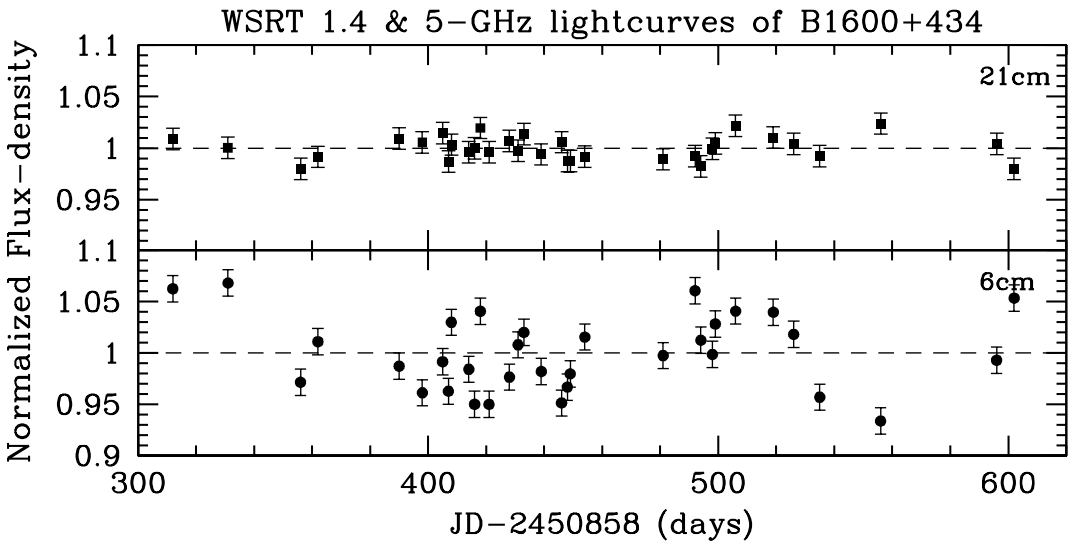

FIGURE 5.4— The normalized WSRT 1.4 and 5–GHz flux–density light curves of B1600+434. Only those epochs of the WSRT light curves are shown that have both a 1.4 and 5–GHz measurement (Fig.5.3). The light curves were created similar to the VLA 8.5–GHz light curves shown in Fig.5.1. One notices a clear increase in the modulation index from 21 to 6 cm by a factor $\sim$3.

ν (GHz)	$m_{\rm part}$ (%)	Epoch (days)	Instr.
1.4	$\leq$1.2	312–602	WSRT
5.0	3.7	312–602	WSRT

TABLE 5.1— The short–term total flux–density modulation indices of B1600+434, as function of frequency.

sources:

1. Scintillation
   - Weak scattering (Sect.5.3.1)
   - Refractive scattering (Sect.5.3.2)
   - Diffractive scattering (Sect.5.3.3)
2. Microlensing (Sect.5.4–5)

In the next two sections, we will investigate in detail whether one or more of these can explain the external variability seen in the VLA 8.5–GHz light curves of B1600+434–A & B. In Sect.5.7, we will combine the conclusions from Sections 5.3–5 with the results from the WSRT 1.4 and 5–GHz observations to further constrain the scintillation and microlensing hypotheses.

5.3 Scintillation

Even though the difference in modulation index between images A and B seems to require a considerable change in the properties of the Galactic ionized ISM over an angular scale of 1.4 arcsec (Sect.5.3.2), we still proceed to investigate whether the short–term variability, superposed on the gradual and presumably intrinsic long–term decrease of the flux–density of the lens images, can be the result of scintillation. We will follow the prescription of Narayan (1992) and its numerical implementation by Walker (1998; [W98]) for the Galactic ionized ISM model from TC93. This assumes that the inhomogeneities of the ionized ISM can be described by a Kolmogorov power–law spectrum (e.g. Rickett 1977; Rickett 1990) and that the ionized ISM model from TC93 is approximately valid. Support for the approximate validity of the TC93 model in the direction to B1600+434 is given by the dispersion and scattering measures of nearby pulsars, showing no apparent deviations from this model. Also,

no evidence is found in the low–frequency (327–MHz) WENSS catalogue (e.g. Rengelink et al. 1997) for diffuse HII emission or SN remnants that could introduce small–scale perturbations in the ionized Galactic ISM.

Depending on the line–of–sight through the galaxy and the observing frequency, the scattering strength of radio waves, expressed in the scattering strength $\xi = r_{\rm F}/r_{\rm diff}$, can be strong ($\xi > 1$) or weak ($\xi < 1$), where $r_{\rm F}$ is the Fresnel scale and $r_{\rm diff}$ is the diffractive scale (e.g. Narayan 1992). The transition between these two regimes occurs near a transition frequency (ν_0). For B1600+434 at a Galactic latitude of b=+48.6°, we find ν_0=4.2 GHz (W98). At the observing frequency of 8.5 GHz, scattering should therefore be in the weak regime ($\xi \sim 0.3$). The transverse velocity of the ISM with respect to the line–of–sight to B1600+434 is determined by projecting the velocity vector of the earths motion on the sky as function of time. We find a transverse velocity (v) between 20 and 40 km s^{-1}. We will therefore adopt an average value of v=30 km s^{-1} throughout this paper. For lack of better knowledge, we assume any intrinsic transverse motion of the scattering medium to be zero.

5.3.1 Weak scattering

The modulation index of a point source in the weak scattering regime is (Narayan 1992)

$$m_{\rm p} = \left(\frac{\nu_0}{\nu}\right)^{17/12}. \qquad (5.1)$$

In the simplest case that B1600+434 is a point source smaller than the Fresnel scale of 3.9 μas (W98), we would expect a modulation index around 35%. This is significantly larger than the observed modulation indices of 2.8% for image A and 1.6% for image B. Hence, the total angular size of the images must be larger than the Fresnel scale. This does, however, not exclude that part of the source might still be compact.

The variability time-scale for a point source is given by (Narayan 1992)

$$t_{\rm p} = \frac{3.3}{v_{30}} \times \sqrt{\frac{\nu_0}{\nu}} \ {\rm h}, \qquad (5.2)$$

where v_{30} is the transverse velocity of the scintillation pattern with respect to the line–of–sight to the source in units of 30 km s^{-1}. Inserting the values for the observing frequency (ν), the transition frequency (ν_0) and v_{30}=1.0, a time–scale around 2 h is found, which is much smaller than the apparent variability time–scales of days to weeks seen in a significant fraction of the light curves (Figs 5.1–5.2).

If 5 to 10% of the flux–density of the source is contained in a compact region ($\lesssim \theta_{\rm F}$), the rms fluctuations decreases to the observed modulation index of 2–3% for B1600+434–A and B. The variability time–scale would still remain $\sim$2 h. Hence, a simple compact source structure can not explain the observed variability and a more extended source ($\gg \theta_{\rm F}$) is required, if we want to explain the observed modulation index in terms of scintillation.

In case the source is extended, with a size $\theta_{\rm s} > \theta_{\rm F}$, both the modulation index and variability time–scale change. The modulation index decreases as follows (Narayan 1992)

$$m = m_{\rm p} \times \left(\frac{\theta_{\rm F}}{\theta_{\rm s}}\right)^{7/6}, \qquad (5.3)$$

whereas the time-scale of variability increases as

$$t = t_{\rm p} \times \left(\frac{\theta_{\rm s}}{\theta_{\rm F}}\right). \qquad (5.4)$$

Combining these two equations, using the transition and observing frequencies for B1600+434, gives the relation

$$m = \left(\frac{0.90^{\rm h}}{v_{30} \cdot t}\right)^{7/6}, \qquad (5.5)$$

for $t \gtrsim t_{\rm p} \approx 2.25^{\rm h}/v_{30}$.

If the lensed source has an angular radius of about 40 μas, the modulation index reduces to 2–3%, as observed. The variability time-scale should then be around 1 day, still significantly smaller than the observed modulation timescale in a major part of the light curves. Although part of the very short–term ($\lesssim$ few days) variability could be due to scintillation, many of the long–term variations seen in Figs 5.1–5.2 certainly can not be explained this way.

The relatively nearby source J1819+387 has a modulation index $m \approx 0.5$ and $t \approx 0.5$–1 hour (Dennett–Thorpe & de Bruyn 1999). Using the relation between m and t (e.g. eqn.5.5), this translates to a variability time scale less than a day for a modulation index of a few percent, in agreement with expectations from the Galactic ionized ISM model from TC93. Similarly, variations with a time–scale of more than a week (Figs 5.1–5.2), require a source size of 0.3 mas, reducing the modulation index to 0.2%, which is well below the noise level in the VLA light curves.

In Fig.5.5, we have summarized the strong and weak scattering regimes, as function of the modulation index, the variability time scale and the source size. The variability seen in image A (but also image B) is especially hard to explain by weak scattering without either invoking unlikely high values for the equivalent distance of the phase screen ($\gtrsim$10 kpc) or a persistently low transverse velocity ($\lesssim$few km s^{-1}). From this, we conclude that in any case weak scattering has great difficulties in accounting for the observed modulation index and longer variability time scales ($\gg$1 day) seen in the VLA 8.5–GHz light curves of the lens images. However, it remains difficult to determine a reliable variability time scale from the image light curves, partly because of the relatively poor sampling (i.e. every 3.3 days). For further discussion we refer to Sect.5.3.2, where we present the structure functions of the observed variations.

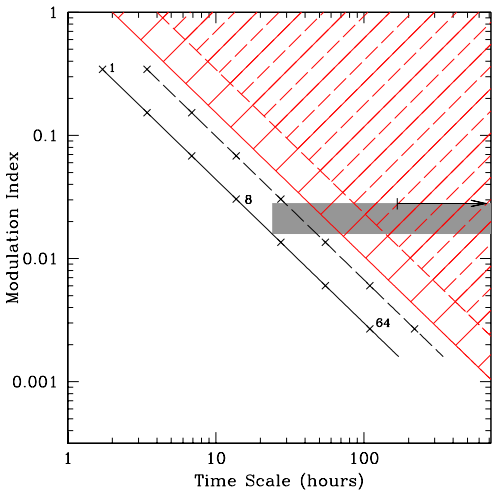

FIGURE 5.5— The modulation index as function of the variability time scale for the weak scattering regime (eqn.5.5), using a transverse velocity v=40 km s^{-1} (solid line) or 20 km s^{-1} (dashed line). The short dashes perpendicular to the lines indicate different source sizes (i.e. 1, 2, 4, ..., 64 in units of the first Fresnel zone, i.e. 3.9 μas). The skewed dashed regions in the upper right corner indicate the strong scattering regime ($\xi > 1$) for the two transverse velocities, using an equivalent phase–screen distance of 0.5 kpc. The gray region indicates a variability time scale of 1–30 days and a modulation index range of 1.6–2.8%, as observed for the lens images. The arrow indicates the observed 2.8% modulation index and time scale $\geq$1 week as seen in the difference light curve (Fig.5.2). Only for an equivalent phase screen distance $\geq$10 kpc (with v=30 km s^{-1}) or a transverse velocity $\leq$few km s^{-1} (with D=0.5 kpc) does most of the gray region enter the weak scattering regime.

5.3.2 Strong scattering

In the strong scattering regime, we can not use the numerical results derived from the TC93 model, from which one expects B1600+434 to be in the weak–scattering regime at 8.5 GHz. We therefore make direct use of the relation between the scattering measure (SM), the distance to the equivalent phase screen ($D_{\rm kpc}$), the observing frequency ($\nu_{\rm GHz}$) and the scattering strength (ξ) (e.g. W98)

$$\xi = 2.6 \cdot 10^3 \times {\rm SM}^{6/10} D_{\rm kpc}^{1/2}\, \nu_{\rm GHz}^{-17/10}. \quad (5.6)$$

The scattering strength and the Fresnel scale determine both the modulation index and variability time scale of a source, given the source size. The Fresnel scale, given by

$$\theta_{\rm F} = 8/\sqrt{D_{\rm kpc}\nu_{\rm GHz}} \;\; \mu{\rm as}, \quad (5.7)$$

specifies the angular distance from the source over which there is about one radian phase difference between rays, due to the difference in path length. The scattering measure (e.g. TC93) for an extra–galactic source is defined as

$${\rm SM} = \int_0^\infty C_{\rm n}^2 {\rm d}l, \quad (5.8)$$

where $C_{\rm n}^2$ is the structure constant normalizing the Kolmogorov power–law spectrum of the ionized ISM inhomogeneities (e.g.

Cordes, Weisberg & Boriakoff 1985). From now on, we assume that SM has units of kpc $\mathrm{m}^{-20/3}$ and C_n^2 units of $\mathrm{m}^{-20/3}$. The distance to the equivalent phase screen (e.g. W98) is defined as

$$D \equiv \frac{1}{\mathrm{SM}} \int_0^\infty C_\mathrm{n}^2 \cdot s \; \mathrm{d}s. \qquad (5.9)$$

Despite the fact that the difference in modulation index of the lens images seems to require very different properties of the Galactic ionized ISM on a scale of 1.4 arcsec, we will investigate the two distinct strong scattering regimes, i.e. refractive and diffractive (e.g. Rickett 1990; Narayan 1992), in more detail in the next two sections.

Refractive scintillation

Using eqn.5.6 and the scaling laws from Narayan (1992), one finds for a point source in the strong scattering regime, that the modulation index is

$$\begin{aligned} m_\mathrm{p} &= \xi^{-1/3} \qquad (5.10) \\ &\approx 7.3 \cdot 10^{-2} \cdot \mathrm{SM}^{-1/5} \, D_\mathrm{kpc}^{-1/6} \, \nu_\mathrm{GHz}^{17/30}, \end{aligned}$$

whereas the variability time–scale is

$$t_\mathrm{p} = \frac{\theta_\mathrm{F} D}{v} \xi \approx \frac{3.3}{v_{30}} \, D_\mathrm{kpc} \, \mathrm{SM}^{6/10} \, \nu_\mathrm{GHz}^{-11/5} \;\; \mathrm{yrs}. \qquad (5.11)$$

We furthermore use D_kpc=0.5 (TC93), v_{30}=1.0 and ν_GHz=8.5 throughout this section. From eqns 5.10–11 it is immediately obvious that for a point source in the refractive regime, an extremely high value for SM is needed ($\gtrsim 10^5$ kpc $\mathrm{m}^{-20/3}$) to obtain the modulation index of images A and B. The time scale of variability would be around 15 yrs. Clearly the point source approximation is not valid.

For extended sources, the modulation index and time scale of variability scale as $(\theta_\mathrm{r}/\theta_\mathrm{s})^{7/6}$ and $(\theta_\mathrm{s}/\theta_\mathrm{r})$, respectively, where θ_s is the source size and θ_r the size of the scattering disk (Narayan 1992). At 8.5 GHz, we find

$$\theta_\mathrm{r} = \theta_\mathrm{F} \cdot \xi \approx 180 \times \mathrm{SM}^{6/10} \;\; \mu\mathrm{as}, \qquad (5.12)$$

which is independent of the distance to the equivalent phase screen. If we subsequently use the scaling laws, combined with eqns 5.10–11, we find a relation between the time scale of variability and the modulation index:

$$m = \xi^{5/6} \left(\frac{\theta_\mathrm{F} D}{v \cdot t} \right)^{7/6}, \qquad (5.13)$$

which is valid only if $\theta_\mathrm{s} > \theta_\mathrm{r}$. Inserting the usual numerical values for v, D and ν, we find

$$m \approx 2.0 \cdot \mathrm{SM}^{1/2} \, t_\mathrm{d}^{-7/6}, \qquad (5.14)$$

with t_d in units of days. We find that a scattering measure SM$\gtrsim 2 \cdot 10^{-2}$ is needed to explain modulations with a time scale of $\gtrsim$1 week in image A. From TC93 we find that SM=$2 \cdot 10^{-4}$ in the direction of B1600+434, corresponding to a time scale of one day. For deep modulations of about 1 month a scattering measure SM$\approx$0.5 is needed for image A. Both values are larger than can be expected on the basis of the ionized ISM model from TC93.

Differences in the scattering measure: One of the strongest arguments against refractive scattering is the large difference between the modulation indices of images A and B. If this is due to a difference in the scattering measure, this requires $\mathrm{SM_A}/\mathrm{SM_B} \approx (0.028/0.016)^2 \approx 3.1$ (eqns 5.13–14), which is substantial over an angular scale of only 1.4 arcsec. The same factor is found for the weak–scattering regime.

Structure function: We have also calculated the structure function (SF; Simonetti et al. 1985):

$$\mathrm{D}^{(1)}(\tau) = \frac{1}{2} < (\delta \mathrm{F}(t) - \delta \mathrm{F}(t+\tau))^2 >, \qquad (5.15)$$

following Blandford, Narayan & Romani (1986 [BNR86]), who investigated intensity fluctuations (i.e. "flickering") of extended radio sources, caused by refractive scattering. $\mathrm{F}(t)$ is the normalized light–curve as shown in Fig.5.1. BNR86 take a slightly steeper spectrum of the phase fluctuations with a power–spectrum slope $\beta = 4$, instead of a Kolmogorov slope of $\beta = 11/3$.

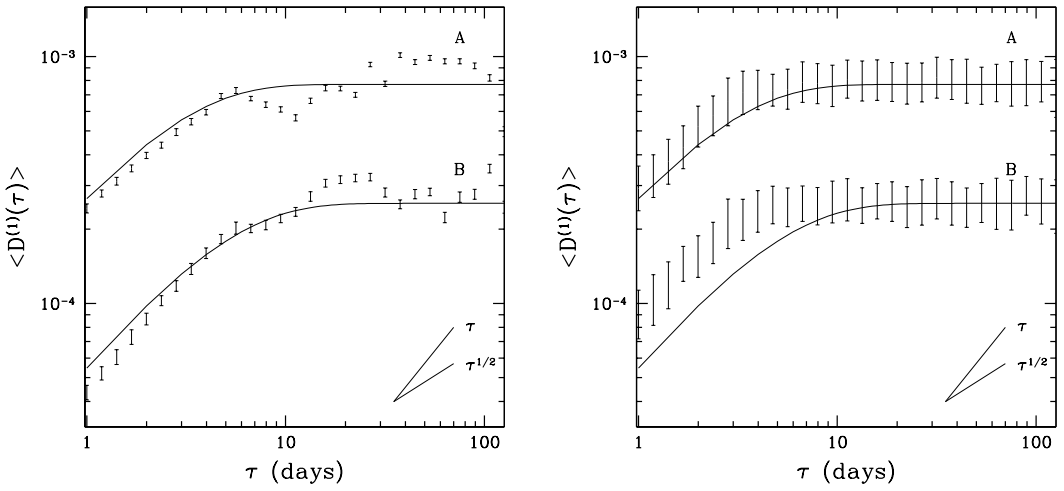

FIGURE 5.6— *Left:* The structure functions of the normalized light curve of images A and B. The solid curves shows the expected structure functions, derived as in BNR86, assuming a scale length of 0.9 kpc for the Gaussian distribution of the ionized scattering medium and v=30 km s^{-1}. Fits are only obtained for very different source sizes of 62 μas and 108 μas for images A and B, respectively. The 1–σ error bars on the structure functions are derived from Monte–Carlo simulations. *Right:* The simulated structure functions of the normalized light curve of images A and B, replacing the observed normalized flux–densities at each epoch with a random Gaussian distributed value with a 1–σ scatter equal to the observed modulation index in the light curves, i.e. 2.8% and 1.6% for images A and B, respectively.

Fitting the theoretical SF from BNR86 to the observed SFs[1] (Fig.5.6) gives a scale length of $L\sim$0.9 kpc, which corresponds to an equivalent phase screen distance of $0.9/\sqrt{\pi}$ $\approx$0.5 kpc (eqn.5.9). The 'best–fit' image sizes are 62 and 108 μas, respectively for images A and B. The saturation time scales (e.g. BNR86) found from these fits are τ_s^A=2.5 days and τ_s^B=4.4 days, even though there are obvious variations with longer time scales in the light curves.

To test the reliability of these saturation time scales, we replaced the normalized flux densities at each epoch in Fig.5.1 by Gaussian–distributed values with a 1–σ scatter equal to the observed modulation index of the light curve. In Fig.5.6 the result is shown, from which it is immediately clear that the light curves are undersampled such that the SFs and the saturation time scales for time lags $\tau\leq$4 days become highly unreliable.

Scatter–broadening: The expected scattering disk at 8.5 GHz due to the Galactic ionized ISM is $\sim$1 μas and cannot account for the apparent difference in the image size, derived from the SFs. This requires a scattering disk of $\gtrsim$90 μas for image B at 8.5 GHz, if image A is not scatter–broadened, implying that $SM_B\approx$1 in the lens galaxy!

If, we take into account that scattering occurs at a frequency of $8.5\times(1+z_l)\approx$12.0 GHz, this gives a scattering disk of 3 mas at 1.7 GHz, which is nearly equal to the very conservative upper limit of $\sim$4 mas found from 1.7–GHz VLBA observations (Neal Jackson 1999, private communication).

Recent polarization observations by Patnaik et al. (1999) gave rotation measures RM=40 rad m^{-2} and has RM=44 rad m^{-2} for images A and B, respectively. The difference of 4$\pm$4 rad m^{-2} is rather low and certainly does not support a high scattering measure in the disk/bulge of the lens galaxy.

[1]The structure function $D^{(1)}(\tau)$, calculated from the normalized light–curves, corresponds to the structure function $D^{(2)}(\tau)$, calculated from the observed light curves (KBXF99), because SFs of order M remove polynomials of order $M-1$ from the time series (e.g. Simonetti et al. 1985).

Diffractive scintillation

For diffractive scintillation at 8.5 GHz to be at work, one requires both a very high scattering measure and a very small source, neither which seems plausible. However, to be complete we briefly discuss this possibility.

The modulation index is unity for a point source,

$$m_{\rm p} = 1, \tag{5.16}$$

much larger than seen in both lens images. However, for a source larger than the scale on which there are phase changes of about 1 radian ($\theta_{\rm d}$), the modulation index becomes $m = (\theta_{\rm d}/\theta_{\rm s})$, where $\theta_{\rm s}$ is the source size. We find (e.g. W98)

$$\begin{aligned} \theta_{\rm d} &= \theta_{\rm F}\,\xi^{-1} \\ &\approx 3.1\cdot 10^{-3}\cdot {\rm SM}^{-6/10}\nu_{\rm GHz}^{6/5}D_{\rm kpc}^{-1}\ \ \mu{\rm as}, \end{aligned} \tag{5.17}$$

and for the point–source variability time–scale

$$t_{\rm d} = t_{\rm F}\cdot\xi^{-1} \approx \frac{0.25}{v_{10}}\cdot {\rm SM}^{-6/10}\nu_{\rm GHz}^{6/5}\ \ {\rm min}, \tag{5.18}$$

where $t_{\rm F}$=$\theta_{\rm F}\,D v^{-1}$=$4.0\cdot 10^4\cdot v_{30}^{-1}\sqrt{D_{\rm kpc}/\nu_{\rm GHz}}$ sec. The time-scale increases by $(\theta_{\rm s}/\theta_{\rm d})$, if the source size is larger than $\theta_{\rm d}$. Combining the eqns above, we find the relation

$$\xi = \frac{t_{\rm F}}{m\cdot t}, \tag{5.19}$$

where m is the observed modulation index. This relation is independent of source size, as long as the source is larger than the diffractive scale $\theta_{\rm d}$. Using this equation, we immediately find that $\theta_{\rm d} > \theta_{\rm F}$ for the deep modulations of $\gtrsim$1 week, which is only true in the weak scattering regime. Thus, diffractive scattering offers no solution either, which comes as no surprise.

5.4 Radio Microlensing: Theory

Microlensing is unlikely for bright ($\gtrsim$1 Jy) flat–spectrum radio sources at low frequencies ($\sim$few GHz), which have typical angular sizes of $\gtrsim$1 mas, determined by the inverse Compton limit on their surface brightness (e.g. Kellerman & Pauliny–Toth 1969). High–frequency ($\sim$10 GHz) sources with flux–densities less than a few tens of mJy, however, can be as small as several tens of micro–arcsec. If part of the source is moving with relativistic velocities ($\beta_{\rm app}c$), Doppler boosting allows an even smaller angular size. In those cases, microlensing can start to contribute significantly to the short–term variability seen in these sources (e.g. Gopal–Krishna & Subramanian 1991).

This is in contrast to optical microlensing, where the time scales are dominated by the transverse velocity ($v_{\rm trans}$) of the galaxy with respect to the line–of–sight to the static source, as in the case of 2237+0305 (e.g. Irwin et al. 1989). Microlensing time scales between strong caustic crossings in the optical waveband are therefore several orders of magnitude (i.e. $\beta_{\rm app}c/v_{\rm trans}\sim 10^{3-4}$) larger than in the radio waveband. This makes superluminal radio sources the perfect probes to study microlensing by compact objects in strong gravitational lens galaxies, using relatively short ($\lesssim$1 year) monitoring campaigns.

5.4.1 Relativistic jet components

If the lensed source consists of a static core and a synchrotron self–absorbed jet–component, which moves away from the core with a velocity $\beta_{\rm bulk}$=v/c, the Doppler factor of this jet–component is given by

$$\mathcal{D} = [\gamma\ (1-\vec{\beta}_{\rm bulk}\cdot\vec{n})]^{-1}, \tag{5.20}$$

where γ=$(1-\beta_{\rm bulk}^2)^{1/2}$ and $\vec{n}$ is the direction of the observer (e.g. Blandford & Königl 1979).

The observed flux–density of a circular–symmetric radio source with observed angular radius $\Delta\theta$ is

$$S(\nu) = \frac{2kT_{\rm b}\nu^2}{c^2}\cdot\pi\Delta\theta^2, \tag{5.21}$$

where ν is the observing frequency and $T_{\rm b}$ the observed brightness temperature of the source. We assume the source has a constant surface brightness. However, due to the Doppler boosting the apparent brightness temperature of a relativistic jet–component moving towards the observer can be significantly brighter than the inverse Compton limit of about $T_{\rm b,ic}$≈$5\cdot 10^{11}$K

(e.g. Kellerman & Pauliny-Toth 1969). The true comoving surface brightness temperature of a flat–spectrum radio source is related to the observed surface brightness temperature ($T_{\rm b}$) through

$$T_{\rm b} = 10^{12} \times T_{12}^{\rm b,ic} \left(\frac{\mathcal{D}}{1+z} \right) \quad {\rm K}, \qquad (5.22)$$

where z is the redshift of the source (e.g. Blandford & Königl 1979). If we substitute eqn.5.22 into eqn.5.21, we find that the flux–density of the relativistically moving jet–component is

$$S_{\rm knot} = 0.23 \left[\frac{\mathcal{D} T_{12}^{\rm b,ic}}{1+z} \right] \nu_{10}^2 \left(\frac{\Delta\theta_{\rm knot}}{\mu{\rm as}} \right)^2 \ {\rm mJy}, \qquad (5.23)$$

with ν_{10}=$\nu/(10\,{\rm GHz})$. Inverting this equation, we find an approximate angular radius of the jet–component

$$\Delta\theta_{\rm knot} = 2.1 \cdot \left[\left(\frac{S_{\rm knot}}{\rm mJy} \right) \frac{(1+z)}{\mathcal{D} T_{12}^{\rm b,ic} \nu_{10}^2} \right]^{1/2} \ \mu{\rm as}. \qquad (5.24)$$

Given the observed frequency, the redshift of the jet–component and $\mathcal{D}$, we can thus set a limit to the angular radius of the jet–component.

In the case of B1600+434, the redshift of the lensed quasar is z=1.59 (Fassnacht & Cohen 1998). The observing frequency is ν_{10}=0.85 and $S_{\rm knot} \approx S_{8.5}^{\rm tot} \cdot f$, where f is the fraction of the total average flux–density in the relativistic jet–component, $S_{8.5}^{\rm tot} \approx 25/\langle\mu\rangle$ mJy (KBXF99) and $\langle\mu\rangle$ is the average magnification at the image position. From the SIE mass model (Kormann, Schneider & Bartelmann 1994), we find $\langle\mu_{\rm A}\rangle \approx 1.7$ (κ=0.2) and $\langle\mu_{\rm B}\rangle \approx 1.3$ (κ=0.9). We use $\langle\mu\rangle \approx 1.5$ as a typical value.

After inserting all the known observables into eqn.5.24 and adopting $T_{12}^{\rm b,ic}$=0.5, we find an approximate relation between the fraction of the total observed flux–density of B1600+434 contained in the jet–component and its angular size in the source plane

$$\Delta\theta_{\rm knot} \approx 20 \cdot \sqrt{\frac{f}{\mathcal{D}}} \ \mu{\rm as}. \qquad (5.25)$$

This equation can be used to put constraints on the light–curve fluctuations seen in B1600+434, and decide whether they are caused by microlensing of a single relativistic jet–component.

5.4.2 Microlensing time scale

The typical time–scale which one would expect between relatively strong microlensing events is the angular separations between strong caustic crossings divided by the angular velocity of the jet–component in the source plane.

In case the source is not lensed, the apparent velocity (in units of c) of the jet–component is

$$\vec{\beta}_{\rm app} = \frac{\vec{n} \times (\vec{\beta}_{\rm bulk} \times \vec{n})}{1 - \vec{\beta}_{\rm bulk} \cdot \vec{n}} = \frac{\vec{\beta}_{\rm bulk} \sin(\psi)}{1 - |\vec{\beta}_{\rm bulk}| \cos(\psi)}, \qquad (5.26)$$

where ψ is the angle between the jet and the line–of–sight and $\beta_{\rm bulk}$ the bulk velocity of the jet–component (e.g. Blandford & Königl 1979). The apparent angular velocity (in vector notation) of the jet–component becomes

$$\begin{aligned} \frac{{\rm d}\vec{\theta}_{\rm s}}{{\rm d}t} &= \frac{\vec{\beta}_{\rm app} c}{(1+z_{\rm s}) D_{\rm s}} \qquad (5.27) \\ &= \frac{1.2 \cdot \vec{\beta}_{\rm app}}{(1+z_{\rm s})} \left(\frac{D_{\rm s}}{\rm Gpc} \right)^{-1} \ \frac{\mu{\rm as}}{\rm week}, \end{aligned}$$

where $z_{\rm s}$ and $D_{\rm s}$ are the redshift and the angular diameter distance to the stationary core, respectively. If the jet–component moves with superluminal velocities ($\beta_{\rm app} \geq 1$), one can expect angular velocities in the order of several tenths of μas per week. Because the source is lensed by the foreground galaxy, its observed angular velocity (in the lens plane) becomes

$$\frac{{\rm d}\vec{\theta}_{\rm d}}{{\rm d}t} = \left[\mathcal{A}^{-1} \cdot \frac{{\rm d}\vec{\theta}_{\rm s}}{{\rm d}t} \right] \left(\frac{D_{\rm d}}{D_{\rm s}} \right), \qquad (5.28)$$

where

$$\mathcal{A} = \begin{bmatrix} 1-\kappa-\gamma_1 & -\gamma_2 \\ -\gamma_2 & 1-\kappa+\gamma_1 \end{bmatrix} \qquad (5.29)$$

is the local transformation matrix of the source plane to the lens plane, with κ and $\gamma_{1,2}$ being the local convergence and shear (e.g. Gopal–Krishna & Subramanian 1991; Schneider et al. 1992).

We calculate the source and caustic structure in the source plane, however. Thus, the angular velocity and source structure undergo the inverse transformation of the angular velocity in the source plane (eqn.5.28). The angular velocity that we need to use, is therefore given by eqn.5.27. Using the observed redshift z=1.59 (Fassnacht & Cohen 1998) of B1600+434 the angular velocity in the source plane reduces to

$$\frac{\mathrm{d}\vec{\theta}_\mathrm{s}}{\mathrm{d}t} = 0.34 \cdot \vec{\beta}_\mathrm{app} \ \frac{\mu\mathrm{as}}{\mathrm{week}}, \tag{5.30}$$

where we assume a flat FRW universe with Ω_m=1 and H_0=65 km s^{-1} Mpc^{-1}.

5.4.3 Microlensing modulation index

The normalized modulation index (m_μ) of a superluminal jet component, due to microlensing, is

$$m_\mu \equiv \sqrt{\frac{\langle\mu^2\rangle}{\langle\mu\rangle^2} - 1}, \tag{5.31}$$

where μ=$\mu(t)$ is the microlensing light curve of the jet component. We determine m_μ as function of the angular size of the source by averaging over randomly–oriented simulated microlensing light curves and find that m_μ can be well approximated by the analytical function

$$m_\mu(\Delta\theta_\mathrm{knot}) = \frac{C_\mu}{1 + \left(\frac{\Delta\theta_\mathrm{knot}}{\Delta\theta_\mathrm{b}}\right)} \tag{5.32}$$

for $\Delta\theta_\mathrm{knot} \lesssim 20\mu$as, where $\Delta\theta_\mathrm{b}$ is the turnover size of the source after which the modulation index m_μ decreases linearly with source size and C_μ is the asymptotic modulation index for a source with $\Delta\theta_\mathrm{knot} \to 0$. We fit this function to the numerical results to obtain both C_μ and $\Delta\theta_\mathrm{b}$.

We subsequently combine eqns 5.25 and 5.32 with the fact that the observed modulation index in the lens images is $m_\mu^\mathrm{obs} = f \cdot m_\mu$ and find

$$m_\mu^\mathrm{obs}(f, \mathcal{D}) \approx \frac{C_\mu \cdot f}{1 + 20\ \Delta\theta_\mathrm{b}^{-1}\ \sqrt{f/\mathcal{D}}}, \tag{5.33}$$

where $\Delta\theta_\mathrm{b}$ is in units of micro–arcsec.

Many jets consist of more than a single jet–component. If we assume that (i) the jet consists of N similar jet–components, each containing a fraction f_1=f/N of the total flux–density and (ii) the magnification curves of the jet–components to be uncorrelated, we expect the modulation index of the combined jet–components to decrease roughly as $\sim 1/\sqrt{N}$. Hence, we find that $m_\mu^\mathrm{obs}(N) \approx \cdot f \cdot m_\mu(f_1)/\sqrt{N}$, or

$$m_\mu^\mathrm{obs}(f, \mathcal{D}) \approx \frac{C_\mu \cdot f/\sqrt{N}}{1 + 20\ \Delta\theta_\mathrm{b}^{-1}\ \sqrt{f/(\mathcal{D}N)}}, \tag{5.34}$$

where f=$N\,f_1 \leq 1$. Hence, multiple jet–components will in general decrease the modulation index. However, if the individual jet–components are very compact – i.e. are much smaller than the typical separation between strong caustics –, the microlensing variability will be dominated by single–caustic crossings, creating strong isolated peaks in the light curve. We expect eqn.5.34 to break down in that case, such that the factor $1/\sqrt{N}$ in the numerator can be removed.

In the case of scintillation, N compact jet–components ($\Delta\theta_\mathrm{knot} \lesssim \theta_\mathrm{F}$) always vary independently, such that the observed modulation index roughly decreases as $1/\sqrt{N}$. However, in the case of microlensing, the modulation index, caused by the same compact jet–components moving over a magnification pattern, can be independent from N or even increase as $\sqrt{N}$. Hence, in the case of a large number of superluminal compact jet–components in a radio source, microlensing variability can quickly start to dominate over scintillation!

5.4.4 Source constraints

At this point, we give a qualitative recipe to obtain constraints on the jet–component parameters from the observed light–curves.

1. First, the observed modulation indices of both lens images can be used to solve for the fraction of flux–density in the jet–component (f), as well as its Doppler factor ($\mathcal{D}$), by comparing

them to those found from numerical simulations for different MFs (which fix C_μ and $\Delta\theta_b$). One obtains a set of two equations (i.e. eqn.5.33) with two constraints (m_μ^A and m_μ^B) and two unknown variables ($\mathcal{D}$ and f), which can be uniquely solved for, in some cases. The combinations of MFs, which do not give a consistent solution, can be excluded, thereby putting constraints on the MFs in front of the lens images.

2. Second, combining the typical observed variability time scale between strong microlensing events and the angular separation of these from the numerical simulations, one can obtain a value for β_{app} (eqn.5.27). Combining eqn.5.20 and eqn.5.26, one then also readily solves for both ψ and β_{bulk}.

Thus, given (i) a mass model of the lens galaxy found from (macroscopic) lens modeling, (ii) some plausible range of MFs near the lens images and (iii) the observed modulation indices and variability time–scales in the light–curves of the lens images, one can in principle solve for several parameters of the simple jet/jet–component structure: $\mathcal{D}$, f, ψ, β_{app}, β_{bulk} and $\Delta\theta$. However, some of the parameters might be coupled, and we do not know true intrinsic brightness temperature of the components.

5.5 Radio Microlensing: Results

In this section, we examine the observed variability in the light–curves of B1600+434 A and B in terms of microlensing and, following the procedure delineated in Sect.5.4.4, derive constraints on the properties of the jet–component, as well as on the MFs near both lens images. In Sect.5.7, we will use these results to determine the microlensing modulation index as function of frequency and compare them to the results from independent WSRT 1.4 and 5–GHz monitoring data of B1600+434 (Sect.5.2). An overview of the combined microlensing/scintillation situation in B1600+434 is given in Fig.5.8, which might act as guide to the overall situation.

From now on, we will (i) use a source structure consisting of a static core plus a *single* relativistically moving spherically–symmetric jet component, (ii) assume that the core and jet parameters do not change appreciably over the time–span of the observations and (iii) assume that *all* short–term variability in the image light curves (Fig.5.1) is dominated by microlensing. The static core does not contribute to the short–term variability, because its velocity with respect to the magnification pattern of the lens is much smaller than that of the jet–component (i.e. $v_{core} \ll v_{jet}$). At this moment, we feel that a more detailed model is not warranted.

5.5.1 Numerical simulations

From KBJ98, we find for B1600+434 that the local convergence and shear are close to κ=γ=0.2 for image A, using a singular isothermal ellipsoidal (SIE) mass distribution for the lens galaxy. Similarly for image B, we find κ=γ=0.9. Using these input parameters, we simulate the magnification pattern of a $50\,\eta_e \times 50\,\eta_e$ field for different MFs, where η_e is the Einstein radius of a 1–$M_\odot$ star in the source plane. We use the microlensing code developed by Wambsganss (1990). Using the lens redshift $z_l = 0.41$, the source redshift z_s=1.59 and H_0=65 km s^{-1} Mpc^{-1} in a flat (Ω_m=1) FRW universe, we find that η_e=2.1 μas. The magnification pattern is calculated on a grid of 1000×1000 pixels. Each pixel has a size of 0.107 μas by 0.107 μas.

We simulate 100 randomly–oriented light curves on this grid, for a range of jet–component sizes ($\Delta\theta_{knot}$=0.125, 0.25,..., 16.0 μas) and mass functions for the compact objects (Sect.5.5.2). Each curve is 54 μas long. For each step (5 pixels) on the light curve, we calculate the magnification of a circular–symmetric jet–component with constant surface-brightness and radius $\Delta\theta$, by convolving the magnification pattern with its brightness distribution (e.g. Wambsganss 1990).

MF	Mass ($M_\odot$)	Slope	$\langle M \rangle$ ($M_\odot$)	C_μ	$\Delta\theta_b$ (μas)
A					
S1	0.1	–	–	0.69	0.94
S2	0.2	–	–	0.70	1.28
S3	0.4	–	–	0.71	1.87
S4	0.6	–	–	0.69	2.44
S5	0.8	–	–	0.70	2.48
S6	1.0	–	–	0.71	2.71
S7	1.5	–	–	0.71	3.07
S8	2.5	–	–	0.69	4.27
S9	5.0	–	–	0.76	4.50
B					
S1	0.1	–	–	1.00	0.90
S2	0.2	–	–	1.01	1.17
S3	0.4	–	–	1.03	1.41
S4	0.6	–	–	1.05	1.98
S5	0.8	–	–	1.06	2.35
S6	1.0	–	–	1.07	2.65
S7	1.5	–	–	1.12	2.95
P1	0.01–1	-2.35	0.031	1.01	1.09
P2	0.01–1	-1.85	0.058	1.05	1.37
P3	0.01–1	-2.85	0.021	0.98	0.71
P4	0.1–10	-2.35	0.309	1.09	2.00

TABLE 5.2— Summary of the modulation index caused by microlensing as function of source size for the power–law MFs (BP1–4) near images B and the single–mass MFs (AS1–9 and BS1–7) near image A and B.

5.5.2 The mass function of compact objects in B1600+434

We use a range of different MFs, subdivided in two classes: (i) power–law MFs and (ii) single–mass MFs.

The power–law MF

In the solar neighborhood it appears that the stellar MF can be represented by a single or segmented power–law (e.g. Salpeter 1955; Miller & Scalo 1979) of the form $\mathrm{d}N(m)/\mathrm{d}M \propto M^{\alpha}$. Recent observations towards the Galactic bulge (e.g. Holtzman et al. 1998) suggest a break in the MF around 0.5–0.7 $M_\odot$, with a shallower slope at lower masses. A lower–mass cutoff is not well constrained, although the break in the MF suggests it might lie around a few tenths of a solar mass. Evolution of the MF from z=0.4 to z=0.0 affects the upper mass cutoff only and has no significant influence on microlensing, which is dominated by the mass concentrated around the lower mass cutoff.

1. First, we simulate the magnification pattern, using a power–law MF with $\alpha = -2.35$ (Salpeter 1955) and a mass range between 0.01–1.0 $M_\odot$.

2. Second, we also investigate the slopes –2.85 and –1.85 for image B – going through the bulge/disk – assuming again a mass range of 0.01–1 $M_\odot$.

3. Third, we use an MF mass range of 0.1–10 $M_\odot$ near image B, with a slope of -2.35. This gives an average stellar mass of about 0.3 $M_\odot$, more in line with observations of the bulge of our Galaxy(e.g. Holtzman et al. 1998).

We only use the power–law MFs for image B, even though it is clearly a rough approximation of the true MF. A similar power–law MF for image A, passing

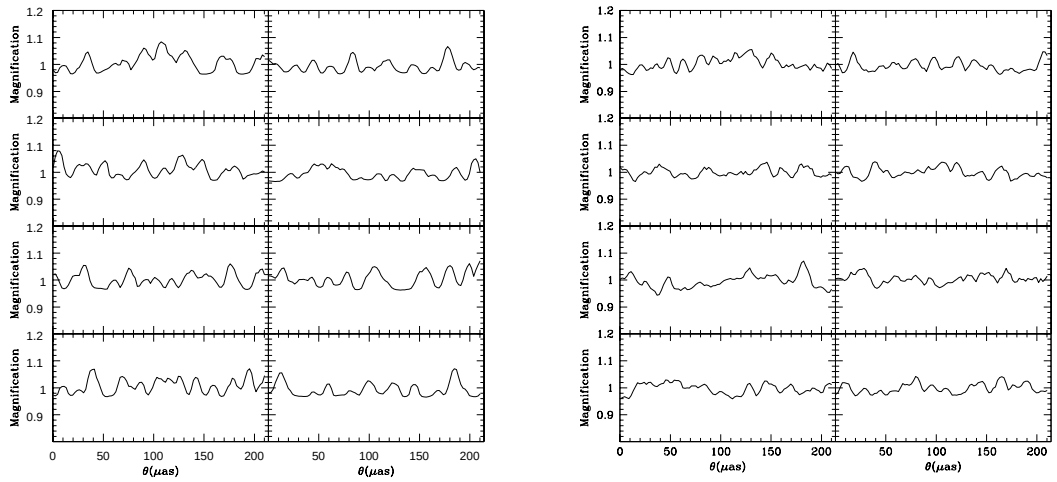

FIGURE 5.7— *Left:* Eight arbitrary simulated light-curves for a single compact 5-μas source, moving over the magnification pattern near image A. The values f and $\mathcal{D}$ from Table 5.3 were used. The simulated curves were subsequently scaled by f. A 1.5–$M_\odot$ single–mass MF was used. The light-curves were created through a convolution of the source surface–brightness distribution with the magnification pattern. The source was moved over a 500-pixels path (i.e. 214 μas), randomly placed on the magnification pattern. *Right:* Idem, for image B, using a 0.2–$M_\odot$ single–mass MF. The ratio between the modulation index for the simulated light–curves, is approximately equal to the observed ratio of modulation indices in the observed light–curves of B1600+434 A and B (Fig.5.1). The scale, in this random example, would correspond to 35 weeks, the duration of the monitoring campaign of B1600+434 ($\beta_{\rm app} \approx 18$).

through the halo, seems unlikely, especially if the halo consists of stellar remnants (e.g. Timmes, Woosley & Weaver 1996).

The results of these simulations – m_μ as function of $\Delta\theta_{\rm knot}$ – are fitted by eqn.5.32. The resulting values for C_μ and $\Delta\theta_{\rm b}$ are listed in Table 5.2 (models BP1–4).

The single–mass MF

In steep ($\alpha < -1$) MFs most of the mass is concentrated close to the lower–mass cutoff in the MF. It therefore seems appropriate to approximate the MF by a delta–function. We simulated single–mass MFs for both image A and B, for 0.1, 0.2, 0.4, 0.6, 0.8, 1.0, 1.5 $M_\odot$ and additionally for 2.5 and 5.0–$M_\odot$ for image A. The results are listed in Table 5.2.

From these simulation, we notice several things: First, C_μ is almost independent from the mass of the compact objects, for a given surface density. Second, there appears to be a strong correlation between the average mass of the compact objects and the turnover angle ($\Delta\theta_{\rm b}$), which means that for a given surface density and source size, the modulation index is stronger for a higher average mass of the compact objects.

5.5.3 Microlensing in B1600+434?

As we can see from Table 5.2, the modulation index in image A can be explained by a relatively small jet–component with a moderate boosting factor. However, from this one expects image B to show similar, if not stronger variability for a similar MF, because of its higher microlensing optical depth ($\tau_{\rm B} > \tau_{\rm A}$). Before we examine this in terms of a different mass function in the disk/bulge and halo of the lens galaxy, we first explore two alternative explanations:

- What if the dimensionless surface density near image B is near unity (i.e. $\kappa \approx 1$)? In that case, the magnification pattern can become very dense and suppress the modulation index due to microlensing (e.g. Wambsganss 1990). For B1600+434 we found that $\kappa_{\rm B} \approx \gamma_{\rm B}$ (Sect.5.5.1), in which case the magnification and density of the

caustics remain relatively small, in contrast with the case where $\kappa \approx 1$ and $\gamma \approx 0$ (e.g. Wambsganss 1990). This is supported by simulations with $\kappa = \gamma = 0.999$ near image B, which give nearly the same results as for $\kappa = \gamma = 0.9$.

- In Sect.5.3.2 we showed that scatter–broadening of image B can suppress scintillation caused by the Galactic ionized ISM. Similarly, is can suppress variability due to microlensing. An overview of the situation is given in Fig.5.8. Image A, however, is seen through the galaxy halo at about 4 h^{-1} kpc above the disk (KBJ98). It is therefore extremely unlikely to pass through a region with a high scattering measure (Sect.5.3.2).

We will now explore the only other plausible solution; a very different MF near images A and B.

Limits on the MF and source structure

In Table 5.3, we have listed all combinations between the simulated MFs for images A and B (Table 5.2), that reproduce the observed short–term modulation indices of 2.8% (A) and 1.6% (B) for a consistent set of parameters f and $\mathcal{D}$ (Sect.5.4.4). Several examples of simulated light–curves are shown in Fig.5.7.

Constraints on the MFs in B1600+434: From Table 5.3 one finds that a significantly higher average mass of compact objects in the halo is needed than in the bulge/disk to explain the modulation index of both images. No consistent solutions are found for an average mass of compact objects in the halo <1 $M_\odot$ for the range of MFs that we simulated. If we furthermore put a conservative upper limit of $\lesssim 0.5$ $M_\odot$ on the average mass of compact objects in the bulge/disk of B1600+434 – which lies around the break in the Galactic bulge MF (e.g. Holtzman et al. 1998) – only MFs BS1–3 and BP1–4 (Table 5.2) remain viable MFs for the bulge/disk of B1600+434.

Constraints on $\Delta\theta$, f and $\mathcal{D}$: Using the MFs assumed viable above, we find from Table 5.3: $0.05 \lesssim f \lesssim 0.11$ and $1.1 \lesssim \mathcal{D} \lesssim 4.0$. Using eqn.5.25 and the values of f and $\mathcal{D}$ listed in Table 5.3, the jet–component size then lies between $2 \lesssim \Delta\theta_{\rm knot} \lesssim 5$ μas.

Constraints on $\beta_{\rm app}$: To estimate a time scale for strong microlensing variability, we calculate the average power spectrum of the 100 light–curves for each MF, for the source size of 2 and 4 μas. The power–spectrum is typically relatively flat at low frequencies, smearing out the long–period modes in the light–curves. At higher frequencies the power drops rapidly. We therefore expect the strongest Fourier modes in the light curves to lie around the turn–over frequency, where the power drops to about 50%. Consequently, we define the typical variability angular scale ($\theta_{\rm t}$) to correspond with the half–power frequency in the power–spectrum. In Table 5.4, we listed the results for those MFs that give a consistent solution (Table 5.3).

If we now take a separation of $\sim$2 weeks as indicative for the separation of strong modulations in light curve of image A (see days 80–140 in Figs 5.1–5.2), we find an angular velocity of the jet–component in the source plane between 3 and 9 μas/week. Using eqn.5.30, we then derive $9 \lesssim \beta_{\rm app} \lesssim 26$. This range clearly dependents on the local structure of the magnification pattern, but is in agreement with observations of confirmed superluminal sources (e.g. Vermeulen & Cohen 1994).

Constraints on $\beta_{\rm bulk}$ and ψ: Using the constraints of the Doppler factor ($\mathcal{D}$) and angular velocity of the jet–component ($\beta_{\rm app}$), one also obtains constraints on the angle between the jet–component direction with respect to the line–of–sight to the observer and the bulk velocity of the jet–component ($\beta_{\rm bulk}$). From Fig.5.9, we subsequently find: $2^\circ \lesssim \psi \lesssim 5^\circ$ and $0.975 \lesssim \beta_{\rm bulk} \lesssim 0.998$, for the allowed ranges of these parameters.

Thus, several combinations of MFs for image A and B (Table 5.3) give solutions that reproduce the observed modulation indices of both images for a consistent, although not unique, set of jet–component

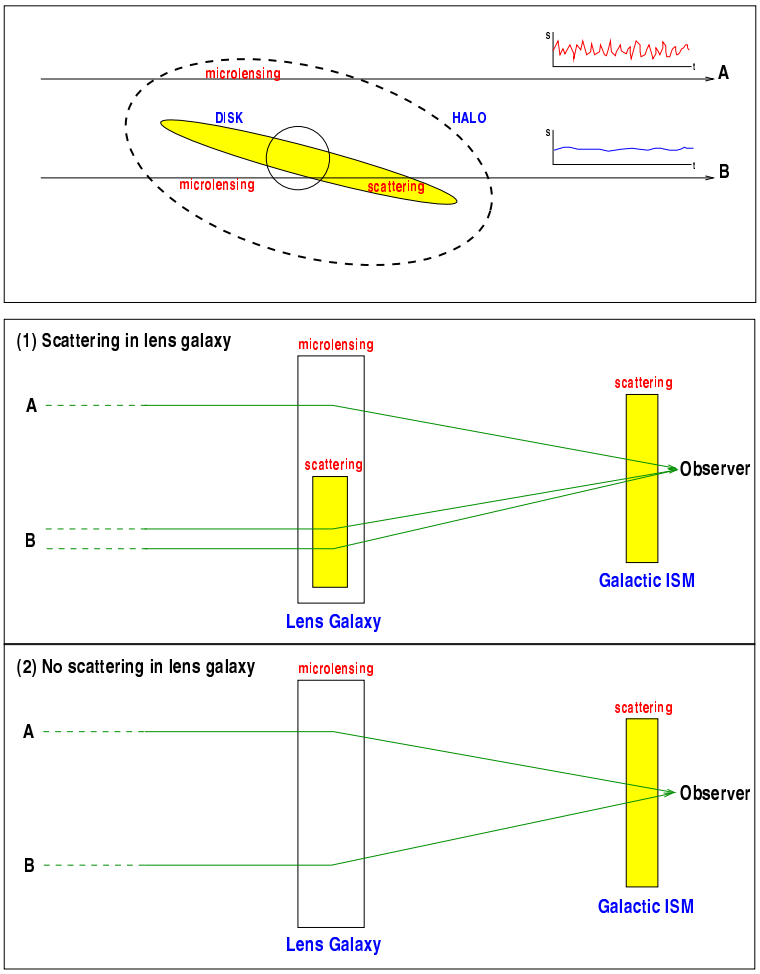

FIGURE 5.8— The overall microlensing and scattering situation in B1600+434, when seen side–ways. The inclination of the disk has been slightly exaggerated (i=75°). Situation 1: Light coming from image A passes predominantly through the halo. Light coming from image B first passes through the bulge/disk, where the image might be scatter–broadened by the lens–galaxy ionized ISM (Sect.5.3.2). The image thus subtends a larger solid angle, suppressing microlensing in the lens galaxy and scintillation caused by the ionized ISM in our galaxy. Situation 2: Only microlensing in the bulge/disk and halo in the lens galaxy occurs. However, subsequent scatter–broadening in our galaxy does not suppress microlensing variability.

parameters. The derived constraints on the jet–component also agree well with observations of confirmed superluminal sources (e.g. Vermeulen & Cohen 1994).

Microlensing by MACHOs

It appears we have found a lower limit of $\sim$1 $M_\odot$ on the mass of compact objects in the halo (MACHOs) around the lens galaxy, under the assumptions that all variability we see is due to microlensing and the jet is dominated by a single component. This lower limit is largely the result of image A varying much stronger than image B, even though this image has a higher optical depth. Let us now explore the implications of this in more detail, first mentioning several potential problems.

- Could microlensing be due to a globular cluster (GC) in the halo of the lens galaxy? It is easy to show that the probability of seeing a lens image through a GC surface density $> \kappa_{\rm GC}$ is

$$P(>\kappa_{\rm GC}) \approx \frac{N}{4\cdot\kappa_{\rm GC}^2}\left(\frac{\sigma_{\rm GC}}{\sigma_{\rm LG}}\right)^4 . \quad (5.35)$$

MF	AS6	AS7	AS8	AS9
BS1	–	0.09,1.3	0.07,2.1	0.05,3.4
BS2	–	0.10,1.2	0.07,2.0	0.05,3.2
BS3	–	–	0.07,1.7	0.06,2.7
BS4	–	–	0.08,1.5	0.06,2.4
BS5	–	–	0.08,1.4	0.06,2.4
BS6	–	–	0.08,1.3	0.06,2.0
BS7	–	–	–	0.07,1.4
BP1	–	0.10,1.2	0.07,2.0	0.05,3.2
BP2	–	–	0.08,1.5	0.06,2.4
BP3	0.11,1.1	0.09,1.6	0.07,2.5	0.05,4.0
BP4	–	–	0.08,1.1	0.06,1.8

TABLE 5.3— All combinations of the MFs (Table 5.2) near image A and B, that give a consistent solution of the parameters: $(f, \mathcal{D})$. Given these two parameters, one reproduces the observed modulation indices in both lens images, using eqn.5.33 and Table 5.3.

We take a population of $N{\sim}150$ GCs, inside the Einstein radius of the lens galaxy (LG), with a velocity dispersion of $\sigma_{\rm GC}$=7 km s^{-1}. These values are typical of those found for our galaxy (e.g. Binney & Merrifield 1999). Using $\sigma_{\rm LG}{\approx}200$ km s^{-1} (KBJ98), $\kappa_{\rm GC}{=}\kappa_{\rm A}{=}0.2$, we then find a probability $P(>\ \kappa_{\rm GC}){\approx}1.7\cdot10^{-3}$ that the microlensing optical depth ($\tau_{\rm ml}{\approx}\kappa_{\rm ml}$) of the GC exceeds that of the dark matter halo. The probability that $\kappa_{\rm GC}$ exceeds $\kappa_{\rm B}$=0.9, thereby causing similar or larger microlensing variability, is $7\cdot10^{-5}$. Hence, it is very unlikely that a GC in the line–of–sight to lens image A could enhance the microlensing optical depth significantly.

- What is the influence of binary systems on the mass limit of a MACHO in the dark matter halo? We know that a large fraction of stars in the bulge is locked up in binary systems (e.g Holtzman et al. 1998). In the case of high microlensing optical depths, one can consider a binary as a single microlensing object, with a mass equal to the sum of the individual masses.

  From Table 5.2 we see that a higher mass of compact objects gives a higher microlensing modulation index for a given source size. Hence, if we know the typical stellar mass of objects in the bulge/disk and assume they are all single objects, not in a binary system, we underestimate its modulation index. One has to take this effect into account.

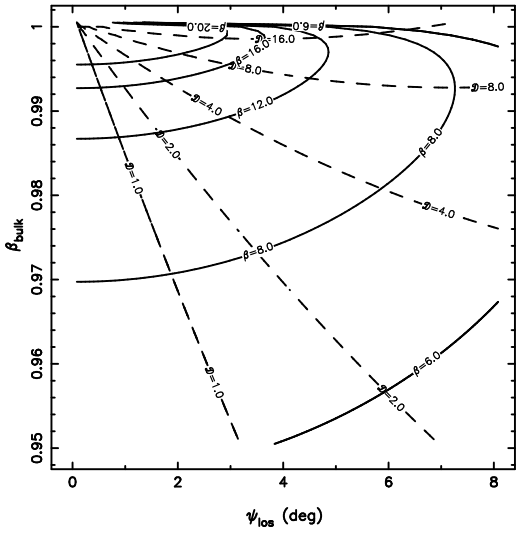

FIGURE 5.9— The bulk velocity ($\beta_{\rm bulk}$) and angle with respect to the the line–of–sight to the observer (ψ) of a relativistic jet–component, as function of its Doppler boosting ($\mathcal{D}$) and apparent velocity ($\beta_{\rm app}$), calculated using eqns 5.20 and 5.26.

Having dealt with these possible complications, let us explore the lower limit of the MACHO mass in more detail. If we assume that (i) all compact object in the bulge/disk are not in binary systems and (ii) all MACHOs are in binary systems and

MF	$\Delta\theta_{\rm knot}$=2 μas	4 μas
AS6	8	14
AS7	8	13
AS8	10	14
AS9	13	14
BS1	7	13
BS2	7	12
BS3	7	12
BS4	8	14
BS5	10	14
BS6	8	15
BS7	8	18
BP1	7	14
BP2	6	12
BP3	7	16
BP4	7	12

TABLE 5.4— The typical angular scale ($\theta_{\rm t}$) in μas between strong microlensing events in the simulated light curves, as defined through the power spectrum (see text). Listed are the values for two source sizes, 2 and 4 μas, approximately corresponding to the range of jet–component sizes that reproduce the observed modulation index in the light curves (see text).

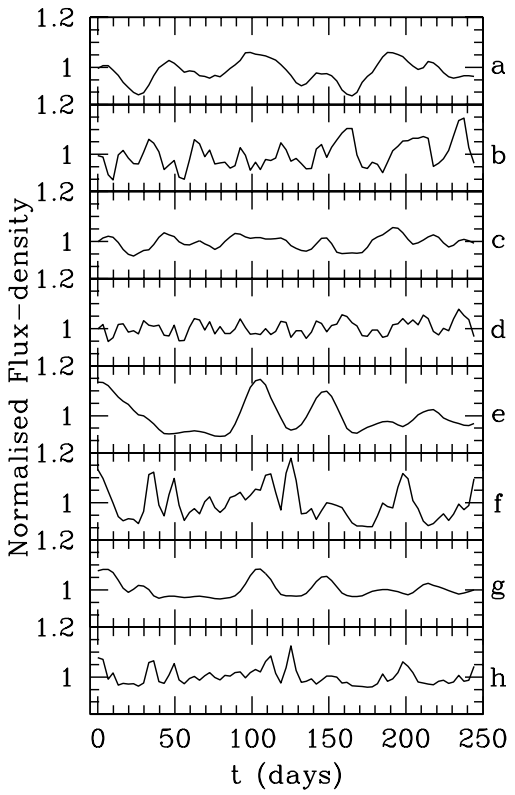

FIGURE 5.10— Eight simulated microlensing light curves of 3C120. The parameters for each light curve are listed in Table 5.6.

(iii) use the lowest average mass of objects in the bulge/disk (Tables 5.2–3), we find a very conservative lower limit of 0.5 $M_\odot$ on the mass of individual MACHOs in the halo. In the more realistic case where most of the stars in the bulge/disk are in binaries and most MACHOs are probably not, a lower limit of 1.5 $M_\odot$ is found, assuming that the average bulge/disk stellar mass in the halo is $\sim$0.1 $M_\odot$. If the bulge/disk stars have average masses somewhere between 0.1 and 0.3 $M_\odot$ and are foremost in binaries, the lower limit increases to $\sim$2.5 $M_\odot$.

As in the case of scintillation, scatter–broadening of image B also suppresses microlensing (Sect.5.5.3). If this happens, one would underestimate the true microlensing modulation index of image B. This would give one more freedom to decrease f and/or increase $\mathcal{D}$ for the microlensed jet component, thereby lowering the required average mass of MACHOs in the halo. It would, however, *never* eliminate the need for them.

5.6 Microlensing of a realistic jet structure

So far, we have only investigated a very simple model of the source structure, consisting of a core plus a single jet–component. To see how a real source behaves, when microlensed by similar MFs as in the lens galaxy of B1600+434, we simulated light–curves of a more complex jet structure.

5.6.1 The jet structure of 3C120

We used the inner jet–structure seen in 3C120 (Gómez et al. 1998; Gómez, Marscher & Alberdi 1999) as a 'template', because it is one of the best–studied nearby jet structures. The inner jet consists of a core plus at least 15 distinguishable jet components (Gómez et al. 1999), which move superluminally, with velocities typically around 4.5c (H_0=65 km s^{-1} Mpc^{-1};

Fraction flux	$0.05 \lesssim f \lesssim 0.11$	
Doppler factor	$1.1 \lesssim \mathcal{D} \lesssim 4.0$	
Size in source plane	$2 \lesssim \Delta\theta_{\rm knot} \lesssim 5$	(μas)
Apparent velocity	$9 \lesssim \beta_{\rm app} \lesssim 26$	
LOS angle of jet	$2 \lesssim \psi_{los} \lesssim 5$	(°)
Bulk velocity	$0.975 \lesssim \beta_{\rm bulk} \lesssim 0.998$	

TABLE 5.5— Summary of constraints on the jet–component parameters, derived within the context of the microlensing hypothesis. We assume $T_{12}^{b,ic}$=0.5 and a flat FRW universe with $\Omega_{\rm m}$=1 and H_0=65 km s^{-1} Mpc^{-1}.

Gómez et al. 1998). The jet was observed at 22 GHz. The total flux–density of 3C120 at this frequency is 5.7±0.9 Jy (O'Dell et al. 1978), whereas the fitted inner–jet components contain about 2.5 Jy (Gómez et al. 1999). We therefore assume that the inner jet contains about 40% of the total flux–density of 3C120.

Note that 22 GHz corresponds to approximately X–band (8.5 GHz) observations, when placed at the source redshift of B1600+434 (1.59). We thus scale the size of the jet structure down by the ratio of angular diameters distances for 3C120 and the lensed source of B1600+434 and its flux–density by the ratio of luminosity distances squared.

At a redshift of 1.59, 3C120 would be a 1.8 mJy source. To obtain a source of about 25 mJy total , as observed for B1600+434, we scale each jet components size by a factor ($\alpha_{\rm r}$) of about 3.7 in radius and assume that about 60% of its flux–density is contained in an extended structure, which is not sensitive to microlensing. We assume their surface brightness temperature to be conserved and associate the radius of the source with half the FWHM of the component size determined by Gómez et al. (1999). The resulting jet structure has a flux–density of about 25 mJy at 8.5 GHz and an angular size of the inner jet less than 1 mas. If, we only use the inner jet and not assume the additional 60% of extended emission, one should scale the inner–jet components by a factor of $\alpha_{\rm r}$=5.7 to obtain a total flux–density of about 25 mJy.

5.6.2 Microlensed light–curves of 3C120

The jet structure is randomly placed on the magnification pattern. We recalculate the jet structure and the resulting normalized light curves at epochs separated by 3.3 days, which is the average sampling of the light curves of B1600+434. For image A, we use the MF AS7, which corresponds to a halo filled with stellar remnants, such as black holes and neutron stars. For image B, we use the MF BS2.

We calculate light curves with a total time span of 35 weeks, corresponding to the length of the observed VLA light curves of B1600+434. We subsequently scale the light–curves by a factor 0.4 ($\alpha_{\rm r}$=3.7 for 40% of the flux–density from the inner jet) or 1.0 ($\alpha_{\rm r}$=5.7 for 100% of the flux–density from the inner–jet). We repeat these simulations using an apparent velocity three times larger ($\alpha_{\rm v}$=3).

In Fig.5.10, one simulated light curve is shown for the images A and B, for each size scale factor ($\alpha_{\rm r}$) and velocity scale factor ($\alpha_{\rm v}$). The modulation index and estimated variability time scale between strong microlensing events are listed in Table 5.6.

5.6.3 A comparison with B1600+434

Not only does the modulation index correspond well with that seen for B1600+434–A and B, also the time scale of variability is in the order of several weeks to months (depending on the choice of $\alpha_{\rm v}$; Table 5.6). The similarity between some of the simulated light curves and those observed for B1600+434 is remarkable, knowing that we have not resorted to extreme assumptions.

We therefore regard these simulations as 'proof of principle', showing that mi-

TABLE 5.6— Scaling parameters for 3C120 and results from eight arbitrary simulated light curves. LCs $a-d$ show light curves using the MF B2, whereas LCs $e-h$ show light curves using the MF A7.

LC	α_r	α_v	rms (%)	t_{typ} (d)
a	5.7	1	4.5	∼50
b	5.7	3	5.4	∼15
c	3.7	1	2.6	∼35
d	3.7	3	2.9	∼10
e	5.7	1	6.4	∼50
f	5.7	3	6.7	∼20
g	3.7	1	3.3	∼40
h	3.7	3	3.4	∼15

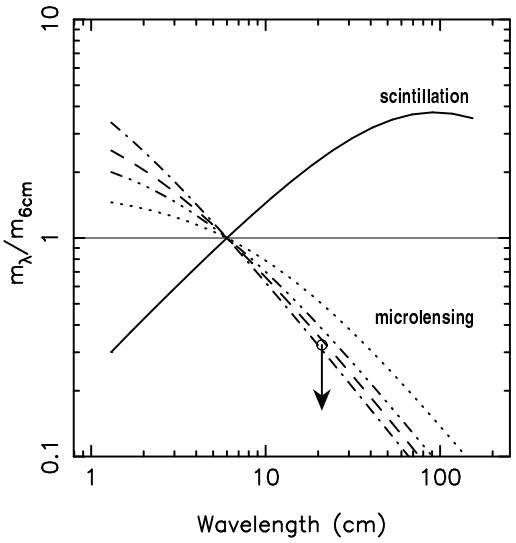

FIGURE 5.11— Dependence of the modulation index from scintillation and microlensing on wavelength. The solid line shows the modulation index from scintillation. The dashed and dot-dashed lines show the modulation indices from microlensing, using $\Delta\theta_{knot}$=2 and 5 μas at 8.5–GHz, respectively, assuming $\Delta\theta_b$=0.9 μas. The dotted and dash-dot-dotted lines indicates the same for $\Delta\theta_b$=4.5 μas. All curves are normalized to the m_{part}=3.7% modulation at 6.0 cm observed with the WSRT in 1999 (Table 5.1). The open circle indicates the upper limit on the ratio m_{21}/m_6 (Table 5.1).

crolensing of multiply–imaged compact flat–spectrum radio sources, of which more and more are being discovered – for example in the CLASS/JVAS survey (e.g Browne et al. 1997; Myers et al. 1999) – can be a very common occurrence, enabling us to study both the structure of these high–z radio sources, as well as the MF of compact objects in the intermediate–z lens galaxies.

5.7 Microlensing versus Scintillation

We have seen many arguments in Sections 5.3–5, for and/or against scintillation and microlensing as the cause of variability in compact flat–spectrum radio sources. Both can in principle explain the observed modulation index and variability time–scales in the VLA 8.5–GHz light curves in the individual lens images of B1600+434, although it remains very difficult to explain the longer ($\gg$1 day) variations in the light curves or the difference in modulation index between the two lens images in terms of scattering. In the case of microlensing, one would expect to see scintillation at some level as well, possibly complicating a straightforward analysis. How can we then separate these mechanisms as the dominant cause of variability?

Scintillation and microlensing have different dependencies on frequency. Although microlensing is achromatic, the frequency dependence of the source structure predicts a clear dependence of the microlensing variability as function of frequency. For flat–spectrum SSA sources, the source size is inverse proportional to frequency (eqn.5.24). Thus the modulation index decreases with decreasing frequency (eqn.5.32). In the case of weak and strong refractive scattering (i.e. flickering), however, the modulation index usually increases with decreasing frequency (e.g. BNR86; Narayan 1992; Rickett et al. 1995). *The key to testing whether the observed short–term variability in gravitationally lensed flat–spectrum radio sources is partly or fully dominated by microlensing or scintillation is therefore their strong opposite dependence on frequency.*

In Fig.5.11, we have plotted the dependence of the modulation index in the case of weak and strong refractive scintillation versus that of microlensing. We assume that the source or jet–component size scales as ν^{-1} and that scatter broadening is negligible. All curves are nor-

malized at $m_{\rm part}$=3.7% at 6 cm, as measured with the WSRT in 1999 (Table 5.1). We determine the modulation index from scintillation following Rickett et al. (1995) and that from microlensing using eqn.5.32. In the case of microlensing, we use the maximum range of the turn–over scale $\Delta\theta_{\rm b}$=0.9–4.5 μas and the jet–component size at 8.5–GHz $\Delta\theta_{\rm knot}$=2–5 μas, found from Tables 5.2 and 5.5. We furthermore assume that the short–term variability is dominated by image A, as observed in the VLA 8.5–GHz light curves. The resulting curves show a clear opposite trend as function of wavelength and therefore act as a strong discriminator between microlensing and scintillation. The constraints on the microlensing curves were determined from the VLA 8.5–GHz light curves only and therefore independent from the WSRT 1.4 and 5–GHz modulation indices.

From these WSRT modulation indices ($m_{\rm part}$) at 1.4 and 5–GHz (Table 5.1), one finds m_{21}/m_6 $\approx$0.31, as indicated by the diamond symbol in Fig.5.11. Although this result is based on two frequencies only, it clearly agrees much better with the predications from microlensing and not that from scintillation! The latter would require a $\sim$8 times larger value for m_{21} (i.e about 9%). We do not plot the VLA 8.5–GHz modulation index, because it was determined from a different epoch. The modulation index from microlensing and scintillation might change as function of time, whereas the ratio of modulation indices, measured simultaneously, is less likely to change.

Thus, if all short–term variability seen in the light curves of B1600+434 is external, it follows the predictions from microlensing. Moreover, if the short–term variability seen in the WSRT 1.4 and 5–GHz light curves is intrinsic, this would be very hard to reconcile with the fact that in 1998 almost all of the VLA 8.5–GHz short–term variability was shown (with 14.6–σ confidence; see Sect.5.2) to be external. The most logical conclusion from all this is that the short–term variability at 1.4, 5 and 8.5–GHz is dominated by microlensing. This explains both the modulation indices as function of frequency at 1.4 and 5–GHz and the longer variability time scale in the VLA 8.5–GHz light curves. In the case of scintillation, one would require either different sizes of the lens images or a very different ionized ISM towards the images and also a different time–scale and frequency–dependence of scattering from that expected from a Kolmogorov spectrum of inhomogeneities of the ionized ISM. All evidence thus far is therefore *only* consistent with microlensing as the dominant cause of the observed short–term variability.

5.8 Summary & Conclusions

We have shown *unambiguous* evidence of external variability in the CLASS gravitational lens B1600+434. The difference between the 8.5–GHz VLA light curves of the two lens images shows external variability at the 14.6–σ confidence level. The modulation indices of the short–term variability are 2.8% for image A and 1.6% for image B. The difference light curve has an rms scatter of 2.8%, indicating that the short–term variability in both light curves is mostly of external origin (Sect.5.2).

We have investigated two plausible sources of this external variability: (i) scattering by the ionized component of the Galactic interstellar medium (ISM) and (ii) microlensing by massive compact objects in the bulge/disk and halo of the lens galaxy.

Based on the 'standard' theory of scintillation (e.g. Narayan 1992) there should be a considerable increase in the modulation index with wavelength (Sections 5.3 and 5.7). From simultaneous WSRT 1.4 and 5–GHz observations we find, however, that m_{21}=1.2% and m_6=3.7% (Table 5.1), which is a considerable decrease. Scintillation theory predict m_{21}=9.0% for m_6=3.7% (Sect.5.7). If the 1.4 and 5–GHz short–term variability is intrinsic, it is hard to reconcile with the fact that in 1998 the VLA 8.5–GHz light curves were dominated by external variability during the full eight months of monitoring (Sect.5.2), although it can not be fully excluded yet. Moreover, from microlensing simulations, we expect that m_{21}=1.2–2.4% if $m_6 = 3.7\%$ (Fig.5.11),

based on constraints on the source structure and mass function of compact objects found from the VLA 8.5–GHz light curves (Sections 5.4, 5.5 and 5.7). This range agrees remarkably well with the observed modulation index $m_{\rm part}$=1.2% at 21 cm.

Supplementary to this argument, the difference in modulation index between the lens images would, in the case of scintillation, argue for either a very different Galactic ionized ISM ($SM_A/SM_B \approx 3.1$; Section 5.3.1–2) towards the lens images or a different image size ($\Delta\theta_B/\Delta\theta_A \approx 1.75$; Sect.5.3.2), although the latter might result from scatter–broadening. Furthermore, the longer variability time scales at 8.5–GHz ($\gg$1 day; Figs 5.1–5.2) are also difficult to explain in terms of scintillation.

However, the strongest argument against scintillation remains the dominant presence of short–term external variability at 8.5–GHz in 1998, combined with the fact that in 1999 significant short–term variability is seen at 5–GHz but almost none at 1.4–GHz.

Under the microlensing hypothesis, we find a consistent, although not unique set of jet–component parameters. A core plus a single–jet–component with a size of 2–5 μas, containing 5–11% of the flux–density and moving superluminally with $9 \lesssim \beta_{\rm app} \lesssim 26$, can explain the modulation index and variability time scale in both lens images (Sections 5.4–5). For image A we find a significantly higher average mass of compact objects ($\gtrsim$0.5 $M_\odot$), compared with those near image B. This lower limit is consistent with a halo filled with compact stellar remnant. A much lower mass of compact object would result in a finer magnification pattern and thus in less variability. If image B is scatter–broadened or dominated by intrinsic source variability, its microlensing modulation index is reduced, which might reduce the lower–limit on the MACHO mass.

However, if one, based on the evidence gathered thus far, accepts that the 1.4, 5 and 8.5–GHz short–term variability in B1600+434–A and B is dominated by microlensing, the profound consequence is that the dark–matter halo at $\sim$6 kpc above the plane of the disk–galaxy lens in B1600+434 is filled with MACHOs, that have a lower mass limit in agreement with stellar remnants, possibly bringing us closer to solving the enigmatic nature of dark matter.

Acknowledgments

The authors especially would like to thank Joachim Wambsganss for making available and giving support in using his microlensing code. They also thank Frank Briggs for providing useful supermongo code and Jane Dennett-Thorpe and Penny Sackett for useful discussions. LVEK and AGdeB acknowledge the support from an NWO program subsidy (grant number 781-76-101). This research was supported in part by the European Commission, TMR Programme, Research Network Contract ERBFMRXCT96-0034 'CERES'. The National Radio Astronomy Observatory is a facility of the National Science Foundation operated under cooperative agreement by Associated Universities, Inc. The National Radio Astronomy Observatory is a facility of the National Science Foundation operated under cooperative agreement by Associated Universities, Inc. The Westerbork Synthesis Radio Telescope (WSRT) is operated by the Netherlands Foundation for Research in Astronomy (ASTRON) with the financial support from the Netherlands Organization for Scientific Research (NWO).

References

Becker, R. H., White, R. L. & Edwards, A. L. 1991, ApJS 75, 1

Biggs, A.D., Browne, I.W.A., Helbig, P., Koopmans, L.V.E., Wilkinson, P.N., Perley, R.A., 1999, MNRAS 304, 349

Blandford, R. D. & Konigl, A. 1979, ApJ 232, 34

Blandford, R., Narayan, R. & Romani, R. W. 1986, ApJL 301, L53 [BNR86]

Browne, et al., 1997, in Cosmology with the new radio surveys, eds. M. Bremer and Jackson, N. J., p305

Chang, K. & Refsdal, S. 1979, Nature 282, 561

Chu, L. B., Baath, F. T., Rantakyroe, F. J., Zhang, H. S. & Nicholson, G. 1996, A&A 307, 15

Clegg, A. W., Fey, A. L. & Lazio, T. J. W. 1998, ApJ 496, 253

Condon, J. J., Ledden, J. E., Odell, S. L. & Dennison, B. 1979, AJ 84, 1
Cordes, J. M., Weisberg, J. M. & Boriakoff, V. 1985, ApJ 288, 221
Cordes, J. M., Ryan, M., Weisberg, J. M., Frail, D. A. & Spangler, S. R. 1991, Nature 354, 121
Dennett–Thorpe, J. & de Bruyn, A. G. 1999, ApJL submitted
Fassnacht, C. D. & Cohen, J. G. 1998, AJ 115, 377
Fassnacht, C.D., Pearson, T.J., Readhead, A.C.S., Browne, I.W.A., Koopmans, L.V.E., Myers, S.T., Wilkinson, P.N., 1999, ApJ accepted
Gomez, J. -L. , Marscher, A. P., Alberdi, A. , Marti, J. M. . & Ibanez, J. M. . 1998, ApJ 499, 221
Gomez, J. -L. , Marscher, A. P., Alberdi, A. 1999, astro-ph/9906199
Gopal-Krishna & Subramanian, K. 1991, Nature 349, 766
Heeschen, D. 1982, IAU Symposia, 97, 327
Heeschen, D. S. 1984, AJ 89, 1111
Holtzman, J. A., Watson, A. M., Baum, W. A., Grillmair, C. J., Groth, E. J., Light, R. M., Lynds, R. & O'Neil, E. J. , Jr. 1998, AJ 115, 1946
Irwin, M. J., Hewett, P. C., Corrigan, R. T., Jedrzejewski, R. I. & Webster, R. L. 1989, AJ 98, 1989
Jackson, N., et al. 1995, MNRAS 274, L25
Jaunsen, A. O. & Hjorth, J. 1997, A&A 317, L39
Kellermann, K. I. & Pauliny-Toth, I. I. K. 1969, ApJL 155, L71
Koopmans, L. V. E., De Bruyn, A. G. & Jackson, N. 1998, MNRAS 295, 534 [KBJ98]
Koopmans, L. V. E., De Bruyn, A. G., Xanthopoulos, E. & Fassnacht, C. D. 1999, A&A submitted [KBXF99]
Koopmans, L. V. E. & Fassnacht, C. D. 1999, ApJ 527, in press
Kormann, R., Schneider, P. & Bartelmann, M. 1994, A&A 284, 285
Kraus, A., et al. 1999, A&A 344, 807
Kundić, T., et al., 1997, ApJ 482, 75
Lewis, G. F. & Williams, L. L. R. 1997, MNRAS 287, 155
Lovell, J. E. J., Jauncey, D. L., Reynolds, J. E., Wieringa, M. H., King, E. A., Tzioumis, A. K., McCulloch, P. M., Edwards P. G., 1998, ApJ 508, L51
Myers, S. T., et al. 1999, in preparation
Miller, G. E. & Scalo, J. M. 1979, ApJS 41, 513
Narayan, R. 1992, Phil. Trans. Roy. Soc., 341, 151
O'Dell, S. L., Puschell, J. J., Stein, W. A., Owen, F., Porcas, R. W., Mufson, S., Moffett, T. J. & Ulrich, M. -H. e. 1978, ApJ 224, 22
Patnaik, A. R., Menten, K. M, Porcas, R. W., Kemball, A. J. 1999, in preparation
Pelt, J., Kayser, R., Refsdal, S. & Schramm, T. 1996, A&A 305, 97
Quirrenbach, A., Witzel, A., Krichbaum, T., Hummel, C. A. & Alberdi, A. 1989, Nature 337, 442
Quirrenbach, A., et al. 1998, American Astronomical Society Meeting, 192, 3603
Readhead, A. C. S. 1994, ApJ 426, 51
Rengelink, R. B. n. a. 1997, Tang, Y., De Bruyn, A. G., Miley, G. K., Bremer, M. N., Roettgering, H. J. A. & Bremer, M. A. R. 1997, A&ASS 124, 259
Rickett, B. J. 1977, ARA&A 15, 479
Rickett, B. J. 1990, ARA&A 28, 561
Rickett, B. J., Coles, W. A. & Bourgois, G. 1984, A&A 134, 390
Rickett., A., Quirrenbach, B. J., Wegner, R., Krichbaum, T. P. & Witzel, A. 1995, A&A 293, 479
Romero, G. E., Surpi, G. & Vucetich, H. 1995, A&A 301, 641
Salpeter, E. E. 1955, ApJ 121, 161
Schechter, P.L., et al., 1997, ApJL 475, L85
Schneider, P. , Ehlers, J. & Falco, E. E. 1992, Gravitational Lenses, Springer-Verlag Berlin Heidelberg New York.
Schramm, K. -J. m. a. et al. 1993, A&A 278, 391
Simonetti, J. H., Cordes, J. M. & Heeschen, D. S. 1985, ApJ 296, 46
Stickel, M., Fried, J. W. & Kuehr, H. 1988, A&A 198, L13
Takalo, L. O., et al. 1998, A&ASS 129, 577
Taylor, J. H. & Cordes, J. M. 1993, ApJ 411, 674
Timmes, F. X., Woosley, S. E. & Weaver, Thomas A. 1996, ApJ 457, 834
Vermeulen, R. C. & Cohen, M. H. 1994, ApJ 430, 467
Wagner, S. J. & Witzel, A. 1995, ARA&A 33, 163
Wagner, S. J., et al. 1996, AJ 111, 2187
Walker, M. A. 1998, MNRAS 294, 307 [W98]
Wambsganss, J. 1990, Thesis Ludwig-Maximilians-Univ., Munich (Germany, F.R.). Fakultaet fuer Physik., 2300
Watson, D., et al. 1999, A&A 345, 414

6

A determination of H_0 with CLASS B1608+656

Originally published as L.V.E. Koopmans & C.D. Fassnacht, 1999, Astrophysical Journal, in press

We present mass models of the four–image gravitational lens system B1608+656, based on information obtained through VLBA imaging, VLA monitoring and *Hubble Space Telescope* (HST) WFPC2 and NICMOS imaging. A mass model for the lens galaxies has been determined that reproduces (i) all image positions within the observational errors, (ii) two out of three flux–density ratios within about 10% from the observed ratios and (iii) the model time delays within 1% from their observed values, given our best estimate of the Hubble parameter. Using the time delays determined by Fassnacht et al. (1999), we also find that the best isothermal mass model gives H_0=59^{+7}_{-6} km s^{-1} Mpc^{-1} for $\Omega_{\rm m}$=1 and Ω_Λ=0.0, or H_0=$(65-63)^{+7}_{-6}$ km s^{-1} Mpc^{-1} for $\Omega_{\rm m}$=0.3 and Ω_Λ=0.0–0.7. The statistical errors indicate the 95.4% (2–σ) confidence interval. A systematic error of ± 15 km s^{-1} Mpc^{-1} is estimated from a 20% (1–σ) uncertainty in the steepness of radial mass profile. This cosmological determination of H_0 agrees well with determinations from three other gravitational lens systems (i.e. B0218+357, Q0957+561 and PKS1830-211), Type Ia Supernovae, the Sunyaev-Zel'dovich effect and local determinations. The current agreement on H_0 – within the 1–σ statistical errors – from four out of five gravitational lens systems (i) emphasizes the reliability of its determination from isolated gravitational lens systems and (ii) suggests that a close-to-isothermal mass profile can describe disk galaxies (e.g. B0218+357 and possibly PKS1830-211), ellipticals (e.g. B1608+656) and central cluster ellipticals (e.g. Q0957+561). The average of H_0 from B0218+357, Q0957+561, B1608+656 and PKS1830-211, gives $H_0^{\rm GL} = 69 \pm 7$ km s^{-1} Mpc^{-1} for a flat universe with $\Omega_{\rm m}$=1 or $H_0^{\rm GL}$=74±8 km s^{-1} Mpc^{-1} for $\Omega_{\rm m}$=0.3 and Ω_Λ=0.0–0.7. When including PG1115+080, these values decrease to 64±11 km s^{-1} Mpc^{-1} and 68±13 km s^{-1} Mpc^{-1}, respectively. The errors are the estimated 2–σ errors on the average. The Hubble parameter from gravitational lenses seems to agree best with local determinations of H_0 for a low density universe, under the assumption that all lenses are nearly isothermal.

6.1 Introduction

Since the discovery of the first gravitational lens Q0957+561 (Walsh, Carswell & Weymann 1979), there has been considerable interest in monitoring the radio and optical emission of its lens images (a quasar at z=1.41), in order to find correlations between their light curves. Strong correlations can give a time delay between the

images and definitively prove that they are lensed images of one background object. Already in 1964 it was shown that such a time delay can be used to constrain the Hubble parameter (H_0), if a good lens mass model can be found (Refsdal 1964).

For Q0957+561 several long-term monitoring programs finally resulted in a robust determination of the time delay (e.g. Kundić et al. 1997). Combined with the lens mass model a value of H_0=63±12 km s^{-1} Mpc^{-1} (95% confidence) was determined (Kundić et al. 1997). However, a new interpretation of the data shed some doubt on the reliability of the confidence levels quoted for the mass models (Barkana et al. 1999), and a new determination the velocity dispersion of the cluster lens by Tonry & Franx (1999) increased the value of H_0 to 70±7 or 72±7 km s^{-1} Mpc^{-1} (1–σ), using the SPLS or FGS models from Grogin & Narayan (1996a, 1996b), respectively. All values of H_0 are given for a flat universe with Ω_m=1, if not specified otherwise.

Three other gravitational lens systems have also yielded values of H_0. From the gravitational lens PG1115+080 (Weymann et al. 1980) a value of H_0=44±4 km s^{-1} Mpc^{-1} (1–σ) was determined (Impey et al. 1997) using the time delays found by Schechter et al. (1997) and an isothermal lens mass model. The gravitational lens system resides near a compact group of galaxies (Kundić 1997; Tonry 1998), which complicates the mass model considerably.

The time delay in B0218+357 (e.g. Patnaik et al. 1993) was recently determined by Biggs et al. (1998) to within 4% accuracy (95% confidence). This significantly reduced the uncertainty compared with a previous determination by Corbett et al. (1996). Preliminary modeling of this system gave $H_0=69^{+13}_{-19}$ km s^{-1} Mpc^{-1} (95% confidence), using an isothermal mass model to describe the lens galaxy (Biggs et al. 1998).

Very recently the time delay in PKS1830-211 (e.g. Jauncey et al. 1991) was determined (Lovell et al. 1998). Combined with the detailed mass model from Nair, Narasimha & Rao (1993) and the source redshift found by Lidman et al. (1998), a value of $H_0=65^{+16}_{-9}$ km s^{-1} Mpc^{-1} (1–σ) was determined (Lovell et al. 1998; Lovell, private communication). When using an isothermal mass model on the galaxy position from Nair et al. (1993) we estimate $H_0=75^{+18}_{-10}$ km s^{-1} Mpc^{-1} (1–σ).

Using the same lens mass model for all five gravitational lens systems makes a more consistent comparison of H_0 from these systems possible (Schechter 1998), especially if their radial mass profile is ill-constrained. We have chosen to use the isothermal mass model.

In sections 6.2 and 6.3 we will briefly discuss the observational status of B1608+656 and new observations that are used in this paper. Section 6.4 introduces the mass distribution and the procedure that is used to solve for the mass model parameters and the Hubble parameter. In section 6.5, the results for different mass models are presented. In section 6.6, a determination of the Hubble parameter from B1608+656 is given. In section 6.7 this estimate is compared with determinations from other gravitational lens systems and in section 6.8 with determinations from Type Ia Supernovae and the Sunyaev-Zel'dovich effect and the local determination of H_0. The conclusions are summarized in section 6.9.

The observed time delays between the lens images in B1608+656 are presented in the companion paper by Fassnacht et al. (1998; hereafter Paper I).

6.2 The four-image gravitational lens B1608+656

The four-image gravitational lens system B1608+656 was discovered by the *Cosmic Lens All Sky Survey* collaboration (CLASS; Myers et al. 1995; Myers et al. 1999, in preparation) and independently by Snellen et al. (1995).

The goal of CLASS is to compose a statistically complete sample of radio-selected gravitational lenses, for which the selection effects are well understood (Browne et al. 1998). For this purpose all flat-spectrum ($\alpha<0.5$ with $S_\nu \propto \nu^{-\alpha}$) radio sources brighter than 25 mJy at 5 GHz were selected between declinations 0 and 75 de-

grees (Browne et al. 1998). These sources (≈12,000 in total) were observed with the VLA in A-array at 8.4-GHz. Promising lens candidates were followed-up with MERLIN and/or the VLBA. So far at least 12 new gravitational lens systems were found (e.g. Jackson et al. 1998; Browne et al. 1998).

The lensed object in B1608+656 is the nucleus of radio galaxy at a redshift z_s=1.394 (Fassnacht et al. 1996) which has a radio luminosity in the transition range between Fanaroff-Riley Class I and II galaxies (Fanaroff & Riley 1974, Snellen et al. 1995; Fassnacht et al. 1996). The primary lens galaxy has a redshift z_l=0.6304 (Myers et al. 1995). Additional multi-frequency observations with several radio telescopes (VLA, MERLIN, VLBA) and HST were done. The relevant results will be summarized in section 6.3.

Flat-spectrum radio sources are often variable. This is one of the prerequisites for determining the time delay between lens images and constraining H_0 (Refsdal 1964). The lensed object in B1608+656 is compact and has varied ≈20% in flux density (8.4-GHz) on time scales of weeks to months (Fassnacht 1997). Thus, a seven-month monitoring campaign was started with the VLA in A- and B-arrays during the 1996–1997 season to determine time delays between the image-pairs (Paper I). The obtained time delays, flux density ratios and additional radio and optical data from B1608+656 will be used in this paper to constrain the mass model of this gravitational lens system, culminating in an estimate of the Hubble parameter.

6.3 Data

Most of the observations and data summarized in this section will be presented in Fassnacht et al. (2000, in preparation). The image light curves, time delays and flux density ratios from the VLA 8.4-GHz monitoring campaign are presented in the companion paper (Paper I).

6.3.1 Image positions

From deep VLBA 5-GHz observations of B1608+656 very precise relative positions of the four lens images were obtained (Fassnacht et al. 2000, in preparation). The results are listed in Table 6.1. The four images are compact and show no extended structure on scales $\gtrsim$1 mas. Data reduction and image fitting was done in the NRAO data reduction package *AIPS*. The statistically expected errors on the image positions are approximately the FWHM of the restoring beam dived by the signal-to-noise of the component (Table 6.1).

6.3.2 Flux density ratios and time delays

The light curves of the four lens images can give (i) the time delays, if correlations between the light curves are found, and (ii) the 'true' flux density ratios between the lens images, after correction for the time delays.

The exact procedure and results from the VLA 8.4-GHz monitoring campaign of B1608+656 are described in the companion paper (Paper I). In Table 6.1, we list the obtained results. We use the flux density ratios and time delays to constrain the lens mass models of B1608+656. The errors on the time delays are between 12% and 23% (2–σ), determined from Monte-Carlo simulations (Paper I).

The errors on the flux density ratios are about 0.002, determined from the same Monte-Carlo simulations. Systematic differences between the light curves, however, appear appreciably larger than the error on the individual light-curve points, because the reduced χ^2 between the light curves is always significantly larger than unity (Paper I). Because the flux density ratios are most sensitive to small changes in the lens potential (e.g. milli-lensing, micro-lensing in the case of a very compact source ($\ll$1 mas), the presence of small nearby companions to the lens galaxies, etc.), small-scale scintillation or systematic self-calibration errors, we will conservatively assume an error of 0.02 on the flux density ratios, which is approximately the scatter between the individual points of each light curve. In Koopmans & de Bruyn (1999) it is shown that a few percent variability in radio light curves at 8.4-GHz can be expected for weak flat-spectrum radio sources, due

Image	A	B	C	D
x_i^o ($''$)	$\equiv$0.0000	-0.7380	-0.7446	+1.1284
y_i^o ($''$)	$\equiv$0.0000	-1.9612	-0.4537	-1.2565
δx_i (mas)	0.0023	0.0043	0.0045	0.0107
δy_i (mas)	0.0023	0.0046	0.0049	0.0124
$r_i^o = S_\nu^i / S_\nu^{\rm A}$	$\equiv$1.000	0.490	0.508	0.172
δr_i	$\equiv$0.000	0.020	0.020	0.020
t_i^o (d)	30	$\equiv$0	36	76
δt_i (d)	+7/-7	$\equiv$0	+7/-7	+9/-10

TABLE 6.1— Properties of the radio lens images of B1608+656. The positions were determined from VLBA observations (Fassnacht et al. 2000, in preparation). The coordinate system is Cartesian with the positive x-axis pointing west. The errors are the formal 1–σ errors (FWHM of the beam divided by the signal-to-noise) from the VLBA data. The flux density ratio and time delays were determined from the VLA monitoring observations (Paper I). The errors on the time delays (95% confidence) were determined from Monte-Carlo simulations. The errors on the flux density ratios are assumed larger than the formal Monte-Carlo errors for reasons given in section 6.3.2.

to micro-lensing A few-percent error on the flux-density ratios is already a considerable improvement on the 20% error used in previous models (e.g. Keeton 1997).

6.3.3 The lens galaxies

Hubble Space Telescope (HST) exposures were obtained of B1608+656, both with the WFPC2 (F555W and F814W) and NICMOS (F160W). The F814W exposure of B1608+656 is presented in Jackson et al. (1998) and Fassnacht et al. (2000, in preparation). The F555W and F160W exposures will be presented in Fassnacht et al. (2000, in preparation).

All three exposures show four optical lens images and two objects confined in the region between the lens images. These objects remain distinctly separated in the F555W, F814W and F160W exposures. We assume they are two individual lens galaxies, perhaps merging (Jackson et al. 1997; Fassnacht et al. 2000, in preparation). Long-slit spectroscopy with the Keck telescope along the two galaxies (G1 and G2) shows no sign indicating different redshifts. Another similar two–lens gravitational lens system (i.e. B1127+385) was recently found by the CLASS collaboration (Koopmans et al. 1999), although it only has two lens images. All three HST exposures (F555W, F814W and F160W) of B1608+656 can be found on the Castles web-page (*http://cfa-www.harvard.edu/glensdata/B1608.html*) as well.

The relative positions (centroid) of the lens images and lens galaxies were determined in *IRAF*[1] with respect to the brightest optical image (A). The optical image positions agree with the radio positions to within the observational errors of $\approx$5 mas. The lens galaxy positions and their errors are listed in Table 6.2. The galaxy centroids change as function of wavelength (i.e. between F555W, F814W and F160W), possibly suggesting that G1 and G2 are interacting dynamically (see section 6.5.3). The galaxy positions are used as additional constraints on the lens mass model.

The surface brightness distributions of G1 and G2 were fitted with elliptical isophotes in *IRAF*. The range of axis ratios and position angles of the elliptical isophotes are listed in Table 6.2.

[1] IRAF (Image Reduction and Analysis Facility) is distributed by the National Astronomy Observatories, which are operated by the Association of Universities for Research in Astronomy under cooperative agreement with the National Science Foundation.

	x_c ($''$)	y_c ($''$)	P.A. ($^\circ$)	$\left(\frac{a}{b}\right)_\Sigma$
G1				
F555W	0.544	-1.060	77→84	≈0.45
F814W	0.521	-1.062	81→77	0.45→0.60
F160W	0.446	-1.063	85→76	–
G2				
F555W	-0.337	-0.976	–	–
F814W	-0.293	-0.965	≈ 75	0.12→0.40
F160W	-0.276	-0.937	–	–

TABLE 6.2— Surface brightness distribution parameters of the lens galaxies G1 and G2. The surface brightness centroid is given by (x_c, y_c), with an estimated error of 15 mas. The surface brightness position angle (P.A; from north to east) and axis ratio ($\left(\frac{a}{b}\right)_\Sigma$) were determined in *IRAF* by fitting elliptical isophotes as function of radius to the surface brightness distributions of G1 and G2. The range of positions angles (P.A.) and axis ratios from the inner to the outer isophotes is indicated by the arrow. The coordinate system is Cartesian with positive x-axis pointing west.

6.4 Modeling

6.4.1 The lens mass model

We describe the surface mass distribution of the two lens galaxies with the parameterized elliptical isothermal mass model from Kormann, Schneider & Bartelmann (1994). The surface density distribution of these models is given by

$$\Sigma(\xi_1, \xi_2) = \frac{\sigma^2}{2G} \frac{\sqrt{f}}{\sqrt{\xi^2 + \xi_c^2}}, \qquad (6.1)$$

where ξ^2=$\xi_1^2 + f^2\xi_2^2$, σ is a measure of the line-of-sight velocity dispersion, ξ_c is the lens core radius and f=$(a\ /b)_\Sigma$ is the surface density axis ratio. All lengths and positions will from now on be given in arcseconds. The deflection angles and shear components of this mass model are also given in Kormann et al. (1994). It is simple to transform the mass distribution and corresponding deflection and shear fields to any required position and position angle.

We will refer to the (non-)singular isothermal ellipsoidal case as the (NIE) SIE mass distribution. We assume Ω_m=1 and Ω_Λ=0 in a smooth FRW universe, if not specified otherwise. In section 6.5.4 we discuss non-isothermal mass models.

6.4.2 χ^2 minimization

We use a χ^2-minimization procedure to search for the free parameters (mass model parameters, source position and Hubble parameter) that best reproduce the observed image positions, flux density ratios and time delays (Table 6.1). The χ^2-function that is minimized is given by

$$\begin{aligned}\chi^2 \;=\; & \sum_{i=1}^{4} \left[\frac{(x_i^o - x_i^m)^2}{\delta x_i^2} + \frac{(y_i^o - y_i^m)^2}{\delta y_i^2} \right] + \\ & \sum_{i=1}^{4} \left[\frac{(r_i^o - r_i^m)^2}{\delta r_i^2} \right] + \\ & \sum_{i=1}^{4} \left[\frac{(t_i^o - t(h)_i^m)^2}{\delta t_i^2} \right]. \end{aligned} \qquad (6.2)$$

The first term on the right-hand side of the equation gives the 'goodness-of-fit' between the observed, $(x,y)_i^o$, and model, $(x,y)_i^m$, image positions, where $\delta(x,y)_i$ are the 1–σ errors on the observed image positions. The second term gives the goodness-of-fit between the observed, r_i^o, and model, r_i^m, flux density ratios. Because the flux density of the lensed object is a free parameter, we normalize the flux density of the brightest observed and model image (i=1) to unity. The third term gives the goodness-of-fit between the observed, t_i^o, and model, t_i^m, time delays. The error on the observed

time delay is given by δt_i. We normalize the time delay of the leading image to zero. The model time delay is a function of the free parameter $h = H_0/(100\ \mathrm{km\ s^{-1}\ Mpc^{-1}})$. Thus, minimizing χ^2 gives not only the mass model parameters and source position, but also a measure of the Hubble parameter, H_0.

A continuous Simulated Annealing Downhill-Simplex algorithm is used to minimize χ^2 (Press et al. 1992). Although relatively slow, this method is robust and allows simple adjustment of χ^2 during the minimization. It also has a high probability of finding the global χ^2–minimum compared with faster methods that need the gradients of a complex multi-dimensional χ^2–function. The latter is of great importance if we search for the minimum–χ^2 solution in a space of many free parameters ($\gtrsim$10).

6.5 Results

We investigate several different isothermal and non-isothermal mass models in an attempt to reproduce the observed properties of B1608+656 (Table 6.1). The two lens galaxies (G1 and G2) are fixed at their observed positions (Table 6.2). The HST exposures were done using different filters (F555W, F814W and F160W), each giving slightly different galaxy positions. Models with the lens galaxies fixed at the positions determined from each filter are therefore considered.

It should also be noted that the resulting model flux density ratio of image D (r_{D}) is the only parameter never close to the observed value, throughout all mass models. The magnification depends critically on a combination of second order derivatives of the lens potential and small perturbations can therefore significantly change flux ratios. The delays and positions directly depend on zeroth and first order derivatives of the lens potential, respectively. Hence, they are less sensitive to perturbations by small masses (e.g. Mao & Schneider, 1998). Both the delay and position of image D are in excellent agreement with observations.

For each filter we construct four mass models: (I) SIE+SIE, using all constraints, (II) SIE+SIE, without r_{D} as a constraint, (III) SIE+NIE, using all constraints and (IV) SIE+NIE, without r_{D} as a constraint. Mass models V and VI, presented in section 6.5.4, are non-isothermal.

6.5.1 SIE+SIE mass model

The first attempt is to model both G1 and G2 with a SIE mass distribution. In total there are 14 constraints (8 from the image positions, 3 from the flux density ratios and 3 from the time delays) and 9 free parameters (source position, Hubble parameter, velocity dispersions, surface density axis ratios and position angles of G1 and G2). The number of degrees of freedom (NDF) is five. This should give a well constrained set of free parameters, if they are non-degenerate.

Using all constraints, we minimize χ^2 for the three sets of galaxy positions (Table 6.2). The resulting model parameters, minimum-χ^2 and Hubble parameters are listed in Table 6.3 (model I). Using different starting values for the model parameters and a slowly decreasing 'temperature' in the Simulated Annealing algorithm (see Press et al. (1992) for a more detailed description of this minimization procedure), we ensure a very high probability of ending up at the global χ^2–minimum.

The minimum–χ^2 value is significantly smaller when the HST WFPC2 F555W galaxy positions are used, in comparison with those from the WFPC2-F814W or NICMOS-F160W observations.

The χ^2–minimization is repeated, this time without the use of the flux density ratio of image D as a constraint. The resulting model and Hubble parameters (Table 6.3; models II) are similar to models I, but χ^2 has decreased more than expected on the basis of the decreased number of degrees of freedom (NDF=4). The flux density ratio of image D contributes disproportionally to χ^2 compared with the other constraints, possibly due to a local perturbation of the lens potential (e.g. milli- or micro-lensing).

Lens model F555W-II has the smallest χ^2 value of all SIE+SIE mass models in Table 6.3. Figure 6.1 (left) shows both the critical-

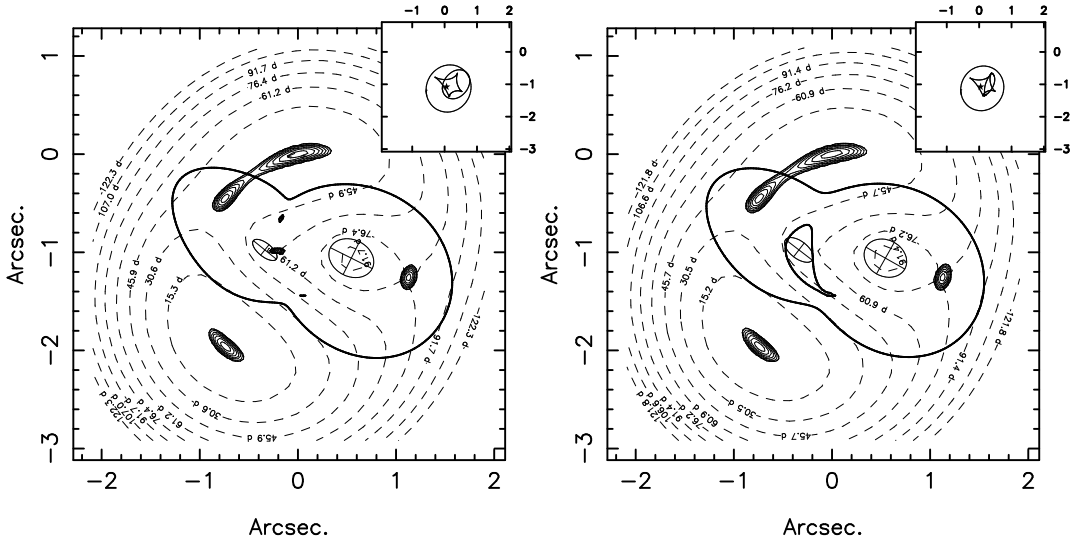

FIGURE 6.1— Left: Time-delay surface (dashed lines), critical curves (thick lines) and caustic structure (sub-panel) of the SIE+SIE lens model F555W-II. The lens images are the projections onto the image plane of a Gaussian shaped source (star) with a FWHM of 0.1 arcsec. The cross-haired ellipses indicate the position, axis-ratio and position angle of G1 and G2. Right: Idem, but for the SIE+NIE mass model F555W-IV.

curve and caustic structure of this model and its time-delay surface. When moving a source from outside the caustic structure – e.g. where the source is singly imaged – the number of lens images changes by two, each time a caustic is crossed. We therefore expect the SIE+SIE models to show seven images, of which two are highly demagnified, because they are located near the surface density singularities of G1 and G2.

However, the fifth image should be visible. It is formed on the saddle point of the time-delay surface near galaxy G2 (Figure 6.1). Its magnification is around 0.2. This should make it visible ($\gtrsim$50–σ detection) in the deep VLA A-array observations available to us (Paper I). The image, however, is not detected, which poses a strong restriction on the allowed set of models.

6.5.2 SIE+NIE mass model

The primary reason to introduce a small core radius for G2 is to remove the fifth image formed at the saddle-point of the time-delay surface between G1 and G2 (Figure 6.1). If the core radius is large enough, there are no extrema on the time-delay surface and thus no images will form between G1 and G2 (e.g. Schneider et al. 1992).

We minimize χ^2 again for the three sets of galaxy positions. The core radius of G2 is left free (NDF=4; models III). We repeat this without $r_{\rm D}$ as a constraint (NDF=3; models IV). The resulting model parameters and Hubble parameters are listed in Table 6.3. Lens model F555W-IV is shown in Figure 6.1 (right). The recovered image positions, flux density ratios and time delays from model F555W-IV are listed in Table 6.5.

A significant improvement in the reduced χ^2 is obtained with models IV over models II (no core radius for G2) and models I and III (with $r_{\rm D}$ as constraint). There is also a decrease in the reduced χ^2 from models F160W-IV to F555W-IV. This suggests that the mass centers of G1 and G2 are more closely associated with the emission centroids from the HST F555W exposure.

The source now only crosses two caustics, when moving it from outside the caustic structure to its model position shown in Figure 6.1 (right). Thus five images instead of seven are formed. This solves the 'central-image' problem, even though no lower limit on the core radius of G2 was imposed. One of the five images

Model	σ (km s^{-1})	$(b/a)_\Sigma$	θ_{PA} (°)	r_c ($''$)	$\Delta t^{(A-B)}$	$\Delta t^{(C-B)}$	$\Delta t^{(D-B)}$	H_0^χ	χ^2	χ^2/NDF
F555W-I	253.1, 201.1	0.78, 0.45	63.4, 51.2	0.000, 0.000	18.9 h^{-1}	22.5 h^{-1}	47.8 h^{-1}	62.5	48.1	9.6
F555W-II	253.1, 201.1	0.78, 0.45	63.4, 51.2	0.000, 0.000	18.9 h^{-1}	22.5 h^{-1}	47.8 h^{-1}	62.5	15.6	3.9
F555W-III	248.8, 210.7	0.80, 0.50	61.5, 52.0	0.000, 0.036	18.3 h^{-1}	21.8 h^{-1}	45.8 h^{-1}	60.1	44.2	11.1
F555W-IV	246.9, 214.9	0.81, 0.51	60.6, 52.3	0.000, 0.052	18.0 h^{-1}	21.4 h^{-1}	44.9 h^{-1}	59.0	9.4	3.1
F814W-I	248.2, 207.2	0.88, 0.39	71.9, 53.1	0.000, 0.000	19.2 h^{-1}	23.2 h^{-1}	45.7 h^{-1}	61.6	159.7	31.9
F814W-II	248.2, 207.2	0.88, 0.39	71.9, 53.1	0.000, 0.000	19.2 h^{-1}	23.2 h^{-1}	45.7 h^{-1}	61.6	53.5	13.4
F814W-III	240.1, 223.8	0.93, 0.47	63.0, 54.8	0.000, 0.058	18.2 h^{-1}	21.9 h^{-1}	42.4 h^{-1}	57.7	141.2	35.3
F814W-IV	233.3, 237.2	0.96, 0.52	36.3, 55.9	0.000, 0.105	17.3 h^{-1}	20.7 h^{-1}	39.4 h^{-1}	54.2	22.4	7.5
F160W-I	249.5, 207.1	0.90, 0.31	122.0, 53.8	0.000, 0.000	19.6 h^{-1}	24.2 h^{-1}	41.0 h^{-1}	59.7	622.7	124.5
F160W-II	249.5, 207.1	0.90, 0.31	122.0, 53.8	0.000, 0.000	19.6 h^{-1}	24.2 h^{-1}	41.0 h^{-1}	59.7	172.0	43.0
F160W-III	236.8, 230.8	0.87, 0.42	-25.3, 57.3	0.000, 0.073	18.9 h^{-1}	22.9 h^{-1}	37.7 h^{-1}	57.7	478.9	119.7
F160W-IV	216.8, 266.6	0.70, 0.54	-13.8, 61.1	0.000, 0.183	17.2 h^{-1}	20.5 h^{-1}	29.2 h^{-1}	48.1	19.2	6.4

TABLE 6.3— Isothermal mass model parameters of G1 and G2 and determinations of H_0. Listed are the velocity dispersion (σ), surface density axis ratio $\left(\frac{a}{b}\right)_\Sigma$, position angle ($\theta_{PA}$; north to east) and core radius (r_c). The first value is for G1, the second for G2. The time delays Δt (in days) are the values determined from the mass model. H_0^χ (in km s^{-1} Mpc^{-1}) was determined through the minimization of χ^2 as discussed in section 6.4.2. The last two columns show the minimum–χ^2 and reduced–χ^2 values, respectively. We assume $\Omega_m = 1$ and $\Omega_\Lambda = 0$ in this table.

forms near the surface density singularity of G1 and is highly de-magnified, because the magnification is almost inversely proportional to the surface density close to the singularity (Kormann, Schneider & Bartelmann 1994). Only four observable lens images remain, as is required by the observational constraints.

6.5.3 Models with constrained position angles

Comparing the mass model position angles of G1 and G2 (Table 6.3), with the observed surface brightness position angles (Table 6.2), we see a systematic ≈20 degree difference.

We attempted several models with position angles for G1 and G2 in the range indicated in Table 6.2. The lens galaxy positions were not constrained and they were allowed to have a finite core radius. Even though the system is close to being underconstrained, no satisfactory solutions with position angles close to those listed in Table 6.2 could be obtained (i.e. $\chi^2 \gg 10^6$).

The ≈20 degree difference in position angle between surface brightness and surface density of G1 and G2 therefore remains. There are several possible solutions: (i) The lens galaxies (G1 and G2) have tri-axial halos, producing a misalignment between surface brightness and the projected surface density of the dark matter halo (Keeton, Kochanek & Seljak 1997). (ii) A dynamical interaction between G1 and G2 could introduce a physical misalignment between the halo and the luminous matter. A 'merger' scenario could explain why G1 and G2 look like post-starburst galaxies (Myers et al. 1995) and have much bluer colors than expected for ellipticals (Keeton et al. 1998; Fassnacht et al. 2000, in preparation). Star-formation associated with the deepest part of the lens potential would also explain why the galaxy positions from the HST F555W exposure seem most closely associated with the lens mass centers, although extinction by dust could make this argument more complicated. (iii) External mass components can create the presence of an external shear near G1 and G2, which introduces an apparent misalignment of surface brightness and density position angles (Keeton, Kochanek & Seljak 1997). B1608+656 is part of a small group of galaxies (Fassnacht et al. 2000, in preparation). However, based on their luminosities, these galaxies do not seem massive enough to cause significant perturbations of the lens potential. Moreover, we have added an external shear to our best isothermal mass model

(F555W-IV; Table 6.3) and find no decrease in χ^2, eventhough NDF decreases by two. (iv) The group of galaxies (including G1 and G2) is associated with inter-galactic gas. This is often seen in Hickson compact groups (Hickson 1982) through X-ray emission (e.g. Pildis, Bregman & Evrard 1995). Although the group of galaxies associated with B1608+656 is not very compact or massive, some gas could still be associated with it. If this gas 'halo' is misaligned with G1 and G2, the inferred surface density position angles can deviate from the surface brightness position angles, if the gas is not accounted for in the mass model.

In the cases (iii) and (iv), it remains peculiar that all image positions, time delays and two out of the three flux density ratios are reconstructed relatively well by the best mass model (F555W-IV). This is hard to understand if a large-scale mass component or external shear is missing from the mass model. We therefore prefer either a tri-axial halo for G1 and G2 or a misalignment of the halo and the luminous matter due to dynamical interactions of G1 and G2. Both can explain the misalignment in position angle without invoking new mass components.

6.5.4 Non-isothermal mass models

To investigate the validity of using an isothermal mass distribution, we also tested models with surface density profiles given by

$$\Sigma(\xi_1,\xi_2) = \frac{\Sigma_0}{\left[1+\left(\frac{\xi^2}{\xi_c^2}\right)\right]^{-\gamma}}. \qquad (6.3)$$

The normalization of Σ_0 is chosen to agree with that of eqn. (6.1) for γ=1/2 (the isothermal model). The mass inside some arbitrary radius diverges for profiles with $\gamma>1/2$ and ξ_c=0. We therefore place a lower limit of 10^{-3} arcsec on the core radii of both G1 and G2. Both galaxies are placed on the observed F555W galaxy positions, which seem to best represent their mass centers (section 6.5.1). We use the code developed by Barkana (1998) to calculate the deflection angle and magnification for models with $\gamma\neq1/2$.

Constraints on the radial mass profile

Using all observational constraints, we minimize χ^2 as described in sections 6.5.1–3 (model F555W-VI). The mass distributions of G1 and G2 are given the same value of γ. We repeat this without flux ratio r_D as a constraint (model F555W-V). The model parameters, Hubble parameters and minimum-χ^2 values are listed in Table 6.4.

The table shows that χ^2 minimizes in the range $\gamma\approx$0.4–0.6, taking both models F555W-V and F555W-VI into account. The use of r_D as constraint (model F555W-VI) increases the χ^2 values by a factor of about 10. If we assume that r_D is correct and one of the other three images has an incorrect flux density ratio, we still find a comparable increase in χ^2. So for all models in this range of mass profiles, r_D is the only observable that can not be reasonably matched to its observed value. The inclusion of r_D as a constraint changes γ of the best model from about 0.4 to 0.6. The lowest values of r_D that we find is 0.24 for model F555W-VI with γ=0.6. Thus, keeping in mind that r_D could be larger than 0.17 – preferred by all models (independent of γ) – the value of γ=0.6 can be overestimated.

When $\gamma<$0.5, the position angle of G1 rapidly decreases until a prolate halo is preferred with $\theta_{PA,G1}\approx-(5-11)$ degrees for γ=0.3. Values of γ much smaller than 0.5 are therefore on the basis of comparison with the surface brightness positions angle not very likely. Moreover, for $\gamma\leq$0.4 all minimum–χ^2 models form a fifth central image, similar to the SIE+SIE models (section 6.5.1). This is not the case for $\gamma\geq$0.5.

The range of $\gamma\approx$0.4–0.6 for G1 and G2 agrees with constraints on γ from the gravitational lenses Q0957+561 (Grogin & Narayan 1996a; Barkana et al. 1999) and MG1654+1346 (Kochanek 1995). The models for both of these prefer values close to γ=0.5 (i.e. isothermal).

The radial mass profile and the Hubble parameter

In Figure 6.2, we plot H_0 versus γ. For models F555W-V, H_0 increases from 27 to 57 km s^{-1} Mpc^{-1} between γ=0.3 and 1.0. For

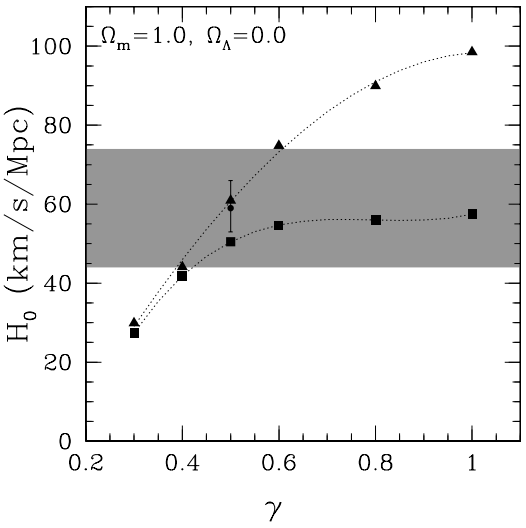

FIGURE 6.2— The Hubble parameter H_0 from B1608+656 plotted against the profile parameter γ for the minimum-χ^2 mass model. The triangles indicate the optimum value of H_0 obtained from the χ^2 minimization with all flux density ratios as constraints. The squares indicate the optimum value of H_0 when omitting the flux density ratio of image D. The shaded region indicates the range of H_0 when γ=0.50±0.10 (section 6.5.4). This introduces a systematic error of ± 15 km s^{-1} Mpc^{-1}. The filled dot and the 2-σ statistical error bars at γ=0.5 indicate the value of H_0 from the 'best' isothermal mass model (F555W-IV; Table 6.3; section 6.6). The dotted lines are a third-order polynomial fit.

models F555W-VI, H_0 increases from about 30 to 99 km s^{-1} Mpc^{-1}.

Because models F555W-V are not constrained by r_D, the core radius of G1 can rapidly increase with γ (Table 6.4). This gives an overall flatter mass profile of G1 inside the Einstein radius compared with larger radii ($\gg \xi_c$), reducing the growth of H_0 for γ>0.5. However, larger core radii of G1 also give values for $r_D \gtrsim 0.5$, which is outside any reasonable range. In models F555W-VI the growth of ξ_c is suppressed by the small value of r_D.

Not only do B1608+656 and Q0957+561 have similar mass profiles, they also give similar values of H_0 as we will see later on. In the rest of the paper we assume that both G1 and G2 are isothermal. The value of γ is conservatively taken as 0.50 ± 0.10 for the reasons given in section 6.5.4. The models for γ=0.3, 0.5 and 1.0 (Table 6.4) are shown in Figure 6.3.

6.6 The Hubble parameter from B1608+656

The best estimate of the Hubble parameter (i.e. H_0^χ) from B1608+656 ranges from 60 to 63 km s^{-1} Mpc^{-1} for the SIE+SIE mass models. This range increases to 48 – 60 km s^{-1} Mpc^{-1} for the SIE+NIE mass models (Table 6.3). All values of H_0 are given for a flat universe with Ω_m=1, if not specified otherwise.

If we only consider models with (i) relatively low reduced χ^2 values ($\lesssim$10) and (ii) models that do not give a fifth observable image, then only models IV (Table 6.3) remain viable candidates. The best isothermal model, F555W-IV, gives $H_0^\chi = 59$ km s^{-1} Mpc^{-1} and a very smaller scatter ($\approx$1%) between the values of H_0 from the individual time delays. This small scatter is a coincidence and not a result from the χ^2–minimization. We have tried different values for the delays, which gave proportionally different values of H_0. Even without the these additional three constraints, model F555W-IV remains the best model (i.e. smallest χ^2).

We will therefore take H_0=59 km s^{-1} Mpc^{-1} to be our best estimate of the Hubble parameter from B1608+656, given that G1 and G2 can be modeled with an isothermal mass distribution. Model F555W-IV reproduces all observables within an acceptable range, except for the flux density ratio of image D. It does not produce a bright central image as required by its absence in the observations. It is the only plausible isothermal model that cannot be excluded at very high confidence level, based on its χ^2 (assuming the flux density ratio of image D is indeed perturbed). The surface density position angles of G1 and G2 are also within an acceptable range from the surface brightness position angles, considering that G1 and G2 could be merging (Jackson et al. 1997; Fassnacht et al. 2000, in preparation). All other models in Table 6.3 can be rejected on the basis of one of these criteria.

Clearly, an uncertainty remains regard-

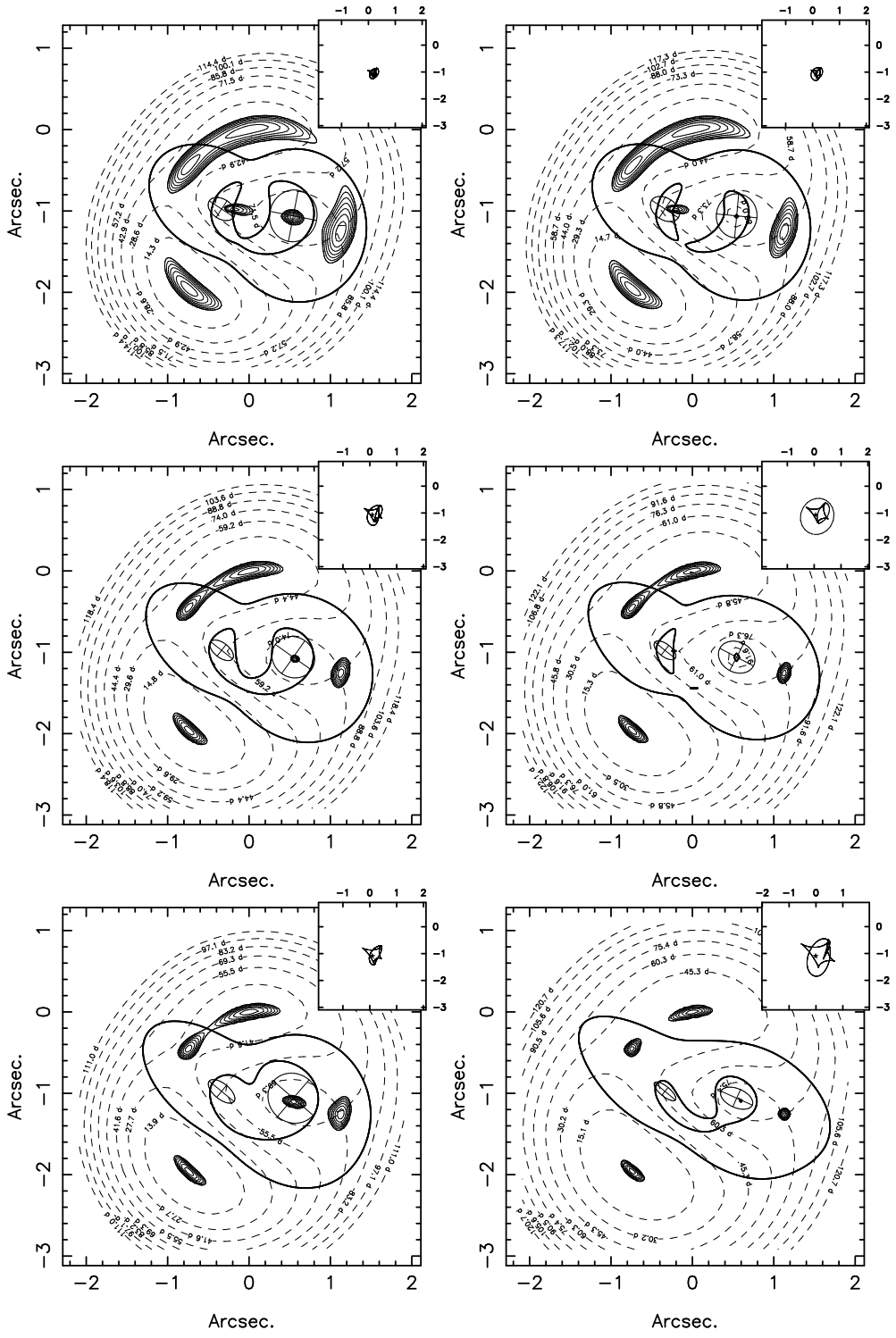

FIGURE 6.3— Same as Figure 6.1, now for models F555W-V and F555W-VI. The figures on the left (upper to lower) show models F555W-V for γ=0.3, 0.5 and 1.0, respectively. The figures on the right are for models F555W-VI.

Model	γ	σ (km s^{-1})	$\left(\frac{a}{b}\right)_\Sigma$	$\theta_{\rm PA}$ (°)	$r_{\rm c}$ ($''$)	H_0^χ	χ^2
F555W-V	0.3	293.2, 220.7	0.91, 0.67	-10.8, 56.5	0.152, 0.017	27.4	5.8
	0.4	274.5, 210.9	0.96, 0.57	36.1, 53.2	0.095, 0.001	41.8	1.4
	0.5	269.6, 214.4	0.91, 0.53	54.7, 52.0	0.148, 0.078	50.5	4.6
	0.6	271.0, 222.4	0.90, 0.51	55.2, 51.6	0.231, 0.150	54.7	7.2
	0.8	294.1, 230.1	0.92, 0.48	49.3, 50.6	0.462, 0.249	56.0	12.3
	1.0	304.1, 243.2	0.93, 0.48	41.9, 50.5	0.599, 0.344	57.4	19.8
F555W-VI	0.3	270.0, 229.4	0.92, 0.68	-5.4, 56.7	0.003, 0.001	29.9	195.6
	0.4	261.4, 216.1	0.94, 0.58	45.4, 53.6	0.007, 0.005	44.1	98.0
	0.5	250.6, 207.1	0.80, 0.48	62.3, 51.7	0.001, 0.022	60.9	45.2
	0.6	237.0, 209.8	0.65, 0.44	64.3, 51.4	0.018, 0.075	74.8	37.0
	0.8	237.8, 211.2	0.55, 0.36	66.0, 50.5	0.118, 0.150	89.9	66.5
	1.0	239.5, 216.3	0.50, 0.33	66.7, 50.2	0.191, 0.211	98.5	105.8

TABLE 6.4— Mass model parameters of G1 and G2 for different mass profiles and determinations of H_0. Listed are the profile parameter γ, velocity dispersion (σ), surface density axis ratio ($\left(\frac{a}{b}\right)_\Sigma$), position angle ($\theta_{\rm PA}$; north to east) and core radius ($r_{\rm c}$). The first value is for G1, the second for G2. The Hubble parameter H_0 (in km s^{-1} Mpc^{-1}) was determined through the minimization of χ^2 (section 6.4.2). The last column shows the minimum-χ^2 value. We assume $\Omega_{\rm m} = 1$ and $\Omega_\Lambda = 0$ in this table.

ing the explicit assumption of the isothermal mass distribution for G1 and G2. This is reflected in the systematic error on H_0, given in section 6.6.1. However, the use of similar isothermal mass models makes a direct comparison with other lens systems possible, if their radial mass profile is ill-constrained (Schechter 1998; section 6.7).

6.6.1 The errors on the Hubble parameter from B1608+656

To estimate the statistical error on H_0 found from model F555W-IV, we vary it over a range of fixed values and minimize χ^2. We determine the range within which the minimum-χ^2 value increases by less than 4.0. This range indicates the 95.4% or 2–σ (statistical) confidence range of H_0 (Press et al. 1992). We find:

$$H_0^{1608} = 59^{+7}_{-6}\ {\rm km\,s^{-1}\ Mpc^{-1}}.$$

for $\Omega_{\rm m}$=1 and Ω_Λ=0. We regard this as the 'best' estimate of H_0 determined from the available observational constraints of B1608+656, under the explicit assumptions mentioned previously.

The ≈0.1 error on γ introduces a systematic error in H_0 of ±15 km s^{-1} Mpc^{-1} (see Figure 6.2). This error incorporates the much smaller uncertainties on H_0 as a result of the chosen galaxy positions, core radii or sets of constraints (Tables 6.3 and 6.4).

6.7 The Hubble parameter from other gravitational lens systems

Four other gravitational lens systems have yielded values for H_0 at present. We will discuss them separately and compare the results with those from B1608+656. All values of H_0 are given for a flat universe with $\Omega_{\rm m}$=1, if not specified otherwise.

(i) The first discovered gravitational lens system Q0957+561 (Walsh et al. 1979) recently yielded H_0=63±12 km s^{-1} Mpc^{-1} (95% confidence) from a time delay of 417±3 days (95% confidence) found from optical light curves (Kundić et al. 1997). Although much less constrained, Haarsma et al. (1999) found a delay consistent with this from radio light curves. The error on H_0 is dominated by uncertainties in the model of the mass distribution of the lens (Kundić et al. 1997). Barkana et al. (1999) showed that the error on H_0 could be some-

what larger than found by Kundić et al. (1997), due to increased uncertainties in the assumed mass model. Moreover, a new determination of the velocity dispersion of the cluster lens by Tonry & Franx (1999) indicates H_0=70±7 or 72±7 km s^{-1} Mpc^{-1} (1–σ), using the SPLS or FGS models from Grogin & Narayan (1996a, 1996b), respectively. The surface density profile of the dominant lens mass distribution in Q0957+561 was shown to be close to isothermal (Grogin & Narayan 1996a; Barkana et al. 1999).

(ii) The second gravitational lens system discovered, PG1115+080 (Weymann et al. 1980), recently gave a value of H_0=44±4 km s^{-1} Mpc^{-1} (1–σ) using an isothermal mass model (Impey et al. 1997) and the time delays found by Schechter et al. (1997). This value is low compared with most determinations of H_0, not only those from gravitational lensing. The lens mass consists of an elliptical galaxy and a nearby galaxy group. For truncated halo models or constant M/L-ratio models, H_0 could go up to as much as 65 ± 5 km s^{-1} Mpc^{-1}. However, the large B-band M/L-ratios ($\geq$13) suggests that dark matter is present. This makes constant M/L models unlikely, if the luminous and dark matter distributions are different (Impey et al. 1997). For H_0 to be $\gtrsim$60 km s^{-1} Mpc^{-1}, the dark matter halo has to be truncated just outside the Einstein radius. This suggests that the lens is almost completely stripped of its halo, possibly by interaction with the nearby compact group (Kundić 1997; Tonry 1998; Impey et al. 1997). PG1115+080 remains a complicated system with large uncertainties, mostly due to the uncertain contribution of the surface density of the group at the position of the primary lens galaxy. The lack of strong radio emission from the lens images limits the information that can be obtained on the mass distribution through deep radio or VLBI observations (e.g. Q0957+561). However, the lensed quasar forms an optical Einstein ring around the lens, providing valuable additional information about the lens potential.

(iii) Recently, a robust time delay of 10.5±0.4 days (95% confidence) was determined between the two compact radio images in the radio Einstein ring B0218+357 (Biggs et al. 1998). Preliminary modeling based on the VLBI structure in both images (Patnaik et al. 1995) yielded $H_0=69^{+13}_{-19}$ km s^{-1} Mpc^{-1} (95% confidence), using an isothermal mass model (Biggs et al. 1998). B0218+357 is an 'isolated' spiral galaxy lens and has no apparent nearby massive companions.

(iv) The gravitational lens PKS1830-211 consists of an extended source lensed into an Einstein ring (e.g. Jauncey et al. 1991). The bright compact core of the flat-spectrum source is lensed in two images embedded in the ring structure. The source is highly variable (e.g. Lovell et al. 1998) and can therefore be used to determine the time delay between the two images. Van Ommen et al. (1995) found a time delay of 44±9 days, derived from very poorly sampled light curves, however. Recently an unambiguous delay of 26^{+4}_{-5} days was found by Lovell et al. (1998). With the mass model from Nair et al. (1993) and the recently found source redshift z_s=2.507±0.002 (Lidman et al. 1998; private communication), this delay yields $H_0=65^{+16}_{-9}$ km s^{-1} Mpc^{-1} (1–σ) (Lovell et al. 1998). To be able to compare the determination of H_0 from PKS1830-211 with those from the other four gravitational lens systems, we model the lens galaxy as a singular isothermal mass distribution (Kormann, Schneider & Bartelmann 1994). We place the mass distribution at the galaxy position determined by Nair et al. (1993) and minimize the difference between the observed and model image positions and flux density ratio. We find $H_0=75^{+18}_{-10}$ km s^{-1} Mpc^{-1} (1–σ). We will use this value in the rest of the paper.

6.7.1 The average of the Hubble parameter

There is excellent agreement between H_0 from B0218+357, Q0957+561, B1608+656 and PKS1830-211 (from now on called sample *L* see Figure 6.4). The rms scatter in H_0 from these four systems is ≈10%, comparable to the 1–σ statistical error on H_0 from the individual gravitational lens sys-

	A	B	C	D
x_i^m ($''$)	0.0000	-0.7380	-0.7446	+1.1284
y_i^m ($''$)	0.0000	-1.9612	-0.4537	-1.2565
r_i^m	$\equiv$1.00	0.55	0.51	0.29
μ_i	6.09	3.36	-3.11	-1.78
t_i^m (d)	18.0 h^{-1}	0.0	21.4 h^{-1}	44.9 h^{-1}

TABLE 6.5— Image properties as determined from our best model (F555W-IV; Table 6.3). Except for r_D all observables are well recovered (see Table 6.1). The best estimate of h is 0.590 from model F555W-IV. The image magnification and parity is given by μ_i. The source position is (0.0459$''$,-1.0774$''$).

tems. This strongly suggests that (i) systematic effects between these four systems are relatively small and (ii) some systematic effect remains in PG1115+080. Is this small number statistics or are the quoted systematic errors on H_0 overestimated? If the systematic errors were not correlated between the different lens systems, a scatter of some 20 per cent could be expected.

The common factor between *all* five gravitational lens systems, however, is the use of the elliptical isothermal mass model. The systematic error on H_0 is dominated by deviations from this mass profile. The rms scatter in H_0 therefore suggests that a 'universal' mass profile can reasonably well describe the spiral galaxies in B0218+357 and PKS1830-211, the two (elliptical) galaxies in B1608+656 and the cluster elliptical in Q0957+561. Moreover, both B1608+656 and Q0957+561 suggest that this profile is close to isothermal (section 6.5.4).

Extra constraints on the radial mass profile will therefore have the largest impact on the reliability of H_0 from these lenses. In B0218+357 and PKS1830-211, constraints on the radial mass profile can be obtained through a detailed analysis of the radio Einstein ring (e.g. Kochanek & Narayan 1992; Biggs et al. 1998), in B1608+656 through analysis of the optical arcs and in Q0957+561 through observations of additional sources in the field and new radio structure (e.g. Barkana et al. 1999). Also in PG1115+080, observations of the optical Einstein ring could provide valuable new information on the lens potential (e.g. Impey et al. 1998).

Thus, under the explicit assumption that the mass models are isothermal, the errors on H_0 appear dominated by statistical errors. We therefore take the average of H_0 (with equal weights) from sample L. We find

$$H_0^{GL} = 69 \pm 7 \text{ km s}^{-1} \text{ Mpc}^{-1},$$

for Ω_m=1 and Ω_Λ=0, where the error is the 2–σ error on the average (i.e not the scatter). We have used the latest determination of H_0 from Q0957+561 by Tonry & Franx (1999). If we add PG1115+080 to the L sample, this value decreases to 64$\pm$11 km s^{-1} Mpc^{-1} (2–σ).

The L sample of gravitational lens systems gives H_0 within 10% accuracy at a 2–σ confidence level. It also excludes the value from PG1115+080 with $\gtrsim$4–σ (see section 6.8 and Table 6.6). However, the systematic errors on this value of H_0 remain around 20 per cent and it is crucial to reduce this through additional observations, which can pin down their precise radial mass profiles.

6.8 Comparing the GL with the SNe Ia, S-Z and local determinations of H_0

To determine H_0 on cosmological scales one can also make use of Type Ia Supernovae or the Sunyaev-Zel'dovich (SZ) effect.

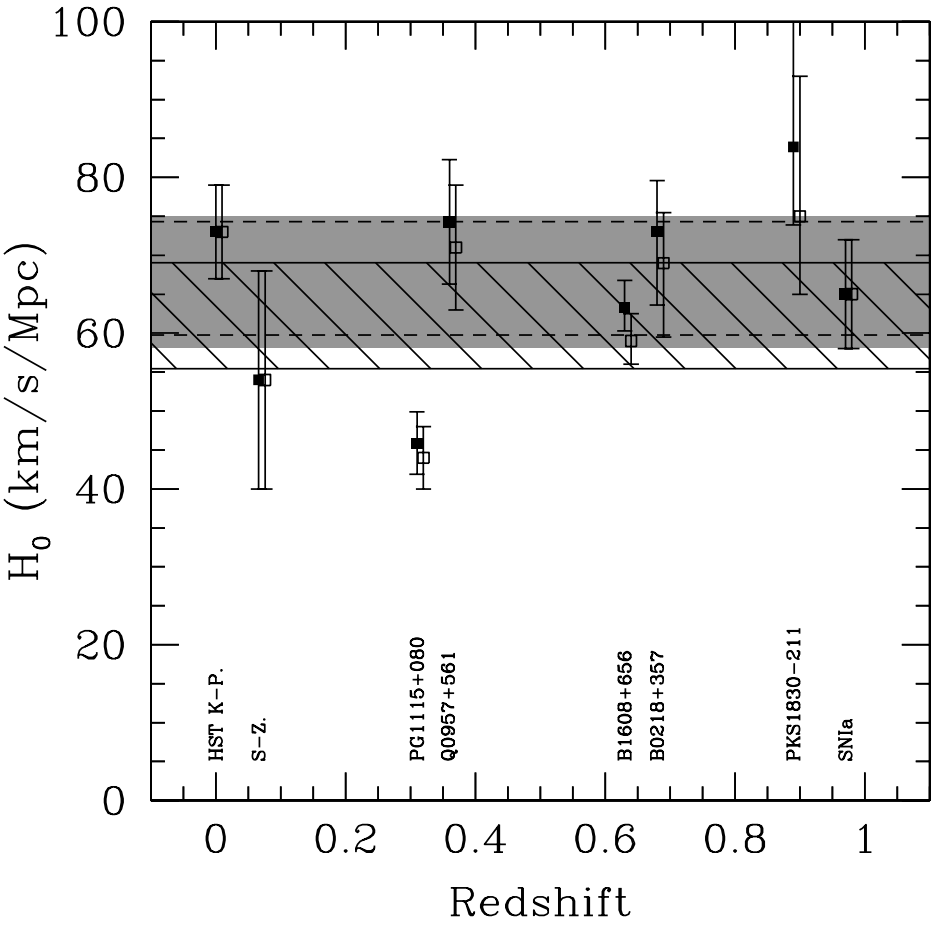

FIGURE 6.4— The Hubble parameter determined on cosmological scales plotted as function of redshift. The average local value, presented by Freedman et al. (1998; HST Key Project for the Extra-galactic Distance Scale) has a redshift $z = 0$. The SNIa determination has been placed on the highest redshift SNIa in the sample (Riess et al. 1998). The redshift for the S-Z determination of H_0 is the average cluster redshift in the sample (Myers et al. 1997). The gravitational lenses have been placed at the primary lens redshift. The open symbols are the values of H_0 for $\Omega_m = 1$ and $\Omega_\Lambda = 0$, the closed symbols for $\Omega_m = 0.3$ and $\Omega_\Lambda = 0.7$. The local, S-Z and SNIa determinations are almost independent of Ω_m and Ω_Λ. The densily shaded region indicates the ± 2–σ region around the average of H_0 determined from the L lens sample for $\Omega_m = 0.3$ and $\Omega_\Lambda = 0.7$. The dashed horizontal lines indicate the ± 2–σ region around the average of H_0 determinated from the L lens sample plus the S-Z, SNIa and local determinations. The lower shaded region indicates the ± 2–σ region around the average of the L lens sample for $\Omega_m = 1.0$ and $\Omega_\Lambda = 0.0$. The 1–σ error-bars indicate the statistical errors.

In principle the S-Z effect is very powerful method to determine H_0, but systematic effects, such as cluster elongation and clumpiness, are poorly understood. Most measurements give relatively low values of H_0. However, X-ray selection minimizes the effects of cluster elongation. From a sample of X-ray selected clusters Myers et al. (1997) recently found H_0=54$\pm$14 km s^{-1} Mpc^{-1} (1–σ).

The best determination of H_0 from Type-Ia Supernovae comes from the High-Z Supernovae Search Team (Riess et al. 1998). Based on 50 SNe-Ia events, they find H_0^{SNIa}=65 $\pm$ 7 km s^{-1} Mpc^{-1} (1–σ; independent of Ω_m and Ω_Λ). The error includes uncertainties on the calibration of the SNIa absolute magnitudes and the zeropoint of the Cepheid distance scale (e.g. Riess et al. 1998). Their results also seem to (i) rule out Ω_m=1 for a flat universe at $\gtrsim$7–σ confidence and (ii) indicate $\Omega_\Lambda > 0$ at $\gtrsim$3–

σ confidence (e.g. Riess et al. 1998). However, the determination of H_0 from SNe Ia is a 'standard-candle' method. It can be influenced by a host of systematic effects, such as evolution, extinction, selection biases and weak lensing (Riess et al. 1998). Moreover, the determination depends on the Cepheid distance scale and is therefore not independent of the local determinations. This value should therefore be regarded with some caution.

So far, we have only regarded H_0 from gravitational lenses in a flat universe with Ω_m=1. But evidence has been mounting over the last few years supporting a low density universe with Ω_m=0.2–0.3 (e.g. Carlberg et al. 1996; Bahcall, Fan & Cen 1997; Riess et al. 1998).

In a low-density universe with Ω_m=0.3 and Ω_Λ ranging from 0.0 to 0.7, the Hubble parameter determined from gravitational lenses increases by about 7%, depending on the precise lens and source redshifts. We then find

$$H_0^{1608} = (65 - 63)^{+7}_{-6} \text{ km s}^{-1}\text{Mpc}^{-1}$$

for Ω_m=0.3 and Ω_Λ=0.0–0.7, with 2–σ errors. The average from sample L becomes

$$H_0^{GL} = 74 \pm 8 \text{ km s}^{-1} \text{ Mpc}^{-1},$$

for Ω_m=0.3 and Ω_Λ=0.0-0.7, with 2–σ errors (including the range in Ω_Λ). If we add PG1115+080 to the L sample, this value decreases to 68$\pm$13 km s^{-1} Mpc^{-1}. For a low density universe with $\Omega_m = 0.3$, a robust value of H_0^{GL} is found which only weakly depends on Ω_Λ ($\lesssim$2%). It is also in good agreement with the determination from Type Ia Supernovae.

Moreover, the cosmological gravitational lens determination of H_0 agrees best with the local determination of H_0 =73$\pm$6 (statistical) $\pm$11 (systematic) km s^{-1} Mpc^{-1} (*Hubble Space Telescope* Key Project for the Extra-galactic distance Scale; Freedman et al. 1998) in a low density universe. Once both the local and gravitational lens determinations of H_0 are well constrained (i.e. small statistical and systematic errors), the agreement between both values can be used to constrain the density of the universe and possibly the cosmological constant (e.g. Refsdal 1966; Kayser & Refsdal 1983). However, if the local determinations of H_0 remain systematically larger than the determinations on cosmological scales, this could suggest that we live in an under-dense part of the universe (e.g. Zehavi et al. 1998).

We have plotted the local determination of H_0 from Freedman et al. (1998) and those determined on cosmological scales in Figure 6.4. It shows that all determinations of H_0 agree with those from sample L to within 1–σ, except for PG1115+080. To be complete, we have listed the averages of H_0 from different combinations of methods and cosmologies in Table 6.6. It shows a maximum of 10 km s^{-1} Mpc^{-1} difference between several determinations of the average of H_0. We have included the determination of H_0 from PG1115+080 in methods 1 and 3 (see Table 6.6), although it lies $\gtrsim$4–σ outside any range listed in Table 6.6. The probability of having one 4–σ outlier in a sample of five is $\ll$ 1%, making it unlikely that this value is due to a statistical fluke only.

The agreement on H_0 from four out of five gravitational lens systems, the SNIa , the S-Z and local determinations is also an independent confirmation that the lens mass models should not deviate too much from isothermal, as was already shown from some of the individual gravitational lens systems. If we combine the strong dependence on γ of H_0 from B1608+656 (Figure 6.2) with the demand that H_0^{GL} should be between the local and SNIa determinations, then on average γ for the L sample should not deviate by more than about 10% from γ=0.50 (isothermal) for Ω_m=0.3 and Ω_Λ=0.0–0.7.

6.9 Conclusions

Using VLBA imaging, VLA monitoring and *Hubble Space Telescope* WFPC2 and NICMOS imaging data, we constrained mass models of the lens galaxies in the gravitational lens system B1608+656. The best mass model gives (i) an agreement between the observed and model image positions

Method	Ω_m	Ω_Λ	H_0
1	1.0	0.0	64±11
1	0.3	0.0–0.7	68±13
2	1.0	0.0	69±7
2	0.3	0.0–0.7	74±8
3	1.0	0.0	64±7
3	0.3	0.0–0.7	67±9
4	1.0	0.0	67±6
4	0.3	0.0–0.7	70±7

TABLE 6.6— The average of H_0 from local and cosmological determinations. The error indicates the 2–σ error on the averages. The methods are: (1) All lenses (i.e. B0218+357, Q0957+561, PG1115+080, B1608+656 and PKS1830-211), (2) all lenses, except for PG1115+080, (3) all methods (i.e. all lenses, SNe Ia, S-Z and local) and (4) all methods, except for PG1115+080.

well within the observational errors, (ii) the radio flux density ratios of the images to within 10% (except for the faintest radio image) and (iii) the observed time delays (Paper I) to within 1%, although this small scatter is a coincidence.

Using the three time delays from B1608+656 (Paper I), the best isothermal mass model gives

$$H_0^{1608} = 59^{+7}_{-6}\,\mathrm{km\,s^{-1}\,Mpc^{-1}},$$

for Ω_m=1 and Ω_Λ=0, and with 2–σ errors. When Ω_m=0.3 and Ω_Λ=0.0–0.7, H_0=(65–63)$^{+7}_{-6}$ km s^{-1} Mpc^{-1}. All models give robust values for H_0, but a systematic error of ± 15 km s^{-1} Mpc^{-1} remains, due to a 20% uncertainty in the radial mass profile.

Also under the explicit assumption of the isothermal mass model, we determine the average of H_0 from a sample of four lenses (B0218+357, Q0957+561, B1608+656 and PKS1830-211). We find

$$H_0^{GL} = 69 \pm 7\,\mathrm{km\,s^{-1}\,Mpc^{-1}},$$

for Ω_m=1 and Ω_Λ=0, with 2–σ errors. For Ω_m=0.3 and Ω_Λ=0.0–0.7 this increases to $H_0^{GL} = 74 \pm 8\,\mathrm{km\,s^{-1}\,Mpc^{-1}}$. When including PG1115+080, these values decrease to 64±11 km s^{-1} Mpc^{-1} and 68±13 km s^{-1} Mpc^{-1}, respectively.

These values agree very well with the local (Freedmann et al. 1998), Type Ia Supernovae (Riess et al. 1998) and S-Z (Myers et al. 1997) determinations, supporting the reliability of the cosmological determinations of H_0 from gravitational lenses. On average the lens determinations agree best with local determinations for a low density universe.

Moreover, we find that the mass model of B1608+656 is close to isothermal (γ=0.50±0.10), in good agreement with Q0957+561 and MG1654+1346. The close agreement on H_0 from four out five gravitational lens systems and the agreement on γ from three gravitational lens systems suggest the existence of a 'universal' mass profile that can describe the mass distribution of spirals, ellipticals and cluster ellipticals. This profile must on average be very close to isothermal, perhaps following the profile found by Navarro, Frenk & White (1996), which is indeed close to isothermal in the intermediate region probed by lensing.

Acknowledgments

We like to thank Phillip Helbig, Ger de Bruyn & Steve Myers for giving useful comments and suggestions to improve this paper. We also like to thank Chris Lidman for providing the redshift of PKS1830-211 prior to publication. LVEK acknowledges the support from an NWO program subsidy (grant number 781-76-101). CDF acknowledges the support from an NSF grant, #AST 9420018. This research was supported in part by the European Commission, TMR Programme, Research Network Contract ERBFMRXCT96-0034 'CERES'.

References

Bahcall, N. A., Fan, X., & Cen, R., 1997, ApJL 485, L53

Biggs, A.D., Browne, I.W.A., Helbig, P., Koopmans, L.V.E., Wilkinson, P.N., & Perley, R.A., 1998, MNRAS 304, 349

Browne, I.W.A., et al., 1998, in Observational Cosmology with the New Radio Surveys, ed. M. Bremer, N. Jackson, & I. Perez–Fournon (Dorcrecht: Kluwer)

Barkana, R. 1998, ApJ 502, 531

Barkana, R. , Lehár, J., Falco, E. E., Grogin, N. A., Keeton, C. R. & Shapiro, I. I. 1999, ApJ 520, 479

Carlberg, R. G., Yee, H. K. C., Ellingson, E., Abraham, R., Gravel, P., Morris, S., & Pritchet, C. J., 1996, ApJ 462, 32

Corbett, E.A., Browne, I.W.A., Wilkinson, P.N., & Patnaik, A.R., 1996, in Astrophysical Aplications of Gravitational Lensing, eds. C.S. Kochanek and J.N. Hewitt (Kluwer Academic Publishers: Dordrecht), p37

Fanaroff, B. L. & Riley, J. M., 1974, MNRAS 167, 31

Fassnacht, C. D., Womble, D. S., Neugebauer, G., Browne, I. W. A., Readhead, A. C. S., Matthews, K., & Pearson, T. J., 1996, ApJL 460, L103

Fassnacht, C., 1997, American Astronomical Society Meeting, 191, 5903

Fassnacht, C.D., Pearson, T.J., Readhead, A.C.S., Browne, I.W.A., Koopmans, L.V.E., Myers, S.T., Wilkinson, P.N., 1999, ApJ, in press (Paper I)

Freedman, W.L., Mould, J.R., Kennicutt, R.C., & Madore, B.F., 1998, *astro-ph/9801080*

Grogin, A., & Narayan, R., 1996a, ApJ 464, 92

Grogin, N. A. & Narayan, R. 1996b, ApJ 473, 570

Haarsma, D. B., Hewitt, J. N., Lehar, J. & Burke, B. F. 1999, ApJ 510, 64

Hickson, P., 1982, ApJ 255, 382

Impey, C. D., Falco, E. E., Kochanek, C. S., Lehár, J., McLeod, B. A., Rix, H. -W., Peng, C. Y. & Keeton, C. R. 1998, ApJ 509, 551

Jackson, N. J., Nair, S. and Browne, I. W. A., in Cosmology with the new radio surveys, eds. M. Bremer, Jackson, N. J., p315

Jackson, N., Helbig, P., Browne, I., Fassnacht, C. D., Koopmans, L., Marlow, D., & Wilkinson, P. N., 1998, A&A 334, L33

Jauncey, D.L., et al., 1991, Nature 352, 132

Kayser, R. & Refsdal, S. 1983, A&A 128, 156

Keeton, C.R, Kochanek, C.S., & Seljak, U., 1997, ApJ 482, 604

Keeton, C.R., Kochanek, C.S., Falco, E.E., 1997, *astro-ph/9708161*

Keeton, C.R., Kochanek, C.S., in Golden Lenses: The Hubble Constant and galaxies at high redshift, 1998, electronic Proceedings of the Workshop on Golden Lenses held at Jodrell Bank, *http://multivac.jb.man.ac.uk:8000/ceres/workshop1/proceedings.html*

Kochanek, C. S., & Narayan, R., 1992, ApJ 401, 461

Kochanek, C.S., 1995, ApJ 445, 559

Koopmans, L. V. E., et al. 1999, MNRAS 303, 727

Koopmans, L.V.E. & de Bruyn, A.G., 1999, å, submitted

Kormann, R., Schneider, P., & Bartelmann, M., 1994, A&A 284, 285

Kundić, T., 1997, AJ 114, 507

Kundić, T., et al., 1997, ApJ 482, 75

Lidman C., Courbin, F., Meylan G., Broadhurst, T.J., Frye B., Welch J., 1999, ApJ 514, 57L

Lovell, J. E. J., Jauncey, D. L., Reynolds, J. E., Wieringa, M. H., King, E. A., Tzioumis, A. K., McCulloch, P. M. & Edwards, P. G. 1998, ApJL 508, L51

Mao, S. & Schneider, P., 1998, MNRAS 295, 587

Myers, S. T., et al., 1995, ApJL 447, L5

Myers, S. T., Baker, J. E., Readhead, A. C. S., Leitch, E. M., & Herbig, T., 1997, ApJ 485, 1

Navarro, J. F., Frenk, C. S., & White, S. D. M., 1996, ApJ 462, 563

Nair, S., Narasimha, D., & Rao, A. P., 1993, ApJ 407, 46

Patnaik, A. R., Browne, I. W. A., King, L. J., Muxlow, T. W. B., Walsh, D., & Wilkinson, P. N., 1993, MNRAS 261, 435

Patnaik, A. R., Porcas, R. W., & Browne, I. W. A., 1995, MNRAS 274, L5

Pildis, R. A., Bregman, J. N., & Evrard, A. E., 1995, ApJ 443, 514

Press, W. H., Teukolsky, S. A., Vetterling, W. T., & Flannery, B. P., 1992, Cambridge: University Press, —c1992, 2nd ed.,

Refsdal, S., 1964, MNRAS 128, 307

Refsdal, S., 1966, MNRAS 132, 101

Riess, A. G., et al., 1998, AJ 116, 1009

Schechter, P.L., et al., 1997, ApJL 475, L85

Schechter, P.L., 1998, electronic Proceedings of a workshop organized by the Observatoire de Strasbourg, *http://astro.u-strasbg.fr/howfar/toc.html*

Schneider, P., Ehlers, J., & Falco, E. E., 1992, Berlin ; New York : Springer-Verlag, [1992], 736.

Snellen, I. A. G., De Bruyn, A. G., Schilizzi, R. T., Miley, G. K., & Myers, S. T., 1995, ApJL 447, L9

Tonry, J.L., 1998, AJ 115, 1

Tonry, J. L. & Franx, M. 1999, ApJ 515, 512

Van Ommen, T. D., Jones, D. L., Preston, R. A., & Jauncey, D. L., 1995, ApJ 444, 561

Walsh, D., Carswell, R.F., Weymann, R.J., 1979, Nature 279, 381

Weymann, R. J., Latham, D., Roger, J., Angel, P., Green, R. F., Liebert, J. W., Turnshek, D. A., Turnshek, D. E., & Tyson, J. A., 1980, Nature 285, 641

Zehavi, I., Riess, A. G., Kirshner, R. P., & Dekel, A., 1998, ApJ 503, 483

7

A new radio double lens from CLASS: B1127+385

Originally published as L.V.E. Koopmans, A.G. de Bruyn, et al. 1999, Monthly Notices of the Royal Astronomical Society, 303, 727

We present the discovery of a new gravitational lens system with two compact radio images separated by 0.701 ± 0.001 arcsec. The lens system was discovered in the Cosmic Lens All Sky Survey (CLASS) as a flat spectrum radio source. Both radio components show structure in a VLBA 8.4 GHz radio image. No further extended structure is seen in either the VLA, MERLIN or VLBA images. *Hubble Space Telescope (HST)* WFPC2 images in F555W and F814W show two extended objects close to the radio components, which we identify as two lens galaxies. Their colours and mass-to-light ratios seem to favour two late-type spiral galaxies at relatively high redshifts ($z_{\rm d}\gtrsim0.5$). Faint emission is also detected at positions corresponding to the radio images.

A two-lens mass model can explain the observed VLBA structure. The best fit model has a reduced χ^2 of 1.1. The relative positions of the VLBA subcomponents are reproduced within 0.08 mas, the flux density ratios within 0.19. We also reproduce the position angle and separation of the two VLBA subcomponents in A and B within the observational errors, which we consider strong evidence for the validity of the lens model. Moreover, we find a surface density axis ratio of $0.74^{+0.10}_{-0.12}$ for the primary lens (G1), consistent with the surface brightness axis ratio of 0.69 ± 0.15. Also, the surface density position angle of $(4.9^{+28.2}_{-22.4})^\circ$ of G1 compares well with the $(-6\pm13)^\circ$ position angle of the surface brightness distribution. The errors indicate the 99 per cent confidence interval.

7.1 Introduction

In the last few years gravitational lensing has proved useful not only in the determination of cosmological parameters, such as the Hubble constant (e.g. Refsdal 1964, 1966) and the cosmological constant (e.g. Kochanek 1996), but also in the study of the mass distribution in the universe and the mass distribution of lensing galaxies. To obtain a sample of gravitational lens systems, relatively unbiased compared to optical lens surveys (Kochanek 1991), which suffer from seeing effects and dust obscuration, two large radio surveys, the Jodrell-Bank VLA Astrometric Survey (JVAS; Patnaik et al. 1992; King et al., in preparation; Wilkinson et al., in preparation) and the Cosmic Lens All Sky Survey (CLASS; Myers et al., in preparation), were set up. To-

gether these surveys targeted ∼12 000 flat spectrum radio sources with flux densities larger than 25 and 200 mJy for CLASS and JVAS, respectively. All sources were observed with the Very Large Array (VLA) in A-array at 8.4 GHz with 0.2 arsec resolution. Objects that showed signs of multiple compact components, or structure that could be due to lensing, were listed for further high resolution radio observations with MERLIN. Those objects still exhibiting compact structure in the MERLIN image were subsequently observed with the VLBA to confirm their identification as a lens system and sometimes HST to observe the optical emission of the lens galaxy and lens images.

In the following sections we give a detailed description of B1127+385, a newly discovered gravitational lens system. In Section 7.2 we describe the radio observations. In Section 7.3 the optical HST observations are presented. In Section 7.4 we present a lens model based on the image positions and flux density ratios from the VLBA observations. In Section 7.5 we summarise our results and conclusions.

7.2 Radio observations

7.2.1 VLA and MERLIN observations

B1127+385 was observed on 1995 August 14 with the VLA in A-array at 8.4 GHz as one of the ∼10,000 flat spectrum CLASS sources. The image shows two compact components separated by ∼0.7 arcsec (Fig. 7.1). The 92-cm (0.327 MHz) WENSS (de Bruyn et al., in preparation) flux density is 12±3 mJy, establishing a slightly inverted radio spectrum. This implies that both components, with similar flux density at 8.4 GHz, most likely have a flat or inverted spectrum. This immediately made B1127+385 a strong lens candidate, because a change alignment within 0.7 arcsec of two unrelated compact flat spectrum radio sources is less than 10^{-6}. Thus there is only a probability <1 per cent of finding such a change alignment in the sample of ∼10,000 flat spectrum sources. No indication of variability has been found sofar. A MERLIN 1.7 GHz long-track observation on 1996 February 13 showed two compact components. Subsequently, a snapshot observation with MERLIN was made at 5 GHz in 1996 December. These observations show only the two compact components A and B (Fig. 7.1). The VLA and MERLIN observations were reduced in AIPS and mapped by the Caltech package DIFMAP (Pearson et al. 1994; Shepherd 1997). The flux densities and positions were determined in DIFMAP by fitting Gaussian models to both components simultaneously. The results are listed in Table 7.1. The spectral indices of the components are -0.08 (A) and 0.05 (B) ($S_\nu \propto \nu^\alpha$) respectively between the VLA 8.4 GHz and MERLIN 5 GHz flux densities, and -0.05 (A) and -0.11 (B) respectively between the VLA 8.4 GHz and MERLIN 1.7 GHz flux densities. The errors on these spectral indices are ∼0.15. The compactness and similarity in spectral index of both radio components underline the lens candidacy of B1127+385. But high resolution radio observations and optical follow-up are necessary to secure its lensing nature.

7.2.2 VLBA observations

VLBA 8.4 GHz observations were made on 1996 November 4. Phase referencing was used, switching between B1127+385 (4 min integration) and the strong nearby JVAS phase-reference source B1128+385 (Patnaik et al. 1992; 2 min integration) for a period of 3.5 hours. The map of B1128+385 shows a sub-mas unresolved point source at 8.4 GHz. Fringe-fitting (Thompson, Moran & Swenson 1986) was therefore performed on B1128+385 and the solutions were directly transferred to B1127+385, which is ∼11 arcmin west of B1128+385. All data reduction was performed in AIPS and mapping was done in DIFMAP. The data was uniformly weighted. The resulting map resolution is 1.7×0.7 mas (PA of 41°).

Components A and B show clear evidence for the presence of substructure (Fig. 7.1). Model fitting in DIFMAP shows that two axisymmetric Gaussian components can well represent the substructure in images A and B. The positions of the Gaussian components and their flux densities are listed in Table 7.2 for their best fit (min-

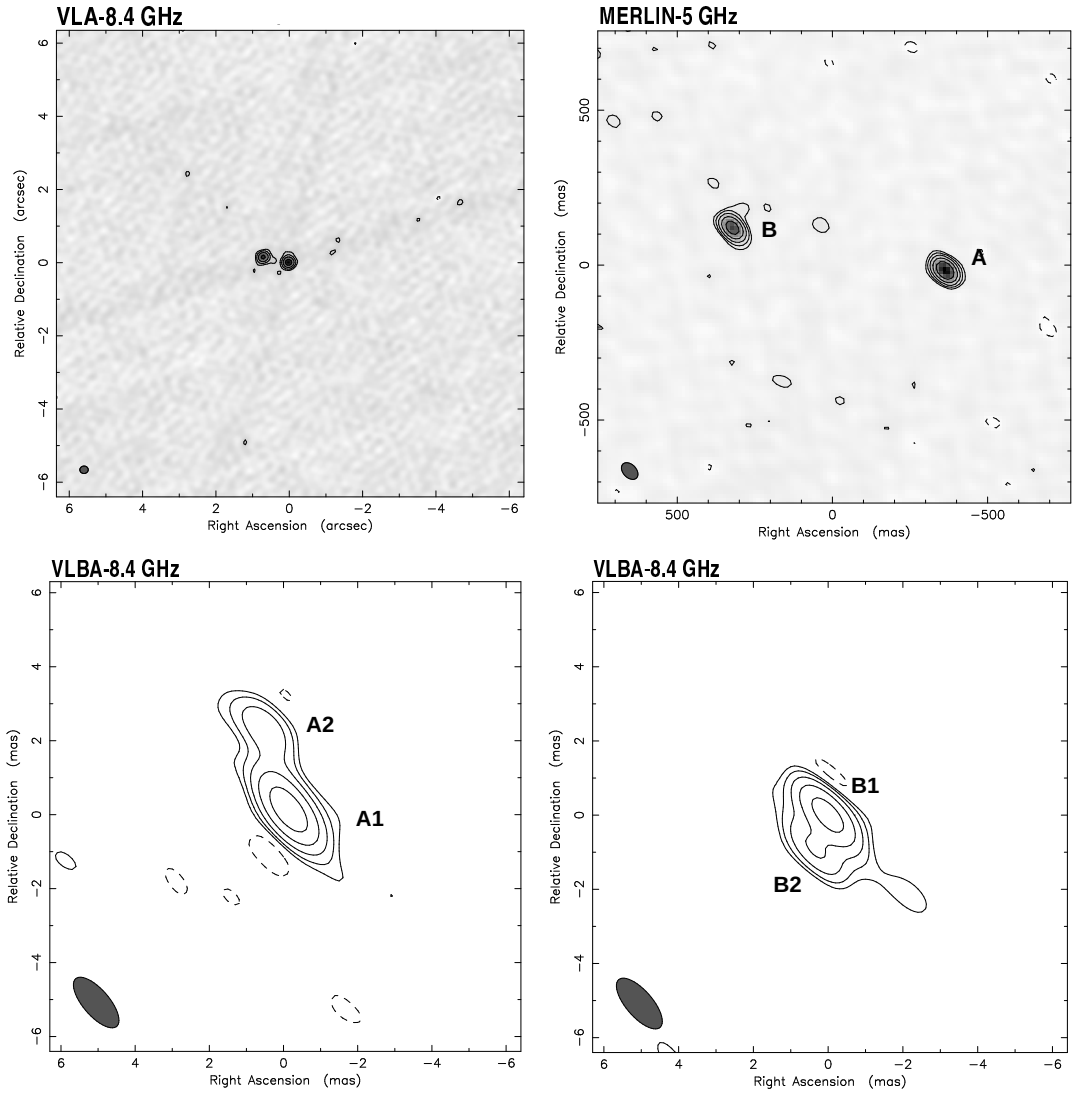

FIGURE 7.1— Upper left: VLA 8.4 GHz snapshot of B1127+385 taken 1995 August 14. The image has a resolution of 0.2×0.2 arcsec and shows two compact components (B is east, A is west) separated by 0.7 arsec. Contours are at $(-3, 3, 6, 12, 24) \times 0.367$ mJy per beam. Upper right: MERLIN 5 GHz observation taken 1996 December. The map has a resolution of 0.06×0.04 arcsec (PA of 44°). Contours are at (−3, 3, 6, 12, 24, 48, 96)×0.146 mJy per beam. Lower left: VLBA 8.4 GHz image of B1127+385 component A, taken 1996 November 4. Contours are at (−4, 4, 8, 16, 32, 64)× 0.090 mJy per beam. Lower right: Idem of component B. Contours are at (−4.5, 4.5, 9, 18, 36, 72)× 0.078 mJy per beam. The VLBA maps have a resolution of 1.7×0.7 mas (PA of 41°).

imum χ^2). The separation between A1 (A2) and B1 (B2) is 700.7 (700.0) mas and the position angle of the line from A1 to B1 is 78.5°. The flux density ratios between A1 and B1, and A2 and B2 are 1.3 and 1.1, respectively. The integrated flux density ratio of A over B is 1.3, consistent with the 8.4 GHz VLA (1.3) and 5 GHz MERLIN (1.3) flux density ratios. The large position angle difference of ∼139° between the subcomponents in A and B is expected if A and B are lensed and given opposite parities (Schneider, Ehlers & Falco 1992).

	$\Delta\alpha$(mas)	$\Delta\delta$(mas)	S_ν(mJy)	Instr.
A	0 ± 5	0 ± 5	14.7	(1)
	0 ± 2	0 ± 2	15.3	(2)
	–	–	16.0	(3)
A1	0.0 ± 0.1	0.0 ± 0.1	13.7	(4)
A2	0.6 ± 0.1	2.1 ± 0.1	|	
B	688 ± 5	145 ± 5	11.8	(1)
	685 ± 2	138 ± 2	11.5	(2)
	–	–	14.0	(3)
B1	686.6 ± 0.1	140.1 ± 0.1	10.8	(4)
B2	687.0 ± 0.1	139.2 ± 0.1	|	

TABLE 7.1— VLA 8.4 GHz (1), MERLIN 5 GHz (2), MERLIN 1.7 GHz (3) and VLBA 8.4 GHz (4) astrometry and flux densities for B1127+385. The integrated flux densities from the VLBA observations are given. The VLBA positions of A1 and B1 are $11^{\rm h}30^{\rm m}0.099^{\rm s}$, $+38^\circ12'3.091''$ and $11^{\rm h}30^{\rm m}0.157^{\rm s}$, $+38^\circ12'3.232''$ (J2000), respectively. The errors on the flux densities are $\sim$10 per cent. All errors are 1σ.

	Sep. (mas)	P.A. (°)	$S_{8.4\rm GHz}$ (mJy)
A	2.20 ± 0.15	16 ± 4	10.5,3.2
B	0.97 ± 0.15	155 ± 9	7.9,2.9

TABLE 7.2— The separations and position angles (north to east) of components A2 (B2) with respect to components A1 (B1). The flux densities are those of (A1, A2) and (B1, B2), respectively. The errors on the flux densities are $\sim$10 per cent. All errors are 1σ.

7.3 HST observations

Hubble Space Telescope (HST) exposures of B1127+385 in the filters F555W (V) and F814W (I) were taken on 1996 June 21, using the Wide Field Planetary Camera (WFPC2). The exposures were taken on the PC chip (45.5 mas pixel^{-1}) and the exposure times in V and I band were 700s + 300s and 2×500s, respectively. A standard reduction was performed on both images. The I-band image is shown in Fig. 7.2. The I-band image shows two clear emission peaks within $\sim$1 arcsec distance from the radio components. Except for a bright nearby galaxy 8 arcsec south, no other galaxies are seen near B1127+385. Because the absolute astrometry of the HST is poorly matched (offsets of $\sim$1 arcsec) to the more accurate VLBI astrometry, we cannot 'blindly' overlay the optical and radio maps. However, the contour plot of the optical I-band emission, convolved to 0.1 arcsec (Fig. 7.3), clearly shows two bright (G1 and G2) and one fainter emission feature. If we assume that the radio component A is associated with the optical emission ($\sim 9\sigma$ peak) west of G1, we find that also radio component B is associated with an emission feature ($\sim 5\sigma$ peak). Although there appears to be a slight offset between the optical emission and the radio position of B, this could be due to the poorer signal-to-noise or the extended nature of the optical emission near B.

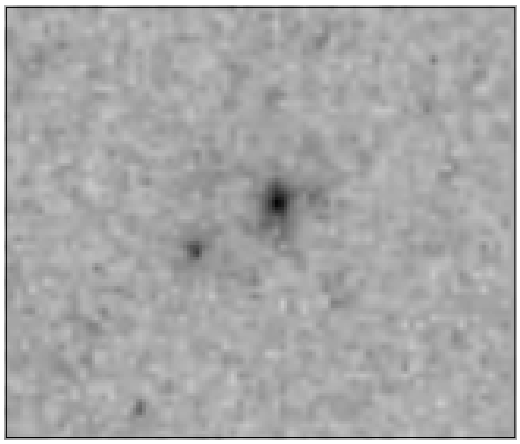

FIGURE 7.2— HST I-band image of B1127+385. The two radio components are associated with two emission features west (A) and east (B) of G1 (see also Fig. 7.3). North is up, east is left. The area shown is 3.1 arcsec $\times$ 2.6 arcsec.

Both G1 and G2 are extended, suggesting that both are galaxies. Photometry and relative astrometry were performed on G1 and G2 in I band, and only photometry in V band (Table 7.3). The $V-I$ colour indices

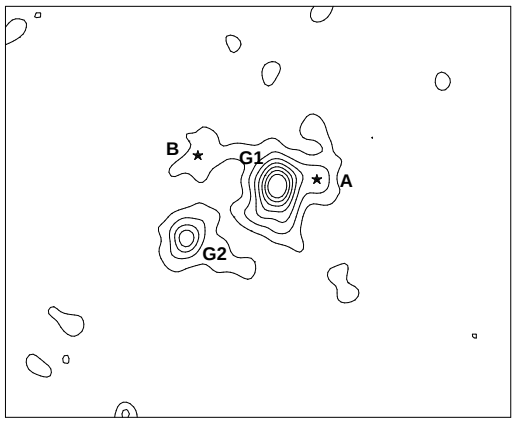

FIGURE 7.3— Contour plot of B1127+385. The HST image has been convolved to 0.1 arcsec to bring out the optical emission more clearly. The two markers show the radio positions of A and B, where A has been placed on the centre of the optical emission as determined by a Gaussian fitting procedure. The contours indicate $(3, 6, 9, 12, 15, 18, 21) \times$ rms noise in the image.

of G1 and G2 are 1.9 and 2.0 mag, respectively. The separation is 0.60 arcsec and the position angle of the line G1-G2 is $120°$.

7.4 Modelling

In this section we present a model that reproduces the observed properties of B1127+385. We use a Singular Isothermal Ellipsoid (SIE) mass distribution (Kormann, Schneider & Bartelmann 1994) to describe the lens galaxies. We assume a smooth FRW universe. If not mentioned otherwise, all errors indicate 99 per cent confidence intervals.

From the VLBA observations we obtain 10 constraints (8 from the image positions and 2 from the flux density ratios). The two source positions give 4 free parameters and the mass model gives 3 (velocity dispersion, surface density (SD) axis ratio and position angle). The number of degrees of freedom (NDF) is therefore 3.

7.4.1 Single lens mass model

Initially we try a model consisting of a single SIE galaxy. We place the mass distribution on the surface brightness (SB) centre of G1, determined by fitting a 2D-Gaussian profile to it. The position of G1 relative to the optical emission feature associated with radio component A is $(-0.228'', -0.038'')$, with a 1σ error of $\sim$5 mas in both x and y. The parities of components A and B are taken as –1 and +1, respectively. Choosing +1 and –1 for A and B, and letting the centre of the SD distribution move freely, give in all cases (both for the single and double lens case) unsatisfactory models ($\chi^2 \gtrsim 5$).

Using the image positions and flux density ratios of the radio components from Tables 7.1 and 7.2, we project rays back on the source plane through the lens. For the two image pairs – A1&B1 and A2&B2 – we simultaneously minimize the distance between the back-projected rays and the difference between observed and model flux density ratios (Kayser 1990). We allow for a 1σ error of 0.1 mas in the relative x and y distances between the positions of the two back-projected rays and their average position. A 1σ error of 0.15 is allowed for the flux density ratios. When the model has converged sufficiently, we use the average source positions to calculate the image positions in the lens plane. These are subsequently used to calculate a χ^2 from the mismatch with the observed image positions. The resulting mass model parameters for minimum χ^2 (lens plane) are listed in Table 7.4 (model I).

7.4.2 Double lens mass model

Although G1 is the primary lens, G2 cannot be neglected as it lies close to G1 and is only $\sim$1 mag fainter. We therefore extend the model by placing a Singular Isothermal Sphere (SIS) at the position of G2 — $(-0.749'', -0.337'')$ relative to component A, with a 1σ error of $\sim$5 mas in x and y. We choose a SIS for G2, because G2 is only an external perturber of the primary lens G1 and as long as there is no need to complicate the model (poor χ^2) one should keep the mass model as simple as possible. Using a SIE for G2 would add two extra free parameter (axis ratio and position angle) and make the mass model less constrained.

The velocity dispersion of G2 is fixed at $0.79 \cdot \sigma_{\|}^{\mathrm{G1}}$, using $L \propto \sigma_{\|}^4$ (e.g. Faber & Jack-

	$\Delta\alpha$(mas)	$\Delta\delta$(mas)	I (magn.)	V (magn.)
G1	0 ± 5	0 ± 5	22.5 ± 0.1	24.4 ± 0.2
G2	521 ± 5	-299 ± 5	23.5 ± 0.1	25.5 ± 0.2

TABLE 7.3— HST relative astrometry (I band) and photometry for B1127+385. Component G1 is located at $11^{\rm h}30^{\rm m}0.1726^{\rm s}$, $+38°12'1.903''$ (according to the STSDAS/METRIC routine in IRAF). All errors are 1σ.

son 1976) in combination with the $\sim$1 mag difference between G1 and G2 and assuming they have similar mass-to-light ratios. We repeat the χ^2 minimization procedure. The resulting model parameters are listed in Table 7.4 (model II). Model II reproduces the relative positions of all four images to within 0.08 mas, compared to 0.16 mas for model I. And although the number of degrees of freedom does not change between models I and II, the reduced χ^2 of model II is significantly smaller than that of model I. A reduced $\chi^2 > 4.5$ corresponds to a probability of $4 \cdot 10^{-3}$ and model I can therefore be rejected as an appropriate model with 99.6 per cent confidence. So adding G2 improves the mass model significantly. A faint image will be formed to the south-east of G2, which can be removed by a very small core radius ($0.01''$) for G2, without changing the model parameters at any signifcant level. The critical and caustic structure of model II is shown in Fig. 7.4, where G2 has been given a core radius of $0.01''$.

If G1 and G2 are spiral galaxies, the relation between luminosity and velocity dispersion is $L \propto \sigma_{\|}^{2.5}$ (Tully & Fisher 1977), hence $\sigma_{\|}^{\rm G2} \approx 0.69 \cdot \sigma_{\|}^{\rm G1}$. The best model then has a slightly increased χ^2 of 1.6, still a considerable impovement over model I. The resulting model parameters deviate by less than 3 per cent in velocity dispersion and axis ratio from model II. The position angle of G1 becomes $-5.3°$, even in better agreement with the observed surface brightness position angle (see below). However, all values are well within the errors determined by Monte-Carlo simulations for model II (see Sect. 7.4.4 and Table 7.4).

Using a SIE for G2 would have the most influence on the position angle and axis ratio of the mass model of G1. However, the close agreement between these parameters and their observed values (see next paragraph), as well as the small resulting minimum χ^2, indicate that adding extra free parameters is not necessary.

7.4.3 Surface density versus surface brightness

The SD axis ratio of G1, $(b/a)_{\Sigma}^{\rm G1}$=0.74 (model II), is only slightly larger than the SB axis ratio of 0.69 ± 0.15 that we find from fitting a 2D-Gaussian profile to the SB distribution of G1. The same Gaussian fit gives a position angle of $(-6 \pm 13)°$, close to the SD position angle of $4.9°$. Although the SB profile of G1 is most likely not Gaussian, the position angle and axis ratio inferred from a 2D-Gaussian fit will give a good indication of the value for these parameters.

Strong evidence that B1127+385 is a gravitational lens system is given by the expected centre of the SD distribution of G1. In Fig. 7.5 the 99 per cent confidence contour of the central SD position of G1 is plotted. The two circles indicate the radio components A and B. If we assume that the two faint optical emission features are associated with A and B, we find that the optical emission peak of G1 (cross) falls perfectly inside the 99 per cent confidence contour. In other words, the position of the SB centre of G1 relative to the faint emission feature west of it coincides with the position of the SD centre of G1 relative to radio component A. This suggests G1 and G2 are indeed two lens galaxies and the faint optical emission features (Fig. 7.3) are associated with the radio components.

7.4.4 Monte-Carlo simulations

To investigate the overall reliability of model II, we performed Monte Carlo simulations. We minimize χ^2 for 10,000 models, where we add Gaussian distributed errors (1σ) to the relative image positions (0.1 mas), flux density ratios (0.15), galaxy pos-

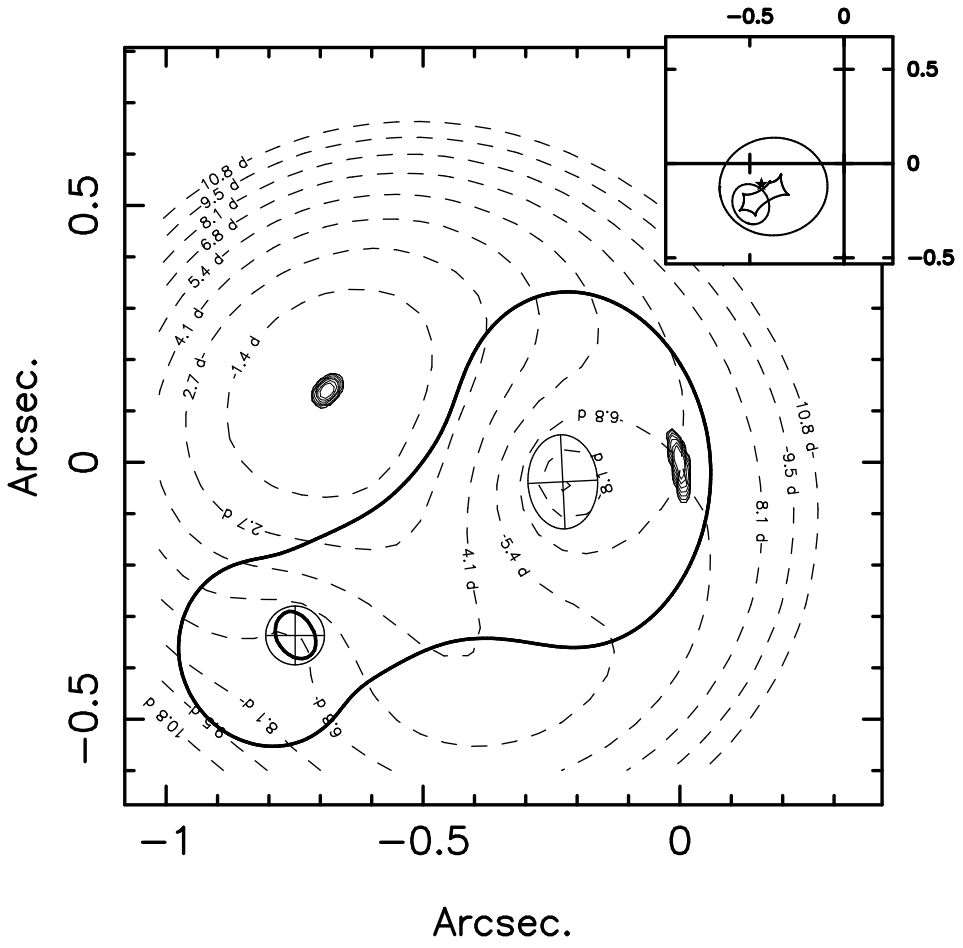

FIGURE 7.4— The critical curves (thick lines) and caustics (subpanel) of model II in Table 7.4. The star (subpanel) indicates the model position of the source as seen in the source plane. The solid contours depict the images at the positions of the radio components, if the source surface brightness is gaussian with a FWHM of 5 mas. The lens galaxy G1 is indicated by the cross-haired ellips, G2 by the cross-haired circle. The dashed contours indicate the time-delay surface for $z_{\rm d} = 0.5$, $z_{\rm s} = 1.5$, H_0=50 km s^{-1} Mpc^{-1}, $\Omega_{\rm m} = 1$ and $\Omega_\Lambda = 0$.

itions (5 mas) and velocity dispersion ratio between G1 and G2 (0.10).

Mass model parameters

The parameter probability density distributions of all models with χ^2<11.3 (99 per cent confidence interval) are shown in Fig. 7.6. The figure also shows the 99 per cent confidence interval (shaded) of the observed SB axis ratio and position angle. We see that the probability distributions of both the SD axis ratio and position angle have considerable overlap with these shaded regions. Hence, the axis ratio and position angle of the luminous matter agree well with those inferred from the SD distribution of G1. The mean values of the recovered position angle and separation of A1 relative to A2 are $(18 \pm 7)^\circ$ and 2.0 ± 0.2 mas and for B1 relative to B2 $(163 \pm 3)^\circ$ and 1.1 ± 0.2 mas, where the errors are the rms values of the parameter probability distributions. These recovered model parameters compare well with the observed values listed in Table 7.2. We consider this as strong evidence for the validity of the lens model.

To investigate the ratio $(\sigma_{\|,\rm G2}/\sigma_{\|,\rm G1})$, we calculate the minimum χ^2 for a range of this ratio, as shown in Fig. 7.6. The two ho-

rizontal lines indicate the 90 per cent and 99 per cent confidence intervals of the χ^2 distribution. The shaded region indicates the 99 per cent confidence interval for the ratio $(\sigma_{\parallel,\mathrm{G2}}/\sigma_{\parallel,\mathrm{G1}})$, determined above. The dot gives the ratio we determined from the $\sim$1 mag luminosity difference. We see that this ratio lies well below the 99 per cent confidence level, which shows that the ratio expected from the mass model agrees with that determined from the F–J relation. Also the ratio from the T–F relation agrees well.

Time delay

The predicted time delay between components A and B is $1.51^{+0.65}_{-0.60} \cdot f^{\mathrm{b}}_{\mathrm{d,s}}$ days (model II), where $f^{\mathrm{b}}_{\mathrm{d,s}}=(1+z_{\mathrm{d}}) \cdot [D_{\mathrm{d}}D_{\mathrm{s}}/(D_{\mathrm{ds}}\,\mathrm{Gpc})]$ with D_{d}, D_{ds} and D_{s} being the angular diameter distances between observer-lens, lens-source and observer-source, respectively and z_{d} the redshift of the lens. For typical lens (0.5) and source (1.5) redshifts, the delay is around $7/h_{50}$ days (flat universe with Ω_{m}=1). The velocity dispersion of G1 is $97.6^{+5.4}_{-5.4} \cdot f^{\mathrm{a}}_{\mathrm{d,s}}$ km s^{-1} (model II), where $f^{\mathrm{a}}_{\mathrm{d,s}}=\sqrt{D_{\mathrm{s}}/D_{\mathrm{ds}}}$. The errors indicate the 99 per cent confidence interval, inferred from the Monte-Carlo simulations. The 68 per cent (1σ) confidence intervals are $\sim$2.5 times smaller. Both the velocity dispersion and time delay depend on the chosen cosmological model through the angular diameter distances. A good description of the dependence of the model time delay and the angular diameter distances on the cosmologcal model is given in Helbig (1997). In a flat universe ($\Omega_{\mathrm{m}}+\Omega_{\Lambda}$=1) the difference in time delay is $\lesssim$10 per cent between Ω_{m}=1 and Ω_{m}=0.3. For a non-flat universe significant ($\gg$10 per cent) differences in time delay are possible, depending on the clumpiness of matter and the combination of Ω_{Λ} (normalised cosmological constant) and Ω_{m} (matter density). All other parameters in Table 7.4 are dimensionless and independent of the cosmological model.

We conclude that model II is in substantial agreement with all available radio and optical observations of B1127+385. However, more detailed studies of the SB distributions of G1 and G2 are necessary to improve the models and tighten the confidence intervals. Moreover both lens and source redshifts are unknown.

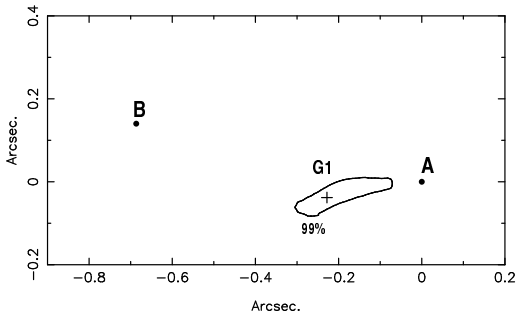

FIGURE 7.5— The 99 per cent confidence contour of the central SD position of G1, determined only on the basis of the VLBA radio images. The cross gives the 99 per cent confidence region of the SB distribution of G1 relative to the optical component west of it. The two circles indicate the two radio components, assuming they are associated with the optical emission features (see text). With this assumption, the SB centre of G1 is in excellent agreement with its inferred SD centre.

7.4.5 Galaxy colours, luminosities and M/L ratios

Having convinced ourselves that G1 and G2 are the lens galaxies, we compare their colours (F555W–F814W$\approx$1.9–2.0) with the synthesized galaxy colours in Fukugita, Shimasaku & Ichikawa (1995). For the different galaxy types approximate photometric redshifts of 0.3 (E), 0.4 (S0), 0.4 (Sab), 0.7 (Sbc) and 0.9 (Scd) are found. G1 and G2 could therefore be early type galaxies (including Sab) at low redshift (0.3–0.4) or late type galaxies at high redshift (0.7–0.9). The integrated luminosities of G1 and G2 in B band for the different types of galaxies are: $\log_{10}(L_{\mathrm{B}\odot})\approx 8.4-2\log(h_{50})$ (E), $8.8-2\log(h_{50})$ (S0 and Sab), $9.6-2\log(h_{50})$ (Sbc) and $9.8-2\log(h_{50})$ (Scd) for G1 ($\mathrm{H}_0 = 50 \cdot h_{50}$ km s^{-1} Mpc^{-1}), where we used the photometric redshifts found above and the B–F814W colours and K corrections from Fukugita et al. (1995). For G2 these values are 0.4 lower.

At a redshift z_{d}=0.3, I=22.5 (G1) corres-

	Model I	Model II
$(b/a)_{\Sigma}^{\rm G1}$	0.56	$0.74^{+0.10}_{-0.12}$
$(x,y)_{\rm G1}$ (mas)	(-228.0,	(-228.0,
	-38.0)	-38.0)
$\sigma_{\parallel}^{\rm G1}$ (km s^{-1})	$108.9 \cdot f_{\rm d,s}^{\rm a}$	$97.6^{+5.4}_{-5.4} \cdot f_{\rm d,s}^{\rm a}$
PA$_{\rm G1}$ (°)	-26.4	$4.9^{+28.2}_{-22.4}$
$(x,y)_{\rm G2}$ (mas)	—	(-749.0,
	—	-337.0)
$\sigma_{\parallel}^{\rm G2}$ (km s^{-1})	—	$0.79 \cdot \sigma_{\parallel}^{\rm G1}$
$(x,y)_{\rm src1}$ (mas)	-350.20±0.03,	-439.81±0.03,
	-1.10±0.07	-113.94±0.02
$(x,y)_{\rm src2}$ (mas)	-350.38±0.03,	-439.89±0.03,
	-1.62±0.07	-114.42±0.02
$r_{\rm B1/A1}$	0.56	0.71
$r_{\rm B2/A2}$	0.57	0.71
$\mu_{\rm A1,A2}$	-3.73	-4.65
	-3.66	-4.60
$\mu_{\rm B1,B2}$	2.09	3.28
	2.09	3.28
$\Delta t_{\rm (B1-A1)}$ (days)	$2.64 \cdot f_{\rm d,s}^{\rm b}$	$1.51^{+0.65}_{-0.60} \cdot f_{\rm d,s}^{\rm b}$
χ^2/NDF	4.5	1.1

TABLE 7.4— The minimum-χ^2 mass model parameters for B1127+385. Listed are the SD axis ratio $(b/a)_{\Sigma}$, the velocity dispersion $\sigma_{\parallel}$, the position angle (PA) of the major axis and the centre $(x,y)_{\rm G1}$ of G1 and the position and velocity dispersion of G2. The errors on axis ratio, velocity dispersion and position angle indicates the 99 per cent confidence interval inferred from Monte-Carlo simulations (Fig. 7.6). $(x,y)_{\rm src1/2}$ give the source positions of the subcomponents A1&B1 and A2&B2, respectively. Furthermore, $r_{A/B}$ and $\mu_{\rm A,B}$ give the derived flux density ratios and image magnifications. The coordinate system has been centered on image A1. The definitions of $f_{\rm d,s}^{\rm a}$ and $f_{\rm d,s}^{\rm b}$ are given in Sect. 7.4.4

ponds to an absolute magnitude $M_I \sim -19 - 5\log(h_{50})$. For an E and S0 type galaxy this would mean it is ∼4 mag underluminous compared to E and S0 type galaxies in the Hubble Deep Field (Mobasher et al. 1996). Placing the galaxy at higher redshifts would make the $V-I$ colours of G1 and G2 inconsistent with those of E or S0 type galaxies (Fukugita et al. 1995). The absolute I magnitude is consistent however with somewhat later type spiral galaxies at higher redshifts ($z_{\rm d} \gtrsim 0.5$). This would also explain why the velocity dispersions of G1 and G2 appears significantly smaller than those expected for L_* E and S0 type galaxies (e.g. Kochanek 1993, 1994).

Using the velocity dispersions listed in Table 7.4 (model II), the mass-to-light ratios (using the mass inside the Einstein radius, the photometric lens redshifts and the total B luminosity) of G1 and G2 are: $(M/L_{\rm B}) \sim 60 \cdot h_{50}$ $\rm M_{\odot}/L_{B,\odot}$ (E), $\sim 35 \cdot h_{50}$ (S0 and Sab), $\sim 10 \cdot h_{50}$ (Sbc) and $\sim 10 \cdot h_{50}$ (Scd) (assuming $z_{\rm s}$=1.5). All of these mass-to-light ratios are significantly larger than normal galaxies of similar type, except for the higher redshift late-type spiral galaxies. Dust obscuration could increase the mass-to-light ratio, however it would also make the F555W–F814W colours less reasonable.

We should note however that at intermediate redshift an error of 0.2 in redshift introduces ∼1 mag error in B and as mentioned, dust obscuration (e.g. B1600+434; Jaunsen & Hjorth 1997; Koopmans, de Bruyn & Jackson 1998) or luminosity evolution (e.g. Bender, Ziegler & Bruzual 1996; Hudson et al. 1998) have not been taken into account.

The results above therefore give only an indication. Redshifts of G1 and G2, and more accurate colours are vital to distinguish between galaxy types and their mass-to-light ratios. To obtain the redshifts of

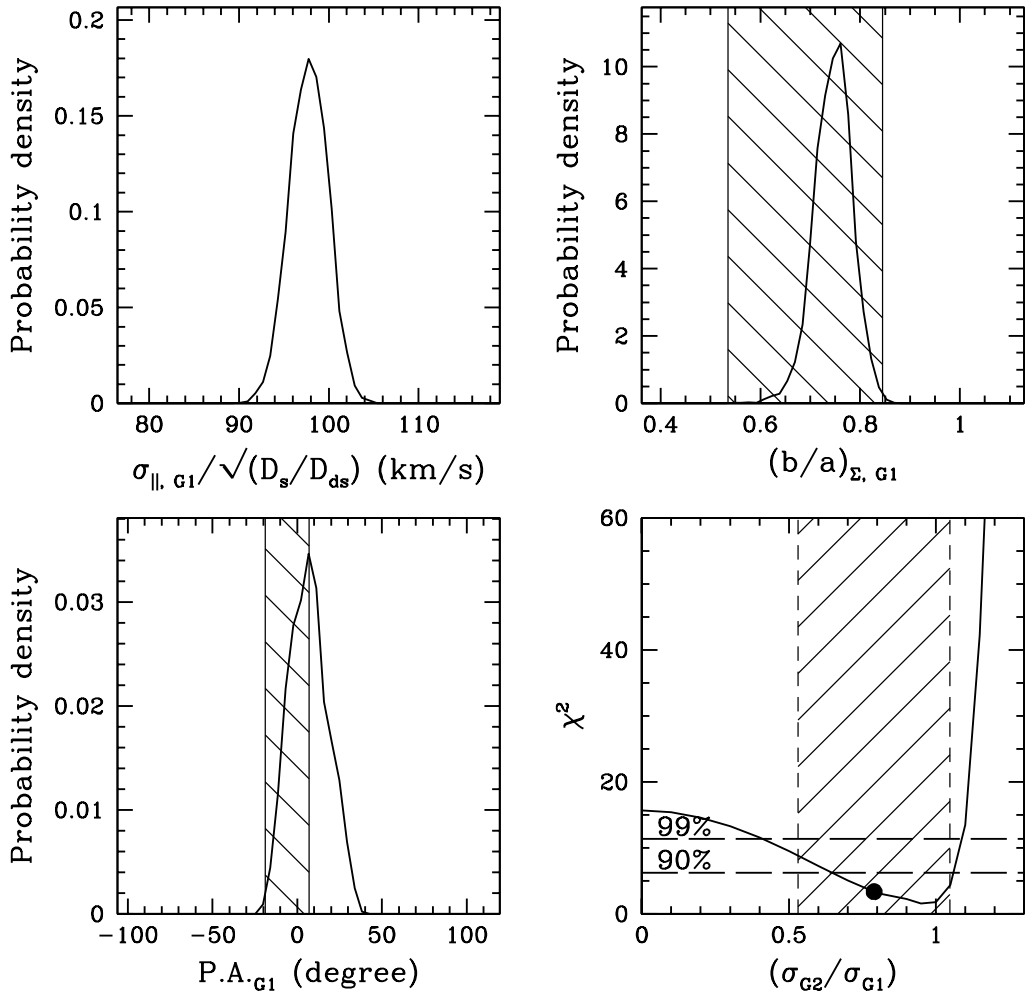

FIGURE 7.6— From upper left to lower right: Monte-Carlo probability density distributions (of models with χ^2<11.3; 99 per cent confidence interval) of $\sigma_{\|,G1}$, $(b/a)_{\Sigma,G1}$ and P.A.$_{G1}$. The shaded regions (99 per cent confidence interval) indicate these parameters as derived from the SB distribution of G1. The lower right panel shows χ^2 as function of $(\sigma_{\|,G2}/\sigma_{\|,G1})$. The observationally derived ratio falls well within the region containing 90 per cent of the χ^2 distribution.

these galaxies in a reasonable integration time, one requires an 8 or 10-m class telescope (e.g. the Very Large Telescope (VLT) or Keck).

7.4.6 Source

We estimate I $\sim$24.5 for the optical emission associated with radio component A. Correcting for a magnification of 4.6 (Table 7.4), this corresponds to an intrinsic I$\sim$26, a luminosity of $\log_{10}(L_{I\odot})\sim 9.8 - 2\log(h_{50})$ at $z_s = 1.5$ and an absolute magnitude $M_I\sim -19 - 5\log(h_{50})$ at $z_s = 1.5$ (no K-corrections applied).

Comparing this with the absolute I magnitudes of galaxies in the Hubble Deep Field, the source is most consistent with a spiral galaxy of type Sbc or later, as most E and S0 type galaxies have $M_I \lesssim -23$ (Mobasher et al. 1996). At a redshift of $\sim$3 the

luminosity increases to $\log_{10}(L_{I\odot})\sim 10.5 - 2\log(h_{50})$, still in the range of spiral galaxies (type Sab or later; Mobasher et al. 1996). We should note here that these values have not been corrected for evolution or dust absorption, internally or by the lens galaxies (G1 and G2).

However, the CLASS lens systems B0712+472 (Jackson et al. 1998) and B1933+503 (Sykes et al. 1998; Jackson, private communication) also appear to have very low luminosity sources, which could indicate that a significant fraction of the weak (few mJy) flat spectrum radio sources are associated with low luminosity objects, possibly late-type spiral galaxies.

7.5 Conclusions

A new gravitational lens system with two images separated by 701 ± 1 mas has been discovered in the CLASS survey. The two radio components have a flat spectrum between 0.327 GHz (WSRT; WENSS), 1.7 GHz (MERLIN), 5.0 GHz (MERLIN) and 8.4 GHz (VLA). VLBA observations show substructure in both images. An HST I-band image reveals two emission features close to the radio components, which we identify with two lens galaxies. The colours and mass-to-light ratios of these galaxies seem to favour two late-type spiral galaxies at relatively high redshifts ($z_{\rm d} \gtrsim 0.5$).

The VLBA radio structure and optical HST emission are consistent with a two-lens mass model, where a SIE and SIS mass distribution are placed on the SB centres of G1 and G2, respectively. This model is able to reproduce the separations and position angles of the VLBA substructure in radio components A and B, and their flux density ratios. Our best model has a reduced χ^2 of 1.1. Assuming both lens galaxies are spiral galaxies, χ^2 slightly increases to 1.6. Omitting G2 in the mass model increases the reduced χ^2 to 4.5, which can therefore be excluded as an appropriate model with 99.6 per cent confidence.

Our best model gives a SD axis ratio of $0.74^{+0.10}_{-0.12}$, position angle of $(4.9^{+28.2}_{-22.4})^\circ$ and velocity dispersion of $97.6^{+5.4}_{-5.4} \cdot f^{\rm a}_{\rm d,s}$ km s^{-1}. The predicted time delay between radio components A and B is $1.51^{+0.65}_{-0.60} \cdot f^{\rm b}_{\rm d,s}$ days. For a typical lens (0.5) and source redshift (1.5), a time-delay of $\sim$7 days is expected for H_0=50 km s^{-1} Mpc^{-1} and $\Omega_{\rm m} = 1$ in a flat universe. WSRT monitoring data is in hand, to see if the lensed object in B1127+385 is variable and therefore useful for determining a time-delay between the lensed images. This time-delay can constrain the Hubble parameter (Refsdal 1964). The errors on these parameters indicate the 99 per cent confidence interval of the probability density distributions found from Monte-Carlo simulations.

Having constructed a consistent model within the lensing hypothesis – explaining both the available radio and optical data of B1127+385 – it appears that B1127+385 most likely is a new gravitational lens system.

Acknowledgments

LVEK and AGdeB acknowledge the support from an NWO program subsidy (grant number 781-76-101). This research was supported in part by the European Commission, TMR Programme, Research Network Contract ERBFMRXCT96-0034 'CERES'. The National Radio Astronomy Observatory is a facility of the National Science Foundation operated under cooperative agreement by Associated Universities, Inc. MERLIN is a national UK facility operated by the University of Manchester on behalf of PPARC. This research used observations with the Hubble Space Telescope, obtained at the Space Telescope Science Institute, which is operated by Associated Universities for Research in Astronomy Inc. under NASA contract NAS5-26555. The Westerbork Synthesis Radio Telescope (WSRT) is operated by the Netherlands Foundation for Research in Astronomy (ASTRON) with the financial support from the Netherlands Organization for Scientific Research (NWO).

References

Bender R., Ziegler B., Bruzual G., 1996, ApJL, 463, 51

Faber S.M., Jackson R.E., 1976, ApJ, 204, 668

Fukugita M., Turner E.L., 1991, MNRAS, 253, 99

Fukugita M., Shimasaku K., Ichiwaka T., 1995, PASP, 107, 945
Helbig, P., Proceedings of the Workshop on Golden Lenses, 1997, http://multivac.jb.man.ac.uk:8000/ceres/workshop1/proceedings.html
Hudson M.J., Gwyn S.D.J., Dahle H., Kaiser N., ApJ, 503, 531
Jackson N., et al., 1998, MNRAS, 296, 483
Jaunsen A.O., Hjorth J., 1997, A&A, 317, L39
Kayser R., 1990, ApJ, 357, 309
Kochanek C.S., 1991, ApJ, 379, 517
Kochanek C.S., 1993, ApJ, 419, 12
Kochanek C.S., 1994, ApJ, 436, 56
Kochanek C.S., 1996, ApJ, 466, 638
Koopmans L.V.E., de Bruyn, A.G., Jackson N., 1998, MNRAS, 295, 534
Kormann R., Schneider P., Bartelmann M., 1994, A&A, 284, 285
Mobasher B., Rowan-Robinson M., Georgakakis A., Eaton N., 1996, MNRAS, 282, 7L
Patnaik A.R., Browne I.W.A., Wilkinson P.N., Wrobel J.M., 1992, MNRAS, 254, 655
Pearson T.J., Shepherd M.C., Taylor G.B., Meyers S.T., 1994, BAAS, 185, #08.08
Refsdal S., 1964, MNRAS, 128, 295
Refsdal S., 1966, MNRAS, 134, 315
Rhee M-H., 1996, PhD Thesis, University of Groningen
Schneider P., Ehlers J., Falco E.E., 1992, Gravitational Lenses, Springer Verlag, Berlin
Shepherd M.C., 1997, ADASS VI, A.S.P Conference Series, vol 125, eds., Gareth Hunt and H.E. Payne, p77
Sykes, C. M., et al. 1998, MNRAS 301, 310
Thompson A.R., Moran J.M., Swenson G.W., 1986, Interferometry and Synthesis in Radio Astronomy, Wiley-Interscience publication, p262
Tully R.B., Fisher J.R., 1977, A&A, 54, 661

8

CLASS B0827+525: 'Dark lens' or binary quasar?

Based on L.V.E. Koopmans, A.G. de Bruyn, et al. 1999, Astronomy & Astrophysics, submitted

We present radio, optical, near–infrared and spectroscopic observations of the source B0827+525. We consider this source as the best candidate from the *Cosmic Lens All–Sky Survey* (CLASS) for a 'dark lens' system or binary quasar. The system consists of two radio components with somewhat different spectral indices, separated by 2.815 arcsec. VLBA observations show that each component has substructure on a scale of a few mas. A deep *K*–band exposure with the W.M. Keck–II Telescope reveals emission near both radio components. The *K*–band emission of the weaker radio component appears extended, whereas the *K*–band emission from brighter radio component is consistent with a point source. *Hubble Space Telescope F160W*–band observations with the NICMOS instrument confirms this. A redshift of 2.064 is found for the brighter component, using the LRIS instrument on the W.M. Keck–II Telescope. The probability that B0827+525 consists of two unrelated compact flat–spectrum radio sources is ∼3%, although the presence of similar substructure in both component might reduce this. We discuss two scenarios to explain this system: (i) CLASS B0827+525 is a 'dark lens' system or (ii) B0827+525 is the first binary radio–loud quasar. B0827+525 has met *all* criteria that thus far have in 100% of the cases confirmed a source as an indisputable gravitational lens system. Despite this, no lens galaxy has been detected with $m_{\rm F160W}\leq$23 mag. Hence, we might have found the first binary radio–loud quasar. At this moment, however, we feel that the 'dark lens' hypothesis cannot be excluded yet.

8.1 Introduction

There are several indirect ways to detect the presence of dark matter in galaxies at relatively low redshifts (e.g. microlensing, rotation curves of spiral galaxies, polar–ring galaxies, etc.). However, at intermediate and high redshifts, weak and strong lensing are the only methods of detecting the presence of dark matter on galaxy scales.

Gravitational lensing does not depend on the luminosity or color of the lensing mass distribution. One can therefore expect to find 'dark lens' galaxies in large GL surveys, if they make up a significant fraction of massive galaxies (e.g. Hawkins 1997; Jackson et al. 1998; Kochanek, Falco & Muñoz 1999). On the basis of confirmed and candidate large–separation ($\gtrsim$3 arcsec) GL systems, which were all optically selected, Hawkins (1997) concludes that around

75% of all galaxies could be 'dark' (i.e. extremely underluminous). This high fraction was recently shown to be inconsistent with observational results (Jackson et al. 1998) from the *Cosmic Lens All–Sky Survey* (CLASS; Browne et al. 1997; Myers et al. 1999). A very high fraction of dark galaxies is thus excluded, although a smaller fraction ($\leq$10%) cannot be ruled out.

In this paper, we present the strongest 'dark lens' candidate found in the CLASS survey: CLASS B0827+525. In Section 8.2, we present radio, optical, near–infrared and spectroscopic observations of this system. In Section 8.3, we derive constraints on the lens galaxy mass–to–light ratio and compare those with observations of 'luminous lens' galaxies. In Section 8.4, we summarize our results and suggest future work on this system.

8.2 Observations

The CLASS survey aims to find all multiply–imaged flat–spectrum ($\alpha \leq 0.5$ for $S_\nu \propto \nu^{-\alpha}$) radio sources in the northern hemisphere with a total flux density of $S_{5\mathrm{GHz}} \geq 30$ mJy, a flux–density ratio between lens images $\leq$10, a Galactic latitude $|b| > 10^\circ$ and a component separation $\geq$0.3 arcsec. The scientific goal of the survey is to create a sample of GL systems, that can be used to study the structure and evolution of lens galaxies at intermediate redshifts *and* constrain the cosmological parameters, in particular the Hubble parameter (H_0). At present CLASS has discovered at least 17 new GL systems (Myers et al. 1999).

8.2.1 Radio observations

If not specified otherwise, the radio data presented in this section are flux–calibrated in the data–reduction package AIPS and self–calibrated, imaged and model-fitted in DIFMAP (Shepherd 1997). To obtain flux–densities of the two radio components of B0827+525, the uv–data was fitted by typically two Gaussian components.

As part of the CLASS sample of around 15 200 flat–spectrum radio sources observed during the 1994, 1995 and 1998 *Very–Large–Array* (VLA) A–array seasons (Myers et al. 1999), a 30–sec snapshot of B0827+525 was made at 8.5 GHz on 1995 August 13. The calibrated VLA image (Fig.8.1) shows two unresolved components that are separated by 2.8 arcsec and have a flux–density ratio of 2.7 [i.e. $S_\mathrm{A} \approx 24$ mJy and $S_\mathrm{B} \approx 9$ mJy].

With an average source density in the CLASS survey of $\approx$1 per sq. deg, the probability of chance alignment of two unrelated compact radio–loud quasars within $\leq$2.8 arcsec is around $2 \cdot 10^{-6}$, whereas the lensing rate is around 10^{-3}. In a sample of 15 200 sources the occurrence of such a close alignment has a probability of only 3%. B0827+525 was therefore regarded as a candidate GL system.

To improve the resolution and obtain a two–point spectral index between the radio components, a snapshot image of B0827+525 was made on 1997 January 3 with the *Multi–Element Radio Linked Interferometer Network* (MERLIN) at 5 GHz. A flux–density ratio of 2.5 was found [i.e. $S_\mathrm{A} \approx 34$ mJy and $S_\mathrm{B} \approx 14$ mJy] and a component separation of 2.8 arcsec, very similar to the VLA 8.5–GHz observations. Subsequent long–track MERLIN 5–GHz observations were made on 1997 December 8, with a total integration time on the source of $\approx$10 hours. The calibrated image (Fig.8.1) has an rms–noise level of 60 μJy beam^{-1} and a resolution of $\approx$50 mas. Both components remain unresolved. The flux–densities are $S_\mathrm{A} \approx 34.0$ mJy and $S_\mathrm{B} \approx 14.8$ mJy, respectively. No sign of extended emission is detected in the image above a level of 0.6%. The similarity in flux–density ratio at 8.5 and 5 GHz strengthened the case for a lensing explanation of this system.

To improve the resolution by another order of magnitude, B0827+525 was observed with the *Very–Long–Baseline–Array* (VLBA) at 5 GHz on 1997 August 2. Snapshots were obtained over a range of hour angles to improve the uv–coverage. Phase referencing was done by rapid switching between the nearby strong calibrator B0828+493 (2 min) and B0827+525 (5–7 min). The total integration time on B0827+525 was 35 min. The final calibrated image (Fig.8.1) has a resol-

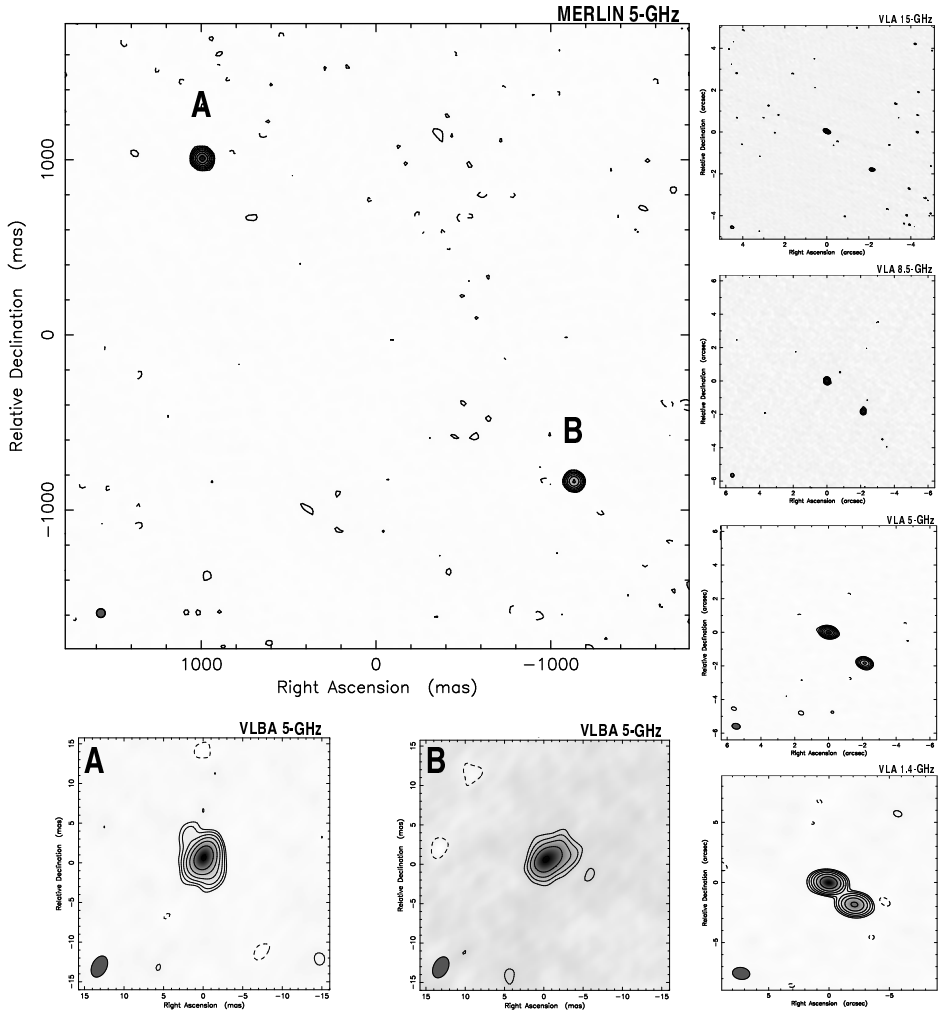

FIGURE 8.1— Summary of the VLA, MERLIN and VLBA radio images of B0827+525 (see text for more details). Contours start at the 3–σ level and increase by factors of 2. The first contours are 0.19 mJy beam^{-1}, 0.37 mJy beam^{-1}, 0.37 mJy beam^{-1}, 1.15 mJy beam^{-1}, 0.88 mJy beam^{-1}, 0.40 mJy beam^{-1}, 0.77 mJy beam^{-1}, for the MERLIN 5–GHz, VLBA 5–GHz (A), VLBA 5–GHz (B), VLA 15–GHz, 8.5–GHz (discovery image), 5–GHZ and 1.4–GHz images, respectively

ution of 2.5 mas and an rms–noise level of 0.1 mJy beam^{-1}. The two radio components were each modeled by two Gaussian sub–components. Component A shows a NE–SW extension, whereas component B shows an area of weak extended emission in the NW–direction. The low SNRs of the NE–component in image A and the NW–extension of image B does not warrant modeling them by more than two sub-components. The positions of the best–fit Gaussians and their respective flux densities are listed in Table 8.1.

Both radio components show fairly flat spectra from 4.9 to 8.5 GHz. The integrated flux density of B0827+525 (A+B) in the WENSS survey, (70±5 mJy at 325 MHz, mean epoch 1992.2), is about equal to the flux density at 1.4 GHz in the NVSS, FIRST and WSRT observations taken in the sum-

	A1	A2	B1	B2
Δx (mas)	1064.02	1063.18	−1074.16	−1076.43
Δy (mas)	930.74	929.89	−900.40	−899.78
maj. (mas)	–	–	1.75	2.23
min/maj	–	–	0.65	0.55
θ (°)	–	–	-31.40	5.80
$S_{4.9}$ (mJy)	24.8±0.1	6.8±0.1	9.3±0.1	3.6±0.1

TABLE 8.1— VLBA 5–GHz data on B0827+525 (1997 Aug. 2) The VLBA phase–center was RA $08^h31^m5\overset{s}{.}36200$, DEC $52°25'20\overset{''}{.}24100$. Positions $(\Delta x, \Delta y)$ are given with respect to to this phase–center. The 4.9–GHz flux–density ($S_{4.9}$) of the sub–components and their deconvolved major axis, axial ratio and position angle (N→E) are also given. The sub–components of component A are unresolved. The positional error is 2.5 mas divided by twice the SNR of the components

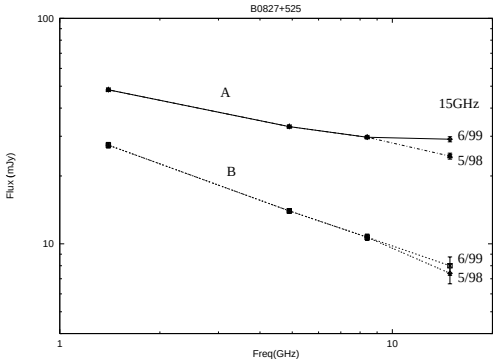

FIGURE 8.2— Radio spectra of B0827+525 A and B, determined with the VLA in A–array at 1.4, 4.9, 8.5 and 14.9 GHz on 1999 June 27

mer of 1997. This suggests that the individual component spectra must flatten to a spectral index of zero below 1.4 GHz. Alternatively, one of the component spectra could become inverted leaving room for the other to remain straight. High resolution low frequency data are needed to distinguish between these possibilities.

A 2–month monitoring campaign (8 epochs) with the WSRT at 1.4 GHz (with 15–arcsec resolution) in the period July-September 1997 indicates variability in the total flux density: the source flux density slowly decreased from 71 to 58 mJy with a typical error of about 1 mJy in individual measurements. It is not clear to which component these variations should be attributed. The variation time scale is rather short even though both components are compact. It is perhaps more likely that the 1.4 GHz variations are due to refractive interstellar scintillation (e.g. Rickett et al. 1984), an explanation requiring a less extreme size for the components.

To examine the radio spectra of both components in more detail, near–simultaneous VLA 1.4, 4.9, 8.5 and 14.9–GHz (L, C, X and U–band) observations in A–array were done on 1999 June 27 (Table 8.2). The radio spectra for both components are shown in Fig.8.2. Components A and B have fairly different radio spectra with spectral indices $\alpha_{1.4}^{8.5} = 0.27 \pm 0.01$ (A) and $\alpha_{1.4}^{8.5} = 0.52 \pm 0.01$ (B) (where $S_\nu \propto \nu^{-\alpha}$). Also variability in component A at 14.9 GHz was detected between the 1998 May 15 and 1999 June 27 VLA observations, which is most likely intrinsic and not scintillation.

Variability at both lower (1.4 GHz) and higher (15 GHz) frequencies makes a direct comparison of the spectral indices difficult. The formal difference in spectral index does not disqualify the source as possible GL candidate, but complicates the argumentation in a 'dark lens' hypothesis. We will return to this issue in Sect.8.4.

8.2.2 Optical and near–infrared observations

Hubble Space Telescope (HST) observations were made on 1998 April 18 with the *Near–Infrared Camera and Multi–Object Spectrometer* (NICMOS) at 1.6 μm (F160W), roughly corresponding to ground–based *H*–band. The NIC1 camera was used which provides a detector scale of 43 mas pixel^{-1} and a field–of–view of $11'' \times 11''$. The total exposure time was

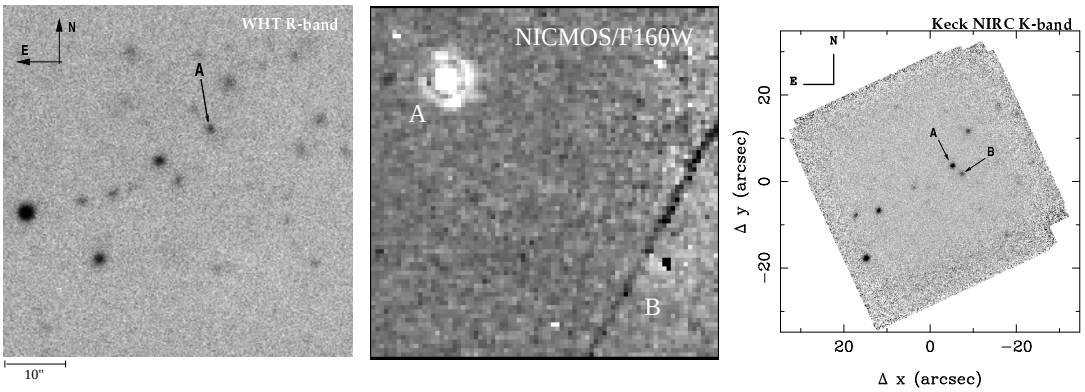

FIGURE 8.3— Left: *R*–band image of B0827+525, observed 1998 May 19 with the WHT on La Palma. Middle: HST F160W NICMOS image of B0827+525, observed on 1998 April 18. The separation between components A and B is 2.8 arcsec. Right: NIRC *K*–band image of B0827+525, observed with the W.M Keck–II Telescope on 1998 May 9

TABLE 8.2— VLA multi–frequency data on B0827+525, taken near–simultaneously on 1999 June 27. The internal errors are indicated.

ν (GHz)	$S_{\rm A}$ (mJy)	$S_{\rm B}$ (mJy)
14.9	29.1±0.4	8.0±0.4
8.5	29.7±0.1	10.7±0.1
4.9	33.1±0.1	14.0±0.1
1.4	48.2±0.3	27.4±0.3

TABLE 8.3— VLA multi–frequency data on B0827+525, taken near–simultaneously on 1999 June 27. The internal errors are indicated.

2624 sec. The data were subjected to the standard NICMOS calibration pipeline in IRAF[1] which corrects for known instrumental effects. The image was cut around B0827+525 and rotated to correct to standard orientation. The final calibrated image is shown in Fig.8.3 (middle). The primary northern component (A) is unresolved and clearly detected ($m_{\rm F160W}$=19.6±0.2 mag). Component B is just barely detected as a region of extended emission ($m_{\rm F160W}$=22.6±0.2 mag). No sign of a lensing galaxy is seen in the image to $m_{\rm F160W}$=23 mag, although the extended emission near image B could partly be from a possible lens galaxy.

[1]IRAF (Image Reduction and Analysis Facility) is distributed by the National Optical Astronomy Observatories, which are operated by the Association of Universities for Research in Astronomy under cooperative agreement with the National Science Foundation.

Similarly, B0827+525 was observed in *K*–band on 1998 May 9 with the *Near InfraRed Camera* (NIRC) at Keck. A total of 25 frames, each having a 60–sec integration time, were obtained of the field. The telescope was moved by approximately 10–15 arcsec between individual integrations. The seeing at the time of the observations was 0.6–0.75 arcsec (FWHM). The exposures were combined and rotated to correct the orientation and the resulting image is shown in Fig.8.3 (right). The observations confirm the conclusions drawn from the *HST* exposure, that image A is consistent with a point source and image B seems somewhat extended.

An *R*–band image was taken on 1998 May 19 on the WHT. Two 600-sec exposures were obtained with a seeing of 1.4–1.5 arcsec (FWHM). It was re-observed on 1998 May 20 with two exposures of 600–sec and one of 300–sec exposure, respectively. The seeing was around 1.0 arcsec (FWHM). All exposures were combined and reduced in the standard way in the data–reduction package IRAF. The resulting image (Fig.8.3 left) only show image A, whereas image B is not detected above the noise level. We estimate for component A an apparent magnitude of $m_{\rm H}\approx22\overset{\rm m}{.}0$–$22\overset{\rm m}{.}5$ and for component B a lower limit $m_{\rm H}\gtrsim24\overset{\rm m}{.}0$.

8.2.3 Spectroscopic observations

CLASS B0827+525 was observed with the *Low Resolution Imaging Spectrograph* (LRIS; Oke et al. 1995) on the W. M. Keck II Telescope on the night of 1998 April 21. Three exposures were taken in longslit mode with a total exposure time of 4500 sec. The 300 grooves mm^{-1} grating was used, giving a dispersion of 2.44 Å per pixel. The slit was placed along both components, with a position angle of 50°. The final spectrum covers a wavelength range of 4024–9012 Å. The spectra were reduced using standard IRAF tasks. A correction for the response of the CCD was determined from observations of the Oke standard star BD332642 (Oke 1990). The corrected spectra were weighted by the squares of their SNRs and co–added to produce the final B0827+525 spectrum. Fig.8.4 shows the spectrum, which has been smoothed using a boxcar kernel with a width of five pixels. Emission lines associated with Si-IV λ1397, C-IV λ1549, He-II λ1641, and possibly C-III] λ1909 are seen, establishing a source redshift of 2.064. No evidence for a second redshift, either from component B or a lens galaxy, is seen in the spectrum.

8.3 Analysis

Before proceeding with our analysis, let us summarize the most important observational results. We have found that B0827+525 consists of two radio components, separated by 2.8 arcsec. Both components are variable and have substructure at a scale of a few mas. The radio spectra from 1.4 to 14.9 GHz are somewhat different. The redshift for the brightest radio component (A) is 2.064. Optical counterparts for both radio components are found in *H* and *K*–band observations. The emission associated with the fainter radio component appears extended, which could suggest that it is very faint galaxy emission.

8.3.1 The 'dark lens' hypothesis

To compare the observed limits on the mass–to-light ratio of a possible lens galaxy with those found for typical lens galaxies, we first calculate the velocity dispersion of the lensing mass, using the Singular–Isothermal–Sphere (SIS) mass model (Binney & Tremaine 1987). This model relates the lens–image separation ($\Delta\theta$) to a line–of–sight velocity dispersion (σ), given the cosmological model and the source– and lens redshifts:

$$\Delta\theta = 8\pi \cdot \left(\frac{\sigma}{c}\right)^2 \left(\frac{D_{\rm ds}}{D_{\rm s}}\right), \qquad (8.1)$$

where c is the velocity of light, and $D_{\rm ds}$ and $D_{\rm s}$ are the angular–diameter distances between lens–source and observe–source, respectively (e.g. Schneider, Ehlers and Falco 1992). The angular–diameter distance is function of redshifts and cosmological model. Using the component separation, we can furthermore calculate the mass contained inside the Einstein radius

$$M(\Delta\theta) = 3.1 \cdot 10^{10} \times \left(\frac{\Delta\theta}{1''}\right)^2 \left(\frac{D}{\rm Gpc}\right) \ {\rm M}_\odot, \qquad (8.2)$$

where $D \equiv D_{\rm d} D_{\rm s} / D_{\rm ds}$ and $D_{\rm d}$ is the angular–diameter distance to the lens galaxy. To calculate the luminosity of the lens galaxy, using the filter band λ (e.g. *U, B, V,* ...), we subsequently use the relation

$$L_\lambda / {\rm L}_{\lambda,\odot} = 10^{0.4 \cdot (M_{\lambda,\odot} - m_\lambda + {\rm DM} + {\rm K}_\lambda)}, \qquad (8.3)$$

where DM is the distance modulus of the lens galaxy, $\rm M_{\lambda,\odot}$ is the absolute magnitude of the sun, m_λ is the apparent magnitude of the lens galaxy and $\rm K_\lambda$ is the K–correction for the filter band λ. We use the lower limit of $m_{\rm F160W}$>23 mag on the lens galaxy, found from the HST exposure (Fig.8.3) to constrain the mass–to–light ratio in *H*–band. We use the *H*–band observations, because K corrections are relatively small (<0.2 mag for $z \leq 1$ and $<0\overset{\rm m}{.}5$ for $z \leq 2$; Poggianti 1997). We do not use evolutionary corrections and assume $M_{\rm H,\odot} = 3\overset{\rm m}{.}46$.

For a source redshift of 2.064, we have plotted the *H*–band mass–to–light ratio in Fig.8.5 for two different cosmologies (A: $\Omega_{\rm m}$=1 and Ω_Λ=0; B: $\Omega_{\rm m}$=0.3 and Ω_Λ=0.7), assuming $\rm H_0$=65 km/s/Mpc. We assume a Friedmann–Robertson–Walker universe. A minimum mass–to–light ratio around 100

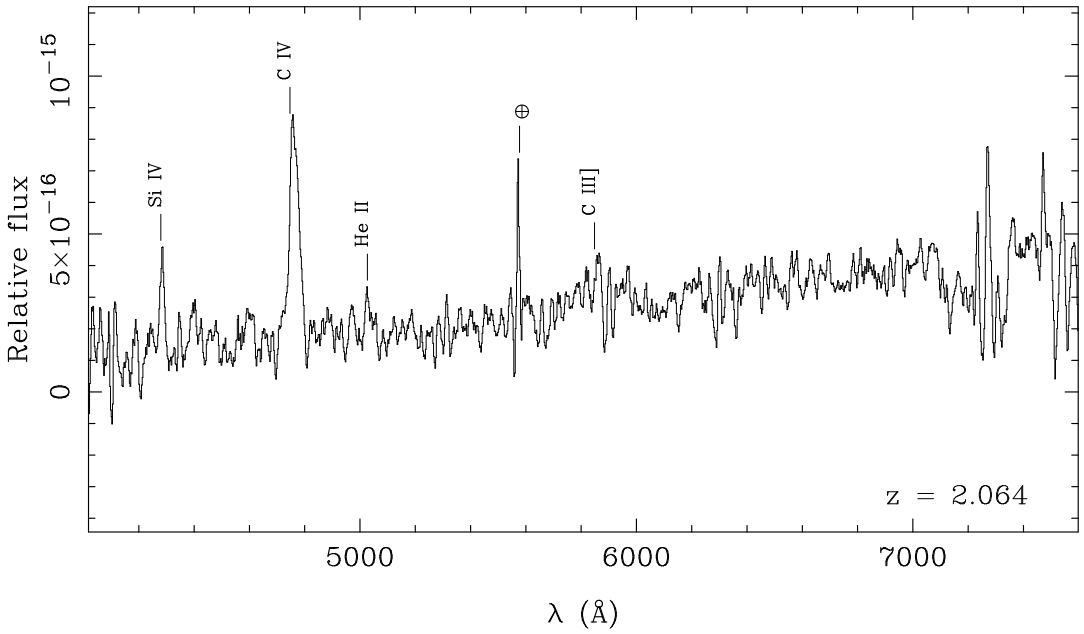

FIGURE 8.4— LRIS spectrum of B0827+525, observed with the W.M Keck II Telescope on 1998 April 21

is found, using cosmology B. This mass–to–light ratio implies a lens–galaxy redshift around 1.5 and a high velocity dispersion of 400–500 km/s. For cosmology A, the minimum mass–to-light ratio would increase to about 200. From Jackson et al. (1998) we find that the mass–to–light ratio in *H*–band for B0827+525 is a factor 15–100 larger than the *H*–band mass–to–light ratios of the other lens galaxies in the CLASS survey.

In Fig.8.6, we have plotted the expected *H*–band magnitude of the lens galaxy as function of redshift, galaxy type and cosmology. We used (i) the velocity dispersion determined from eqn.8.1, (ii) the relation between velocity dispersion and *B*–band magnitude of elliptical and spiral galaxies from Fukugita et al. (1991) and (iii) the colors and K–corrections from Poggianti (1997). From Fig.8.6 an upper limit on $m_{\rm H}$ of 17 mag is found, nearly independent of galaxy type. If evolutionary corrections are applied (Poggianti 1997), we find no significant differences in these results. The upper limit is at least 6 mag brighter than the lower limit on the *H*–band magnitude of the possible lens galaxy, whereas for all confirmed GL systems (Jackson et al. 1998), for which the lens and source redshifts are known, differences between the observations and the model is $\lesssim$1 mag.

Hence if B0827+525 is a lens system then the object is indeed a 'dark lens' system. However, also image B must be darkened and reddened by the 'dark lens' galaxy. For further discussion of this possibility we refer to Sect.8.4.

8.3.2 The binary quasar hypothesis

As argued in Sect.8.2.1 the probability of a chance alignment of two radio–loud quasars is rather small. Hence, *if* the source is not a lens systems it is most likely a pair of physically close quasars. We call this the 'binary quasar' hypothesis even though we have no evidence for the quasar nature of component B in the optical.

The compact flat–spectrum radio source population selected via CLASS is gener-

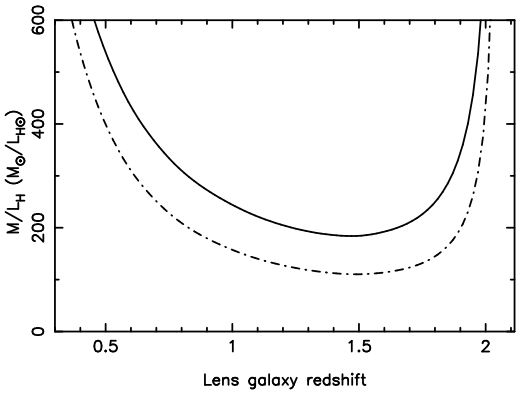

FIGURE 8.5— Estimated lower limit on the *H*–band mass–to–light ratio of the lens galaxy, as function of redshift (see text). The solid line is for a (Ω_m=1, Ω_Λ=0) cosmology, the dot–dashed line for a (Ω_m=0.3, Ω_Λ=0.7) cosmology. We assume H_0=65 km/s/Mpc

ally believed to emit its radio emission in a highly non-isotropic manner (e.g. Orr & Browne 1982) with the radio axis pointed in our direction within a small angle. As first argued by Scheuer and Readhead (1979) there should then be many radio–quiet quasars (QSO) for every radio–loud quasar (QSR). It is then obvious that the probability of finding two related radio–loud quasars pointed at us is rather small. In fact we can probably state that for every QSR–QSR pair there should be around 20 QSR-QSO pairs in the CLASS survey, if $\approx$5% of all QSOs are also radio–loud, i.e. $\geq$30 mJy at 8.5 GHz (e.g. Hooper et al. 1995; Bischof & Becker 1997).

Under the assumption that B0827+525 is the only QSR–QSR pair (i.e. binary radio–loud quasar) in CLASS, the probability that a flat–spectrum radio source is part of a QSR–QSR pair is around 1 in 15 000. This means that the probability that a CLASS source is part of a QSR–QSO pair is around 1 in 750. If we assume that only about 50% of the CLASS sources are of AGN origin, this number increases to 1 in about 375. In the Large Bright Quasar Survey (LBQS; Hewett et al. 1998) two QSO–QSO pairs were found from a sample of around 1000 optically selected quasars, hence 1 in 500. This number is very close to that found from the CLASS survey, which means that the presence of one QSR–QSR pair in the CLASS survey is consistent with the rate of QSO–QSO pairs in optical quasar surveys (see also Kochanek et al. 1999).

However, if B0827+525 is a binary radio–loud quasar and we compare it with the list of wide separation quasar pairs in Kochanek et al. 1999, we notice two things: First, B0827+525, has the smallest separation (2.8″ or 23 kpc/h_{50}) of all quasar pairs. Second, only 2 out of 13 non–lens quasar pairs have higher redshifts (i.e. LBQS 1429-008 and Q2345+007). On the other hand, B0827+525 would also be one of the largest separation lens systems (e.g. Jackson et al. 1998; CASTLES[2] survey). B0827+525 thus appears to be at the parameter–space border delineated by the optical quasar pairs listed by Kochanek et al. (1999) and the confirmed GL systems. It is difficult to see how significant these issues are in the context of binary quasars and how it possibly relates to the fact that both quasars are radio-loud.

8.4 Discussion & Conclusions

If taken at face value, most of the observational evidence seems to be in favor of B0827+525 being a binary radio–loud quasar: (i) somewhat different radio spectra from 1.4 to 14.9 GHz for the two components, (ii) a different radio and optical brightness ratio, (iii) the weaker radio component appears slightly resolved, (iv) the extended nature of the optical and near–infrared emission near component B, whereas that of image A is compact and (v) the agreement with the number statistics of binary radio–loud quasars in the CLASS survey with those of optical surveys.

However, the most interesting explanation of B0827+525, a "dark lens" system, cannot convincingly be excluded and in view of the cosmological importance of the presence of galaxy–sized concentrations of dark matter – even though they must be rare (e.g. Jackson et al. 1998) – we now discuss why we believe the dark lens hypothesis can not yet be discarded: (1) We have seen that the radio components are

[2]http://cfa-www.harvard.edu/glensdata/

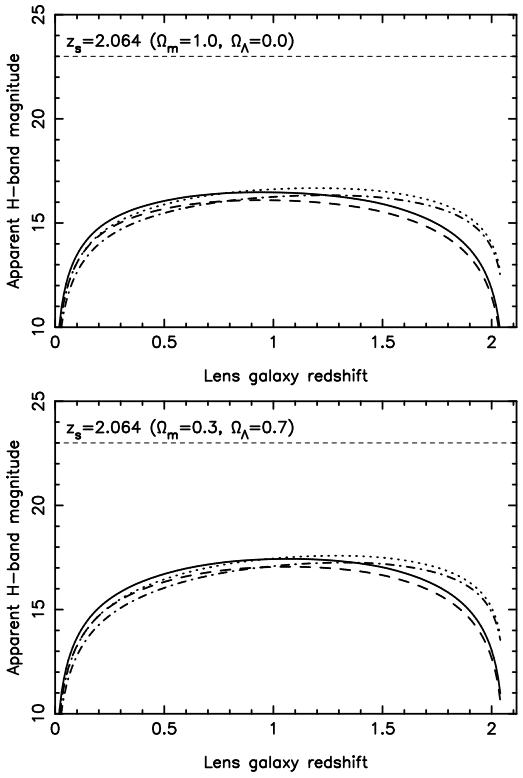

FIGURE 8.6— The estimated *H*-band magnitude of the lensing galaxy for 4 galaxy types – E (solid), S0 (dash), Sa (dot–dash) and Sc (dot) –, plotted as function of redshift (see text). The horizontal dashed line indicates the observed lower limit of 23 mag on the *H*–band magnitude. Two cosmologies are shown

variable. If they are lens images, a time delay between them combined with variability of the source can result in a difference in simultaneously measured spectral indices, especially if the time delay is of the order of the variability time scale. (2) If we place a massive 'dark lens' galaxy near component B, containing a large amount of dust, this galaxy would obscure most optical and a significant fraction of the near–infrared emission from component B. In the secure lens system B0218+357 a similarly large discrepancy has been observed between the optical and radio brightness ratios of the lens images (see CASTLES survey), which can also be explained in terms of obscuration by the high–column density of the rich ISM in the lens galaxy (e.g. Wiklind & Combes 1995; Menten & Reid 1996; Combes Wiklind & Nakai 1997; Combes & Wiklind 1997; Gerin et al. 1997; Combes & Wiklind 1998). This dust, however, would probably not block all of the lens–galaxy emission. In fact, most of the extended emission seen near radio component B could be coming from the lens galaxy itself and not from the quasar. (3) The optical brightness of image B is surprisingly low for a radio–loud quasar, which might suggest some form of extinction. (4) A high scattering measure, associated with the ionized component of the ISM in the lens galaxy (e.g. Marlow et al. 1999; Jones et al. 1996), could furthermore scatter–broaden radio component B, explaining why it appears somewhat resolved.

So far in the 'dark lens' hypothesis we have assumed that the lensing mass is a single galaxy dominated by non–baryonic matter in its inner parts and therefore extremely underluminous. If the lensing mass distribution is a high–redshift ($z \gtrsim 1$) group or cluster, the constraints on the mass–to–light ratio, which is usually an order of magnitude larger in clusters and groups of galaxies than in the inner parts of galaxies (e.g. van der Marel 1991; Carlberg, Yee & Ellingson 1997), is somewhat alleviated. However, for most of the lens galaxies from the CLASS survey , the *H*–band mass–to–light ratios are around unity (Jackson et al. 1998). This is two orders of magnitude smaller than the minimum *H*–band mass–to–light ratio found in Sect.8.3.1 and can therefore not entirely account for the high mass–to–light ratio within the context of a 'normal' galaxy evolution. Hence also if the lensing mass is a group or cluster, it must be underluminous.

Thus, although the binary quasar hypothesis seems more likely at face value, the 'dark lens' hypothesis can not be ruled out convincingly. However, the latter hypothesis does give concrete predictions: First, the substructure in both radio components should be related, although distorted by the intervening gravitational potential. We have obtained multi–frequency global VLBI data on B0827+525 at three frequencies to test this. (2) If the variability of the radio components is intrinsic, one should be

able to correlate their light–curves to find a time–delay. This could definitively prove or disprove whether B0827+525 is a "dark lens" system. (3) If the extended *H* and *K*–band emission seen near component B is partly from a lens galaxy, it should have a redshift smaller than 2.064. Near–infrared spectroscopy of this emission should therefore be attempted.

Acknowledgments

The authors would like to thank Lee Armus and David Hogg for obtaining a Keck NIRC *K*–band image. LVEK and AGdeB acknowledge the support from an NWO program subsidy (grant number 781-76-101). This research was supported in part by the European Commission, TMR Programme, Research Network Contract ERBFMRXCT96-0034 'CERES'. The National Radio Astronomy Observatory is a facility of the National Science Foundation operated under cooperative agreement by Associated Universities, Inc. The Westerbork Synthesis Radio Telescope (WSRT) is operated by the Netherlands Foundation for Research in Astronomy (ASTRON) with the financial support from the Netherlands Organization for Scientific Research (NWO). MERLIN is a national UK facility operated by the University of Manchester on behalf of PPARC. This research used observations with the Hubble Space Telescope, obtained at the Space Telescope Science Institute, which is operated by Associated Universities for Research in Astronomy Inc. under NASA contract NAS5-26555.

References

Binney, J. & Tremaine, S. 1987, Galactic Dynamics, Princeton, NJ, Princeton University Press, 1987

Bischof, O.B., Becker, R.H., 1997, AJ, 113, 2000

Browne, I.W.A., et al., 1997, in Observational Cosmology with the New Radio Surveys, ed. M. Bremer, N. Jackson, & I. Perez–Fournon (Dorcrecht: Kluwer)

Carlberg, R. G., Yee, H. K. C. & Ellingson, E. 1997, ApJ 478, 462

Combes, F., Wiklind, T. & Nakai, N. 1997, A&A 327, L17

Combes, F. & Wiklind, T. 1997, ApJL 486, L79

Combes, F. & Wiklind, T. 1998, A&A 334, L81

Condon, J.J., Cotton, W.D., Greisen, E.W., Yin, Q.F., Perley, R.A., Taylor, G.B., Broderick, J.J., 1998, AJ 115, 1693

Fassnacht, C.D., 1998 Oct. 19, PhD thesis, Caltech

Fukugita M., Turner E.L., 1991, MNRAS, 253, 99

Gerin, M. , Phillips, T. G., Benford, D. J., Young, K. H., Menten, K. M. & Frye, B. 1997, ApJL 488, L31

Hawkins, M.R.S., 1997, A&A 328, L25

Hewett, P.C., Foltz, C.B., Harding, M.E., Lewis, G.F., 1998, AJ 115, 383

Hooper, E.J., Impey, C.D., Foltz, C.B., Hewett, P.C., 1995, ApJ, 473, 746

Jackson, N., Helbig, P., Browne, I.W.A., Fassnacht, C.D., Koopmans, L., Marlow, D., Wilkinson, P.N., 1998, A&A 334, L33

Jones, D. L., Preston, R. A., Murphy, D. W., Jauncey, D. L., Reynolds, J. E., Tzioumis, A. K., King, E. A., MCCulloch, P. M., Lovell, J. E. J., Costa, M. E., Van Ommen, T. D., 1996, ApJ 470, 23

Kochanek, C.S., Falco, E.E., Muñoz, J.A., 1999, ApJ 510, 590

Kormann, R., Schneider, P. & Bartelmann, M. 1994, A&A 284, 285

Makino, J. 1997, ApJ 478, 58

Marlow, D. R., Browne, I. W. A., Jackson, N., Wilkinson, P. N., 1999, MNRAS 305, 15

Menten, K. M. & Reid, M. J. 1996, ApJL 465, L99

Myers, S.T, et al., 1999, MYERS_A4.PS-GZ[3]

Oke, J.B., 1990, AJ 99, 1621

Oke, J.B., et al., 1995, PASP 107, 375

Orr, M. J. L. & Browne, I. W. A. 1982, MNRAS 200, 1067

Poggianti, B.M., 1997, A&AS 122, 399

Rengelink, R. B. 1997, Tang, Y., De Bruyn, A. G., Miley, G. K., Bremer, M. N., Roettgering, H. J. A. & Bremer, M. A. R. 1997, A&ASS 124, 259

Rickett, B. J., Coles, W. A. & Bourgois, G. 1984, A&A 134, 390

Scheuer, P. A. G. & Readhead, A. C. S. 1979, Nature 277, 182

Schneider P., Ehlers J., Falco E.E., 1992, Gravitational Lenses, Springer Verlag, Berlin

Shepherd M.C., 1997, ADASS VI, A.S.P Conference Series, vol 125, eds., Gareth Hunt and H.E. Payne, p77

Van Der Marel, R. P. 1991, MNRAS 253, 710

Wiklind, T. & Combes, F. 1995, A&A 299, 382

[3] http://multivac.jb.man.ac.uk:8000/ceres/papers/boston99/

9

Summary & Future Research

9.1 General summary

It should have become clear that gravitational lenses are useful in a diverse range of research areas. Until the end of the 1980s, most GL systems were discovered serendipitously and only a handful of GL systems was known. To create a larger better–defined sample of GL systems, a number of surveys were initiated. One of these surveys, the *Cosmic Lens All–Sky Survey*, was started in 1994, as a collaboration between different institutes in Europe and the US. Thus far CLASS has been very successful in uncovering new GL systems, contributing about one third of the presently confirmed lenses. It is expected that the survey database will uncover a few more (Sect.9.2).

A number of beautiful GL systems has been discovered. One of these systems, B1933+503, has a record number of ten lensed components! Monitoring by Andy Biggs et al. could give one of the most accurate values of H_0 in the near future, using the mass models developed by Sunita Nair and Martin Norbury. Monitoring of B1608+656 by Chris Fassnacht et al. resulted in the determination of three independent time delays. Similarly, Andy Biggs et al. have done a beautiful job in tightening the constraints on the time delay in B0218+357, only surpassed in fractional accuracy by Q0957+561. Other surprising results from the CLASS survey were the high rate of multiple lens–galaxy systems (e.g. B1127+358, B1359+154 and B1608+656), sometimes even with lens–galaxies at different redshifts (e.g. B2114+022 and B2319+051), and the occurrence of lensed sources other than radio–loud quasars (e.g. the CSO sources in B1933+503 and B1938+666). Much effort has been put into detailed modeling of the CLASS GL systems (by Dave Rusin, Sunita Nair, Chris Fassnacht, Martin Norbury, Roger Blandford and myself). Through the work by Phillip Helbig and Steve Myers, we are getting a handle on the statistics and selection biases of the CLASS survey. Also the serendipitous discoveries of radio microlensing in B1600+434 and a 'dark lens' or binary radio–loud quasar system, B0827+525, were only a few of the unexpected results from the CLASS survey.

In the next sections, the main results from Chapters 2–8, augmented with some more recent results, are summarized. In Section 9.9, some general conclusions are drawn. In Sect.9.10, I look towards the future. In Sect.9.11, I give abstracts of several papers to which I have contributed significantly, concluding with a full publication list (Sect.9.12).

9.2 CHAPTER 2:

Thus far, the *Cosmic Lens All–Sky Survey* has lived up to expectations. CLASS[1] set

[1]The people involved in CLASS are: Ian Browne (coordinator), Neal Jackson, Peter Wilkinson, Emily Xanthopoulos, Phillip Helbig, Andy Biggs, Paul Phillips and Martin Norbury at NRAL/Jodrell Bank; Roger Blandford, Tim Pearson, Tony Readhead and Donna

out to find a large well–defined sample of GL systems – which can be used to solve a range of cosmological and astrophysical problems – and has succeeded in doing so.

Already 17 confirmed GL systems have been discovered[2] from a sample of more than 15 000 flat–spectrum radio sources, that were observed with the VLA in A–array in 1994, 1995 and 1998. We expect several additional GL systems to be found in the last phase of the survey (observed in 1998) for which the follow–up observations and analysis is still ongoing.

Four systems have already been monitored for time delays[3]. In three instances (i.e. B0218+357, B1608+656 and B1600+434), time delays have actually been measured. New observations are currently ongoing to improve these measurements. Other CLASS GL systems are being observed, to see if they are suitable for time–delay measurements as well.

In the field of GL statistics – with the aim to constrain the cosmological constant – CLASS presently offers the largest and best–defined sample of GL systems. Although the statistics of the complete CLASS survey has not yet been charted entirely, the JVAS subsample has already placed an upper limit on the cosmological constant (Helbig et al.; Sect.9.11). In the near future, the completed CLASS survey can be used to place stronger constraints.

Many of the CLASS GL systems have or are being modeled. The aim is to compare the obtained mass models with the colors and luminosity of the lens galaxies and constrain either their evolution (e.g. mass–to–light ratios) or study their dark–matter halo properties. Much of this work is still in progress.

Womble at Caltech; Steve Myers and Chris Fassnacht at NRAO; Dan Marlow and David Rusin at U.Penn.; Sunita Nair at the Raman Research Institute; Ger de Bruyn at NFRA&KAI; George Miley and Malcom Bremer at Leiden Observatory, and myself at KAI. Of them, some have left the project and others have joined.

[2]JVAS has been integrated in to CLASS, because of its similar selection criteria; see Chapter 2.

[3]B0218+357 & B1933+503 by Biggs et al.; B1608+656 by Fassnacht et al.; B1600+434 by Koopmans et al.

9.3 CHAPTER 3:

In this chapter, an attempt was made to use the CLASS gravitational lens system B1600+434 – unique in the sense that the lens galaxy at z=0.41 is an edge–on early–type spiral or disk galaxy – to constrain the shape and velocity dispersion of its dark–matter halo. This is the first attempt to constrain the oblateness of the dark–matter halo of a spiral galaxy using the phenomenon of gravitational lensing. *A lower limit of $q_{\rm h}=(c/a)_{\rm h}\gtrsim 0.5$ was found for the oblateness of the dark–matter halo, independent of the mass model. Thence, the dark–matter mass distribution in this spiral galaxy does not trace the luminous mass distribution. We also find that the dark–matter halo contributes $\gtrsim$50% of the total lensing mass inside the Einstein radius ($\lesssim 3.5$ kpc for H_0=65 km s^{-1} Mpc^{-1}). This rules out the maximum–disk hypothesis for this spiral galaxy.*

The time delay between the two lens images in B1600+434 was predicted for two different dark–matter halo mass models: $\Delta t_{B-A}=(54\pm3)\,h_{50}^{-1}$ days for the NIE mass model and $\Delta t_{B-A}=(70\pm4)\,h_{50}^{-1}$ days for the MHP mass model (see Chapter 3). Hence, the time delay critically depends on both the slope of the surface mass–density profile of the dark–matter halo and the Hubble parameter (H_0). If the time delay between the two lens images can be measured *and* the mass model for the dark–matter halo can be constrained from independent observations, one can subsequently determine the value of H_0.

In the case of B1600+434, however, the precise slope of the surface mass–density profile of the dark–matter halo is ill–constrained. This makes the determination of H_0 from this system exceedingly difficult. However, instead of focussing on the determination of H_0, the time delay between the lens images can be used to contrain the slope of the dark–matter halo. This requires that the value of H_0 is known with an accuracy better than 10%, measured from other GL systems or independent methods.

Recently, a deep HST NICMOS H–band image of B1600+434 became available, as

part of the CASTLES[4] survey. This image allows one to place tighter constraints on the surface–brightness distribution – presumably tracing the mass distribution – of the disk and bulge of lens galaxy. In our analysis this image was not available, forcing us to investigate a large range of possible disk and bulge mass models. However, Maller et al. have recently, using this HST image, confirmed the results we obtained on the halo parameters, the dark–matter mass inside the Einstein radius *and* the time delay. The consistency between these independent analyses strengthens the believe in these results. It also demonstrates the usefulness of gravitational lensing to constrain the mass distribution of (spiral) galaxies at intermediate redshifts.

9.4 CHAPTER 4:

To obtain the time delay between the two lens images in B1600+434, we undertook an eight–month monitoring campaign in 1998 with the VLA in A&B arrays. *This resulted in a value for the time delay of* $\Delta t_{\rm B-A}=47^{+12}_{-9}$ *d (95%), with an estimated maximum systematic error of* $-8/+7$ *d.*

If one assumes that the dark–matter halo around the lens galaxy is isothermal, then $H_0=57^{+14}_{-11}$ (95%) $^{+26}_{-15}$ (maximum systematic error) km s^{-1} Mpc^{-1} ($\Omega_{\rm m}$=1 and Ω_Λ=0). However, for the MHP mass distribution, this increases to $H_0=74^{+18}_{-15}$ (95%) $^{+22}_{-22}$ (maximum systematic error) km s^{-1} Mpc^{-1}. For $\Omega_{\rm m}$=0.3 and Ω_Λ=0.7, which seems to become the new paradigm these days, these values increase by 5.4%.

At present H_0 *and* the time delay in B1600+434 have not been measured well enough to use them as additional constraints on the halo mass distribution. However, most values of H_0 seem to converge to 65–70 km/s/Mpc (see Chapter 6), which implies that the mass distribution of the dark–matter halo in B1600+434 is maybe slightly steeper than isothermal, but less steep then the MHP mass distribution. In both cases *the dark–matter halo has a mass profile which falls off significantly slower than the luminous stellar disk, supporting our earlier conclusion that it does not trace its luminous counterpart. Hence, not only does the dark–matter halo have a different shape, it also has a different mass profile!*

Independently from our radio monitoring campaign with the VLA, B1600+434 has also been monitored with the Nordic Optical Telescope (NOT). Recently, I. Burud reported a preliminary time delay between the lens images of ∼44 days (Gravitational Lens Conference, Boston, US, July 25–29, 1999), in good agreement with our determination . This confirms and strengthens our results and the conclusions drawn from them.

9.5 CHAPTER 5:

A very noticeable feature in the light curves of the radio images of B1600+434 is the strong quantitative difference in their short–term variability behavior. The short–term variability in the two light curves does not seem to correlate, whereas it should if it were intrinsic source variability. However, the brighter image – passing through the dark–matter halo – displays strong variability of up to 10% peak–to–peak on time scales of weeks, opposite to the fainter image – passing predominantly through the bulge and disk of the spiral galaxy – which shows much less variability. The difference light curve, corrected for the time delay and flux–density ratio, is inconsistent with a flat curve at the 15–σ confidence level. *Hence, unambiguous external variability is present in the radio light curves of B1600+434, which makes this the first GL systems for which this has been reported.*

In Chapter 5, two plausible origins of this external variability were examined: scintillation due to the ionized component of the Galactic interstellar medium (ISM) and microlensing by massive compact objects in the bulge/disk and halo of the lens galaxy. *After a detailed analysis of all available data combined with simulations, we come to the conclusion that at present only radio microlensing is in full agreement with the VLA and WSRT observations of B1600+434 at different frequencies.* If our conclusion

[4] http://cfa-www.harvard.edu/glensdata/

is true, the lensed source has to contain a superluminal radio component, which is not uncommon for flat–spectrum radio sources at high redshifts. This radio component moves over the microlensing magnification pattern with a large angular velocity, resulting in short–term variability of the images.

The microlensing interpretation of the observed external variability implies that a significant fraction of the dark–matter halo around this edge–on spiral galaxy must consist of compact objects. A lower mass limit of $\gtrsim 0.5\ M_{\odot}$ is found for these objects, from detailed microlensing simulations, in agreement with that of stellar remnants.

Recently (June 1999), a new monitoring campaign of B1600+434 with the VLA in A&B-arrays was started. We are observing the source at three frequencies and hope to extend this to five. Preliminary results seem to strengthen the microlensing hypothesis. Similarly, we plan to continue the long–term WSRT monitoring campaign at several frequencies. With these new multi–frequency observations, we hope to better disentangle the effects of the source structure and the mass function of compact objects. This would be greatly simplified, if individual caustic crossings can be identified, which can place constraints on the relative size of the source with respect to strong changes in the magnification pattern (i.e. the caustics). With longer and better–sampled light curves at different frequencies, it might also become possible to determine the power–spectrum of the light curves and compare those directly to those determined from the simulations.

9.6 CHAPTER 6:

In some cases the determination of the mass distribution of a lens galaxy is extremely interesting in its own right, as we have seen in Chapter 3. In other cases the prime objective is to constrain the value of H_0 – as in the case of the CLASS GL system B1608+656 – and the determinations of the mass distributions is a necessary step in this process. CLASS is rapidly becoming the most important contributor to this field; the ultimate goal being an accurate determination of H_0.

B1608+656 consists of four lens images, providing information on the mass distribution of the two lens galaxies. Three time delays have been measured between the different image pairs, which give direct information on the depth of the local potential. The image positions and flux–density ratios tell us about its higher order derivatives and are much more sensitive to small perturbations. If there are two or more independent time delays in a GL system, one can use both the mass model parameters and the value of H_0, as free parameters which can be solved for. This is possible because two or more constraints are added against one free parameter (i.e. H_0). In Chapter 6, this technique was applied to B1608+656.

We find that the mass distribution of the lens galaxies does not deviate strongly from isothermal ($\lesssim$20% in the slope of the mass profile). Under the assumption that both galaxies are exactly isothermal, one finds that $H_0 = 59^{+7}_{-6}$ km s^{-1} Mpc^{-1} for $\Omega_{\rm m}$=1 and Ω_{Λ}=0.0, or $H_0 = (65\text{-}63)^{+7}_{-6}$ km s^{-1} Mpc^{-1} for $\Omega_{\rm m}$=0.3 and Ω_{Λ}=0.0–0.7. The statistical errors indicate the 95.4% (2–σ) confidence interval. However, the 20% uncertainty in the slope of the mass profile introduces a ± 15 km s^{-1} Mpc^{-1} systematic error.

Continued monitoring and a more detailed analysis of the available HST NICMOS *H*–band image of B1608+656 should help us to improve the mass model and determination of H_0 in the future. Critical in this respect is the precise slope of the radial surface mass distribution of the lens galaxies. Future work has to focuss on this aspect.

9.7 CHAPTER 7:

In this chapter the discovery of a new CLASS GL system, B1127+385, was presented. The system consists of two images, lensed by two lens galaxies. VLBI observations revealed substructure in both images. Constraints from these VLBI observations were subsequently used to constrain the mass distribution of the lens

galaxies. Although less spectacular than many other lens systems, like B1600+434 and B1608+656, this case does show that *substructure in lens images can be essential in constraining the mass distribution of lens galaxies.* This is certainly the case for many two–image GL systems, where the number of independent constraints is relatively small.

Because no obvious optical counterparts to the radio components were detected in the V and I–band HST images of B1127+385, the center of mass distribution of the lens galaxies was allowed to move freely in the process of minimizing the difference between the observations and the model. The end–result is that the radio components correspond to very low signal–to–noise optical features on both sides of the lens galaxies. Moreover, the flattening *and* position angle of the model surface–mass distribution of the primary lens galaxy agree well with those of the observed surface–brightness distribution.

Recently, the lens model was confirmed by a deep HST NICMOS H–band image, showing strong infrared counterparts to both radio components at the positions that we had previously predicted. The HST image shows an Einstein ring structure around the lens galaxies, which leaves no doubts that this system is indeed a new GL system.

9.8 CHAPTER 8:

In this chapter, *a candidate for the first binary radio–loud quasar or "dark lens" system from the CLASS survey, B0827+525, was presented.*

The selection criteria in the CLASS survey are aimed at detecting new GL systems. However, also binary radio–loud quasars (i.e. physically related pairs of radio–loud quasars) or chance alignments of unrelated quasars will pass most filters. The selection criteria try to pick out those systems that consist of two or more compact components within a small angular distance from each other. Evidently, this does not, for example, select against binary radio–loud quasars. Hence, if the latter systems are common, they will certainly be found in the CLASS survey.

B0827+525 has passed all selection criteria which, thus far, have always uncovered a source as a true GL system. But while all other candidates passing these criteria have shown an unambiguous lens galaxy after HST observations, no object was found that could act as a lens. The most plausible interpretations of B0827+525 are that the system is either a 'dark lens' system or a binary radio–loud quasar. Also a chance alignment still remains a viable possibility. Statistically we expect to find one binary radio–loud quasar in a sample of $\sim$15 000 flat–spectrum radio sources, which is the source–sample size of the CLASS survey. Hence, B0827+525 might be the first example of such a system. The observations of B0827+525 have so far not convincingly ruled out either of these possibilities yet.

Recently, multi–frequency deep global VLBI observation of B0827+525 were obtained to examine the tentative substructure found in both radio components. This data hopefully allows us to decide in favor of one of these interpretations.

9.9 An overall reflection

First, one third to a half of this thesis has been devoted to the analysis of the gravitational lens system B1600+434. Because of its unique nature – i.e. the presence of an edge–on spiral–lens galaxy – we quickly realized that this system offered an opportunity to study the mass distribution of the dark–matter halo of an intermediate–redshift spiral galaxy. One of the most important results of this study has undoubtedly been that the dark–matter halo around this galaxy does *not* trace its luminous mass distribution. The time delay between the lens images is globally consistent with our predictions and supports the conclusion that the dark–matter does not trace the luminous mass (Chapter 4). Moreover, a significant fraction ($\gtrsim$50%) of the mass in the inner part of the galaxy is contributed by the dark–matter halo (Chapter 3), suggesting that the maximum–

disk hypothesis is not valid for this galaxy.

Perhaps the single-most important result from this thesis has been the discovery of unambiguous external variability in the radio lens images of B1600+434 (Chapter 5). Because of the edge–on nature of the lens galaxy, the two lens images can probe very different parts of the lens galaxy. We came to the conclusion that this external variability is most likely due to microlensing by compact halo objects (i.e. MACHOs), lensing a superluminal jet component in the flat–spectrum radio source. Hence not only does this system provide information on the shape of the dark–matter halo, it may very well tell us about the nature of its content!

Second, related to the entire issue of the shape and nature of dark–matter halos, is the presence or absence of so called "dark lens" galaxies, which might provide important clues on the formation history of galaxies in dark–matter potential wells. A large GL survey, such as CLASS, offers the opportunity to uncover these systems, if they make up a significant fraction of galaxy–scale masses in the universe. Recently, Jackson et al. (see Sect.9.11) showed that these systems must be very rare. However, one system that might be a good candidate, B0827+525, has been discovered (Chapter 8).

In the case this system is a binary radio–loud quasar, the question arises how these systems form. The small distance of $\lesssim$25 kpc between the two quasars suggests they might have formed in a common potential well. The absence of any obvious stellar light surrounding these quasars then suggests that this potential well is dominated by dark or very underluminous matter. Could it be that two massive black holes, which have formed in a single dark–matter potential well, can efficiently 'sweep up' the local HI–gas and stop star–formation from taking place, leaving behind a dormant dark–matter halo? In that sense, ironically, the "dark lens" and binary quasar hypothesis might both suggest the presence of dark galaxy–scale masses!

Third, constraints on the expansion speed of the universe have been placed, using the CLASS GL system B1608+656 (Chapter 6). This is a global single–step method and avoids the problems inherent to "distance–ladder" methods. The main obstacle in determining H_0 with an accuracy of a few percent remains the uncertainty in the mass distribution of the lens galaxies. We have shown that if we assume that all lens galaxies have isothermal mass distributions, they all give values for H_0 that are consistent within their 1–σ errors (Chapter 6) *and* agree with the determination from the S–Z effect, SNe–Ia and local determinations. What can we make of this? For those that have more faith in the isothermal state of the mass distribution of lens galaxies – which has some physical significance – than in the non–GL determinations of H_0, this probably means that we have found the "true" value of H_0, being around 65–75 km s^{-1} Mpc^{-1} (Chapter 6). Those that believe more in the non–GL determination of H_0 would probably conclude that most galaxies have mass distribution close to isothermal. The consistency of all values suggests to me that probably both are right.

9.10 The future

In this thesis, we have touched upon and tried to answer several important questions in cosmology and astrophysics, but before laying out a strategy for future research, let us first summarize three key questions that could be answered using GL systems:

1. What is the nature of dark matter [i.e. are they really MACHOs?]. How is it distributed in and around galaxies and how can we further constrain the mass distribution of lens galaxies?

2. How is the dark–matter halo related to the luminosity and color of these lens galaxies and how does this compare with low–redshift galaxies of similar type?

3. How can we improve the determination of the cosmological parameters, in particular H_0?

To try to answer these questions I am involved in or have initiated several different projects. Below I will describe these projects, the results obtained so far and how they can be extended in the near future:

LENS MONITORING AND H_0: Together with Ger de Bruyn, I am engaged in a three–frequency VLA A&B–array monitoring campaign of B1600+434, not only to improve the determination of the time delay, but also to further examine the external variability seen in the 1998 light curves. We plan to extend the monitoring campaign to higher frequencies with the VLA in C–array (in Febr. 2000) to study the frequency–dependent variability behavior of the lens images in more detail. This can place rigorous constraints on the contributions from scintillation and microlensing to the observed external variability. Similarly, we are continuing to monitor this systems with the WSRT at different frequencies and on different time scales, specifically to determine the contribution of scintillation.

Because no single "Golden Lens" seems to exist, from which H_0 can be measured with high accuracy, the way to go in reducing the uncertainty on H_0 appears to be the composition of a large sample of GL systems from which time delays are determined. This will reduce the statistical error and unveil possible systematic errors. CLASS has gone a long way in achieving this. Parallel to enlarging the sample and improving the time–delay determinations, more constraints on the lens galaxy have to be obtained, which can improve the mass modeling of the systems. Especially VLBI observations, to find substructure in the compact lens images, and deep optical and infrared observations, to find arc–like structures and constrain the lens galaxy, are important. Deep HST NICMOS *H*–band observations of a number of CLASS GL system have already unveiled the presence of extended lens images (i.e. arcs). Similarly, many CLASS GL systems show jet–like substructure when observed with VLBI.

DETERMINATION OF Ω_m AND Ω_Λ: Whereas the Hubble constant can be measured from individual GL systems, this is not the case for the other cosmological parameters. To determine Ω_m and Ω_Λ one has to compare the GL rate in a well–defined survey with that expected for different cosmological models. By assigning likelihoods to these models, based on how well they reproduce the observations, one can subsequently put constraints on Ω_m and Ω_Λ.

Recently, we (i.e. Helbig et al.; Sect.9.11) used the results from the JVAS survey – a subsample of CLASS – to place constraints on both of these cosmological parameters. The obtained constraints are not yet very strong. However, the results from the completed CLASS survey, which ultimately will consist of ∼20 GL systems, can be used to improve these constraints.

GALAXY STRUCTURE & EVOLUTION: To model the mass distribution of new GL systems, I have developed a lens–modeling code. This code has been used to model several of the CLASS GL systems (see Sect.9.12). The mass distribution can be compared directly with the optical and infrared properties of the lens galaxies. A comparison with low–redshift galaxies of similar type can place constraints on their structure and evolution. For individual lens systems, where either more information is available or which are special cases (e.g. B1600+434), more detailed studies of their properties have been undertaken.

To improve these mass models, one would ideally want to have a much larger number of constraints than those provided by only two or four, often compact, radio images. In the optical, however, many of the lens images of CLASS GL systems are extended (e.g. B0712+472, B1127+385, B1608+656, B1933+503 and B1938+666; see Table 2.2 in Chapter 2), because one is looking at the larger stellar components associated with the compact radio AGN. Precisely these extended images provide the required additional constraints on the mass models. The future goal is therefore to extend the lens–modeling code to make full use of these more extended lens im-

ages.

THE ISM OF LENS GALAXIES: To investigate the HI–gas content of lens galaxies at intermediate redshifts, Ger de Bruyn and I, in collaboration with several other CLASS members, have started a survey of all known bright radio lenses ($\geq$50 mJy at 1.4 GHz) to search for HI absorption against the bright background source. We are in the process reducing/analyzing this data. Detection of HI–gas can put additional constraints on the lens galaxy mass distribution and tell us about the dust content in galaxies.

"DARK LENS" SYSTEMS & BINARY QUASARS: The large size of the CLASS survey ($\geq$17 GLs) allows us to put limits on the fraction of "dark lens" systems. If the lensing mass distribution is not correlated with its luminosity, CLASS would have found these systems if they make up a significant fraction of the galaxy population at intermediate redshifts. Recently, in collaboration with Jackson et al. (see Sect.9.11) it was shown that *all* CLASS lens systems show the unambiguous presence of a lensing galaxy. This places an upper limit of $\lesssim$10% on the fraction of "dark lens" systems. Thus far, we found only one dark–lens candidate in the entire CLASS survey, although it might be a binary radio–loud quasar. In collaboration with Dan Marlow and Dave Rusing, we have also initiated a project to uncover more binary quasar systems, using the CLASS survey.

THE REDSHIFT DISTRIBUTION OF THE CLASS PARENT SAMPLE: To understand the statistics of the CLASS survey, the redshift distribution of the source population, which is being lensed, has to be known. This redshift distribution enables one to determine the radio luminosity function (RLF) of these faint sources, which is essential to constrain the Cosmological Constant (Ω_Λ) and density of the universe (Ω_m). Recently a sample of $\sim$1400 faint ($\sim$5 mJy at 5 GHz) flat-spectrum radio sources between the NVSS and GB6 catalogs was selected, which were observed with the VLA, similar to the CLASS survey. A subsample was spectroscopically followed–up with the INT and WHT. We submitted a VLT proposal to obtain redshifts of the remaining faintest of these.

STATISTICAL PROPERTIES OF LENS GALAXIES: To constrain the mass distribution of lens galaxies, one makes use of the properties of the lens–image configuration. In certain cases, however, the resulting mass–distribution parameters are degenerate. However, even if a given mass distribution might formally be able to reproduce the lens–image properties, the a-priory probability that these particular lens–image properties are being caused by that mass distribution can be very small. One can make use of this to assign a likelihood to certain mass distributions, given the lens image properties. I have developed software to calculate these probabilities for arbitrary lens mass models, which can be used to constrain degenerate lens models.

SPIRAL GALAXIES AT INTERMEDIATE REDSHIFTS: Knowing the mass distribution of (spiral) lens galaxies is important for (i) understanding their evolution and (ii) constraining H_0 from the time delay between their lens images. These mass distributions are usually described by parameterized mass models, constrained by the positions, flux–ratios and distortions of the lens images. Most of the time, however, the parameters are degenerate. In particular, the slope of their radial mass profile is often ill–constrained. To improve on this situation, one would ideally want both gravitational lens and independent kinematic data on the mass distribution of the lensing galaxy over a wide range of radii. The mass distribution of the lens galaxy then has to agree with both independent data sets, alleviating these degeneracies.

To remedy this in the unique gravitational lens system PKS1830–211, Ger de Bruyn and I observed this system with MERLIN at 1.7 and 5–GHz to obtain high–resolution images of the radio Einstein–ring structure around it. This provides the necessary lensing information over a

range of radii. To acquire the independent kinematic data, we obtained high signal–to–noise OH and HI–line profiles with the WSRT in collaboration with J. Chengalur. The plan is to combine these data sets with archival HST NICMOS (*I*, *H* and *K*–band) data, to constrain the mass distribution of the lens galaxy in a self–consistent way, taking also a possible second galaxy at z=0.19 into account. In particular, we plan to deconvolve the Einstein–ring structure to obtain a first guess of the lens mass distribution. Given an OH and HI–gas disk inside this mass distribution, one can subsequently calculate the expected OH and HI–absorption line profiles, using a background emission screen created from the two high–resolution MERLIN maps. If the calculated and observed line profiles disagree, one changes the parameters of OH and HI–gas disks and the mass–distribution, until finally the mass model agrees with both lens and kinematic data. Because the OH and HI–line profiles provide a direct measurement of the potential depth of the lens galaxy, they also lift the degeneracy between H_0, Ω_m and Ω_Λ. Using the recently measured time delay, we thus obtain detailed information on the mass distribution and velocity field of this spiral galaxy at z=0.9 *and* constrain H_0 in a much more systematic and detailed way then has been possible in any other lens system thus far.

RADIO MICROLENSING: A project which I also hope to spend more time on in the near future is the detection of MACHOs in intermediate–redshift lens galaxies.

Much effort has been put into the detection of compact objects in the halo of our Galaxy. Because the microlensing optical depth of our Galaxy is $\tau \sim 10^{-6}$, this remains a challenging observational effort. The microlensing optical depth of a strong–lens galaxy, however, is always near unity. All multiply–imaged sources are therefore affected by microlensing, which is clearly demonstrated in the lens system 2237+0305. The time scales of optical microlensing events are typically many years, which makes optical monitoring a rather difficult long–term undertaking. In the radio things are different. Many compact flat–spectrum radio sources have jet structures with near or super–luminal motion. The microlensing time scale is therefore not dominated by the velocity of the compact lens objects ($v_* \leq 1000$ km/s), but by the much faster jet components ($v_j \sim c$). Hence, the radio–microlensing time scale will be smaller by a factor $\sim c/v_* \geq 10^{2-3}$. Time scales of many years in optical microlensing events reduce to several weeks or less for radio microlensing events! Fast compact jet–components thus significantly increase the microlensing rate, making a monitoring campaign much more efficient. Monitoring of multiply–imaged flat–spectrum radio sources thus offers an efficient means to search for compact objects in intermediate–z lens galaxies and constrain their mass function, if they contain superluminal compact ($\leq$ few μas) jet components.

9.11 Abstracts of selected papers

"A Determination of H_0 with the CLASS Gravitational Lens B1608+656: I. Time Delay Measurements with the VLA", C.D. Fassnacht, T.J. Pearson, A.C.S. Readhead, I.W.A. Browne, *L.V.E. Koopmans*, S.T. Myers, P.N. Wilkinson, 1999, ApJ, in press

We present the results of a program to monitor the four-image gravitational lens B1608+656 with the VLA. The system was observed over a seven month period from 1996 October to 1997 May. The 64 epochs of observation have an average spacing of 3.6 d. The light curves of the four images of the background source show that the flux density of the background source has varied at the ∼5% level. We measure time delays in the system based on common features that are seen in all four light curves. The three independent time delays in the system are found to be $\Delta t_{\rm BA}$=31±7 d, $\Delta t_{\rm BC}$=36±7 d, and $\Delta t_{\rm BD}$=76^{+9}_{-10} d at 95% confidence. This is the first gravitational lens system for which three independent time delays have been measured. A companion paper presents a mass model for the lensing galaxy which correctly reproduces the observed image positions, flux density ratios, and time delay ratios. The last condition is crucial for determining H_0 with a four-image lens. We combine the time delays with the model to obtain a value for the Hubble constant of H_0=59^{+8}_{-7} km/s/Mpc at 95% confidence (statistical) for ($\Omega_{\rm m}$, Ω_Λ)=(1,0). In addition, there is an estimated systematic uncertainty of ±15 km/s/Mpc from uncertainties in modeling the radial mass profiles of the lensing galaxies. The value of H_0 presented in this paper is comparable to recent measurements of H_0 from the gravitational lenses 0957+561, PG1115+080, B0218+357, and PKS1830-211.

"Time delay for the gravitational lens system B0218+357", A.D. Biggs, I.W.A. Browne, P. Helbig, *L.V.E. Koopmans*, P.N. Wilkinson, R.A. Perley, 1999, MNRAS 304, 349

Measurement of the time delay between multiple images of a gravitational lens system is potentially an accurate method of determining the Hubble constant over cosmological distances. One of the most promising candidates for an application of this technique is the system B0218+357 which was found in the Jodrell Bank/VLA Astrometric Survey (JVAS). This system consists of two images of a compact radio source, separated by 335 milli–arcsec, and an Einstein ring which can provide a strong constraint on the mass distribution in the lens. We present here the results of a three-month VLA monitoring campaign at two frequencies. The data are of high quality and both images show clear variations in total flux density, percentage polarization and polarization position angle at both frequencies. The time delay between the variations in the two images has been calculated using a chi-squared minimization to be 10.5±0.4 days at 95 per cent confidence, with the error being derived from Monte-Carlo simulations of the light curves. Although mass modeling of the system is at a preliminary stage, taking the lensing galaxy to be a singular isothermal ellipsoid and using the new value for the time delay gives a value for the Hubble constant of 69^{+13}_{-19} km/s/Mpc, again at 95 per cent confidence.

"Lensing galaxies: light or dark?", N. Jackson, P. Helbig, I.W.A. Browne, C.D. Fassnacht, *L.V.E. Koopmans*, D.R. Marlow, P.N. Wilkinson, 1998, A&A 334, L33

In a recent paper, Hawkins (1997) argues on the basis of statistical studies of double-image gravitational lenses and lens candidates that a large population of dark lenses exists and that these outnumber galaxies with more normal mass-to-light ratios by a factor of 3:1. If correct, this is a very important result for many areas of astronomy including galaxy formation and cosmology. In this paper we discuss our new radio-selected gravitational lens sample, JVAS/CLASS, in order to test and constrain this proposition. We have obtained ground-based and HST images of all multiple-image lens systems in our sample and in 12 cases out of 12 we find the lensing galaxies in the optical and/or near infrared. Our success in finding lensing galaxies creates problems for the dark lens hypothesis. If it is to survive, ad hoc modifications seem to be necessary: only very massive galaxies (more than about one trillion solar masses) can be dark, and the cutoff in mass must be sharp. Our finding of lens galaxies in all the JVAS/CLASS systems is complementary evidence which supports the conclusion of Kochanek et al. (1997) that many of the wide-separation optically-selected pairs are physically distinct quasars rather than gravitational lens systems.

"Gravitational lensing statistics with extragalactic surveys. II. Analysis of the Jodrell Bank-VLA Astrometric Survey", P. Helbig, D.R. Marlow, R. Quast, P.N. Wilkinson, I.W.A. Browne, *L.V.E. Koopmans*, 1999, A&ASS 136, 297

We present constraints on the cosmological constant λ_0 from gravitational lensing statistics of the Jodrell Bank-VLA Astrometric Survey (JVAS). Although this is the largest gravitational lens survey which has been analyzed, cosmological constraints are only comparable to those from optical surveys. This is due to the fact that the median source redshifts of JVAS are lower, which leads to both relatively fewer lenses in the survey and a weaker dependence on the cosmological parameters. Although more approximations have to be made than is the case for optical surveys, the consistency of the results with those from optical gravitational lens surveys and other cosmological tests indicate that this is not a major source of uncertainty in the results. However, joint constraints from a combination of radio and optical data are much tighter. Thus, a similar analysis of the much larger Cosmic Lens All-Sky Survey should provide even tighter constraints on the cosmological constant, especially when combined with data from optical lens surveys. At $95\lambda_0 - \Omega_0$, using the JVAS lensing statistics information alone, are respectively -2.69 and 0.68. For a flat universe, these correspond to lower and upper limits on λ_0 of respectively -0.85 and 0.84. Using the combination of JVAS lensing statistics and lensing statistics from the literature as discussed in Quast & Helbig (Paper I) the corresponding $\lambda_0 - \Omega_0$ values are -1.78 and 0.27. For a flat universe, these correspond to lower and upper limits on λ_0 of respectively -0.39 and 0.64.

"CLASS B1152+199 and B1359+154: Two New Gravitational Lens Systems Discovered in the Cosmic Lens All-Sky Survey", S.T. Myers, D. Rusin, C.D. Fassnacht, R.D. Blandford, T.J. Pearson, A.C.S. Readhead, N. Jackson, I.W.A. Browne, D.R. Marlow, P.N. Wilkinson, *L. V.E. Koopmans*, A.G. de Bruyn, 1999, ApJ 117, 658

The third phase of the Cosmic Lens All-Sky Survey (CLASS) has recently been completed, bringing the total number of sources imaged to over 15000 in the CLASS and JVAS combined survey. In the VLA observations carried out in March and April of 1998, two new candidate lensed systems were discovered: CLASS B1152+199 and B1359+154. B1152+199 is a 1.6 arcsecond double, with a background quasar at z=1.019 lensed by a foreground galaxy at z=0.439. The relatively flat radio spectra of the lensed images, combined with a previous ROSAT detection of the source, make B1152+199 a strong candidate for time delay studies at both radio and X-ray wavelengths. B1359+154 is a quadruply lensed quasar at z=3.235, with a maximum image separation of 1.7 arcseconds. As yet, the redshift of the lensing object in this system is undetermined. The steep spectral index of the source suggests that B1359+154 will not exhibit strong variability, and is therefore unlikely to be useful for determining the Hubble constant from measured time delays.

"Micro & strong lensing with the Square Kilometer Array: The mass–function of compact objects in high–redshift galaxies", *L.V.E. Koopmans* & A.G. de Bruyn, 1999, in Perspectives in Radio Astronomy: Scientific Imperatives at cm and m Wavelengths (Dwingeloo: NFRA), Edited by: M.P. van Haarlem & J.M. van der Hulst

We present the results from recent VLA 8.5–GHz and WSRT 1.4 and 4.9–GHz monitoring campaigns of the CLASS gravitational lens B1600+434 and show how the observed variations argue strongly in favor of microlensing by MACHOs in the halo of a dark–matter dominated edge–on disk galaxy at z=0.4. The population of flat–spectrum radio sources with micro–Jy flux–densities detected with the *Square–Kilometer–Array* is expected to have dimensions of micro–arcsec. They will therefore vary rapidly as a result of Galactic scintillation (diffractive and refractive). However, when positioned behind distant galaxies they will also show variations due to microlensing, even more strongly than in the case of B1600+434. Relativistic or superluminal motion in these background sources typically leads to temporal variations on time scales of days to weeks. Scintillation and microlensing can be distinguished, and separated, by their different characteristic time scales and the frequency dependence of their modulations. Monitoring studies with *Square–Kilometer–Array* at GHz frequencies will thus probe both microscopic and macroscopic properties of dark matter and its mass–function as a function of redshift, information very hard to obtain by any other method.

9.12 Publications

9.12.1 Refereed

1. **"The edge-on spiral gravitational lens B1600+434"**, *Koopmans, L.V.E.*, de Bruyn, A.G., Jackson, N., 1998, MNRAS, 295, 534

2. **"A new radio double lens from CLASS : B1127+385"**, *Koopmans, L. V. E.*, de Bruyn, A. G., Marlow, D. R., Jackson, N., Blandford, R. D., Browne, I. W. A., Fassnacht, C. D., Myers, S. T., Pearson, T. J., Readhead, A. C. S., Wilkinson, P. N., Womble, D., 1999, MNRAS, 303, 727

3. **"A determination of H_0 with the gravitational lens B1608+656: II. Mass models and the Hubble constant from lensing"**, *Koopmans, L.V.E.*, Fassnacht, C.D., 1999, in press (ApJ, 527–2), astro-ph/9907258

4. **"A time-delay determination from VLA light curves of the CLASS gravitational lens B1600+434"**, *Koopmans, L.V.E.* , de Bruyn, A.G., Xanthopoulos, E., Fassnacht, C.D., 1999, A&A, submitted

5. **"Microlensing of multiply–imaged compact radio sources: Evidence for MACHOs at z=0.4"**, *Koopmans, L.V.E* & de Bruyn, A.G., 1999, submitted

6. **"B0827+525: Dark lens or binary quasar"**, *Koopmans, L.V.E.*, et al., 1999, A&A, submitted

7. **"A determination of H_0 with the gravitational lens B1608+656: I. VLA measurements of time delays"**, Fassnacht, C.D., Pearson, T.J., Readhead, A.C.S., Browne, I.W.A., *Koopmans, L.V.E.*, Myers, S.T., Wilkinson, P.N., 1999, in press (ApJ, 527–2), astro-ph/9907257

8. **"Time delay measurement for the gravitational lens system B0218+357"**, Biggs A.D., Browne I.W.A., Helbig P., *Koopmans L.V.E.*, Wilkinson P.N., Perley R.A., 1999, MNRAS, 304, 349

9. **"Lensing galaxies: light or dark?"**, Jackson, N., Helbig, P., Browne, I.W.A., Fassnacht, C.D., *Koopmans, L.V.E.*, Marlow, D.R., Wilkinson, P.N., 1998, A&A, 334L, 33

10. **"Gravitational Lensing Statistics with Extra-galactic Surveys. II. Analysis of the Jodrell Bank-VLA Astrometric Survey"**, Helbig, P., Marlow, D.R., Quast, R., Wilkinson, P.N., Browne, I.W.A., *Koopmans, L.V.E.*, 1998, A&ASS,136, 297

11. **" VLA 8.4 GHz monitoring observations of the CLASS gravitational lens B1933+503"**, Biggs, A., Xanthopoulos, E., Browne, I. W. B., *Koopmans, L. V. E.*, Fassnacht, C. D., 1999, MNRAS, submitted

12. **"Redshifts for a complete sample from the CLASS"**, Marlow, D.R., Browne, I.W.A., Wilkinson, P.N., Jackson, N.J, Helbig, P.J., *Koopmans, L.V.E.*, 1999, MNRAS, submitted

13. **"CLASS B1152+199 and B1359+154: Two New Gravitational Lens Systems Discovered in the Cosmic Lens All Sky Survey"**, Myers, S.T., Rusing, D., Fassnacht, C.D., Blandford, R.D., Pearson, T.J., Readhead, A.C.S., Jackson, N., Browne, I.W.A., Marlow, D., Wilkinson, P.N., *Koopmans, L.V.E.*, de Bruyn, A.G., 1998, ApJ, 117, 658

14. **"B2045+265: A new Four-Image Gravitational Lens from the CLASS Survey"**, Fassnacht C.D., Blandford R.D., Cohen J.G., Matthews K., Neugenbauer G., Pearson J., Readhead A.C.S., Womble D.S., Myers S.T., Browne I.W.A., Jackson J., Marlow D., Nair S., Wilkinson P.N., de Bruyn A.G., Schilizzi R.T., *Koopmans L.*, Bremer M., Miley G., 1999, ApJ, 117, 658

15. **"The new gravitational lens system B1030+074"**, Xanthopoulos, E., Browne, I.W.A., King, L.J., *Koopmans, L.V.E.*, Jackson, N.J., Marlow, D.R., Patnaik, A.R., Porcas, R.W., Wilkinson, P.W., 1998, MNRAS, 300, 649

16. **"A complete infrared Einstein ring in the gravitational lens system B1938 +666"**, King, L. J., Jackson, N., Blandford, R. D., Bremer, M. N., Browne, I. W. A., de Bruyn, A. G., Fassnacht, C., *Koopmans, L.*, Marlow, D., Nair, S., Wilkinson, P. N., 1998, MNRAS, 295L, 41

17. **"B0712+472: a new radio four-image gravitational lens"**, Jackson, N., Nair, S., Browne, I.W.A., Wilkinson, P.N., de Bruyn, A.G., *Koopmans, L.*, Bremer, M., Snellen, I., Miley, G.K., Schilizzi, R.T., Myers, S., Fassnacht, C., Womble, D., Readhead, A.C.S., Blandford, R.D., Pearson, T.J., 1998, MNRAS, 296, 483

18. **"CLASS B1555+357: A new four-image gravitational lens system"**, Marlow, D.R., Myers, S.T., Rusin, D., Jackson, N., Browne, I.W.A, Wilkinson, P.N, Muxlow, T., Fassnacht, C.D., Lubin, L., Kundic, T., Blandford, R.D., Pearson, T.J., Readhead, A.C.S., *Koopmans, L.V.E.*, de Bruyn, A.G., 1999, AJ, 118,654

19. **"A new gravitational lens system from CLASS: B0739+366"**, Marlow, D.R., Browne, I.W.A., Jackson, N.J., Wilkinson, P.N., Blandford, R.D., Cohen, J., Fassnacht, C.D., Hogg, D., Pearson, T.J., Readhead, A.C.S., Womble, D.S., Myers, S.T., de Bruyn, A.G., *Koopmans, L.V.E.*, Bremer, M., Miley, G.K., Schilizzi, R., 1999, MNRAS, submitted

20. **"A new radio double lens from CLASS: B2319+051"**, Marlow, D.R., Browne, I.W.A., Jackson, N.J., Wilkinson, P.N., Blandford, R.D., Cohen, J., Fassnacht, C.D., Hogg, D., Pearson, T.J., Readhead, A.C.S., Womble, D.S., Myers, S.T., de Bruyn, A.G., *Koopmans, L.V.E.*, Bremer, M., Miley, G.K., Schilizzi, R., 1999, MNRAS, submitted

9.12.2 Proceedings

21. **"Microlensing & Scintillation of Gravitationally Lensed Compact Radio Sources: Evidence for MACHOs?"**, *Koopmans, L.V.E.* & de Bruyn, A.G., 1999, in "Gravitational Lensing: Recent progress and Future Goals", eds: T.Brainerd and C.Kochanek, ASP Conf Series, in press

22. **"Micro & strong lensing with the Square Kilometer Array: The mass–function of compact objects in high–redshift galaxies"**, *Koopmans, L.V.E.* & de Bruyn, A.G., 1999, in Perspectives in Radio Astronomy: Scientific Imperatives at cm and m Wavelengths (Dwingeloo: NFRA), Edited by: M.P. van Haarlem & J.M. van der Hulst

23. **"The edge-on spiral gravitational lens B1600+434"**, *Koopmans, L.V.E.*, de Bruyn, A.G., Jackson, N., 1998, Large Scale Structure: Tracks and Traces. Proceedings of the 12th Potsdam Cosmology Workshop, held in Potsdam, September 15th to 19th, 1997. Eds. V. Mueller, S. Gottloeber, J.P. Muecket, J. Wambsganss World Scientific 1998, p. 325-326

24. **"Spiral galaxy lensing"**, *Koopmans L.V.E.*, Nair S., 1997, http://multivac.jb.man.ac.uk:8000/ceres/workshop1/proceedings.html, Proceedings of the 'Golden Lens' workshop in Jodrell Bank

25. **"The JVAS/CLASS gravitational lens surveys."**, I.W.A. Browne, N. Jackson, P. Augusto, D.R. Henstock, D.R. Marlow, S. Nair, P.N. Wilkinson, A.G. de Bruyn, *L. Koopmans*, S.T. Myers, C.D. Fassnacht, R.D. Blandford, T.J. Pearson, A.C.S. Readhead, D. Womble, A.R. Patnaik, 1998, In "Observational Cosmology with the new radio surveys", eds. M. Bremer, N. Jackson, I. Perez-Fournon, Kluwer Academic Publs., in press

26. **"Cosmological parameters from the CERES project"**, A. Biggs, R. Blandford, M. Bremer, I. W. A. Browne, A. G. de Bruyn, J. Cohen, C. Fassnacht, P.Helbig, N. Jackson, L. King, *L. Koopmans*, D. Marlow, A. McGuinness, G. Miley, S. Myers, S. Nair, A. Patnaik, T. Pearson, A. Readhead, C. Sykes, P. Wilkinson, D. Womble, E. Xanthopoulos, 1997, http://multivac.jb.man.ac.uk:8000/helbig/ research/publications/ info/iau183.html, Proceedings of IAU Symposium 183

27. **"Light on dark lenses"**, Jackson N., Helbig P., Browne I.W.A., *Koopmans L.*, 1998, Proceedings of the workshop "Gravitational Lensing: Nature's own Weighing Scales", Oxford, New Astronomy Reviews

28. **"CLASS: Cosmic Lens All-Sky Survey."**, S.T. Myers, N. Jackson, I. Browne, G. de Bruyn, A. Readhead, P. Wilkinson, C. Fassnacht, *L. Koopmans*, D. Marlow, M. Norbury, D. Rusin, A. Biggs, R. Blandford, P. Helbig, T. Pearson, E. Xanthopoulos, 1999, in "Gravitational Lensing: Recent progress and Future Goals", eds: T.Brainerd and C.Kochanek, ASP Conf Series, in press

29. **"Measuring H_0 with CLASS B1608+656: The Second Season of VLA Monitoring"**, C.D. Fassnacht, E. Xanthopoulos, *L.V.E. Koopmans*, T.J. Pearson, A.C.S. Readhead, S.T. Myers, 1999, in "Gravitational Lensing: Recent progress and Future Goals", eds: T.Brainerd and C.Kochanek, ASP Conf Series, in press

30. **"B0218+357: Time Delays and New MERLIN/VLA 5GHz Maps of the Einstein Ring"**, A.D. Biggs, I.W.A. Browne, P.N. Wilkinson, T.W.B. Muxlow, P. Helbig , *L.V.E. Koopmans*, 1999, in "Gravitational Lensing: Recent progress and Future Goals", eds: T.Brainerd and C.Kochanek, ASP Conf Series, in press

31. **"CLASS B0827+525: Dark Lens or Binary Quasar?"**, D.R. Marlow, *L. Koopmans*, C. Fassnacht, D. Rusin, P. Wilkinson, N. Jackson, I. Browne, S. Myers, G. de Bruyn, L. Armus, D. Hogg, 1999, in "Gravitational Lensing: Recent progress and Future Goals", eds: T.Brainerd and C.Kochanek, ASP Conf Series,in press.

32. **"The gravitational lens system B1030+074. Discovery and follow-up"**, Xanthopoulos, E., Browne, I. W. B., King, L. J., *Koopmans, L. V. E.*, Jackson, N. J., Marlow, D. R., Patnaik, A. R., Porcas, R. W., Wilkinson, P. N., 1998, Proceedings of the IAU 194, Activity in Galaxies and Related Phenomena, in press

33. **"Everything you ever wanted to know about the JVAS gravitational lens system B1030+074 but were afraid to ask"**, E. Xanthopoulos, I.W.A. Browne, P.N. Wilkinson, N.J. Jackson, A. Karidis, R.W. Porcas, A.R. Patnaik, *L.V.E. Koopmans*, D.R. Marlow, 1999, in "Gravitational Lensing: Recent progress and Future Goals", eds: T.Brainerd and C.Kochanek, ASP Conf Series, in press

34. **"Everything you ever wanted to know about the JVAS gravitational lens system B1030+074 but were afraid to ask"**, Xanthopoulos, E., Browne, I. W. B., Wilkinson, P. N., Jackson, N., Karidis, A., Porcas, R. W., Patnaik, A. R., *Koopmans, L. V. E.*, Marlow, D. R., 1999, in Proceedings of the 4th Hellenic Astronomical Society Meeting, in press

9.12.3 Popular (in Dutch)

35. **"De ver-infrarood-radio relatie in M33"**, *Koopmans, L.V.E.*, 1995, MUON

36. **"Gravitatie lenzen als kosmologisch gereedschap"**, *Koopmans, L.V.E.*, de Bruyn, A.G., 1998, ZENIT, May issue

10

Gravitatielenzen als kosmologisch gereedschap

Gedeeltelijk gebaseerd op L.V.E. Koopmans & A.G. de Bruyn, 1998, ZENIT, mei (#5), p231–236

In 1979 werd door de Britse astronoom Dennis Walsh een quasar ontdekt die op optische foto's bestond uit twee componenten op slechts zes boogseconden van elkaar. Omdat de gemiddelde dichtheid van heldere quasars aan de hemel ongeveer één per vierkante graad is, leek het uitgesloten dat we hier te maken hadden met een toevallige samenstand. Uit optische spectroscopische waarnemingen bleek vervolgens dat deze componenten dezelfde roodverschuiving hadden, dus op dezelfde afstand stonden, en ook nog eens een bijna identiek spectrum hadden. Walsh en zijn collega's Carswell en Weymann begonnen zich toen serieus af te vragen of ze misschien twee keer *dezelfde* quasar zagen. Ze concludeerden dat het het meest waarschijnlijk was dat de 'dubbel-quasar' het eerste voorbeeld was van een gravitatielens. Gravitatielenzen zijn niet alleen als verschijnsel, en als bewijs van Einsteins zwaartekrachtstheorie, buitengewoon boeiend. Ook de mate waarin lenzen voorkomen en hun eigenschappen kunnnen ons veel leren over de massa dichtheid, de verdeling van materie en de 'geometrie' (de ruimtekromming) van het heelal. Bovendien, zo liet de Noorse astronoom Sjurd Refsdal in 1964 zien, zou onderzoek aan gravitatielenzen ook een van de meest fundamentele vragen uit de kosmologie kunnen beantwoorden, namelijk die van de kosmologische afstandschaal, 'Hoe groot is het heelal?', en de daaraan gerelateerde vraag 'Hoe oud is het heelal?'. Al met al genoeg fundamentele vragen om het onderzoek aan gravitatielenzen grootschalig aan te pakken! De ontdekking van de eerste gravitatielens – Q0957+561 genaamd – was toeval. Maar er is een hele nieuwe, uiterst vruchtbare, tak van de sterrenkunde uit ontstaan. Tot op heden zijn er zo'n veertigtal meervoudige lenzen ontdekt en jaarlijks komen daar nieuwe bij.

Algemene relativiteitstheorie en gravitatielenzen

Tussen 1905 en 1915 ontwikkelde Albert Einstein zijn algemene relativiteitstheorie, die Newtons concepten van massa en traagheid verenigde. De algemene relativiteitstheorie beantwoorde de aloude vraag waarom het perihelium van de baan van Mercurius om de zon precessie vertoond, maar voorspelde ook een groot aantal nieuwe verschijnselen, welke niet door Newtons gravitatie theorie verklaard konden worden. Twee van deze – de afbuiging van een lichtstraal die door het gravitatie

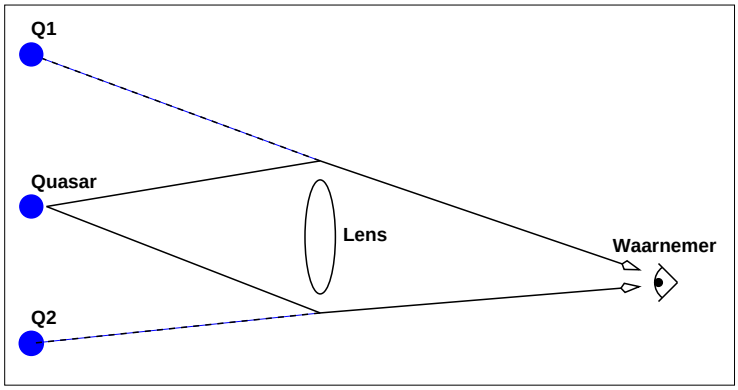

FIGUUR 10.1— Doordat een massief object (lens) het licht van een achtergrondbron (quasar) afbuigt, kunnen er twee (Q1 en Q2) of meerdere afbeelding van deze achtergrondbron ontstaan. De waarnemer ziet deze afbeeldingen van de achtergrondbron op andere posities (gestreepte lijnen), dan waar de bron werkelijk staat.

veld van een massief object beweegt, en de tijdsvertraging die deze lichtstraal daardoor oploopt – vormen de basis van het fenomeen 'gravitatielens' en de mogelijkheid om dat verschijnsel te gebruiken als gereedschap bij de bepaling van de kosmologische afstandschaal en de massaverdeling van het lens–sterrenstelsel.

Volgens de algemene relativiteitstheorie kromt elk massief object de ruimte eromheen. Doordat de ruimte gekromd is, zal een lichtstraal die langs dit object beweegt niet in een rechte lijn bewegen, maar enigszins worden afgebogen (zie Figuur 10.1). Een mooi voorbeeld hiervan is afbuiging van sterlicht als we vlak lang de rand van de zon kijken. Dit werd voor het eerst waargenomen in 1919. De metingen leverden een afbuiging van twee boogseconden op en dit kwam binnen de foutenmarge overeen met de door Einstein voorspelde afbuiging van 1.8 boogseconden.

Als we ons nu een sterrenstelsel voorstellen, zoals de onze, op een afstand van enkele miljarden lichtjaren, dan blijkt dat ook deze zware sterrenstelsels licht van objecten op nog grotere afstand over een hoek van enkele boogseconden afbuigen. Dit werd voor het eerst beseft door Zwicky in 1937, maar het duurde nog ruim veertig jaar voordat Walsh en zijn medewerkers dit in 1979 waarnamen. Hoewel deze sterrenstelsels dus zo'n honderd tot duizend miljard keer zwaarder zijn dan onze zon, is de afbuiging van licht door deze sterrenstelsels vergelijkbaar met die door de zon. Dit komt omdat de afstanden in kwestie zo veel groter zijn.

Afbeeldingsvormen en eigenschappen

Het interessante aan gravitatielenzen is dat ze van een achtergrond object (meestal een quasar) niet één, maar meerdere afbeeldingen kunnen maken. Dit in tegenstelling tot bijvoorbeeld (goed geslepen) telescooplenzen, die het licht van een object ook afbuigen, maar slechts één keer afbeelden in een goed gedefineerd brandpunt. Toch zijn de meervoudige beelden van gravitatielenzen niet zo mooi scherp als ze op het eerste gezicht lijken. In bepaalde gevallen kan een gravitatielens een achtergrond object namelijk ook afbeelden als een langgerekte boog of zelfs als een ring rondom het lens stelsel. In Figuur 10.2 hebben we een aantal van deze gevallen nagebootst op de computer. In het tweede paneel van deze figuur zien we bijvoorbeeld langgerekte bogen, terwijl in paneel 3 twee afbeeldingen van het achtergrondobject tot een boog zijn 'samengesmolten'. In de panelen 4 en 6 zijn deze bogen dermate lang dat ze een ring rond de lens vormen. Merk op dat we in panelen 1–4 vier afbeeldingen van het achtergrond object zien, terwijl de lens in panelen 5 en 6 slechts twee afbeeldingen vertoont. Welke afbeeldingsvorm men waarneemt, hangt af van de exacte positie van de achtergrondbron ten opzichte van het lens–sterrenstelsel. Al deze afbeeldingsvormen zijn de laatste twintig jaar ook werkelijk aan de hemel waargenomen en verderop zullen we van elk een voorbeeld tonen.

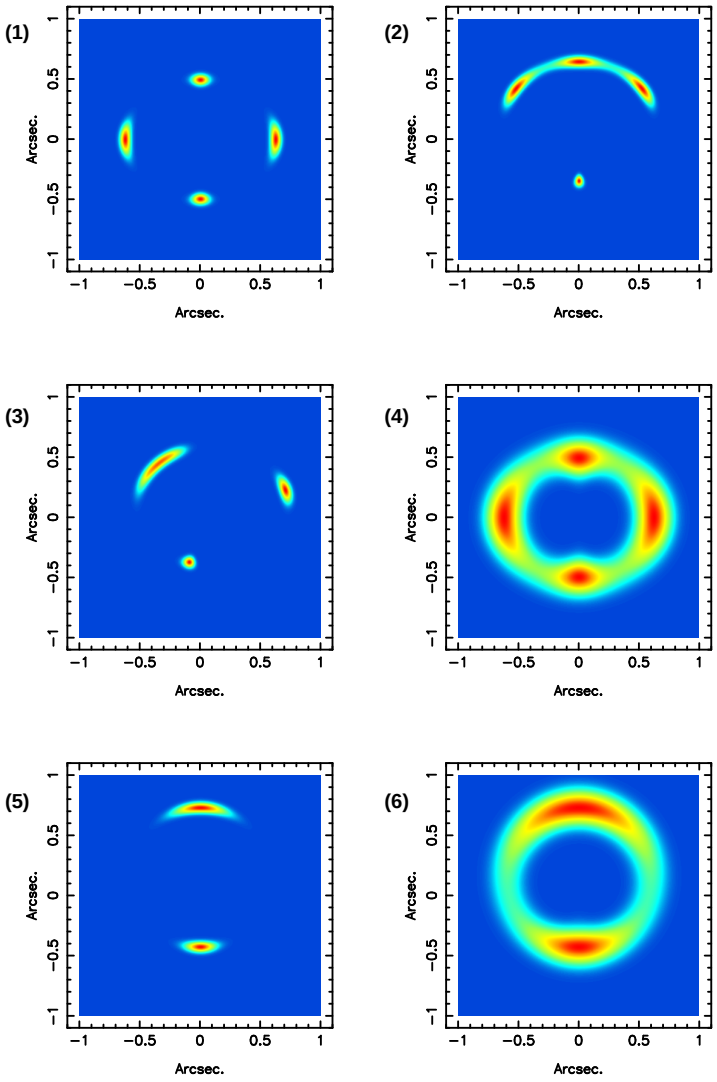

FIGUUR 10.2— Zes voorbeelden van de door een gravitatielens gemaakte beelden. De eerste vier laten viervoudige afbeeldingen van één achtergrondbron zien, de laatste twee laten tweevoudige afbeeldingen zien. De massa van het lens–sterrenstelsel (dat niet te zien is in de figuren) is vergelijkbaar met die van ons melkwegstelsel. Van linksboven naar rechtsonder zien we achtereenvolgens: (1) Een viervoudige afbeelding, waar de achtergrond bron (0.015 boogseconden groot) gelensd wordt in vier vergelijkbare afbeeldingen. De bron ligt in dit geval precies achter het midden van het lens stelsel. (2) Idem, maar nu ligt de bron zo'n 0.15 boogseconden boven het lens–centrum (0,0). (3) Idem, de bron ligt 0.1 boogseconde naar rechts van en 0.1 boogseconde boven het lens–centrum. (4) Als (1), met een bron die 0.05 boogseconde groot is. Men ziet dat er één gesloten ring ('Einstein ring') rond de lens wordt gevormd. (5) Een tweevoudige afbeelding van de achtergrond bron (6) Als (4), maar nu met twee bronafbeeldingen in de Einstein ring.

Als een sterrenstelsel een achtergrond object meerdere keren afbeeldt, staan deze afbeeldingen niet alleen op verschillende posities ten opzichte van het sterrenstelsel, maar worden ze ook vervormd. We zien het achtergrond object dus niet zoals het werkelijk is, maar afhankelijk van de vervorming kan het object vergroot of verkleind worden, waardoor ze helderer of minder helder worden. Door nu de posities en helderheden van de verschillende afbeeldingen te vergelijken kunnen we de massa, de afplatting, de plaats van het centrum en de oriëntatie van de massaverdeling in het lens–sterrenstelsel berekenen. Met viervoudige afbeeldingen kunnen we dat beter en nauwkeuriger dan met tweevoudige. Het leuke is dat we daarvoor het lens–sterrenstelsel dus niet eens hoeven te 'zien'. We kunnen als het ware voorspellen waar de lens moet staan en hoe die er uit zou moeten zien. Men kan dus iets leren over sterrenstelsels die zo ver weg staan, dat we er normaal gesproken weinig of niets over te weten zouden kunnen komen.

De verschillende afbeeldingen die de waarnemer ziet, worden gevormd uit lichtstralen die verschillende paden hebben afgelegd. De 'lengte' van die paden is verschillend, en het licht dat we in de verschillende afbeeldingen ontvangen is dus

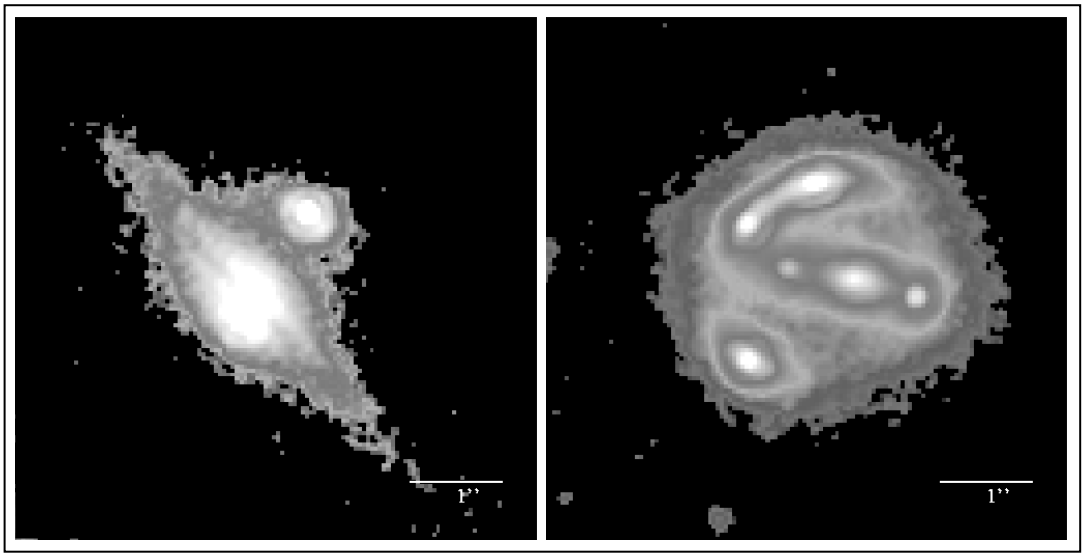

FIGUUR 10.3— **Links** : De gravitatie lens B1600+434. De twee heldere bronnen aan weerszijde van het middelste sterrenstelsel, zijn de twee quasar afbeeldingen. Het lens sterrenstelsel is in dit geval een spiraalstelsel dat we van opzij zien. De separatie tussen de twee quasars is 1.4 boogseconden. **Rechts** : De gravitatie lens B1608+656. Het heldere object in het midden is het lens stelsel. Het zwakkere object links daarvan kan een ander stelsel zijn, maar ook deel uitmaken van één lens stelsel verduisterd door stof. De vier objecten rond het lens stelsel zijn afbeeldingen van het achtergrond object, in dit geval ook een sterrenstelsel. De twee afbeeldingen linksboven vormen een fraaie *arc*. In het radio gebied is dit object minder spectaculair: vier puntbronnen elk kleiner dan 1 milli-boogsekonde.

niet op hetzelfde moment van de bron vertrokken; de lichtsnelheid is immers eindig! Dat tijdsverschil kan oplopen tot vele jaren, maar meestal bedraagt het enkel weken of maanden. Naarmate het lens–sterrenstelsel zwaarder is en de afbeeldingen verder van elkaar staan, zal het tijdsverschil meestal groter zijn. Als het achtergrond object nu veranderlijk is en plotseling helderer of minder helder wordt, zal dat in de verschillende afbeeldingen dus op verschillende momenten worden waargenomen. Omdat de meeste door gravitatie–lenzen afgebeelde objecten quasars zijn, is de kans dat het object in intensitiet verandert vrij groot.

In 1964 liet Refsdal zien dat het tijdsverschil tussen de verschillende afbeeldingen evenredig is met de grootte van het heelal. Een twee keer zo groot heelal geeft dus een twee keer zo groot tijdsverschil. Door nu naar gravitatielenzen te kijken waarvan het achtergrond object variabel is, kan men het tijdsverschil tussen de afbeeldingen meten, en – als men een goed massa model van het sterrenstelsel heeft – kan men vervolgens de zogenaamde Hubble–constante en daaruit de grootte en leeftijd van het heelal bepalen.

Dubbele quasars...

Ongeveer de helft van alle waargenomen gravitatielenzen tonen twee afbeeldingen van het achtergrond object. Een voorbeeld van deze afbeeldingsvorm is te zien in Figuur 10.3, de in 1994 ontdekte gravitatielens B1600+434. De hoekafstand tussen de twee quasar afbeeldingen is slechts 1.4 boogseconden. Uit de hoekafstand kunnen we meteen al iets zeggen over de massa van het lens–sterrenstelsels. Het verschil in visuele helderheden van de twee quasar afbeeldingen daarentegen leert ons iets over de verdeling van deze massa in het lens–sterrenstelsels. We zullen in een latere paragraaf iets dieper op dit punt ingaan. De achtergrondbron in B1600+434 is variabel en kan derhalve worden gebruikt om de Hubble–constante te bepalen. Een langdu-

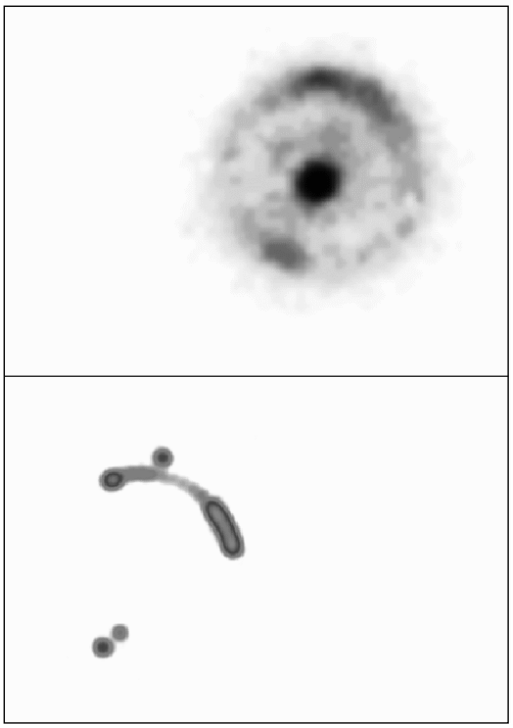

FIGUUR 10.4— De gravitatie lens B1938+666. Onder ziet men de lens structuur waargenomen door een radiotelescoop. Boven, de structuur zoals de Hubble ruimtetelescoop die ziet.

rige waarneemcampagne met behulp van radiotelescopen heeft onlangs een tijdsvertraging van ongeveer 47 dagen tussen de twee quasar–afbeeldingen opgeleverd.

Viervoudige quasars...

Het andere vaak voorkomende geval is de viervoudige afbeelding van het achtergrond object. Deze geven ons vaak meer informatie over de massaverdeling in het lens–sterrenstelsel dan een dubbele afbeelding. Een voorbeeld van een viervoudige afbeelding is te zien in Figuur 10.3. De lens, B1608+656, is – net als B1600+434 – in 1994 gevonden in de *Cosmic Lens All–Sky Survey* (eng.), kortweg CLASS. Dit project is een samenwerkingsverband tussen Nederland, Groot–Brittannië en de Verenigde Staten en heeft in vijf jaar tijd, al zo'n twaalf nieuwe lenzen gevonden, waarmee het de meest succesvolle zoektocht naar nieuwe lenzen is. Het bijzondere van de CLASS–survey is dat deze uitgaat van een lijst met meer dan tienduizend radiobronnen. Men kan bij radiogolflengten betere hoekresoluties bereiken dan met optische methoden. Omdat de ontdekking van een lens een hoekresolutie van (veel) beter dan 1 boogsekonde vergt, is de radiospeurtocht naar lezen dus eenvoudiger en effectiever. Toch blijkt slechts één op de 500 à 700 radiobronnen meervoudig afgebeeld te zijn.

In tegenstelling tot B1600+434, waar de lens een enkelvoudig spiraalstelsel is, is de lens in B1608+656 waarschijnlijk een sterk afgeplat elliptisch sterrenstelsel. In Figuur 10.3 is te zien dat het sterrenstelsel bestaat uit twee delen. Dit zouden twee sterrenstelsels kunnen zijn, maar ook één met daaromheen een stofband, waardoor het twee sterrenstelsels lijken. Kleurwaarnemingen van dit systeem met de Hubble ruimtetelescoop hebben onlangs laten zien dat de twee delen inderdaad twee afzondelijke sterrenstelsels zijn. We zien ook dat het achtergrond object in B1608+656 uitgebreid is – in dit geval een sterrenstelsel, maar wel met een heldere, zeer kompacte radiokern. Het sterrenstelsel wordt vervormd tot een langgerekte boog, vergelijkbaar met die in onze computer simulatie (zie paneel 3 in Figuur 10.2). Ook de achtergrondbron in B1608+656 is variabel, vergelijkbaar met B1600+434, en kan dus ook worden gebruikt om de Hubble–constante te bepalen, zoals we verderop zullen laten zien.

Einstein ringen...

Naast dubbele en viervoudige afbeeldingen zijn er ook Einstein ringen. Dit zijn situaties waar de afbeelding zodanig is vervormd dat het een gesloten ring om het lens–sterrenstelsel vormt. Hoewel deze systemen vaak erg complex zijn, geven ze veel informatie over de massaverdeling in het lens–sterrenstelsel. Een recent voorbeeld van een zeer fraaie Einstein ring – B1938+666 – is te zien in Figuur 10.4.

Gravitatie lenzen en de Hubble–constante

Zoals is gebleken uit de voorgaande voorbeelden, kunnen gravitatielenzen ons iets

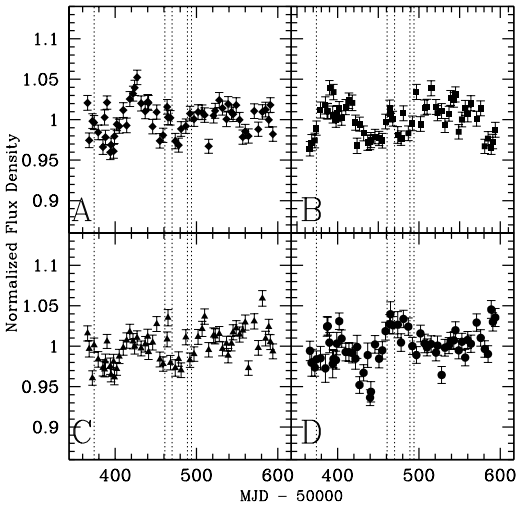

FIGUUR 10.5— De lichtkrommen van de vier radio–afbeeldingen van de gravitatielens B1608+656. Alle vier lichtkrommen laten dezelfde variaties zien, elk met een bepaalde tijdsvertraging. Door de lichtkrommen te verschuiven langs de tijdsas, totdat ze met elkaar overeenkomen, kan men deze tijdsvertraging bepalen (naar C.D.Fassnacht).

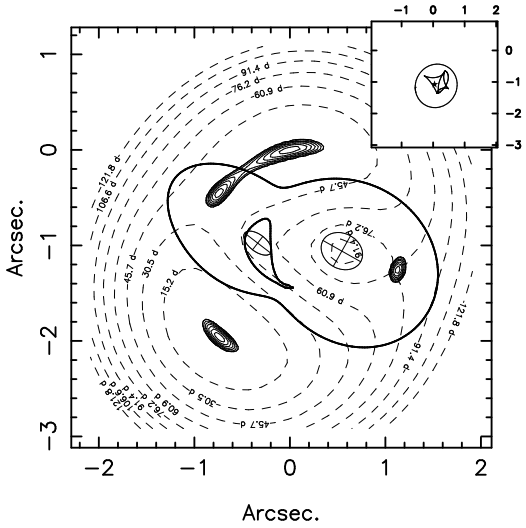

FIGUUR 10.6— Een massamodel van de gravitatielens B1608+656. De twee ellipsen geven de posities en oriëntaties van de twee lens–sterrenstelsels aan. De volle contouren beschrijven de bron afbeeldingen. De gestreepte contouren geven het tijdsverschil aan tussen de verschillende bron afbeeldingen. De andere contouren en het subpaneel duiden meer gedetaileerde eigenschappen van het model aan. Zie Figuur 10.3 voor de goede overeenkomst van de berekende bron afbeeldingen met de waarnemingen.

leren over de massaverdeling in het lens–sterrenstelsel. Maar aan de hand van B1608+656 zullen we laten zien waarom gravitatie lenzen ook een zeer krachtig 'gereedschap' zijn in de beantwoording van fundamentele vragen in de kosmologie.

In een eerdere paragraaf is uitgelegd dat we de Hubble–constante (H_0) kunnen bepalen met behulp van gravitatielenzen, namelijk door het tijdsverschil te meten waarmee licht van twee verschillende afbeeldingen van dezelfde achtergrond bron ons bereikt. We hebben daarvoor niet eens de afstand tot het sterrenstelsel nodig, maar kunnen direct uit het tijdsverschil H_0 bepalen.

Vlak na onze ontdekking van de gravitatielens B1608+656 in de CLASS–survey is een campagne gestart om deze lens geregeld waar te nemen, om zo de radio–helderheid van de vier quasars over een langere periode te bepalen. Omdat de 'lichtkrommen' identiek moeten zijn (ze zijn immers van dezelfde bron afkomstig) kan men, door ze langs de tijdas te verschuiven, het tijdsverschil tussen twee quasar afbeeldingen bepalen.

Uit de acht maanden durende campagne in 1996–1997, konden uiteindelijk drie tijdsverschillen tussen de verschillende afbeeldingsparen worden bepaald (Figuur 10.5). Het moge duidelijke zijn dat deze drie onafhankelijke tijdsverschillen een betere bepaling van H_0 geven dan slecht één enkel tijdsverschil, welke men tussen dubbele afbeeldingen kan bepalen. Aangezien er ook niet stil werd gezeten met de bepaling van een goed massa model van het lens–sterrenstelsel (Figuur 10.6), beschikten we toen over een goede relatie tussen de Hubble–constante en het tijdsverschil. Soms kunnen meerdere massamodellen de positie en helderheid van de lensafbeeldingen verklaren, waarbij elk model een andere H_0 geeft. Het is daarom van belang met goede waarnemingen het juiste massamodel te bepalen. Dit resulteerde uiteindelijk in een Hubble–constante van

$$H_0 = 59 \pm 7 \ \ \mathrm{km/s/Mpc}.$$

Hieruit volgt een leeftijd van het heelal van zo'n 8 à 10 miljard jaar (voor een gesloten

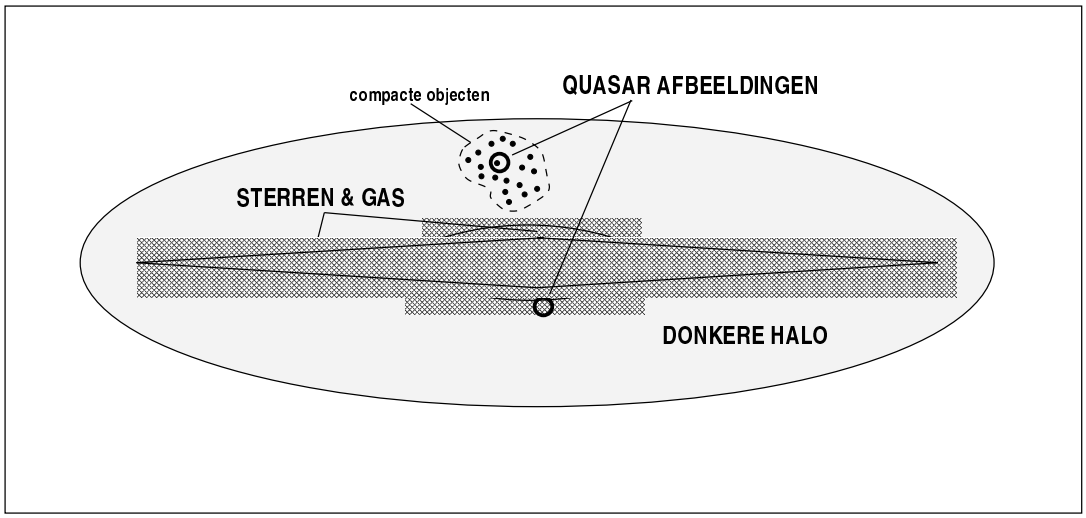

FIGUUR 10.7— Een schematisch model van de massaverdeling in het lens–sterrenstelsel van B1600+434 (zie Figuur 10.3). De dunne schijf en het enigszinds rondere centrum (beiden gearceerd) geven de plaatsen aan waar zich de sterren en het gas zich bevinden. Doordat de quasar afbeeldingen dóór de donkere materie halo worden gezien, kan men zowel de afplatting hiervan bepalen alsook de massa. In het geval de donkere materie halo bestaat uit compacte objecten, kan dit worden waargenomen als snelle variaties in de helderheden van de quasar afbeeldingen.

of kritisch heelal).

De bepaling van H_0 uit B1608+656 is op dit moment één van de meest nauwkeurige. Omdat de bepaling van H_0 geschiedt op een schaal van vele duizenden megaparsec (20%–70% van de schaal van het heelal), verwacht men geen grote verschillen tussen de uitkomsten van verschillende gravitatielenzen te vinden. Als de massa in het heelal uniform verdeeld is – en op grote schaal lijkt dit zeker het geval te zijn – moet de expansiesnelheid immers in alle richtingen nagenoeg gelijk zijn.

Hoewel slechts uit enkele andere gravitatielenzen de Hubble–constante is bepaald (zie tabel), geven ze toch al een betrouwbare indruk en lijkt het erop dat we geen grote verrassingen hoeven te verwachten. Vier van de vijf gravitatielenzen in de tabel geven een Hubble–constante van ongeveer 60–75 km/s/Mpc ligt, met een gemiddelde van ∼65 km/s/Mpc. Zowel verbeteringen van de massamodellen, alsook een nauwkeuriger bepaling van de tijdsverschillen, zal in de toekomst de Hubble–constante bepaling uit deze systemen verbeteren. Daarnaast zijn er nog diverse nieuwe lens–systemen – waaronder enkele uit de CLASS survey – die ook geschikt zijn voor de bepaling van H_0. We verwachten dan ook dat binnen enkele jaren de Hubble konstante bepaald zal zijn met een fout kleiner dan tien procent

Lens	H_0 (km/s/Mpc)
B0218+357	69±16
Q0957+561	71±14
PG1115+080	44±8
B1600+434	57±13
B1608+656	59±7
B1830−211	75±14

TABEL 10.1— Tabel met bepaling van de Hubble–constante uit verschillende gravitatie lenzen.

Gravitatie lenzen en de massaverdeling in sterrenstelsels

We hebben gezien dat bij de bepaling van de Hubble–contante met behulp van gravitatielenzen, de massaverdeling van het lens–sterrenstelsel van groot belang is.

Maar het bepalen van de massaverdeling kan op zich ook al erg interessant zijn. In het geval van B1600+434 bijvoorbeeld, zien we het spiraalstelsel van opzij (Fi-

guur 10.2) en vertelt het verschil in quasar–helderheden ons iets over de verdeling van de 'donkere materie' rond dit sterrenstelsel. Modellen van dit sterrenstelsel laten zien dat deze donkere materie waarschijnlijk niet in de schijf van het sterrenstelsel zit (daar waar zich gas and sterren bevinden), maar een meer bolvormige verdeling moet hebben (Figuur 10.6). Bovendien draagt de donkere materie halo aanzienlijk bij aan de totale massa in de binnendelen van dit sterrenstelsel. Dit laatste is vooral van belang bij het begrijpen van de bijdragen van lichte en donkere materie aan de snelheid waarmee het gas en de sterren rond het centrum van het sterrenstelsel draaien.

Bovendien, helderheidsveranderingen van de quasar afbeeldingen hoeven niet alleen het gevolg te zijn van variabiliteit van de bron zelf, maar kunnen ook veroorzaakt worden doordat de donkere materie uit compacte objecten bestaat, vergelijkbaar in massa met sterren. Wanneer deze objecten zich voor de quasar afbeeldingen bewegen, veroorzaken ze variabiliteit in de waargenomen helderheid. Een nauwkeurige bestudering van deze helderheidsveranderingen kan ons iets leren over de aard van de donkere materie.

Onlangs lieten de lichtkrommen van de twee quasar afbeeldingen in B1600+434 precies dit soort sterke variaties zien. We denken dan ook dat de donkere materie halo van dit lens–sterrenstelsel gevuld is met compacte objecten, misschien wel steroverblijfselen of zwarte gaten! Dit zou de eerste detectie van dit soort objecten zijn op hogere roodverschuiving.

De toekomst

We hebben laten zien dat gravitatielenzen op veel terreinen toepassingen kennnen. Eén van de meest aansprekende daarvan is natuurlijk de bepaling van de afmeting en leeftijd van het heelal. Maar de aard en verdeling van de donkere materie, in individuele en groepen van melkwegstelsels, zal een steeds belangrijkere rol gaan spelen in dit onderzoek.

Hoewel niet besproken, zijn gravitatie lenzen verder ook uitstekende proefobjecten die ons iets vertellen over het interstellaire medium in de lens–sterrenstelsels. Bovendien kunnen ze ons ooit vertellen of er echt 'donkere materie' melkwegstelsels zijn, die geen licht uitstralen, en wat de geometrie (kromming) van de ruimte is.

"In deze Nederlandse samenvatting heb ik geprobeerd een aantal aspecten, die in mijn proefschift naar voren komen, in simpele bewoordingen uit te leggen. Natuurlijk is het onmogelijk het hele proefschrift uitvoerig te behandelen en ik heb daarom gekozen voor een tweetal aansprekende voorbeelden: de expansie-snelheid van het heelal en de bepaling van de eigenschappen van de donkere materie rond een lens–sterrenstelsel op kosmologische afstand. De lezer die hierdoor geïnteresseerd is geraakt en meer wil weten, kan een poging ondernemen de rest van het proefschrift ook te lezen."

Acknowledgments

FIRST and foremost, I would like to thank my promotor Ger de Bruyn for finding the precise balance between giving me the freedom to pursue some of my own research interests, but not let me fly off in the wrong direction. I sincerely appreciate the amount of time and effort he spend in helping me to shape the work in this thesis, both scientifically and in its appearance. In this, his knowledge on almost any conceivable subject in astronomy has been essential.

I would also like to thank all my other collaborators in the *Cosmic Lens All–Sky Survey*: Andy Biggs, Roger Blandford, Ian Browne, Chris Fassnacht, Phillip Helbig, Neal Jackson, Dan Marlow, Steve Myers, Sunita Nair, Martin Norbury, Tim Pearson, Paul Phillips, Tony Readhead, David Rusin, Peter Wilkinson and Emily Xanthopoulos. Also without them this thesis would not have existed. In particular, I pay credit to Ian, who manages both the CERES and CLASS collaborations. I have enjoyed working more closely with Andy, Chris, Phillip, Dan, David and Emily on different projects and hope to continue this in the future. Although back in India now, I have enjoyed the many long discussions with Sunita Nair about many different subjects and thank her for introducing me in the art of gravitational–lens modeling. Similarly, I enjoyed the discussions with Phillip.

I would like to thank all those at the *Kapteyn Institute* who have made my 4–year stay as a PhD–student an unforgettable and invaluable experience. It is impossible to personally name everybody from whom I have learned new things, both in and outside of science. I would like to thank all the staff that keep the institute running and in particular Rien, Penny, Koen, Frank and Bob for interesting conversations.

I have enjoyed the company and long discussions with and between my roommates Henk and Inigo. I thank Willem for his humor, often placing things in perspective. Furthermore, I am indebted to the entire PhD & post-doc community, also those that have left the institute already, for all they contributed to making my stay a pleasant one; Hanadi, Jocelyn, Marco, Jeronimo, Roelof, Adwin, Erwin, Enzo, Jan, Stéphanie, Jane, Martin, Mercedes, Joris, César, Jim, Rolf, Jorge, Jacquie, Hans, Michiel, Wendy, Leticia, Richard, Mark, Els, Peter, Tim, Emilio, Aaron, Remco, Diah, Ronald, Marc, Wim and Martin, my thanks!

In the little spare time you have as a PhD–student, I enjoyed the interesting pool games with Wim, Hans, Tim and all the other voluntary victims. Thinking about it still gives me a headache. I have always enjoyed going to good restaurants and movies with Christiaan and Erwin. Similarly, I will not forget all those parties, especially the one at Jean–Philippe's place! I thank Marc Verheyen and Allen Roy for making my three–week visit to Socorro into one not to forget. Chris, thanks for showing me the ways of Caltech. I enjoyed it.

I thank all those that have made it financially possible to carry out my work: NWO, CERES, LKBF, NWO–SIR and the Kapteyn Institute for providing a work–place.

Niet te vergeten, bedank ik mijn moeder en broer, die mij altijd hebben gesteund in wat ik wilde doen!

Léon Koopmans
Groningen, December 1999